

All the tests were performed considering the ASTM C 393 standard test method in 3 point bending, Fig. 3 a), and 4 point bending in quarter point loading, Fig. 3 b).

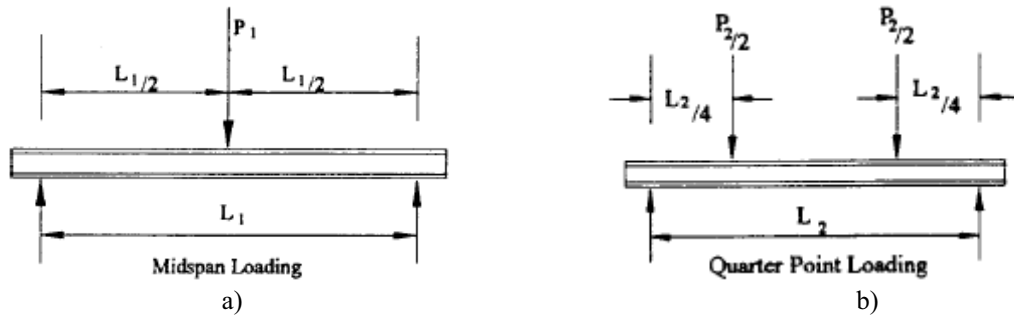


Figure 3: ASTM C 393 loading methods: a) Three point bending; b) Quarter-point four point bending

The 3 point bending tests were performed in a servo-hydraulic Instron 8502 universal test machine with a 30 kN loading cell and all of the 4 point bending tests were performed in a electro-mechanical Instron 3369 universal test machine with a 30 kN loading cell. All specimens were tested at a loading rate of 6.0 mm/min until failure occurs in the specimens. Load and correspondent deflection were taken from the test, and results were obtained by application of the simplified beam theory, [1]. All of the test results were plotted in load-displacement graphs, with the tests which presented facing failures being discarded from the calculations. The specimen dimensions and physical properties are shown in Tables 1 and 2.

Material	Dimensions [mm]	Density [kg.m ⁻³]
Rohacell	320x51x11	75
ECA Honeycomb	320x51x14	48

Table 1 : Dimensions and density of Rohacell and honeycomb specimens

Material	Reference	Dimensions [mm]	Grain size [mm]	Density [kg.m ⁻³]
Cork agglomerates	8303	320x50x11	1/2	224
	8123	320x50x11	1/4	270
	8810	320x50x9.5	2/3	137

Table 2 : Dimensions and physical properties of cork agglomerate specimens

3 ANALYTICAL FORMULATION USED FOR THE CALCULATION OF THE MECHANICAL PROPERTIES

This study calculated the mechanical properties using the simplified beam theory as proposed by ALLEN [1], with the final result of the deductions reproduced in this paper.

Core Shear Stress (Single-Point Midspan load):

$$\tau = \frac{P}{(d+c)b} \quad (1)$$

Where τ is the core shear stress, P is the load, d is the sandwich thickness, c is the core thickness and b is the sandwich width.

Sandwich Beam Deflection (Midspan Load):

$$\Delta = \frac{PL^3}{48D} + \frac{PL}{4U} \quad (2)$$

Where Δ is the total beam midspan deflection, U is the Panel Shear Rigidity, D is the panel bending stiffness and L is the span length.

Panel Bending Stiffness:

$$D = \frac{E_f(d^3 - c^3)b}{12} \quad (3)$$

Where E_f is the facing modulus.

Panel Shear Rigidity:

$$U = \frac{G(d+c)^2 b}{4c} \quad (4)$$

Where G is the core shear modulus.

Sandwich panel deflection (two-point load, one-quarter span):

$$\Delta = \frac{11PL^3}{768D} + \frac{PL}{8U} \quad (5)$$

4 RESULTS AND DISCUSSION

4.1 Load and displacement

Almost all of the tests performed ended with core failure in shear. The notable exceptions were the 3 point bending tests of the Rohacell and Honeycomb cores, which failed by normal compression stresses on the upper face.

All of the cork agglomerate cores showed similar crack appearance and progression, i.e., the first macroscopic crack appearance occurs on maximum load for all agglomerates, and in all of them it progressed to the specimen extremity. Figures 4 and 5 show that the cork agglomerate 8123 obtained the best 3 and 4 point bending behavior, supporting the highest loads with averages loads of 311N and 211N, respectively, although at a much higher displacement in the 3 point bending tests.

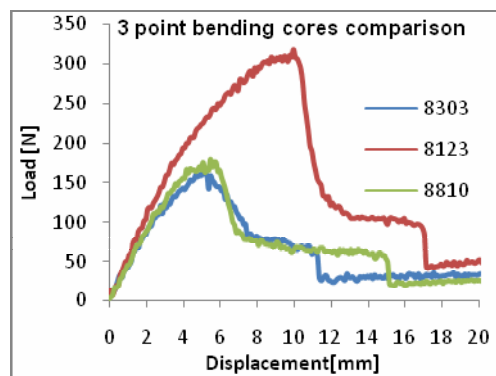


Figure 4: Three point bending cork agglomerate cores comparison

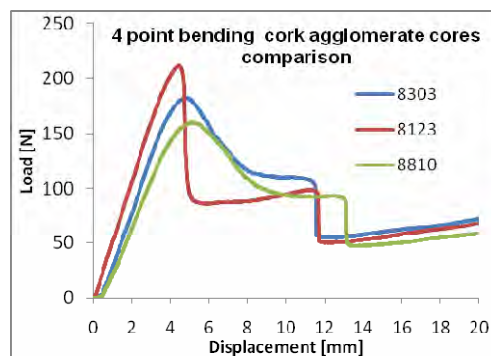


Figure 5: Four point bending cork agglomerate cores comparison

The Rohacell and Honeycomb cores, as mentioned in the beginning of this section, failed by normal compression stresses in the upper faces. This can be seen in Figures 6 and 7. The Rohacell cores also exhibited debonding failure in two of the tests, attributed to poor

fabrication. In four point bending, both core types failed in core shear, with the Rohacell cores obtaining the highest average load at 1658 N, well ahead of the cork agglomerate cores. Table 3 presents the results obtained.

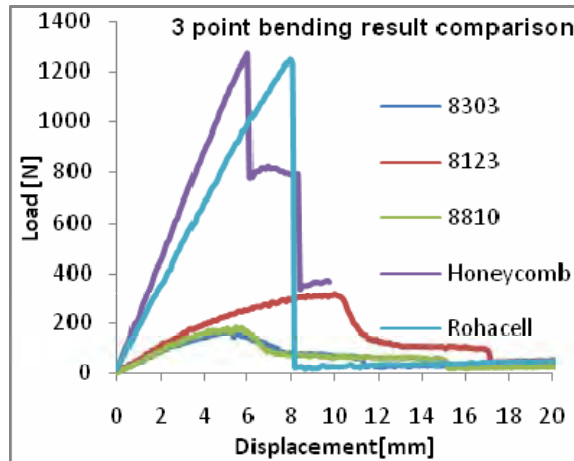


Figure 6: Three point bending comparison

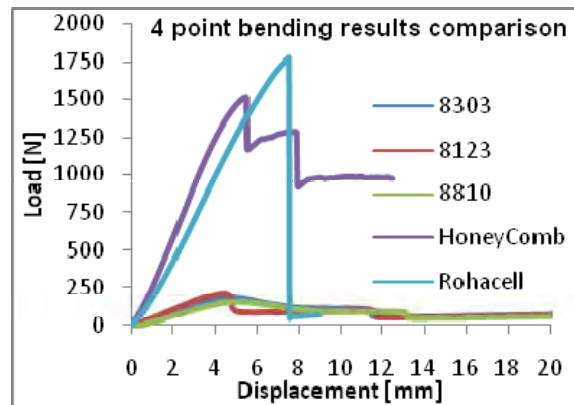


Figure 7: Four point bending comparison

	3 point bending					4 point bending				
	8303	8123	8810	Honey comb	Rohacell	8303	8123	8810	Honey comb	Rohacell
Load Avg. [N]	173	311	181	1253	1224	180	211	167	1479	1658
Displacement Avg. [mm]	5,16	9,59	5,10	5,92	7,99	4,84	4,55	4,93	5,44	7,48

Table 3 : Load and Displacement averages in 3 and 4 point bending

4.2 Specimen behavior in bending

Figures 8 and 9 show the typical behavior of the cork agglomerates in the 3 and 4 point bending tests. It can be summarized the bending specimen behavior in three stages: In Fig.(s) 8 and 9: a) test start; b) macroscopic crack appearance and progression; c) crack progression to the specimen extremity.

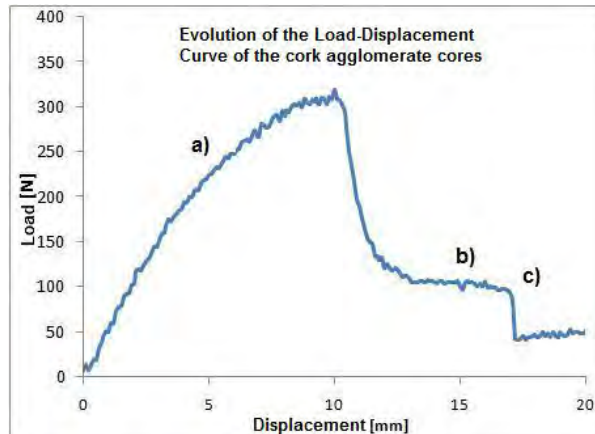


Figure 8: Evolution of the load-displacement curve of the Cork agglomerate cores in bending

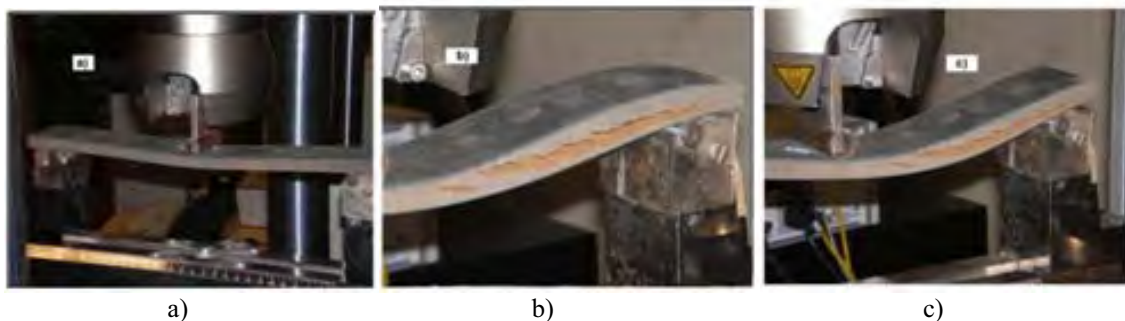


Figure 9: Specimen progression in bending: a) test start; b) crack appearance and propagation; c) crack propagation ends at the specimen extremity

As mentioned in section 4.1, all of the 3 point bending tests of Rohacell and Honeycomb cores were discarded since the failure did not occur in the cores. Fig.(s) 10 and 11 show the typical failure mode of the Honeycomb core specimens: a) Crushing of the facing in compression, followed by b) core collapse. The Rohacell cores presented two different modes of failure, as shown in Fig.(s) 12 and 13: a) core failure in the compression facing; b) facing debonding.

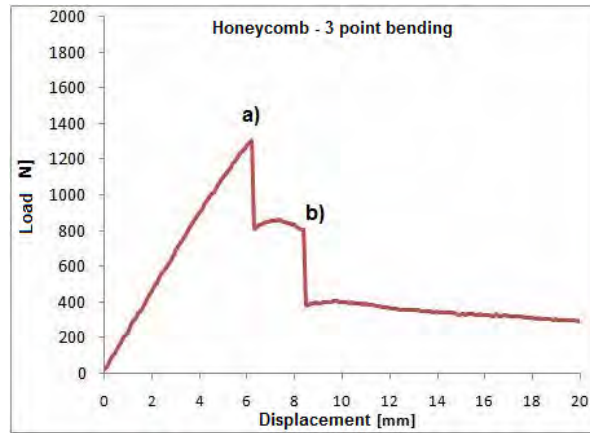


Figure 10: Three point bending behavior of honeycomb cores



Figure 11: Failure sequence of the Honeycomb core specimens: a) Crushing of the facing in compression; b) core collapse

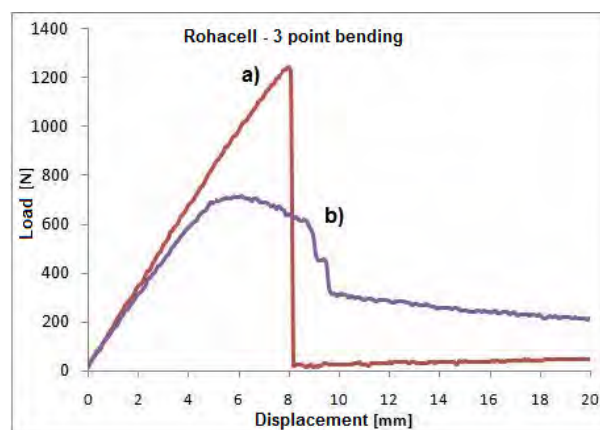


Figure 12: Three point bending behavior of Rohacell cores



Figure 13: Rohacell modes of failure: a) core failure in the compression facing; b) facing debonding

4.3 Core shear stress

The average values obtained in the core shear failure, see Table 4, can be considered constant for the cork agglomerate 8810 and 8303 specimens, which indicates that, for these specimens, the compressive stresses and bending moments that may have appeared in the 3 point bending tests have a negligible effect on the core shear stress.

	Three point bending					Four point bending				
	8303	8123	8810	Honey comb	Rohacell	8303	8123	8810	Honey comb	Rohacell
Avg. Core Shear Stress [MPa]	0,173	0,311	0,201	0,945	1,200	0,180	0,211	0,186	1,115	1,625

Table 4: Average core shear stress values

The cork agglomerates 8123 specimens show a very significant drop in the core shear stress values from the 3 point bending test to the 4 point bending test, as had happened with the average displacement and average loads with a 30% difference between values, but maintaining the biggest core shear stress values of all the cork agglomerate specimens. The Rohacell and Honeycomb specimens cannot be compared between test sets, since the average core shear values in the 3 point bending tests are merely the core shear stress value at the time of the facing failures. In fact, had the Honeycomb specimens possessed the same thickness as the Rohacell specimens, the core shear stress values would have fallen in the same range, as in the average load, in the 3 point bending test. In the 4 point bending test, the Rohacell specimens, obtained the highest core shear stress average value, 1,625MPa, followed by the Honeycomb specimens with 1,115MPa.

4.4 Core shear modulus

Table 5 shows the average core shear modulus in the 3 and 4 point bending tests. As explained in section 4.1, it is not possible to calculate the core shear modulus of the

Rohacell and Honeycomb cores, since the failure occurred in the facings and not in the core. In the 3 point bending tests, the cork agglomerate 8123 obtained the lowest value of core shear modulus of all the cork agglomerate specimens, since the core shear modulus, G , is inversely proportional to the displacement, or deflection, and the cork agglomerates 8123 present the highest average value of displacement of all cork agglomerate specimens. However, by looking at Fig. 4, the specimens 8123 have a much higher load applied at the displacement in which failure occurs in the 8810 and 8303 specimens. This presents an interesting paradox, since by being able to withstand greater loads, cause smaller values of G , due to the higher displacement failure. This paradox is explained in section 4.5.

In the 4 point bending tests, the 8123 specimens obtain the highest average values of G due to the highest average load values, as in the 3 point bending tests, but now with the average displacement values closer to the other cork agglomerate specimens.

The Honeycomb and Rohacell specimens have a much higher average value of G than the cork agglomerate specimens, with the Rohacell specimens achieving the highest core shear modulus, G , of all the specimens with an average of 17,9 MPa.

The presented values serve only as comparison, since the facings influence cannot be neglected, even though the formulation used to obtain the values of G tries to compensate for this influence.

Material	Three point bending			Four point bending				
	8303	8123	8810	8303	8123	8810	Honey comb	Rohacell
Core shear stress Avg. [MPa]	4,789	4,618	5,374	2,619	3,318	2,502	14,845	17,913

Table 5: Average core shear modulus values

4.5 Core shear modulus variation in the 3 point bending tests

As referred in section 4.4, the cork agglomerate 8123 specimens obtained the lowest values of Core shear modulus, G , even though it presented the highest load values at the failure of the cork agglomerate cores 8810 and 8123.

This section tries to ascertain why this happened, by applying formulas (2) through (5) at all of the load displacement pair of values obtained in the 3 point bending tests.

Fig. 14 shows the result of these calculations in a core shear modulus vs. displacement graph. Analyzing Fig. 14, it can be observed that the value of G of the cork agglomerate 8123 is higher than the values of G of the cork agglomerate 8303 and 8810 specimens when these cores fail. However, given the ability of the cork agglomerate 8123 cores to withstand greater bending, the value of G continues to diminish until, at the displacement when failure finally occurs, it is lower than the values of the cork agglomerates 8810 and 8303.

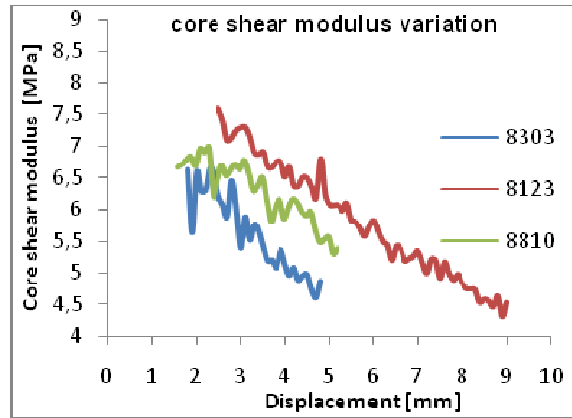


Figure 14: Core Shear modulus variation vs. Displacement in 3 point bending

It can then be considered that the cork agglomerates 8123 specimens are better than the other cork agglomerates due to the fact that, not only the 8123 specimens are able to withstand greater loads and displacements, but they also provide constantly higher values of G in all loading spectrum, until the failure of the other cork agglomerate cores.

4.6 Comparison with results obtained by Silva et al. [3]

Table 6 shows the comparison between the study results and manufacturer's data and Table 7 shows the comparison between the study and the results obtained by Silva et al. [3], that tested the same cork agglomerate specimens, but using the ASTM C 273 standard test method.

The values of G obtained in the tests, Table 6, are about half of those provided by the manufacturers, coinciding with what was pointed out by Nordstrand, [4].

As Table 7 shows, the results of the cork agglomerate specimens are different than those obtained by Silva et al., in the 3 point bending tests with the best cork agglomerate specimens being 8810 and the worst 8123 in this study, while the tests performed by Silva et al. were the opposite.

In the 4 point bending tests the values of G are qualitatively the same, although with lower average values of the core shear modulus.

Values of G [MPa]	Paper results	Manufacturer's data
Rohacell	17,9	42
Honeycomb	15,531	38 (L) 24 (W)

Table 6: Comparison between paper results and manufacturer's data

Avg. values of G	Paper results		Silva et al. results
	3 point bending	4 point bending	
8303	4,789	2,619	4,38
8123	4,618	3,318	4,86
8810	5,374	2,502	2,46

Table 7: Comparison between paper's results and results obtained by Silva et al. [3]

5 CONCLUSIONS

After reviewing the whole study it can be concluded that:

- The cork agglomerate specimens 8810 and 8303 present similar load-displacement curves, indicating a common behavior under load.
- The cork agglomerate specimens 8123 present a completely different behavior between the 3 and 4 point bending tests. It was concluded that the fact that the 3 point bending test has roughly twice the volume being deformed, allow the specimens 8123 to withstand higher loads.
- All of the cork agglomerate specimens have the same failure modes, with a crack with a 45° orientation appearing at maximum load, progressing the to the specimens extremity.
- In all the tests, the Honeycomb and the Rohacell cores obtained much higher values than the cork agglomerate specimens, indication that there is still a long road ahead for the cork agglomerate cores to become competitive in its mechanical properties.
- In all the results obtained, maximum loads, core shear stresses and core shear modulus, there is a clear relation between grain size/ density and behavior of the cork agglomerate specimens. The smaller the grain size and the higher the density, the better the results are for the cork agglomerate specimens.

ACKNOWLEDGMENTS

The authors acknowledge the support from Corticeira Amorim Indústria, SA, for providing the raw materials for testing, as well as all the technical details necessary to test and evaluate the natural cork composites. Also, the support of OGMA, SA is greatly appreciated.

REFERENCES

- [1] H. G. Allen, H. G., "Analysis and Design of Structural Sandwich Panels". Oxford New York, Pergamon, (1969).
- [2] ASTM C 393; Standard Test Method for Flexural Properties of Sandwich Constructions. American Society for Testing and Materials Annual Book of ASTM Standards, (2000).
- [3] A. Silva, J. Lopes, P. Almeida, L. Reis and M Leite, "Experimental Testing of a Natural Cork-Based Composite, (2006).
- [4] T. M. Nordstrand and L. A. Carlsson, "Evaluation of transverse shear stiffness of structural core sandwich plates". *Composite Structures* 37(2),145-153 (1997).

METHODS OF EXPERIMENTAL DETERMINATION OF SOFT CORE PARAMETERS IN SANDWICH PANELS

Monika Chuda-Kowalska, Andrzej Garstecki and Zbigniew Pozorski

Faculty of Civil Engineering
Poznan University of Technology
ul. Piotrowo 5, 60-965 Poznan, Poland
e-mail: monika.chuda.kowalska@ikb.poznan.pl

Key words: Sandwich structures, Shear modulus, Experimental mechanics, Numerical modeling.

Summary. *Experimental determination of shear stiffness parameters is discussed. New method based on measurements of plate rotational angles was presented and used. Obtained results were compared with results of classical methods basing on vertical displacement measurements.*

1 INTRODUCTION

Sandwich panels with flat or slightly profiled thin steel facings and a thick soft core are considered in the paper. Static and dynamic response of such structures depends strongly on mechanical parameters of the core. Therefore, it is very important to precisely monitor experimentally mechanical parameters of the core in the production process. In the class of panels under consideration the Young modulus of the core E_C is 30÷40 times smaller than the modulus E_F of the steel cover sheets. Therefore, in engineering practice it is acceptable to neglect the normal stress in the core. Hence, the critical parameter of the core is the Kirchhoff modulus G_C . Indeed, experiments and computer simulations prove that this coefficient strongly influences the mechanical response of a panel. Proper assumption of G_C is crucial in design for both, serviceability and ultimate limit states.

This modulus can be determined in different tests proposed in the literature and in the code [4]. Unfortunately, large scatter of results is observed when these methods are used in tests of panels of variable dimensions. In this paper various testing methods are surveyed. A new method for experimental determination of G_C is proposed. A large number of tests carried out by the authors using different methods is described. The values of coefficients G_C determined from these tests are studied in view of their applicability to numerical models, which should correctly predict the response of a sandwich panel under different loading and support conditions. The numerical models are based on Timoshenko beam and Reissner plate theories generalized to sandwich structures [1, 6]. Advanced computer simulation [5, 2] using ABAQUS system and employing shell finite elements for cover layers and 3-D elements for the core is carried out, too.

2 METHODS OF DETERMINATION OF SOFT CORE PARAMETERS

In practice, mechanical parameters of sandwich structures with soft core are determined by the way of indirect methods recommended in the literature and in the code [4]. These methods are based on bending and shear tests of panels with measurement of the transverse displacement w . These experiments are much easier than direct methods carried out on samples cut out of core. In the present paper another indirect method will be proposed and studied, namely tests with the measurement of angles of rotation instead the transverse displacement. We refer the considerations to sandwich panels, which consist of polyurethane core and micro-profiled steel facings. Overall depth of the panels is 120 mm. The thickness of the face sheet is 0.47 mm. In the analyzed class of panels we can assume that material of core is isotropic and the elastic modulus of the core E_C equals zero. The results obtained from different methods will be compared and discussed.

2.1 Tests on short panels

In short panels we can observe that basic damage mechanism is shear failure of the core. Hence, the limit shear strength and the shear modulus of elasticity can be determined indirectly from the four-point test of bending of a short panel (Fig. 1b). The span L should be sufficiently small to induce failure mechanism by shear of the core. Hence, usually $L = 1000$ mm is used. Two types of samples are used: beam like strips with the width 100 mm and panels of the actual width. The loads are increased and the deflection w in the middle point of the span is recorded till the failure occurs. It is assumed, that the deflection can be decomposed $w = w_B + w_S$ in such a way, that w_B and w_S represent the deflections due to bending and shear, respectively. Since the Young modulus E_F of steel facing is known, evaluation of w_B is relatively easy and precise. Knowing $w_S = w - w_B$ one can compute G_C from respective formulae basing on a chosen theoretical model of the sandwich panel. Fig. 1a shows a typical load - displacement relation $F - w_S$ obtained in experiments carried out by the authors. Note that the relation is non-linear. Softening in the range of higher stress is observed. In fact softening in time appeared, too. Thus, the linear part of the function $F(w_S)$ was used for the assessment of the modulus G_C .

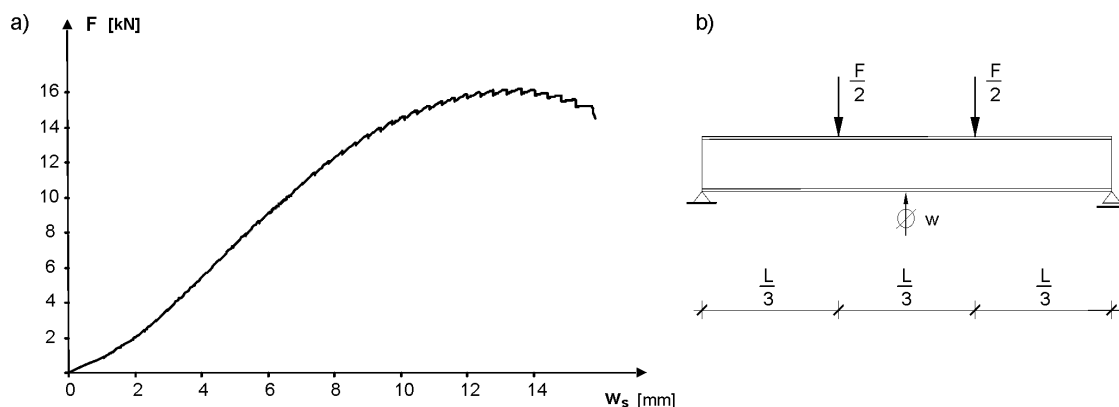


Figure 1: a) Typical load – displacement curve F/w_S , b) 4-point bending test

In case of a 4-point bending (Fig. 1b) of a panel with flat facing, the following formulae follow from the Timoshenko theory generalized to sandwich beams:

$$w_B = \frac{23 \cdot F \cdot L^3}{1296 \cdot B_S}, \quad (1)$$

$$B_S = \frac{E_{F1} \cdot A_{F1} \cdot E_{F2} \cdot A_{F2}}{E_{F1} \cdot A_{F1} + E_{F2} \cdot A_{F2}} \cdot e^2, \quad (2)$$

where B_S represents the flexural rigidity, A_{F1} , A_{F2} , and E_{F1} , E_{F2} denote the area and the Young modulus of facings, respectively. The distance between centers of facings is e . Next, the shear modulus G_C can be evaluated from

$$G_C = \frac{\Delta F \cdot L}{6 \cdot B \cdot d_C \cdot \Delta w_S}, \quad (3)$$

where d_C is depth of the core and B is width of the specimen.

2.2 Identification of core material by tests on long panels

Experiments carried out on the panels, in which the span L is relatively large, first of all is used to determine the bending strength of panels. However, this test can also be used for identification of the shear modulus of the core in a panel with flat or lightly profiled faces.

The length of span is definitely larger than in shear tests described in subsection 2.1. It must guarantee that the failure in bending occurs starting from local buckling of the compressed facing.

The method of identification of G_C is similar as presented above. However, a larger span L results in an increased role of bending in relation to the shear. Despite the reduced role of shear, the identified value of G_C well describes the mechanical response of panels with greater span lengths.

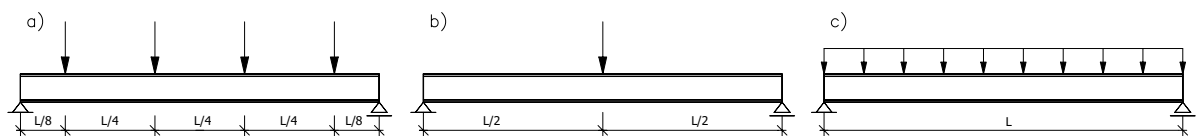


Figure 2: Loading systems used in bending tests

The Authors used three loading systems shown in Fig. 2 and the displacement was always considered in the middle point of the span. The respective formulae referring to the loading systems 2a and 2b are:

a) four line loads – Fig.2a:

$$w_B = \frac{41 \cdot F \cdot L^3}{3072 \cdot B_S}, \quad G_C = \frac{F \cdot L}{8 \cdot B \cdot d_C \cdot (w - w_B)}, \quad (4)$$

b) one line load – Fig. 2b:

$$w_B = \frac{F \cdot L^3}{48 \cdot B_S}, \quad G_C = \frac{F \cdot L}{4 \cdot B \cdot d_C \cdot (w - w_B)}, \quad (5)$$

where w denotes the measured displacement and $w - w_B = w_S$.

The methods described in section 2.1 and 2.2 were used for the comparison with the results obtained from the measurements of angles of rotation, described in subsection 3.

3 MESUREMENT OF ANGLES OF ROTATION

3.1 Assumptions

In classical theory of sandwich panels with a soft core [1] it is assumed that: the materials of steel facings and foam core are isotropic, homogeneous and linearly elastic; the facings are parallel; normal stress in the foam core is negligible ($\tau_{xz} = 0$); the shear stresses are constant in transverse direction ($\tau_{xz} = \tau_{yz} = \text{const.}$) and the in-plane strains ε_x , ε_y and γ_{xy} are small compared to unity. The considerations are limited to small strains and displacements (linear geometric relations). Shear stresses and strains in the facings are neglected, hence, the Bernoulli hypothesis can be applied independently for both facings. The shear deformation of the core makes that normal element 1-4 before deformation becomes piecewise linear 1'-2'-3'-4' after deformation (cf. Figs. 3a and 3b). Similarly as in Timoshenko beam theory one can distinguish between the angle of rotation α_0 of the normal element 1-4 and the slope of the facings represented by the angle $\gamma_0 = \gamma_{01} = \gamma_{02}$. In our measurements a small difference between angle γ_{01} and γ_{02} was observed, therefore we used $\gamma_0 = 0.5(\gamma_{01} + \gamma_{02})$. Note that the formulae (1) to (5) have been derived using the similar assumptions as described above.

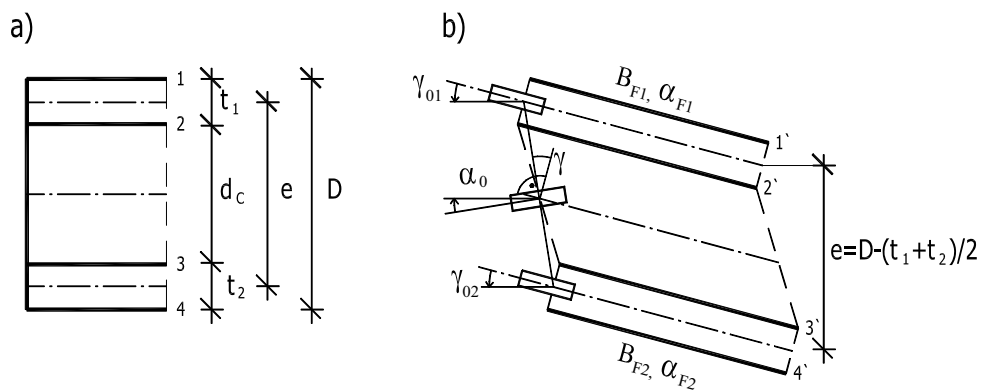


Figure 3: Cross sections of a panel a) before deformation, b) after deformation

3.2 Assessment the shear modulus of the core

Following Timoshenko theory, the shear contributes to the slope by an angle γ

$$\gamma = \gamma_0 - \alpha_0 \quad (6)$$

where γ_0 is the total slope of deflection line and α_0 is the angle of rotation of the normal element. Note that in Fig. 3b the angle γ_0 is denoted in clockwise direction, whereas α_0 is counter-clockwise oriented. In our experiments variable orientation of α_0 was observed. In the frame of the hitherto assumptions we can write

$$G_c = \frac{T}{\gamma \cdot B \cdot d_c}, \quad (7)$$

where T denotes the shear force and d_c is depth of the core.

3.3 Testing stand and apparatus

The angles γ_{01} , γ_{02} and α_0 were measured using laser pointers attached to the panel in the vicinity of the support and a precise leveling staff standing in a distance of 4 m from the lasers. The diameter of the laser light beams was 2 mm. The accuracy of measurement the angles was 0.0005 rad. The testing stand is shown on the Fig. 4a.

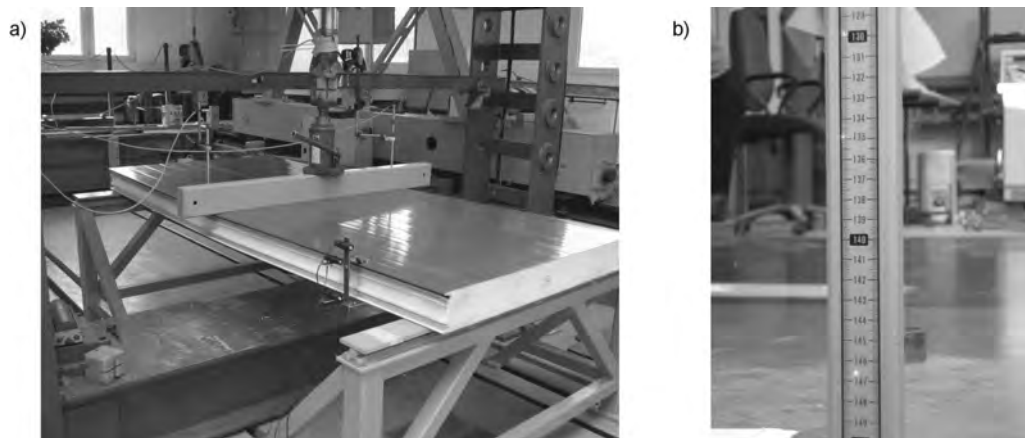


Figure 4: Testing stand a) the plate with laser modules, b) leveling staff with light points

3.3 Testing method

Three laser pointers were attached to the panel (Figs. 4a,b and 5b). Two of them are attached to upper and lower facings. They indicate the angles γ_{01} and γ_{02} , respectively. The middle one is attached to the section of a panel in such a way that it indicates the angle α_0 . The positions of the laser light points at the leveling staff were recorded for increasing values of the load. The displacements of these light points divided by the distance of the leveling

staff $L_1 + L_2$ gave the rotation angle in radians. Simultaneously the deflection of the middle point of the panel (Fig. 5a) was measured to compare the values of G_C resulting from different methods. The tests were carried out in normal temperature and humidity.

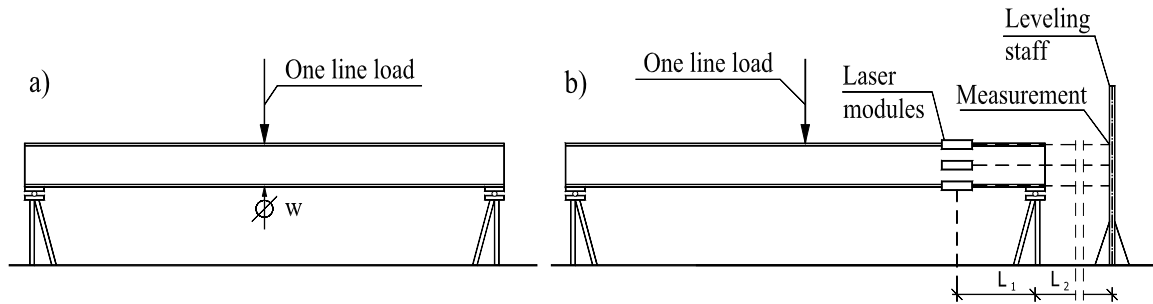


Figure 5: The testing stands for identification of G_C a) Measurement of displacements, b) Measurement of rotation angles

4 NUMERICAL ANALYSIS

Basing on experimental and theoretical results, numerical model of sandwich panel was created. The numerical examples refer to structures investigated in real scale during laboratory experiments. Numerical models were prepared in ABAQUS system environment. The analysis was carried out for two various spans: $L = 0.888$ m (short panel) and $L = 5.4$ m (long panel), overall depth $D = 120$ mm, depth of core $d_c = 119.53$ mm, and width $B = 1.1$ m.

Steel facings were assumed as elastic material. Typical material parameters are: the Young modulus $E_F = 210$ GPa, the Poisson ratio $\nu_F = 0.3$ and the yield stress $f_y = 270$ MPa. Both facings have the same thickness $t = 0.47$ mm.

Facings were modeled using four node, doubly curved, thin or thick shell, reduced integration, hourglass control, finite membrane strains elements S4R. The core of the panel was modeled using eight node linear brick elements C3D8R. Important point of the model is a connection between facings and core elements. Interaction TIE was applied, which keeps all active degrees of freedom equal at two nodes.

Support conditions refer to real structures. Therefore, it was assumed that a base plate modeled as rigid body is lying at both support. Reference points describing respective boundary conditions of the whole support are localized in the middle of contact surface between lower face sheet and the supporting plate. For the left supporting base plate all three translations and the rotations with respect to axes x and z are equal to zero. Unconstrained rotation with respect to the axis y is assumed. The right base plate has additionally the possibility of the translation in the direction x .

The numerical model developed in this paper and assumed material parameters were validated by the way of experiments. Final numerical results were compared with experimental and theoretical ones and presented in the section 5.

Example 1 ($L = 0.888\text{ m}$)

At the beginning we considered simply supported plate, one span sandwich panel with the length $L = 0.888\text{ m}$ and width $B = 1.1\text{ m}$. The geometry of the structure is presented on the Fig.6. Width of the support is $b = 100\text{ mm}$. The sandwich structure was subjected to two line loads acting on the upper facing. Shell elements S4R has dimension $4 \times 4\text{ cm}$. Its thickness is $t = 0.47\text{ mm}$. Brick element has dimension $4 \times 4 \times 4\text{ cm}$.

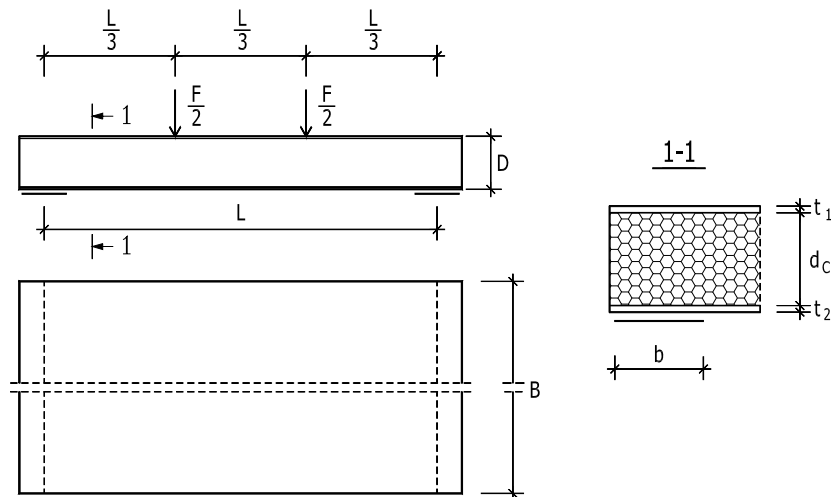


Figure 6:Geometry of sandwich panel

An example of behavior panels and its deformation under loads is presented on the Fig.7.

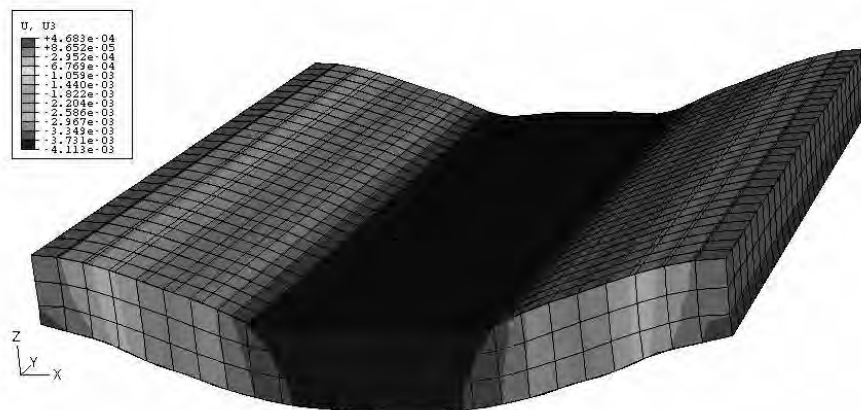


Figure 7: Deformation and displacement of short sandwich panel

Example 2 ($L = 5.4$ m)

In this example we considered simply supported plate, one span sandwich panel with the length $L = 5.4$ m and width $B = 1.1$ m. Width of the support is $b = 100$ mm. The sandwich structure was subjected to one line load acting on the upper facing in the mid-span. Shell elements S4R has dimension 5×5 cm. Its thickness is $t = 0.47$ mm. Brick element has dimension $4 \times 4 \times 4$ cm.



Figure 8: Deformation and displacement of long sandwich panel

5 VERIFICATION OF PROPOSED METHOD

Experiments carried out on the sandwich panels consist of two lightly profiled steel facings ($t_1 = t_2 = 0.47$ mm) and polyurethane foam core (PUR). The density of the foam core is 40 kg/m^3 . The tests were executed on the short and long panels. The results of mentioned tests are presented in subsection 5.1 and 5.2. The numerical 3-D models were validated and the obtained results were compared and presented in Tabs. 2 and 4.

All symbols presented in the tables were explained on the Figs. 3 and 5 and described in the Section 3.

5.1 Tests on short panels

The panels with the full width B and the span $L = 888$ mm were tested. Laser modules were located in the distance $L_1 = 150$ mm and leveling staff was situated $L_2 = 3000$ mm from the support.

In the experimental tests, displacements w , rotation angles of the facings γ and a rotation of normal element α_0 are measured. The shear modulus G_C was calculated in two ways. In the first case we used measured displacements w , equations (1-3) and procedure described in the code [4]. The second way consists in measurement of rotation angles and application of

equations (6) and (7). The results obtained in the tests are presented in the Table 1. Unfortunately, the results received into these two methods differ more than 30%. The reasons of such discrepancies are still investigated.

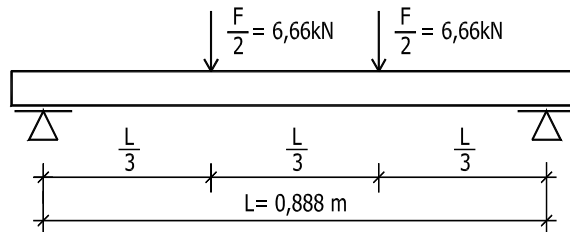


Figure 9: Scheme of loading system used to 4-point shear test

	γ_{01}	γ_{02}	α_0	w	γ	G_C
	[rad]	[rad]	[rad]	[mm]	[rad]	[MPa]
MEASUREMENT OF ANGLES OF ROTATION	0.006377	0.008149	-0.000498	-	0.0077601	6.60
MEASUREMENT OF DISPLACEMENT	-	-	-	3.98	-	4.06

Table 1 : Experimental results from short panel

At the next stage we would like to verify if the created numerical model corresponds to the analytical one. Therefore, introducing $G_C = 4.06$ MPa, the displacements γ and w were calculated using theoretical model presented in [1] and numerical model 3-D. Please note that in the analytical model, the values of Young modulus and Poisson ratio of the core are not required.

	G_C	E_C	ν_C	γ	w
	[MPa]	[MPa]	[-]	[rad]	[mm]
ANALYTICAL MODEL	4.06	-	-	0.012611	3.95
NUMERICAL MODEL	4.06	8.50	0.05	0.011737	3.94

Table 2 : Theoretical results from short panel

The results presented in the Table 2 confirm that these models give similar results, however, differences in γ are about 6.7%. It is caused by relatively large local deformations in the vicinity of supports and applied loads. It can be observed on the Fig. 7. Similar effects occur in the laboratory tests.

5.2 Tests on long panels

The experiments for the panels with the span $L = 5400$ mm were carried out. In this case, the leveling staff was located 2200 mm or 3800 mm from the middle of support. Laser modules were located in the different distances L_1 equal to: 300 mm, 1200 mm and 2300 mm. The results obtained in the tests are presented in the Table 3.

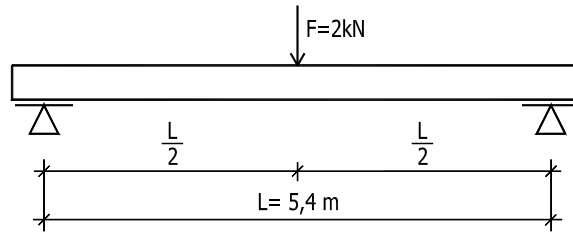


Figure 10: Scheme of loading system used to bending test

	L_1	γ_{01}	γ_{02}	α_0	w	γ	G_C
	[mm]	[rad]	[rad]	[rad]	[mm]	[rad]	[MPa]
MEASUREMENT OF ANGLES OF ROTATION	300	0.005170	0.005168	0.003691	-	0.001478	5.20
	1200	0.003477	0.003671	0.001957		0.001617	4.76
	2300	0.000278	0.000277	-0.001361		0.001638	4.70
MEASUREMENT OF DISPLACEMENT	-	-	-	-	14.10	-	3.83

Table 3 : Experimental results from long panel

	G_C	E_C	ν_C	L_1	γ	w
	[MPa]	[MPa]	[-]	[mm]	[rad]	[mm]
ANALYTICAL MODEL	3.80	-	-	-	0.002007	13.99
NUMERICAL MODEL	3.80	7.98	0.05	300	0.001968	13.83
				1200	0.001973	
				2300	0.001971	

Table 4 : Theoretical results from long panel

Similarity as in the tests described in the section 5.1, the two methods of identification of the G_C provide different results. We are not able to calibrate neither numerical nor analytical models to simultaneously fulfill measured displacements w and γ . The real experiments were carried out many times and the results are recurrent. It leads to the conclusion that the models are not suitable or there are certain errors in the laboratory procedure or results interpretation.

6 CONCLUDING REMARKS

The numerical analysis, theoretical study and experimental tests proved, that behavior of sandwich panels is a complex problem, especially determination of shear modulus.

A group of methods proposed in [4] and in the literature is based on the bending tests of panels and measurement of the transverse displacement w . In the method proposed by the authors similar bending test is carried out, but instead of transverse displacement, two angles of rotation are measured in the vicinity of a support, namely total rotation of cross section and the slope of deflection line. In our method, G_C is computed from the angle due to shear. The authors used also the test of direct shear, where the shear stress τ is induced and the strain γ is measured. Now, it follows directly $G_C = \tau/\gamma$. This test is the best from theoretical point of view, however, the evaluation of G_C from bending tests seems to be worth of interest. The first reason is that the tests are simple. Moreover, since the coefficient G_C is needed for simulations of mechanical behavior of slabs in the state of bending and shear, therefore determination of G_C from tests of slabs in this state of stress seems to be reasonable. Hence, the conclusion is that the discrepancies in G_C determined from different bending tests do not result from improper testing methods, but from the theory inadequately capturing shear effects in simplified approaches to sandwich panels with a soft core.

REFERENCES

- [1] K. Stamm, H. Witte, *Sandwichkonstruktionen*, Berechnung, Fertigung, Springer-Verlag, Wien 1974.
- [2] N.J. Mills: *Polymer foams handbook. Engineering and Biomechanics Applications and Design Guide*, Butterworth – Heiemann, 2007.
- [3] C.M. Wang, J.N. Reddy, K.H. Lee, *Shear deformable beams and plates. Relationships with Classical Solutions*, Elsevier 2000.
- [4] prEN 14509 *Self-supporting double skin metal faced insulating panels-Factory made products-Specifications*, 2004.
- [5] M. Chuda-Kowalska, A. Garstecki, Z. Pozorski, R. Studziński, *Numerical modelling of sandwich panels with deep profiled facings*, Proc. of the 17th International Conference on Computer Methods in Mechanics, Łódź -Spała, Poland (2007).
- [6] M.D. Hayes, *Structural analysis of a pultruded composite beam. Shear stiffness determination and strength and fatigue life predictions*, Dissertation of the Virginia Polytechnic, Blacksburg, Virginia, 2003.
- [7] J.R. Hutchinson, *Shear coefficients for Timoshenko beam theory*, Journal of Applied Mechanics, pp. 68 – 87, 2001.

ACKNOWLEDGMENT

Financial support by Poznan University of Technology BW 11-004/2008 is kindly acknowledged.

NONDESTRUCTIVE EVALUATION OF SANDWICH STRUCTURES

David K. Hsu

Center for Nondestructive Evaluation
Iowa State University, Ames, Iowa, USA 50011
e-mail: dkhsu@iastate.edu

Key words: Nondestructive Evaluation, Sandwich structures, Honeycomb.

Summary. *This paper is a summary of 15 years of research and development conducted by the author's group at Iowa State University for the nondestructive evaluation (NDE) of sandwich structures in aviation, space, and marine applications. The targets of inspection include manufacture defects, in-service damage due to human and natural causes, and the inspection of repairs on sandwich structures. The emphases adopted in the development of NDE techniques and instruments for sandwich structures are imaging capability, quantitative inspection, and the ease of use in the field. This paper describes the various NDE methods for sandwich structures, especially those techniques and instruments developed at Iowa State University that had gone through the research, development, and field test stages.*

1 INTRODUCTION

Adhesively bonded sandwich structures, with its advantages of light weight, design flexibility, high specific-stiffness, and good specific-strength, is attractive structural material and are therefore widely used in aviation, space, and marine applications. The facesheet (skin) and core of sandwich structures can encompass a myriad of materials, both composite and metallic. Composite sandwiches of carbon fiber reinforced plastic (CFRP) facesheet and Nomex or fiberglass honeycomb core are ubiquitous on airplanes and are frequently used as flight control surfaces, such as rudder skin panels, spoilers, elevator trims and for making engine nacelles. Sandwiches of glass fiber composite (GFRP) facesheet and honeycomb core are widely used as fairings, floor boards, and for making radomes. Metallic sandwich structures, especially aluminum facesheet over aluminum honeycomb, are widely used as slat wedge, trailing edge, ailerons on aircraft and in satellite structures. Mixed composite and metallic sandwiches, including CFRP skin and aluminum honeycomb core, have found space applications, and foam-cored sandwich structures are used in helicopter blades and in boat building.

The nondestructive evaluation (NDE) of sandwich structures can be divided into two categories: inspection of manufacturing defects for quality assurance purposes and in-service inspection for damage originated from natural or human causes. Manufacturing defects of concern include delamination in the composite facesheet, disbond between the facesheet and the core, foreign object inclusions, and porosity in the composite skins. While in service, sandwich structures can suffer damage or degradation that require periodic inspection or

repair. The primary concern in composite sandwiches is damage caused by foreign object impact, especially those caused by low velocity foreign objects that defy visual detection. Other damage can be attributed to static overload, fatigue, and environmental factors such as water ingress, heat, chemical, ultraviolet radiation, extreme temperature excursion, and lightning strike. In composite sandwich structures with Nomex or fiberglass honeycomb core, an impact can cause a fracture or buckle of the honeycomb cell walls, usually leading to a crescent shaped damage profile (a “smiley face”) located below the skin-to-core adhesive bondline. The lowest point of the fracture can be located well below the impacted facesheet, sometimes at a depth of almost one half of the core thickness. Low velocity impact damage rarely causes a disbond at the adhesive fillet between the facesheet and the core, but can lead to delaminations in the facesheet if it is a multi-ply laminate. The damage morphology of foam-cored composite sandwich with CFRP or GFRP facesheet resembles that of an impacted honeycomb core. The impact can cause extensive cell breakage and lead to the formation of fracture and large voids in the foam. Like honeycomb sandwiches with composite facesheet, the foam-cored sandwich can also suffer substantial internal damage without leaving visible indication on the surface [1].

The fractured and crushed honeycomb core in a sandwich are sources for nonlinear mechanical response and energy dissipation. When a damaged sandwich is subjected to a compressive static load, the load-displacement curve becomes nonlinear and the loading and unloading curves combine to form a hysteresis loop. The area enclosed by the loop is a measure of the energy dissipation or the severity of the damage. In contrast, an undamaged sandwich would show a linear load-displacement curve, with little or no hysteresis, and a higher slope or stiffness than the damaged case. The mechanical hysteretic behavior of damaged sandwich structures can be exploited in the nondestructive evaluation of the degree of internal damage in a sandwich [2].

For sandwiches with aluminum honeycomb core, the impact damage morphology is quite different from that of brittle composite honeycomb cores [3]. The failure mode of the ductile aluminum honeycomb core under impact or static loading is a buckling of the cell walls. When the load exceeds the “bare compressive strength” of the honeycomb cells, the cell walls fail suddenly by buckling and the load drops down to a constant “crush strength” of the cell structure. The buckling initiates at the top where the load is applied and propagates downward. For a CFRP sandwich with aluminum honeycomb core, the spring back of the CFRP facesheet may cause a disbond with the buckled core. For a honeycomb sandwich with aluminum skin and core, an impact causes a permanent dent of the skin and a buckled honeycomb core that often remains bonded to the skin.

2. NONDESTRUCTIVE EVALUATION OF SANDWICH STRUCTURES

Sandwich structures in aviation, space, and marine applications generally have a good safety record, although there were major events attributed to failures of sandwich structures. For example, the loss of an F-15E fighter in the United States in 2002 was attributed to a structural failure of the honeycomb material in a vertical stabilizer leading edge. In March 2005, the rudder on a (Canadian) Air Transat A310-300 separated in flight over the

Caribbean, see photo in Fig. 1, but the plane managed to return and land in Cuba [4]. The composite rudders on A300s and A310s are made of honeycomb sandwich panels. Structural failures like these have affected the inspection and maintenance practice of critical, load-bearing sandwich structures on airplanes.



Figure 1. In-service failure of a critical composite sandwich structure in March, 2005.

A number of NDE modalities are available for inspecting sandwich structures [5]. Ultrasonic inspection in the transmission mode, using waves in the megahertz range and facilitated with water squirter scanners, is probably the most widely used inspection method by the manufacturers of sandwich structures for airplanes. The unique feature of the honeycomb core is that the cell walls serve as the path for the propagation of the sound energy from one facesheet to the other. A through-transmission ultrasonic (TTU) scan of a honeycomb sandwich will reveal a number of defects and damage, including foreign object inclusions in the laminated composite facesheets or in the adhesive bond between a facesheet and the core, delaminations of the facesheets, and the fracture, buckling, or crinkle of the cell walls caused by impact damage. In recent years, the technology of non-contact, air-coupled ultrasonic inspection has also gained maturity and began to find applications [6]. (Air-coupled ultrasonic NDE will be discussed in greater detail in Section 4 below.) X-ray radiography and thermography are effective methods for detecting water ingress in sandwich structures. Thermography and thermal wave imaging are capable of detecting delaminations, disbond, and impact damage [7]. Another non-contact NDE method, laser shearography has been proven effective in the inspection of sandwich structures [8]. The application of shearography requires the application of a stress disturbance to the structure, either by mechanical means (such as a vacuum) or by thermal means (lamp, hot air). Electromagnetic methods of NDE are applicable to metallic sandwich structures but are ineffective on CFRP or GFRP composites. However, the impact damage of aluminum honeycomb core under a CFRP

facesheet with no visual indication of damage can be detected and imaged using eddy current. Finally sandwich structures have historically been inspected with simpler mechanical means of inspection, including manual tap test and low frequency bond test techniques [9]. Bond testing techniques generally include mechanical impedance analysis (MIA), low frequency resonance method, and pitch-catch mode. The author's group at Iowa State University has devoted considerable effort on the development of an instrumented tap tester with quantitative and imaging capability for inspecting sandwich structures. The instrumented tap tester will be discussed in Section 3.2 below.

3. TAP TEST OF SANDWICH STRUCTURES

The practice of tapping a sandwich structure with a mass to detect defect or damage based on the sound it makes is probably the most widely used nondestructive inspection in the field over the years. This inexpensive technique, despite its qualitative and subjective nature, is reasonably effective for thin-skinned sandwich structures. The tap test is a local test (as opposed to a global test like a wheel tap), where the local stiffness of the structure determines the contact time (τ) between the mass and the surface [9]. Typical contact time for most sandwich structures is of the order of several hundreds of microseconds. The contact time is short for solid, undamaged area, whereas the contact time for a less stiff damaged region can be substantially lengthened. One important characteristic about the tap test response is that, for a given mass, the contact time τ is largely independent of the force or the velocity of tap. The test results in Fig. 2 obtained on a composite rudder skin panel using an accelerometer as the tapping mass demonstrated this effect. The accelerometer was used to tap on a good region and a damaged region of the rudder skin panel with increasingly greater force; the figure shows that the voltage output of the accelerometer is greater for harder taps, but the duration of the contact time remained roughly the same.

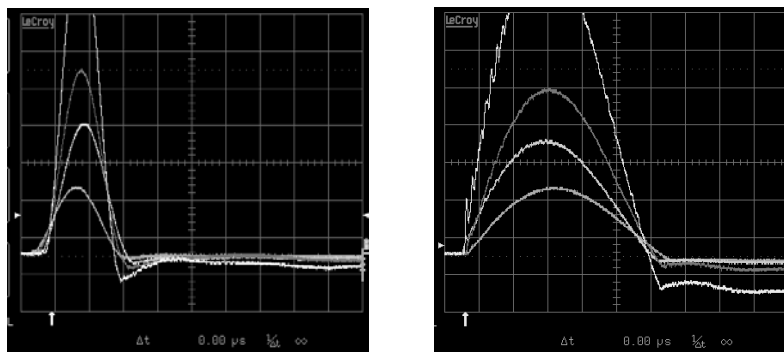


Figure 2. Voltage output of accelerometer versus time (horizontal axis, 100 μ s per division) for taps in a good region (left) and in a damaged region (right) of a honeycomb rudder skin panel.

3.1 A Simple Model of Tap Test Response

The physical basis of a tap test was analyzed and reported previously [10]. A simple model captures the relationship between the contact time and the local stiffness of the structure. Since the tap response, shown in Fig. 2, resembles one half a cycle of a sine wave, one may model the vibrating surface as that of a grounded spring with a spring constant k , upon which a mass m is dropped. Thus, $\tau = 1/2f = \pi/\omega = \pi (m/k)^{1/2}$. This simple approximate relationship shows that the contact time depends on the local stiffness k of the surface and on the mass m . A greater stiffness corresponds to a shorter contact time. It also allows one to deduce the local stiffness of the structure from the measured contact time τ and the known mass of the tapper m . We have compared the local stiffness at locations of different damage severity on a number of composite honeycomb sandwich panels, deduced from tap test contact time using the formula $k = m (\pi/\tau)^2$, with the stiffness measured experimentally at the same locations in static compressive loading tests. The stiffness deduced from the tap test contact time agreed quite well with the mechanically measured stiffness [11], as shown in Fig. 3. This indicated that quantitative information, namely the stiffness in units of Newtons per meter, can be derived from a simple tap test. This has then become the impetus for developing an instrumented tap tester with the capability of mapping out the location, size, shape, as well as the severity (stiffness reduction) of damages on sandwich structures.

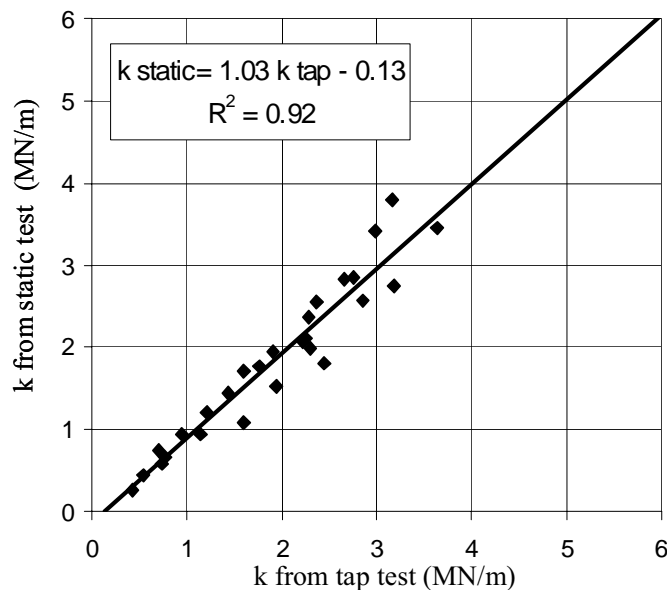


Figure 3. Agreement of stiffness deduced from tap test and measured directly in static test for locations of different damage severity on composite honeycomb sandwich panels.

3.2 Application of Instrumented Tap Tester

In order to elevate the tap test from a qualitative, operator-dependent manual check into an instrumented, quantitative, field-usable tool with imaging capability, a system known as the Computer Aided Tap Tester (CATT) was developed at Iowa State University [12]. The system makes use of a piezoelectric accelerometer as the tapping mass and measures the

contact time between the mass and the surface with an electronic timing circuit. To improve the inspection speed and the consistency of the tapping, a semi-automated cart can be pushed across the surface while the accelerometer taps on the surface in its up-and-down vibration driven by the repulsive forces between magnets contained in the cart [13]. The contact time data can be converted into the local stiffness of the surface and both may be displayed as an image during the test. The CATT had been extensively tested in the field on a variety of composite and aluminum sandwich structures [14]. It has been proven particularly effective for mapping out disbond and impact damage in various flight control components and helicopter rotor blades. The images produced by the CATT may be used in the planning of repairs or for making accept/reject decisions. Figure 4 shows the CATT used in the verification of the soundness of a repair made on a UH-60 Black Hawk helicopter blade. The CATT scan image showed that the repair was good and there were no voids or disbonds.

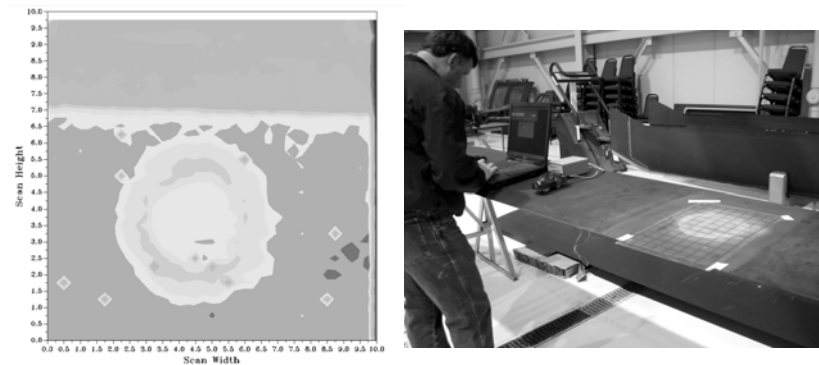


Figure 4. Verification of a 13 cm (5") diameter repair on a composite rotor blade of a Black Hawk helicopter using the Computer Aided Tap Tester (CATT).

The CATT instrument was also used in the damage assessment of a large composite sandwich structure. When the American Airlines flight 587, an Airbus A300, crashed in Belle Harbor, New York in November 2001 [15], the damages on the recovered rudder were mapped out with the CATT. The A300 rudder, measuring approximately 8.5 m (28 ft) tall, is box-like composite structure with honeycomb-cored sandwich panels as its skins and front spar. The CATT was used to scan 90 x 60 cm (3 x 2 ft) areas at a rate of approximately 12 to 15 minutes per scan. All the scan images, with a combined total area of nearly 40 square meters (400 ft²) were assembled to form the image of the whole structure shown in Fig. 5. The figure shows the scan images of the inner and outer surfaces of the left and right skins, as well as the front spar of the rudder. The fracture pattern and failure conditions revealed by the scan images served as part of the data gathered in the investigation.

3.3 Mechanical Hysteresis and Tap Test

The energy dissipative nature of internal damages caused by impact on a sandwich structure leads to nonlinear load-displacement curves and mechanical hysteresis loops. As the damage severity increases, the area enclosed by the hysteresis loop increases and the average

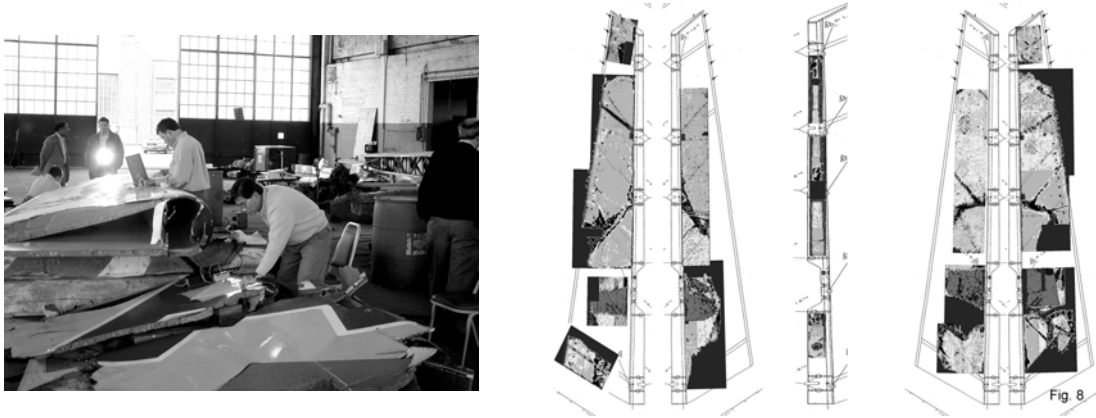


Figure 5. CATT scan images of the composite rudder of the crashed flight AA587 in November, 2001.

slope (stiffness) decreases. Figure 6 shows the hysteresis loops obtained on a thin-walled CFRP/Nomex honeycomb sandwich with damages induced by impact energies of 0.7, 1.3, 1.8, 3.4, 4.0, and 4.7 Joules respectively going from left to right.

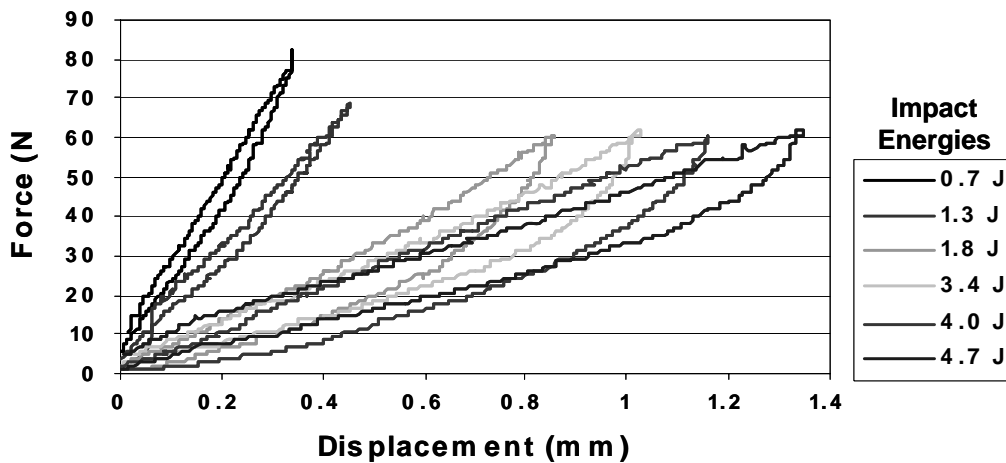


Figure 6. Mechanical hysteresis loops of damages on a CFRP/Nomex honeycomb sandwich caused by increasing impact energies (from left to right).

Although the results in Fig. 6 suggest a means for evaluating the severity of internal damage in sandwich structures, the compressive loading test requires two sided access and is not conducive to applications in the field. We therefore explored the relationship between the response to a quasi-static loading and the dynamic response to a tap test on the surface. In a tap test using an accelerometer as the tapping mass, the voltage output as a function of time is a bell shaped curve. Knowing the sensitivity of the accelerometer (e.g., 10 mV/g) and its mass, one can convert the output to a force-time curve. To obtain the force-displacement

curve, one needs the displacement-versus-time response of the tap test to convert the force-time history into a hysteresis loop of a load-versus-displacement plot. To do so, one can integrate the acceleration-versus-time curve twice to obtain the displacement-versus-time curve. Upon combining this with the force-time curve, one arrives at the (dynamic) load-displacement curve. Figure 7 below shows the acceleration, velocity, and displacement, all as a function of time, of a tap made by a 10.4 gram accelerometer on the surface of a composite sandwich. Figure 8(a) shows a comparison of the hysteresis loop obtained from a quasi-static load test and from a tap test of the same impact damage site caused by 4.04J of impact energy. Figure 8(b) shows that, after normalizing both the force and the displacement axes, the static

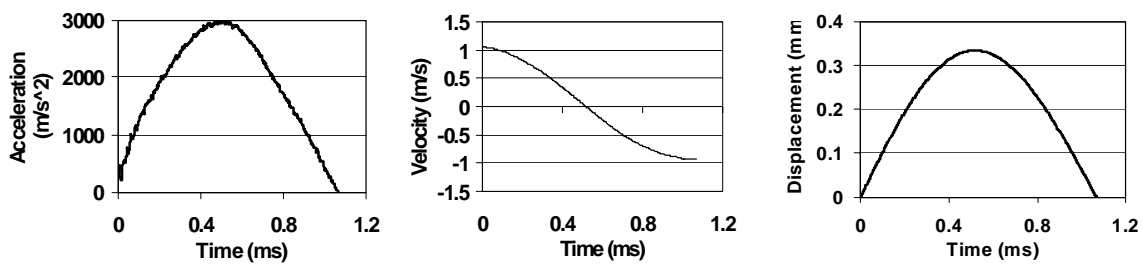


Figure 7. Dynamic response of a tap test: acceleration, velocity, and displacement as functions of time. Velocity and displacement were obtained by consecutive integration of the acceleration data.

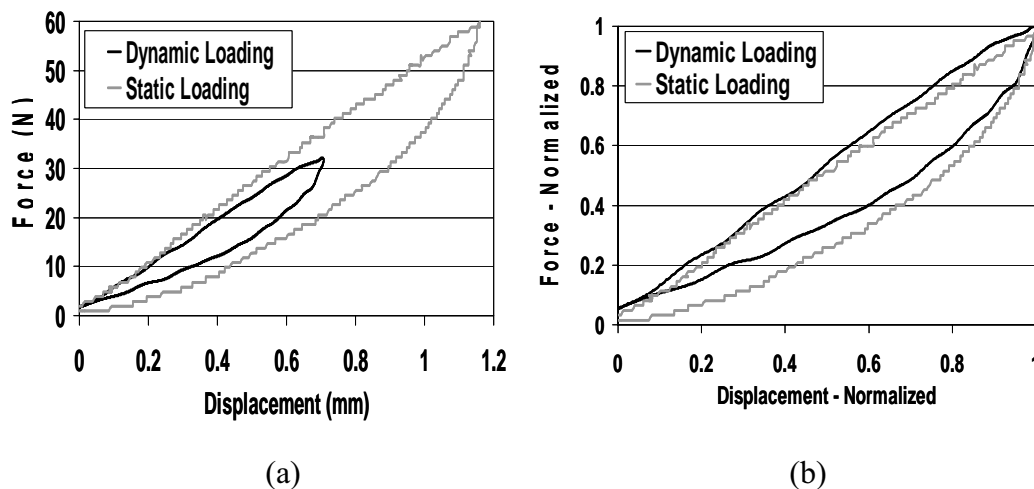


Figure 8. (a) Hysteresis loops obtained in a static test and deduced from a tap test. Note that the peak loads were different. (b) Normalized load-displacement curves showing good agreement between hysteresis loops obtained statically and dynamically.

hysteresis loop and the dynamic hysteresis loop have the same shape and slope. This demonstrated the feasibility of evaluating the damage-induced mechanical hysteresis with a simple tap test on the outer surface of a composite sandwich. Work is underway in the development of instrumental setup for performing consistent and controlled tap test and the necessary data acquisition and processing software.

4. NDE OF SANDWICH STRUCTURES WITH AIR-COUPLED ULTRASOUND

In the area of air-coupled ultrasound for nondestructive inspection of structures, there has been considerable progress in the technology of transduction. The performance and capabilities of air-coupled piezoceramic transducers, composite transducers, and electrostatic capacitive transducers have all made significant advances in the last two decades [16]. Air-coupled ultrasonic inspection of sandwich structures is typically conducted in the 50 kHz to 400 kHz range. Air-coupled ultrasound has the obvious advantage that it is non-contact, non-contaminating, and free from liquid or gel couplants. However, the primary challenge in air-coupled ultrasonic NDE is the enormous acoustic impedance difference between that of air and a solid. As a result, the energy transmission coefficient from air to a CFRP solid laminate is only about 0.04%, as compared to 75% for the water-solid interface. To overcome this extremely inefficient energy transfer between a gas and a solid, air-coupled ultrasonic instruments must be operated at very high gain and often aided by external low noise pre-amplifiers. In addition, the transmitting transducer is driven with a high voltage long toneburst in order to increase the energy content, and hence the penetrating power, of the sound wave. A combination of the low transmission efficiency and the long pulse length has so far prevented the usual pulse-echo mode of flaw detection from being achievable. Nonetheless, air-coupled through transmission ultrasonic scans have proven quite valuable in the NDE of sandwich structures, especially for components with perforated facesheets where water-coupled ultrasound is difficult to apply.

4.1 Air-Coupled Ultrasonic Imaging of Honeycomb Sandwiches

Sandwich structures with honeycomb core are widely used as flight control surfaces on airplanes, such as spoilers, flaps, rudders, slats, and trailing edge. Since these components do have two-sided access, air-coupled ultrasonic transmission inspection is appropriate. Since the transmission of airborne ultrasound through an empty cell of a honeycomb sandwich would encounter four air-solid interfaces, the transmitted signal would not be detectable; the transmission of the ultrasonic energy through the honeycomb core therefore takes place along the cell walls. The usual construction of the honeycomb core is such that each hexagonal cell is enclosed by two double-walls and four single-walls. A double-wall is where the adhesive layer joins one cell to the next adjacent cell. It was also observed that, in honeycomb panels containing large cells, the double-walls were the locations for the highest transmitted amplitude, as shown in Fig. 9. Here the scan image revealed three flaws (skin-to-core discontinuity) and a background of hexagonal honeycomb pattern. When the beam of the air-coupled ultrasound is unfocused and broad, and when the cells of the honeycomb are small, the individual cells and the hexagon pattern of the honeycomb would not be discernable. Furthermore, when a number of cells are illuminated by a broad beam, the periodicity of the honeycomb core would sometimes behave like a two-dimensional diffraction grating and lead to interference fringes in the image.

It should be pointed out that, due to the large ratio of the acoustic impedances of solid and air, the transmission of air-coupled ultrasonic energy through a solid plate is dominated by

resonance phenomenon. High transmissions occur at frequencies where the thickness of the plate matches integral multiples of a half wavelength. Theoretically, the transmission of a monochromatic plane wave is non-zero only at the resonance frequencies. In reality, the finite bandwidth of the toneburst ultrasonic waves makes the contrast not as severe, but the

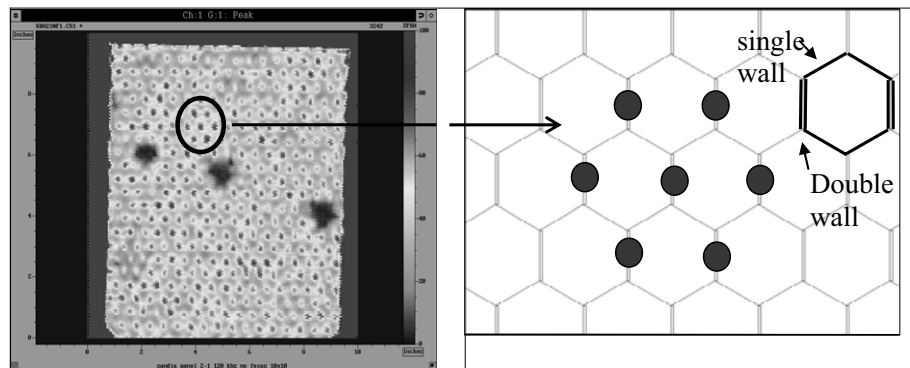


Figure 9. Air-coupled ultrasonic transmission scan image of a large-celled honeycomb sandwich using focused 120 kHz transducers.

resonance effects still dominate the transmission through solid plates. Similar phenomenon can also be observed in more complex structures. For example, when air-coupled ultrasonic transmission scan was performed on a honeycomb sandwich containing embedded solid cylindrical metallic inserts that served as attachment hard-points, extraordinarily high transmission through the cylindrical insert was observed at certain frequencies. Finite element modeling of the vibration modes of the metallic insert verified that the high transmissions corresponded to the frequencies where the cylindrical metal insert exhibited a strong resonance in its length mode [17].

4.2 Probability of Detection (POD) of Air-Coupled Ultrasonic NDE

In sandwich structures, air-coupled ultrasonic transmission scans can readily reveal the presence of foreign object inclusions, disbonds between the facesheet and the core, delaminations in the facesheet, and damages of the core caused by impact or static overloading. The defects and damage usually appear as regions of reduced transmission amplitude, as shown in Fig. 9. To assess the sensitivity of flaw detection by air-coupled ultrasound, Iowa State University participated in a large scale study of nondestructive inspection of flaws in composite sandwich structures organized by the Airworthiness Validation Center (AANC) at the Sandia National Laboratory. In the round-robin study, we performed flaw imaging scans for a large set of test panels that consisted of 42 GFRP and CFRP honeycomb sandwiches measuring 46 cm x 46 cm (18 x 18 inches) and containing a variety of engineered flaws and induced damage. The air-coupled ultrasonic transmission scan images of all the panels were analyzed by AANC to determine the probability of detection (POD) of the technique; the results are shown in Fig. 10. The results showed that 12

mm (0.5”) diameter flaws can be detected in sandwich panels with 3-ply carbon skin with 90% POD. In 9-ply GFRP skinned honeycomb panels, 25 mm (1”) diameter flaws can be detected with 90% POD. Air-coupled ultrasound transmission was found to have one of the highest probabilities of detection among the NDE techniques evaluated in the study.

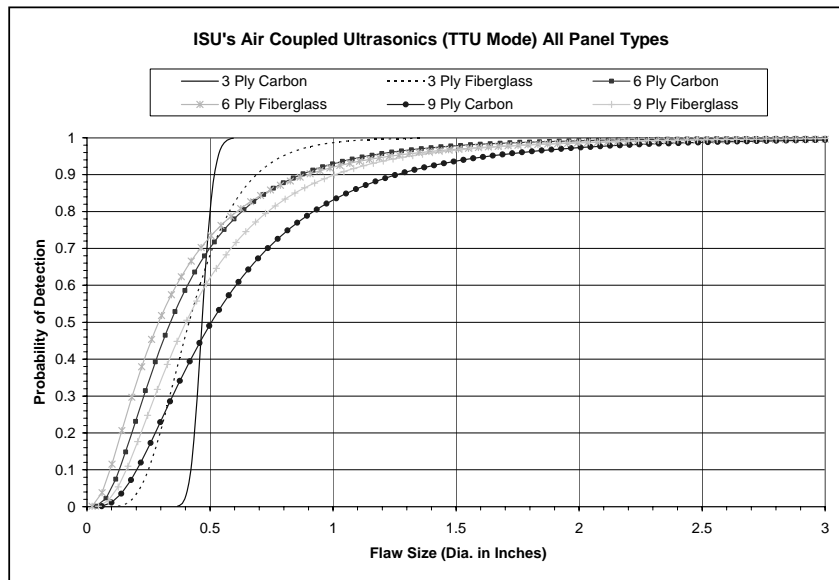


Figure 10. Probability of detection (POD) curves of air-coupled ultrasonic transmission for defects of different size in honeycomb sandwiches with carbon and fiberglass skins.

5. CONDUCTING IN-SITU NDE SCANS ON SANDWICH STRUCTURES

When inspecting a sandwich structure in the field, such as a flight control surface on an airplane, the value of a “C-scan” image (a graphical display of the NDE data as a function of the xy position) cannot be over-emphasized. The generation of a C-scan ensures full coverage of the inspected area and aids the inspector in the visual interpretation of the test results. With a visual image, flaws and damage may be differentiated from the normal substructures. However, in order for a technique or instrument to be field-usable, it must be easily portable and cannot be too complicated to operate. For example, motorized scan frames are usually too bulky to be used on airplanes. The author’s group at Iowa State University has made a sustained effort in developing field-usable NDE instruments such as the CATT described above. An effort in recent years has been the development of a generic manual scanning system (dubbed the “GenScan”) [18,19]. At the present stage, the GenScan makes use of low cost position encoding devices, such as handwriting capturing devices used in classroom or in conferences (the Mimio system [20] being one example), to track the position of the NDE probe. The tracking of the probe position and orientation can also be accomplished by using a magnetic tracker (the “Flock of Birds” [21]) designed for virtual reality and medical applications. Interface software has been developed to merge the position data and the NDE

data in order to generate the C-scan image. The system can be used with a number of NDE modalities, including ultrasound, eddy current, and bond testing techniques such as mechanical impedance analyzer (MIA). A GenScan system configured for detecting corrosion behind aluminum skin using contact mode ultrasound is shown in Fig. 11.



Figure 11. The Generic Scanner (“GenScan”) designed for generating C-scan images in the field.

The GenScan system can be configured to generate C-scan images of air-coupled through transmission ultrasonic scans of sandwich structures on aircraft. The transmitting and receiving transducers are mounted on a yoke for inspecting flight control surfaces that afford two-sided access. The position data of the aligned transducers are combined with the transmitted signal amplitude data in the generation of the C-scan image. Figure 12 shows the

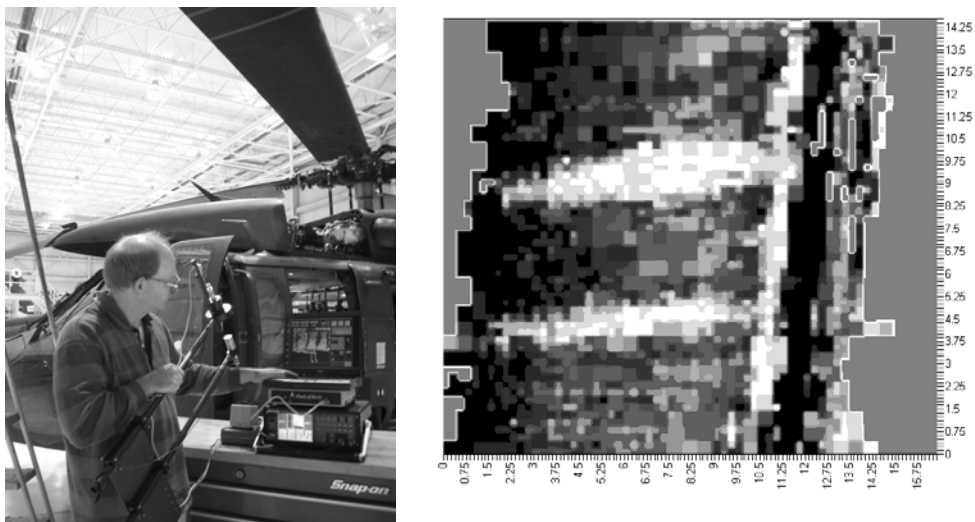


Figure 12. Inspecting helicopter rotor blade damage with air-coupled transmission ultrasonic C-scan.

inspection of tree-strike damage sustained by a helicopter rotor blade using air-coupled ultrasonic transmission and the Flock-of-Birds magnetic position tracker. In the scan image to the right, the two horizontal bands are the tree-strike damage in the circumferential direction of the blade.

6. CONCLUSION

Sandwich structures are an important class of engineering materials. New materials, new combination of skin and core materials, and new ways of construction, such as “grid-lock,” are continually being added to this class of structures. To ensure sound performance, structural integrity, and safety operation of the diverse group of sandwich structures, nondestructive inspection and testing methods will always be required. NDE results are needed to manage the accept/reject decisions and are used in the planning for repair, overhaul and refurbishment of in-service structures. The challenge on the NDE capability will continue to be the ability to not only detect the presence of the defects and damage, but the classification of the nature of the flaw and a quantitative evaluation of the severity of the damage and its effects on the performance of the structure. For sandwich structures, this would include the ability to differentiate between a skin-to-core disbond and a buckled core with the adhesive bond in tact. With the recent dramatic increase of composite usage in the aviation industry on primary, load-bearing structures, the demand on NDE capabilities will expand from sandwich structures to thick solid laminates as well. The NDE approaches and techniques described here represent only one facet of this evolving field of engineering.

7. ACKNOWLEDGMENT

This material was based upon work supported by the Federal Aviation Administration under Contract #DTFA03-98-D00008, Delivery Orders IA047 and 0038, and performed at Iowa State University's Center for NDE as part of the Center for Aviation Systems Reliability program; technical monitor is Paul Swindell, and work supported by the NSF Industry/University Cooperative Research Center for Nondestructive Evaluation of Iowa State University. The author gratefully acknowledges the contributions of D. J. Barnard, J. J. Peters, V. Dayal, Cory Foreman, Sara Blatz, Adam Donar, and Adam Kite of Iowa State University and D. Roach of Sandia National Laboratories.

REFERENCES

1. D. K. Hsu, “Nondestructive evaluation of damage in composite structures,” Proc. Amer. Soc. Composites, 21st Technical Conference, Sep 17-20, 2006, Dearborn, Michigan.
2. C. D. Foreman, M.S. Thesis, Iowa State University, May, 2008.
3. D. K. Hsu, V. Dayal, A. L. Harris, and J. J. Peters, “Buckling of aluminum honeycomb core and its effects on ultrasonic velocity,” Rev. of Prog. in Quantitative NDE, 23, 922-929 (2004), AIP, Melville, NY.

4. F. Fiorino, "Rudder Alert," *Aviation Week and Space Technology*, April 3, 2006. p.41.
5. Keith B. Armstrong and Richard T. Barrett, *Care and Repair of Advanced Composites*, Society of Automotive Engineers, Inc., Warrendale, PA 1998.
6. D. K. Hsu, "Nondestructive testing using airborne ultrasound," *Ultrasonics*, 44, Suppl 1, 1019-1024 (2006).
7. R. L. Thomas, L. D. Favro, Xiaoyang Han, and Ouyang Zhong, Vol. 5, *Comprehensive Composite Materials*, Eds. L. Carlsson, R. L. Crane, and R. Davidson, Pergamon/Elsevier Science, Oxford (2000).
8. J. Newman, "New compact, portable shearography system for composite repairs," 49th Air Transport Association NDT Forum, October 16-19, 2006, Fort Worth, Texas, USA.
9. P. Cawley and R. D. Adams, "Sensitivity of coin tap method of nondestructive testing," *Materials Evaluation*, 47, 558-563 (1989).
10. D. K. Hsu, D. J. Barnard, and J. J. Peters, "Physical basis of tap test as a quantitative imaging tool for composite structures on aircraft," *Rev. of Prog. in Quantitative NDE*, 19, 1857-1864 (2000).
11. J. J. Peters, Z. A. Nielsen, and D. K. Hsu, "Comparison of local stiffness of composite honeycomb sandwich structures measured by tap test and mechanical test," *Rev. of Prog. in Quantitative NDE*, 20, xxxxx (2001), AIP, Melville, NY.
12. J. J. Peters, D. J. Barnard, N. A. Hudelson, T. S. Simpson, and D. K. Hsu, "A prototype tap test imaging system: Initial field test results," *Rev. of Prog. in Quantitative NDE*, 19, 2053-2060 (2000), AIP, Melville, NY.
13. D. J. Barnard, J. J. Peters, and D. K. Hsu, "Development of a magnetic tapper for the computer aided tap test system," *Rev. of Prog. In Quantative NDE*, 20, 1966-1971 (2001), AIP, Melville, NY.
14. D. Roach and K. Rackow, "Improving in-service inspection of composite structures: It's a game of CATT and MAUS," NASA/FAA/DoD Aging Aircraft Conference, Sep 8 – 11, 2003, New Orleans, Louisiana.
15. NTSB website at <http://www.nts.gov/events/2001/AA587/default.htm>.
16. D. K. Hsu and D. J. Barnard, "Inspecting composites with airborne ultrasound: Through thick and thin," *Rev. of Prog. in Quantitative NDE*, 25, 991-998 (2006), AIP, Melville, NY.
17. D. K. Hsu, D. J. Barnard, J. J. Peters, and D. L. Polis, "Application of air-coupled ultrasound in NDE of composite space structures," *Rev. of Prog. in Quantitative N DE*, 23, 851-858 (2004), AIP, Melville, NY.
18. D. K. Hsu, J. J. Peters, and D. J. Barnard, "Development of fieldable systems for inspecting aircraft composite structures," *Advances in Nondestructive Evaluation*, Trans Tech Publications, Switzerland, 1845-1851 (2004).
19. D. J. Barnard and D. K. Hsu, "A scan for all seasons – development of a generic manual scan system," 9th FAA/DoD/NASA Aging Aircraft Conference, March 6-9, 2006, Atlanta, Georgia, USA.
20. Mimio[®], Virtual Ink Corporation, Boston, MA 02135, USA.
21. Flock of Birds[®], Ascension Technology Corporation, Burlington, VT 05402, USA.

EVALUATION OF NEW CRACK SUPPRESSION METHOD FOR FOAM CORE SANDWICH PANEL VIA FRACTURE TOUGHNESS TESTS AND ANALYSES UNDER MODE-I AND MODE-II TYPE CONDITIONS

Yasuo Hirose^{*}, Go Matsubara^{}, Masaki Hojo^{***} and Hirokazu Matsuda^{**}**

^{*} Commercial Aircraft Project Engineering Division, Aerospace Company, Kawasaki Heavy Industries, Ltd., 1 Kawasaki-cho, Kakamigahara City, Gifu Pref. 504-8710, Japan
e-mail: hirose_yasuo@khi.co.jp

^{**} Strength Research Department, Technical Institute, Kawasaki Heavy Industries, Ltd., 1 Kawasaki-cho, Akashi City, Hyogo Pref. 673-8666, Japan
e-mail: matubara@ati.khi.co.jp, matuda@ati.khi.co.jp

^{***} Department of Mechanical Engineering and Science, Kyoto University, Sakyo-ku, Kyoto City, Kyoto Pref. 606-8501, Japan
e-mail: hojo_cm@mech.kyoto-u.ac.jp

Key words: Foam core sandwich structures, Crack suppression.

Summary. *A new type of crack arrester was proposed for interfacial crack suppression. Analytical predictions of its performance were validated by conducting experiments under mode-I-type and mode-II-type loading conditions.*

1 INTRODUCTION

The direct replacement of metal as an aircraft structural material is most commonly carried out by applying composite materials. However, owing to the incumbent concept for metal integral structures, the full potential of composite materials (i.e., weight and part count reduction) has not been yet realized. A foam core sandwich panel structure is a promising concept for integral structures [1-4]. However, an interfacial crack between the surface skin and the core has a critical effect on the structural integrity of foam core sandwich panels by degrading the static and fatigue strength [5]. The suppression of this interfacial crack is a significant issue in applying foam core sandwich panels to aircraft structures. Although various fundamental studies on the foam core sandwich panel have been conducted [6-9], there has been little research on crack suppression methods [10]. The authors previously proposed a new simple structural element to suppress interfacial crack propagation in the foam core sandwich panel and evaluated it analytically [11]. In this paper, we mainly describe the experimental validation of our analysis under mode I-type and mode II-type loading conditions.

A new type of crack arrester was proposed to suppress interfacial crack propagation. It was

considered that a different material on the crack propagation path with higher stiffness would suppress crack propagation [12]. The concept of the crack arrester is shown in Fig. 1. An arrester with a semicylindrical shape was selected to avoid the unfavorable stress concentration on its periphery and to achieve high manufacturing efficiency.

2 ANALYTICAL ESTIMATION

2.1 ANALYTICAL PROCEDURE

Two different FE models, with and without the crack arrester, consisting of 4 plies of surface skins and a foam core were prepared. The material in the surface skin was Toho Tenax UT500/#135, the twill weave fabric carbon fiber and toughened epoxy. The core material was Rohacell WF110, a PMI (Polymethacrylimide) foam. The crack arrester was made of Toho Tenax UT500/#135, the unidirectional carbon fiber and toughened epoxy, whose fiber direction was perpendicular to the longitudinal axis of the specimen. An FEM code, ABAQUS version 6.4.1, was used to obtain nodal forces and nodal displacements. The energy release rates at crack tip locations 0.085 mm, 0.17 mm, 1.19 mm, 2.38 mm, 5.1 mm, 10.2 mm, 14.98 mm and 20.4 mm from the edge of the arrester were calculated by the CCI (crack closure integral) method [13] and from FEM results. The mode-I-type and mode-II-type loading conditions employed are shown in Figs. 2 (a) and (b), respectively.

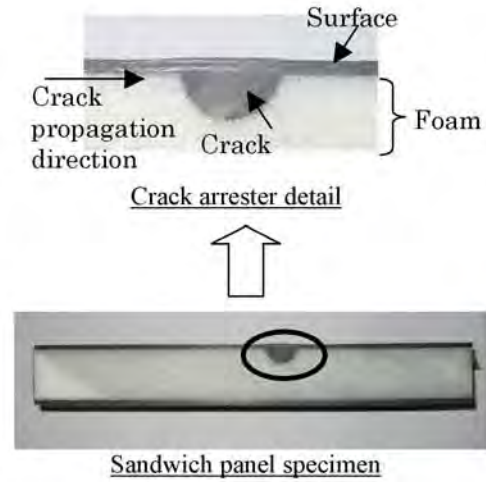
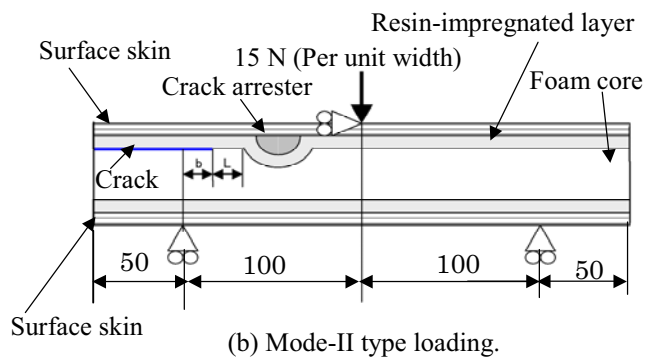
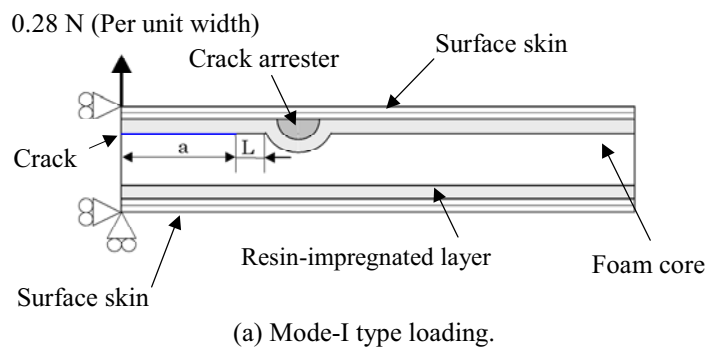


Fig. 1: Concept of Crack arrester.



Unit :mm

$L = 0.085, 0.17, 1.19, 2.38, 5.1, 10.2, 14.96, 20.4$

$a = 100, b = 30 \text{ or } 50$

Fig. 2: Loading conditions.

2.2 Analytical results

FEM analyses indicated that the energy release rate at the crack tip started to decrease at a point 15 mm from the leading edge of the crack arrester under mode-I-type loading and 20 mm under mode-II-type loading, and rapidly decreased from a point 5 mm from the leading edge of the crack arrester. The energy release rate converged to a value close to zero near the leading edge of the arrester for both types of loading modes. These analyses were conducted

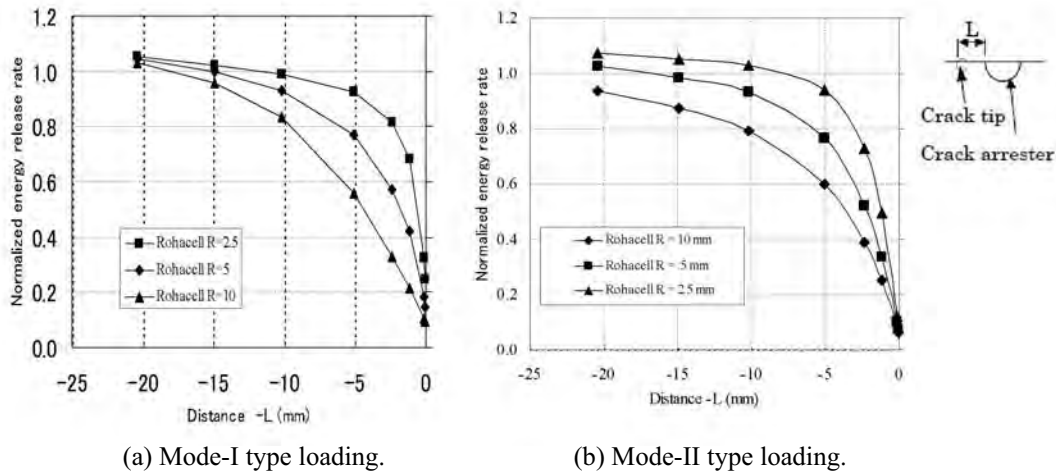


Fig. 3: Relationship between normalized energy release rate and distance L.

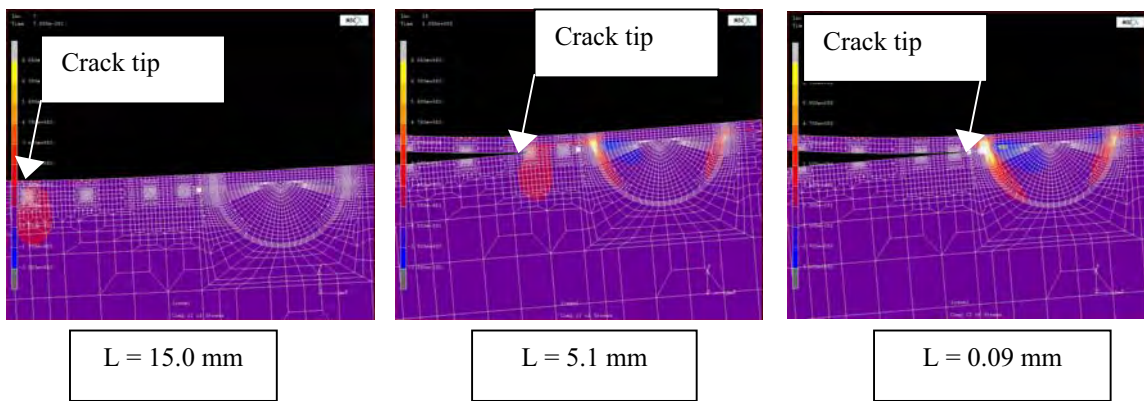
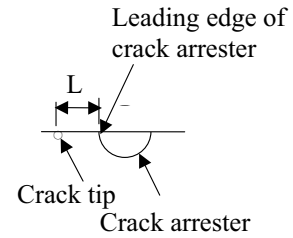
under constant loading conditions. The relationship between the normalized energy release rate and the distance L from the leading edge of the crack arrester is shown in Fig. 3. The normalized energy release rate was defined as the ratio of the energy release rate of the specimen with the crack arrester to that of the specimen without the crack arrester at a given crack length. The authors also obtained similar results for a specimen with a different surface skin thickness of two plies and a core material of Airex R82.60 [11].

The analytical estimation revealed that the stress field near the crack tip was reduced owing to the local load redistribution between the core material near the crack tip and the crack arrester. The reduction of the stress field near the crack tip led to the decrease in the energy release rate at the crack tip as it approached the leading edge of the crack arrester. The relationships between the stress field and the distance L under mode-I-type and mode-II-type loading are shown in Fig. 4.

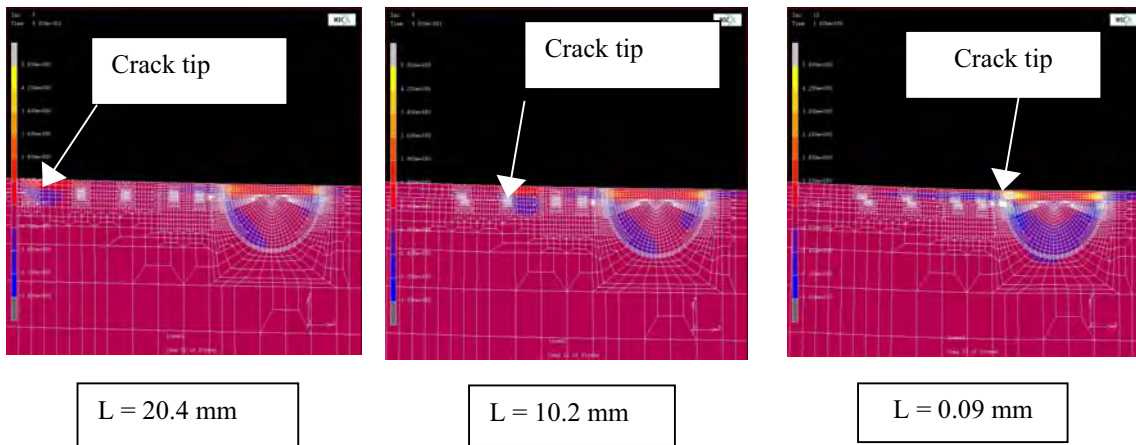
2.3 Summary of analyses

The effect of the crack arrester on suppressing the crack propagation was analytically estimated by the FE analyses and the CCI for the test specimen configuration under constant loading. Similar results were also obtained for a different configuration of the sandwich panel specimen. It was revealed by detailed analyses that the load redistribution between the core material near the crack tip and the crack arrester led to the reduction of the energy release rate

at the crack tip. Experimental fracture toughness tests are necessary to validate this concept as a next step. In these tests, the critical loads of the test specimens are expected to increase owing to the crack arrester.



(a) σ_{YY} under mode-I-type loading (arrester radius: 5 mm).



(b) τ_{XY} under mode-II-type loading (arrester radius: 5 mm).

Fig. 4: Stress distribution near the arrester.

3 EXPERIMENTAL VALIDATION

3.1 Experimental procedure

For the fracture toughness test, sandwich panel specimens were composed of a Toho Tenax UT500/#135 carbon / epoxy surface skins and a WF110, a PMI foam core. The arrester had a semicylindrical cross section with 10 mm radius and was made of unidirectional UT500/#135 with 90° ply orientation. The mechanical properties of these materials are shown in Table 1. The mechanical properties of another core material, Airex R82.60, are also included in this table for reference.

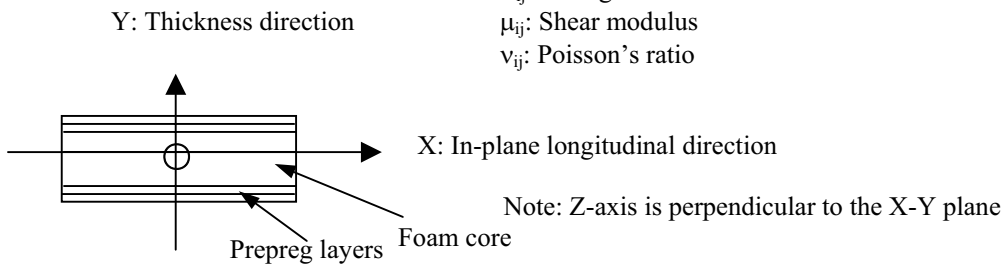
Table 1: Mechanical properties of materials used in fracture toughness test.

	Surface plate					Resin layer	Foam core	
	CFRP (0,90) V _f =46%	CFRP (+45,-45) V _f =46%	CFRP (0,90) V _f =56%	CFRP (+45,-45) V _f =56%	CFRP UD 90 V _f =56%	Neat Resin	Airex R82.60	Rohacell WF110
E _{XX} [GPa]	54.9	12.6	66.3	15.1	8.61	4.1	0.028	0.17
E _{YY} [GPa]	8.61	8.61	8.61	8.61	8.61			
E _{ZZ} [GPa]	54.9	12.6	66.3	15.1	127			
ν _{XY}	0.33	0.33	0.33	0.33	0.55	0.33	0.25	0.18
ν _{YZ}	0.052	0.23	0.043	0.019	0.022			
ν _{XZ}	0.33	0.33	0.33	0.033	0.022			
μ _{XY} [GPa]	3.23	3.23	3.23	3.23	2.78	1.54	0.011	0.070
μ _{YZ} [GPa]	3.23	3.23	3.23	3.23	4.23			
μ _{XZ} [GPa]	3.53	26.1	4.24	31.6	4.23			

E_{ij}: Young's modulus

μ_{ij}: Shear modulus

ν_{ij}: Poisson's ratio



The dimensions of the specimen are shown in Fig. 5. Here the width of the specimen, W , is 100 mm for mode-I-type loading and 50 mm for mode-II-type loading. The ply orientation of the surface skin was $[(+45,-45)/(0,90)/(0,90)/(+45,-45)]_s$ and a symmetric stacking sequence was selected to avoid unfavorable deformation during molding. A DuPont-Toray Kapton film with 12.5 μm thickness and 100 mm in length was installed from the end of the specimen between the surface skin and the core as a crack initiator. The distance between the edge of the release film and the leading edge of the arrester was 20 mm. The test specimens were molded by one-stage curing without the use of an adhesive using an autoclave. The test specifications outlined in concept of JIS K 7086 [14] for CFRP solid laminate specimens were applied because these for the foam core sandwich panel have not been prepared yet. The cross-head speed was 2.0 mm/min. without a precrack. An Instron 8500 servo hydraulic fatigue-testing machine and a 5 kN load cell were used under the mode-I-type loading condition, and an Instron 8501 servo hydraulic fatigue-testing machine and a 100 kN load cell were used under the mode-II-type loading condition. Crack tip locations were measured using a traveling microscope at 50x magnification. The initial crack length under mode-I-type loading was 50 mm. For mode II-type loading, two different initial crack lengths of 30 mm and 50 mm were selected. The test apparatus used for mode-I-type and the mode-II-type loading are shown in Figs. 6 and 7, respectively.

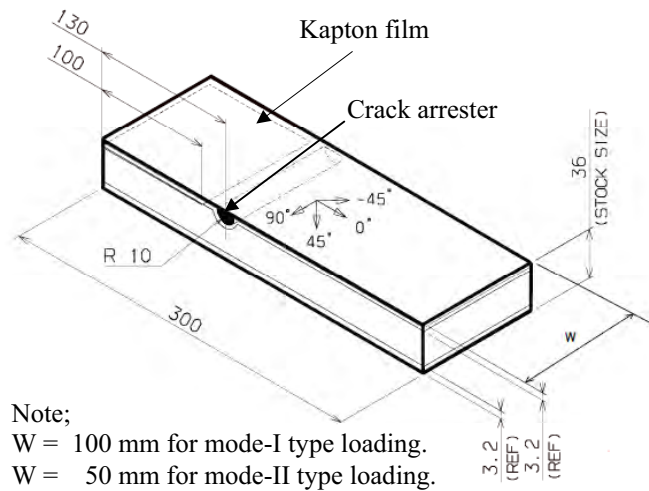


Fig. 5: Dimensions of test specimen.



Fig. 6: Mode-I type test apparatus.



Fig. 7: Mode-II type test apparatus.

The test apparatus used for mode-I-type and the mode-II-type loading are shown in Figs. 6 and 7, respectively.

The ABAQUS Version 6.4.1 FEM code was used in this calculation. The energy release rate was obtained using equation (1) based on the CCI for the specimen.

$$G = \lim_{\Delta a \rightarrow 0} \frac{1}{2\Delta a} \int_0^{\Delta a} \sigma_{YY}(\Delta a - r, 0) \bar{v}(r, \pi) dr + \lim_{\Delta a \rightarrow 0} \frac{1}{2\Delta a} \int_0^{\Delta a} \tau_{XY}(\Delta a - r, 0) \bar{u}(r, \pi) dr \quad (1)$$

Here, G is the total energy release rate and σ_{YY} and τ_{XY} are the normal and shear stress components near the crack tip, respectively. \bar{u} and \bar{v} are the in-plane shear and vertical displacement between the upper and lower crack surfaces, respectively. Δa is the crack extension. The values of σ_{YY} , τ_{XY} , \bar{u} and \bar{v} were calculated by FEM analyses using FE models of the test specimen and critical loads obtained from the fracture toughness test. Δa was also measured during the fracture toughness test. An apparent fracture toughness, G^* , was introduced to evaluate the inhibition of crack growth owing to the crack arrester. The apparent fracture toughness was defined by the energy release rate obtained from equation (1) using FEM results for the FE model without the crack arrester and the critical load of the test specimen with the crack arrester. Using this parameter, the crack suppression effect of the crack arrester could be evaluated appropriately.

3.2 Experimental results of fracture toughness test

3.2.1 Test results under mode-I-type loading

A typical load-displacement diagram obtained under the mode-I-type loading is shown in Fig. 8. Four specimens, two with the crack arrester and two without the crack arrester, were prepared for the fracture toughness test under the mode-I-type loading condition.

The locations of

the crack tip in the specimen with the crack arrester are shown in this figure as black arrows and values of L . Under the mode-I-type loading condition, the critical load of the specimen with the crack arrester increased as the crack approached the leading edge of the arrester. On the other hand, for the specimen without the crack arrester the crack grew unstably in a stick-

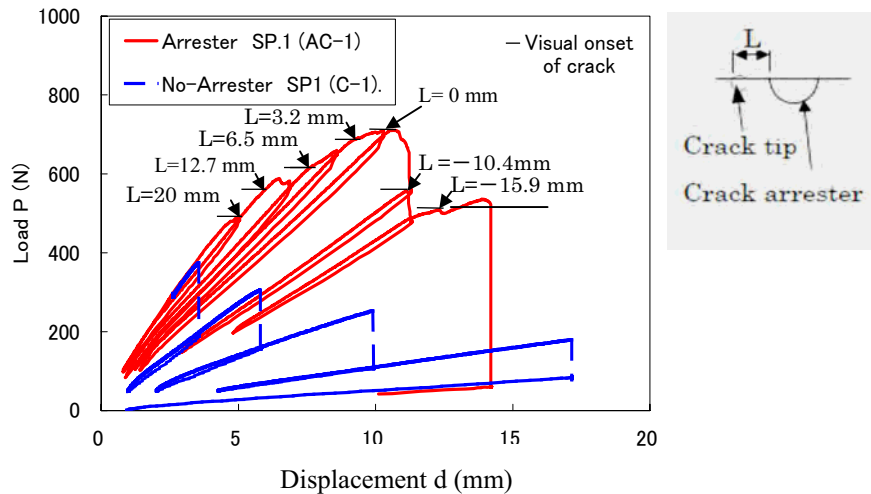


Fig. 8: Typical load-displacement diagram under mode-I-type loading.

slip manner, similarly to results obtained from fracture toughness tests for CFRP laminates at low temperatures [15]. Comparing these data in Fig. 8, the specimens with the crack arrester have a 2.3 times larger critical loads than those of the specimens without the crack arrester. Figure 8 indicated that the effect of the crack arrester on crack suppression was considerable under mode-I-type loading.

3.2.2 Test results under mode-II-type loading

The load-displacement diagram under mode-II-type loading is shown in Fig. 9. Six specimens, three with the crack arrester and three without the crack arrester, were prepared for the fracture toughness test under the mode-II-type loading condition. For the three specimens with the crack arrester, two of them had an initial crack length of 30 mm and the other had a length of 50 mm. For the specimen with the crack arrester and the initial crack length of 30 mm, the crack propagated unstably from the edge of the crack initiator. It was then stopped near the leading edge of the arrester.

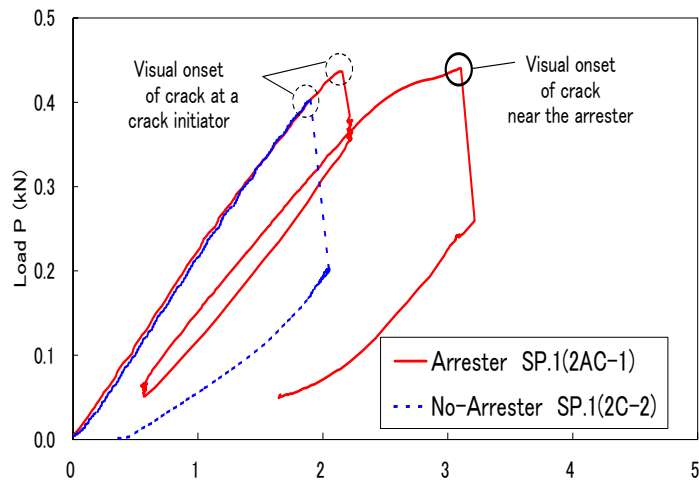


Fig. 9: Relationship between load and displacement in mode-II-type test.

These specimens were fractured due to the shear failure of the core material without the crack propagation in the second loading. Although this fact demonstrates the effect of the crack arrester on crack suppression, only the load-displacement diagram of the specimen with the initial crack of 50 mm is shown in Fig. 9. The crack propagation behavior in the first loading for the specimen with the crack arrester and the initial crack length of 50 mm was similar to those of specimens with the initial crack length of 30 mm. After unloading and reloading, the crack was kinked into the core at a critical load that was almost equal to the initial critical load in spite of the longer crack length. For the specimen without the arrester, the crack propagated unstably to the central loading point for initial crack lengths of both 30 mm and 50 mm.

The apparent fracture toughness for the specimen with the crack arrester, G^* , and the interfacial fracture toughness for the specimen without the arrester, G_c , are shown in Fig. 10. The apparent fracture toughness for the specimen with the arrester was calculated by the procedure described in 3.1. This figure shows that an approximate twofold increase in apparent fracture toughness is obtained owing to the crack arrester. This value would have been larger if the crack kinking had been prevented.

3.3 Summary of the experiments

The verification tests under mode-I-type and the mode-II-type loading conditions were conducted using sandwich panel specimens with and without a crack arrester. The test results indicated that the critical load increased for the specimen with the crack arrester under mode-I-type and mode-II-type loadings. The apparent fracture toughness was used as a parameter to estimate the effect of the crack arrester. A quantitative estimation of effect of the crack arrester effect was possible using this parameter.

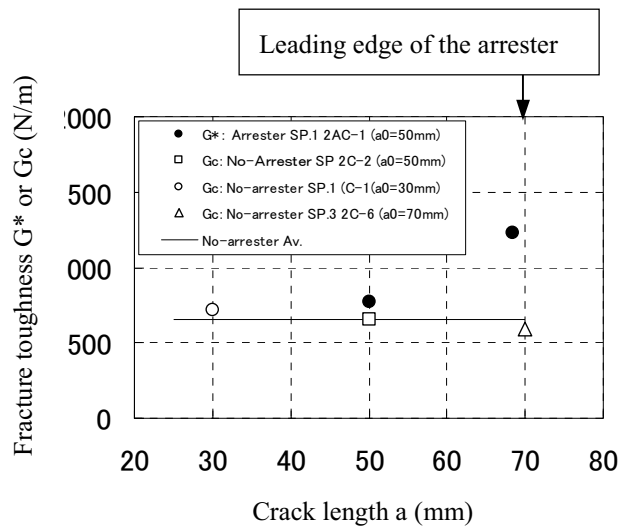


Fig. 10: Relationship between apparent / interfacial fracture toughness and crack length in mode-II-type test.

4 CONCLUSIONS

The proposed crack arrester is expected to become a promising structural element for suppressing crack initiation and propagation in foam core sandwich panels. The damage tolerance of foam core sandwich panels can be improved by introducing the crack arrester. Our study also revealed the reason why this simple structural element can effectively suppress interfacial crack propagation in the foam core sandwich panel. The application of this concept to various types of structural component should be possible [16]. As further studies, inspection methods to detect the location of a suppressed crack near the arrester and the development of the design criteria for the sandwich panel structure with the arrester are necessary.

5 ACKNOWLEDGEMENT

The experimental part of this paper was conducted under contract for the Society of Japanese Aerospace Companies. The authors sincerely appreciate the financial support by the Society.

REFERENCES

- [1] Y. Hirose, M. Konishi, K. Kosugi, M. Imuta and H. Kikukawa, "Industrial application of CFRP sandwich panel for aircraft structure", *Proc Conference ICCE/8*, Tenerife, Canary Islands, Spain, pp.355-356 (2001).

- [2] L. Herbeck, H. Wilmes and M. Kleineberg, "Material and processing technology for CFRP fuselage", *SAMPE 2004*, Long Beach, CA, USA (2004).
- [3] S. Ochi, Y. Hirose, M. Nishitani, T. Sana, T. Ito, Y. Ikeda and H. Kikukawa, "Development of CFRP sandwich panel structure for transport nose component", *Proc. 9th European-Japanese Symposium on Composite Materials*, Hamburg, Germany (2004).
- [4] S. E. Hellbrantt, "Experience from design and production of the 72m CFRP-sandwich corvette Visby", *Proc. 6th International Conference on Sandwich Structure*, Ft. Lauderdale, Florida, pp15-24 (2003).
- [5] Y. Hirose, M. Nishitani, M. Imuta, H. Fukagawa and H. Kikukawa, "Development of foam core sandwich panel structure for transport nose component", *SME Technical Paper TP03PUB317* (2003).
- [6] M. Bruman, "Fatigue crack initiation and propagation in sandwich structures", *Report No. 98-29*, Department of Aeronautics, Royal Institute of Technology, Sweden (1998).
- [7] A. Shipsha, "Failure of sandwich structures with sub-interface damage", *Report 2001-13*, Department of Aeronautics, Royal Institute of Technology, Stockholm, Sweden (2003).
- [8] L. Carlson and S. Prasad, "Debonding and crack kinking in foam core sandwich beams-I Analysis of fracture specimen", *Engng. Fracture Mech.*, 47, pp.813-824 (1994).
- [9] L. Carlson and S. Prasad, "Debonding and crack kinking in foam core sandwich beams-II Experimental investigation", *Engng. Fracture Mech*, 47, pp.825-841 (1994).
- [10] J. Jacobson, E. Bozhevolnaya and O. Thomsen, "New crack arrester concept for sandwich structures", *Proc. 16th International Conference on Composite Materials*, Kyoto, Japan, Vol.1, pp.100-101 (2007).
- [11] Y. Hirose, M. Hojo, A. Fujiyoshi and G. Matsubara, "Suppression of interfacial crack for foam core sandwich panel with crack arrester", *Adv. Composite Mater.*, Vol.16, No.1, pp.11-30 (2007).
- [12] Y. Hirose, M. Hojo, A. Fujiyoshi and G. Matsubara, "Suppression of interfacial crack for foam core sandwich panel with new crack arrester", *Proc. 9th Japan International SAMPE Symposium & Exhibition*, Tokyo (2005).
- [13] E. F. Ryubicki and M. F. Kanninen, "A finite element calculation of stress intensity factors by a modified crack closure integral", *Engng. Fracture Mech.*, Vol.9, pp.931-938 (1977).

- [14] JIS K 7086, “Testing methods for interlaminar fracture toughness of carbon fiber reinforced plastics”.
- [15] S. Matsuda, M. Hojo, S. Ochiai, K. Moriya and H. Aoyama, “Mode I interlaminar fracture under static and fatigue loading of alumina fiber/epoxy laminates in liquid nitrogen”, *JSME Int. J, Ser. A*, 65(640), pp.27-33 (1999).
- [16] Y. Hirose, M. Nishitani, S. Ochi, K. Fukumoto, T. Kawasaki and M. Hojo, “Proposal of suppression of delamination for foam core sandwich panel joint with filler “, *Adv. Composite Mater.*, Vol.15, No.3, pp.319-339 (2006).

Mode I Fracture Toughness of PMI Sandwich Core Materials

E. Saenz^{*}, A. Roth[†], F. Rosselli^{*}, X. Liu^{*}, R. Thomson^{*}

^{*}Cooperative Research Centre for Advanced Composite Structures Ltd,
506 Lorimer Street, Fishermans Bend, Victoria 3207, Australia
e.saenz@crc-accs.com.au, f.rosselli@crc-accs.com.au, x.liu@crc-accs.com.au,
r.thomson@crc-accs.com.au, web page: <http://www.crc-accs.com.au>

[†]Evonik Röhm GmbH, Kirschenallee, 64293 Darmstadt, Germany
alexander.roth@evonik.com, web page: <http://www.rohacell.com>

Key words: ROHACELL, Mode I, Fracture Toughness, Modelling, Sandwich Core Foams.

Summary. *The Mode I fracture characteristics of ROHACELL[®] polymethacrylimid foam core were obtained using single edge notch bending specimens, with a pre-crack length-to-specimen depth ratio of 0.2, loaded in three-point bending. Three grades of ROHACELL[®] foams: RIMA, RIST and WF, at densities from 51 to 110 kg/m³, were studied. A proper procedure was established for cutting the pre-crack tip to ensure that the crack propagated in a Mode I fashion. The Mode I critical stress intensity factor, K_{Ic} , of the foams was evaluated from the experimental data using a semi-analytical solution and Linear Elastic Fracture Mechanics Finite Element Analysis (LEFM-FEA). Values obtained by these two methods agreed very well. The fracture toughness parameters, K_{Ic} , J_{Ic} , were discussed as a function of foam density and cell structure. It was determined that the relationship between foam density, cell size and cell wall thickness was different for each foam grade, and that this affected the values of K_{Ic} and J_{Ic} . As a result, an empirical power law model was proposed to relate the fracture toughness and the relative density, and its parameters determined for the PMI foams investigated.*

1 INTRODUCTION

Foam cored sandwich structures offer a light weight, cost effective design solution, not only for aerospace but also for automotive, wind generation and naval applications. These structures can be relatively susceptible to damage, particularly impact damage, which may cause significant damage to the core without being easily detected. The damage can then act as a stress concentrator, leading to fracture and eventual failure of the structure.

ROHACELL[®] foams are produced by thermal expansion of a co-polymer sheet of methacrylic acid and methacrylonitrile. During the foaming process, the copolymer sheet is converted to polymethacrylimid (PMI). Alcohol is used as a blowing agent, thus ROHACELL[®] contains no fluorinated carbon hydrates and is halogen free. As a result of the process, rigid closed-cell foam with a very homogeneous cell structure is obtained. Different grades of ROHACELL[®] foams are commercially available (e.g. WF, RIST, RIMA), which

are made with a similar raw material but different production processes are used to control the cell dimensions. The cell size characteristics define the manufacturing process for which the foams are suitable. For instance, WF foams are best suited for pre-impregnated composites skins since these products have a larger cell size compared with RIST and RIMA. Since RIST and RIMA foams have the smaller cell size, they are most appropriate for liquid moulding processes such as the Vacuum Infusion Process (VIP) and Resin Transfer Moulding (RTM).

ROHACELL[®] is extensively used for structural sandwich applications offering the highest strength-to-weight ratio when compared to other plastic foam cores [1]. Applications include aerospace, train, automotive and marine structures, sport articles, electronics, radiation (X-ray table) and acoustic technologies and tooling [1-3]. To further the use of ROHACELL[®] foam sandwich structures in load-bearing elements, an understanding of the fracture behaviour is required along with fracture toughness values, that until now are only available for few ROHACELL[®] grades. Furthermore, in most published research [4-7], the mechanical properties were studied for foams whose cell size decreased as the density increased, and little has been reported for foams whose cell size increases as the density increases, such as RIMA. The work presented in this paper focuses on the Mode I fracture behaviour of three grades of ROHACELL[®] foams, RIMA, RIST and WF, at a range of densities and is part of a larger study to establish a validated design methodology for the fracture of ROHACELL[®] foams.

2 MATERIAL

The ROHACELL[®] foam grades tested were RIMA, RIST and WF. The foams were supplied by Evonik Röhm GmbH at densities from 51 to 110 kg/m³.

The density and cell dimensions of tested specimens are presented in Table 1. In general, a low standard deviation was observed between specimens of the same density. The average cell size and the cell wall thickness were determined from the fractured surfaces of tested specimens using image analysis software.

ROHACELL [®] foam grade	WF			RIST			RIMA		
	51	71	110	51	71	110	51	71	110
Foam density, ρ (kg/m ³) (Standard deviation)	54.1 (0.1)	75.6 (1.8)	111.4 (0.4)	52.1 (0.2)	77.6 (0.5)	110.7 (0.1)	51.3 (0.4)	72.2 (0.5)	90.1 (0.2)
Average cell size, ℓ (μm)	714	743	562	296	295	219	13	21	49
Cell wall thickness, t (μm)	2 to 17	2 to 18	5 to 20	1.5 to 6.5	2 to 9	2 to 12.5	0.1 to 0.3	0.1 to 0.5	0.3 to 3
t_{middle}^1/ℓ ($\times 10^2$), ratio	1.33	1.35	2.22	1.35	1.86	3.31	1.53	1.43	3.36

Table 1: Density, cell wall thickness and average cell size of ROHACELL[®] foams

As expected, the foams had different cell structure characteristics. For WF and RIST, as the density of the foam increased, the average cell size decreased and the cell wall thickness increased. However, for RIMA, as the density increased, both the cell size and the cell wall thickness increased. WF had the largest cell size and cell wall thickness whilst RIMA had the

¹ t_{middle} refers to the middle value for the given range on cell wall thickness.

lowest, and their cell size differed by one order of magnitude. The cell size of RIST was approximately half that of WF. Moreover, the cell wall thickness was not constant.

Mechanical properties of PMI raw material and of the foams used for the calculation and FE modelling are summarised in Table 2, interpolated or extrapolated from data supplied by Evonik Röhm GmbH for the same foam grades but of slightly different densities. The Young's modulus (E) used was taken as an average of the compression and tensile moduli provided, which were obtained according to DIN 53421 [8] and ISO 527-2 [9] test standards, respectively. The shear modulus (G) was obtained according to DIN 53294 [10] test standard. The Poisson's ratio (ν) was evaluated by Equation (1).

$$\nu = \left[\frac{E}{2G} \right] - 1 \quad (1)$$

PMI raw material									
Density, ρ_S (kg/m ³)	1400								
Young's modulus, E_S (MPa)	6479								
Tensile strength, σ_S (MPa)	112.7								
ROHACELL [®] foam grade	WF			RIST			RIMA		
	51	71	110	51	71	110	51	71	110
Foam density, ρ (kg/m ³)	54.1	75.6	111.4	52.1	77.6	110.7	51.3	72.2	90.1
Young's modulus, E (MPa)	77.4	114.5	181.9	70.4	123.4	192.3	75.2	117.0	152.9
Shear modulus, G (MPa)	32	46.3	69.2	30	45.4	72.2	29.4	43.3	55.2
Poisson's ratio, ν	0.209	0.236	0.314	0.173	0.359	0.332	0.280	0.351	0.384

Table 2: Mechanical properties of PMI, and ROHACELL[®] foams

3 EXPERIMENTAL PROCEDURE

To characterise the Mode I fracture behaviour, single edge-notched bending (SENB) specimens loaded in three-point bending (TPB), with a support span (S) equal to four times the specimen width² (W), were used. The geometry of the specimen is shown in Figure 1 which followed that given in ASTM E1820 standard [11]. The ratio of pre-crack length (a) to specimen width (parallel to the loading direction) was fixed at $a/W=0.2$.

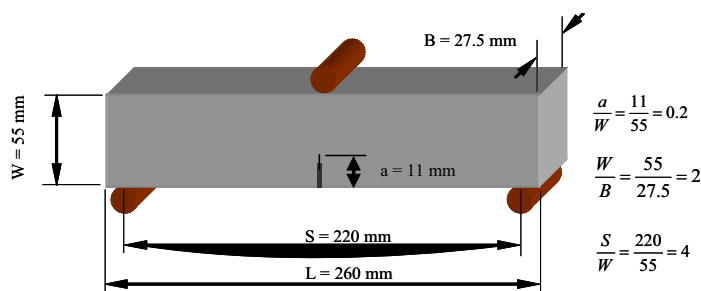


Figure 1: Single-edge notched bending (SENB) specimen geometry.

² The SENB specimen width coincides with the foam sheet thickness.

3.1 Preparation of Specimens

An artificial pre-crack was introduced to the specimens using a two step process: a dry diamond saw was used to create the first notch and a blade was used to create the pre-crack tip.

During initial testing, it was observed that foam fracture morphology was sensitive to the quality of the pre-crack tip, which was related to blade cutting edge. A study to investigate the influence of blade quality on foam fracture toughness was performed. It was concluded that if a blade with cutting edge defects, such as burrs or discontinuities, was used, small tears were initiated, which at times led to out-of-plane fracture. The chance of such undesirable damage increased if the same blade was used repeatedly without being ultrasonically cleaned, as debris was found embedded within the blade defects. Similar tear damage was also observed when scalpels were used because of the jagged cutting edge. The different cutting edge of razor blades and scalpels are shown in Figure 2.

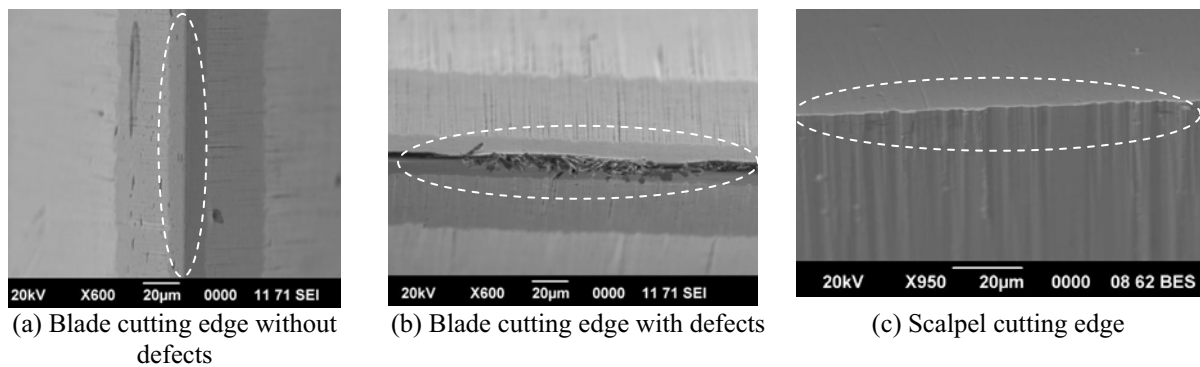


Figure 2: Cutting edge characteristics of different blades.

The above effect of cutting defects was observed most obviously for RIMA specimens, where a triangular pattern was produced (Figure 3(a)), or after the TPB test, where tears were observed in the pre-crack tip surface (Figure 3(b)). The tear produced local load redistribution around the pre-crack tip that reduced or eliminated the pre-crack tip stress concentration effect such that the crack propagated around the tear (Figure 3(a)). Therefore, an out-of-plane fracture was obtained (Figure 3(b)) as opposed to an in-plane fracture surface (Figure 3(c)). This behaviour was less observed for WF and RIST specimens.

When out-of-plane failures were produced, higher peak load were recorded and hence higher apparent Mode I critical stress intensity factor (K_{Ic}) values were obtained, as compared to the specimens with in-plane failures. In some cases, an overestimation of more than 50% was observed. The more severe the out-of-plane fracture, the higher the K_{Ic} value and its standard deviation. Hence, careful initial pre-crack preparation was critical to obtaining an accurate measure of the fracture parameters.

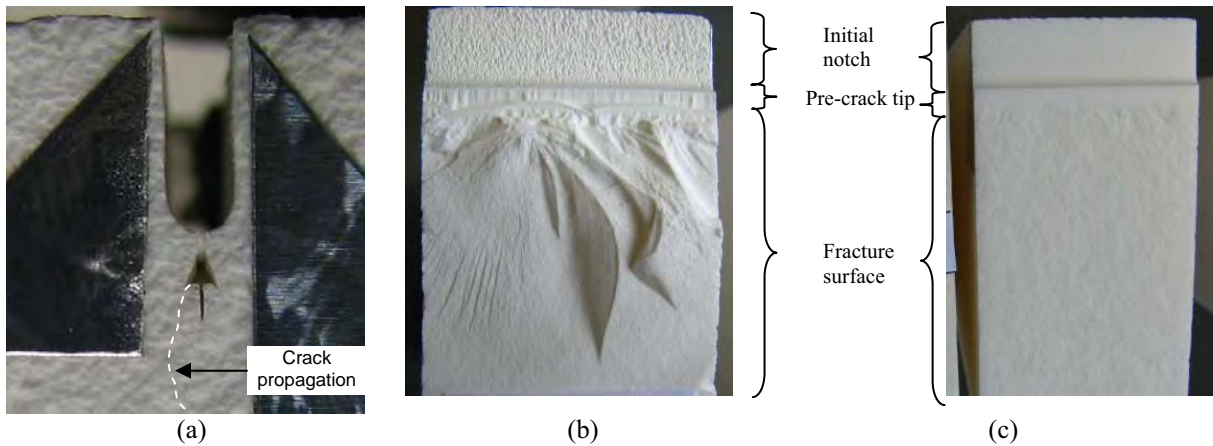


Figure 3: (a) Out-of-plane crack propagation that started from a tear instead of pre-crack tip; (b) Out-of-plane fracture surface; (c) In-plane fracture surface.

After reviewing the cutting edge of different blades (e.g. single and double edge razor blades, snap blade cutter, scalpels, microtome knife, etc), it was observed that all had cutting edge defects. Moreover, blade suppliers could not guarantee a product free of defects. Nevertheless, it was decided to use single edge razor blades supplied by GEM[®], covered with Teflon to reduce friction during cutting.

Before the test specimens were prepared for the test, blades with minimal defects were selected using an optical microscope at 520 \times magnification. Additionally, each blade was used for not more than three cuts and was ultrasonically cleaned before each cut.

The specimens were prepared using the following procedure:

1. All specimens were dehumidified and sealed in special aluminium bags by Evonik Röhm GmbH. The fracture test was conducted not more than five days after a bag was opened in order to minimise moisture absorption.
2. After a specimen was taken out of the bag, its dimensions were measured using a calliper and the weight was recorded using an analytical balance with 0.1 mg resolution.
3. In the first step of the two-step procedure for introducing an artificial pre-crack to the specimen, a 2 mm thick dry diamond saw was used to create the initial notch between 8 to 9 mm in depth.
4. A piece of Airtech Flashbreaker 1R tape was positioned at the end of the initial notch on both specimen surfaces, to measure the pre-crack length.
5. A razor blade mounted to a lathe was used to obtain the pre-crack tip that was between 2 to 3 mm in depth, which ensured that at least two cells were clean cut.
6. The specimen was checked using a microscope at 50 \times magnification to make sure that the nominal pre-crack length of 11 mm was achieved.

3.2 Test Procedure

The TPB tests were run at a constant crosshead speed of 1 mm/min. The specimen mid-span displacement was measured using an LVDT. At least six specimens were tested per foam grade density. The K_{Ic} of the foams were calculated using Equation (2) [11].

$$K_{Ic} = \left[\frac{PS}{BW^{3/2}} \right] F(a/W) \quad (2)$$

where: P is the peak load, S is support span, W is specimen width, B is specimen thickness and $F(a/W)$ is a geometric factor related to the ratio of a/W obtained by Equation (3).

$$F(a/w) = \frac{3(a/W)^{1/2} [1.99 - (a/W)(1 - a/W)(2.15 - 3.93(a/W) + 2.7(a/W)^2)]}{2(1 + 2a/W)(1 - a/W)^{3/2}} \quad (3)$$

Because visual crack extension was not observed during the test, the Mode I critical J-integral, J_{Ic} , was determined by Equation (4) [11].

$$J_{Ic} = \frac{K_{Ic}^2 (1 - \nu^2)}{E} \quad (4)$$

4 FINITE ELEMENT MODELLING

The TPB testing of SENB specimens was modelled using MSC.Marc finite element (FE) software. The foams were considered as isotropic in the model because they generally have homogeneous cell structures. Since the studied foams had linear elastic behaviour up to fracture, they were modelled using Linear Elastic Fracture Mechanics Finite Element Analysis (LEFM-FEA), and mechanical properties listed in Table 1, were used. The displacements predicted at the peak load, obtained from testing, were used to calculate K_{Ic} .

As per the derivation of the analytical solutions, the specimens were assumed to deform in a plane-strain fashion under load. Due to symmetry, only half of the specimen geometry was considered in the model. It was meshed using 2-D triangular plane strain elements.

As shown in Figure 4(a), a higher mesh density was used around the support and load application points, and triangular crack tip elements were used around the crack tip (see Figure 4(b)). The FE mesh used next to the crack tip elements consisted of 6-noded triangular elements covering a small region around the crack. It was then transitioned to 3-noded triangular elements for the rest of the geometry considered.

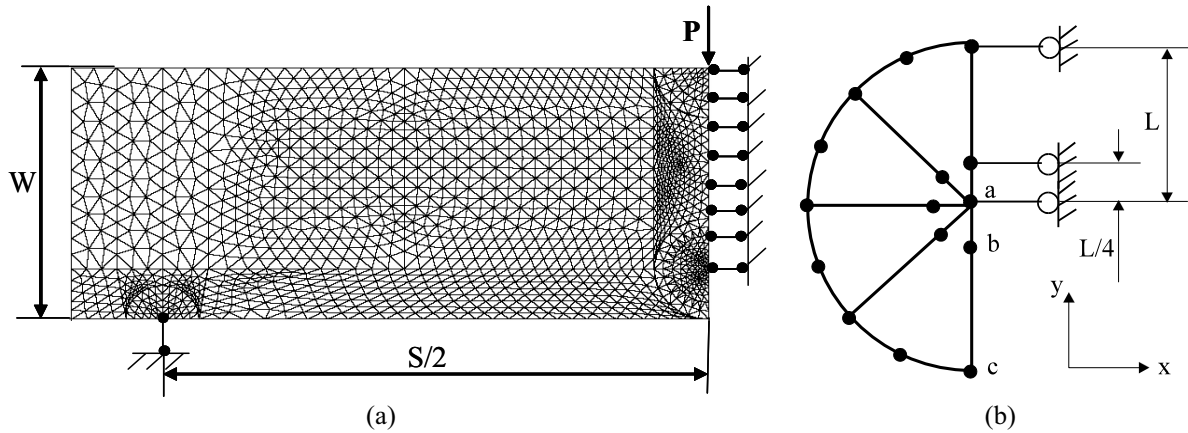


Figure 4: (a) Finite element mesh for half of specimen geometry; (b) Crack tip elements

The displacement correlation method was used to calculate the Mode I stress intensity factor from the nodal displacements predicted by FE analysis. As shown in Figure 4(b), displacements at nodes “b” and “c” were used to calculate K_I by Equation (5).

$$K_I = \frac{G\sqrt{2\pi}}{2(1-\nu)\sqrt{L}} (u_x^c - 4u_x^b) \quad (5)$$

where: L is the length of the crack tip element and u_x are nodal displacements in x direction.

5 RESULTS AND DISCUSSION

5.1 Foam Fracture Toughness

Typical load-displacement curves for RIMA are shown in Figure 5, where it was observed that as the foam density increased, the peak load and the foam stiffness also increased while the peak displacement had the opposite behaviour. All tested foams had an initial nonlinearity, known as the toe region that does not represent a property of the material [12], and was not considered in test results. This was followed by a linear region to failure, which occurred by fast and unstable fracture without any visual crack extension. Similar behaviour was observed with WF and RIST.

The FE predictions with the experimental results are compared in Table 3. Excellent correlation was obtained between K_{Ic} fracture toughness values evaluated using the semi-analytical solution of Equation (2) and the FE displacement correlation method. However, the FE models predicted in general lower mid-span displacements compared to the test results. This could be due to the initial looseness of the test set-up during each test and local indentation of the foam specimen at the loading and supporting locations. Both the looseness and local indentation resulted in rigid body movement of the specimen in the loading direction, which was recorded by the LVDT sensor but was not considered by the FE model.

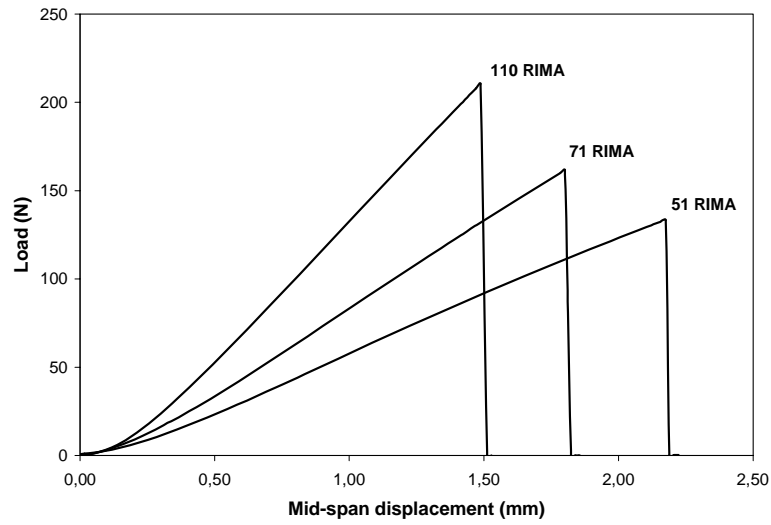


Figure 5: Typical load-displacement curves for RIMA for Mode I test ($a/W=0.2$)

ROHACELL® foam grade	Foam density, ρ (kg/m ³)	Peak load from test, P (N)	Fracture toughness, K_{Ic} (MPa.m ^{0.5})		Mid-span displacement (mm)	
			LEFM-FEA	Test	LEFM-FEA	Test
51WF	54.1	119.6	0.087	0.087	1.42	1.72
71WF	75.6	180.3	0.131	0.130	1.43	1.60
110WF	111.4	309.7	0.225	0.223	1.48	1.55
51RIST	52.1	96.8	0.071	0.070	1.28	1.54
71RIST	77.6	196.9	0.143	0.144	1.34	2.06
110RIST	110.7	252.9	0.183	0.183	1.13	1.24
51RIMA	51.3	133.6	0.097	0.097	1.58	2.01
71RIMA	72.2	171.7	0.124	0.124	1.24	1.70
110RIMA	90.1	212.4	0.153	0.153	1.14	1.32

Table 3: Comparison between average test results and LEFM-FEA results

The graphs that relate relative density to fracture toughness are shown in Figure 6 and Figure 7, where the data points represent the test results. The graphs were fitted to power law curves, by Equation (6), using a least-square fitting procedure.

$$y = c(x)^n = c\left(\frac{\rho}{\rho_s}\right)^n \quad (6)$$

where: y is fracture toughness, c is equation factor, and n is power law equation exponent.

As observed in Figure 6, as the foam density increased, so did K_{Ic} for all studied foams. When K_{Ic} was compared between the foams, WF values were higher than RIST, but these

foams had similar equation factor (5.91 and 5.08) and exponent values (1.3 and 1.28). RIMA however, at low density had the highest K_{Ic} . Its behaviour changed as the density increased, having similar K_{Ic} to WF and RIST around the density of 70 kg/m^3 , and for higher densities the tendency was that RIMA had the lowest K_{Ic} , resulting in a lower equation factor (1.36) and lower exponent value (0.8) than WF and RIST.

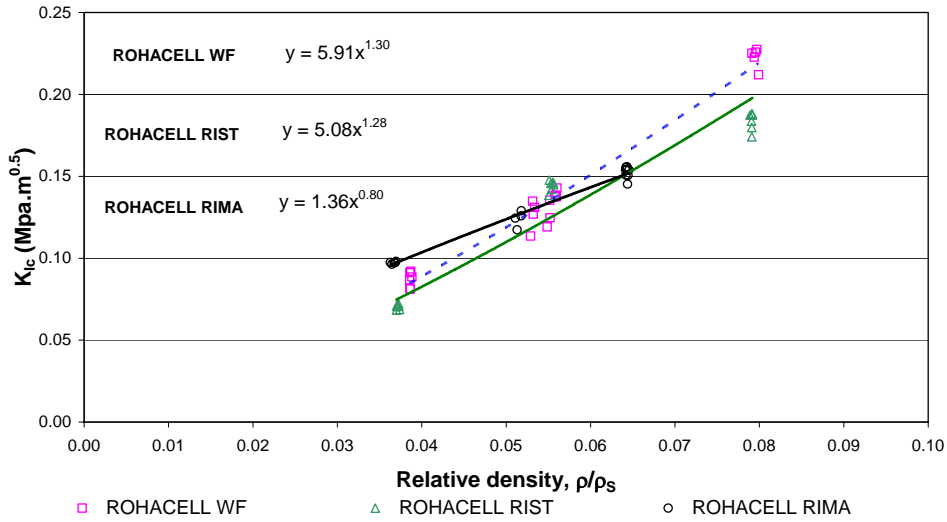


Figure 6: Stress intensity, K_{Ic} , for ROHACELL[®] foams ($a/W=0.2$)

As shown in Figure 7, J_{Ic} behaviour was consistent with K_{Ic} : as the density increased, J_{Ic} also increased, and WF had higher values than RIST. However the difference between WF and RIST increased as the density increased resulting in different equation factor and exponent value. RIMA, on the other hand, only had a small J_{Ic} increase with density (i.e. if density increased 75%, from 51.3 to 90.1 kg/m^3 , J_{Ic} increased by only 12%) with the lowest equation factor and exponent values.

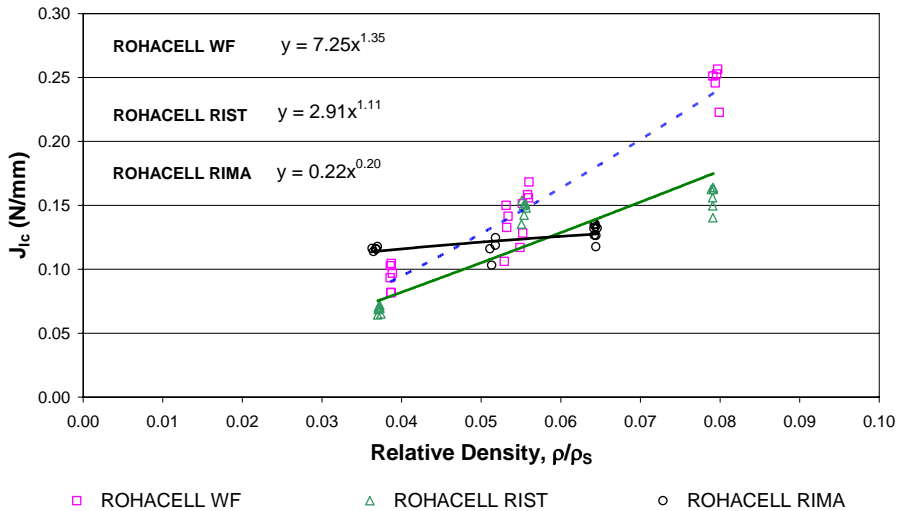


Figure 7: Fracture toughness, J_{Ic} , for ROHACELL[®] foams ($a/W=0.2$)

5.2 Effect of Density and Cell Dimensions

Ashby and Gibson [6] proposed that K_{Ic} can be obtained by Equation (7), where c_1 is a constant, σ_f is the tensile fracture strength of the cell wall that can be approximated to the tensile fracture of raw material σ_s , and $n=2$ for closed-cell foams. According to this equation, K_{Ic} depends strongly on foam density (macro level) and weakly on cell size (micro level).

$$K_{Ic} = c_1 \sigma_f \sqrt{\pi \ell} \left(\frac{\rho}{\rho_s} \right)^n \quad (7)$$

For closed-cell foams the density is related to cell dimensions by Equation (8), where the following cases can be generated and discussed based on Table 1:

- *Case 1*, for ρ to remain constant while ℓ increases: then t will also have to increase which was observed in all foam grades. Furthermore the ratio t_{middle}/ℓ was approximately constant for all studied foams at a particular density.
- *Case 2*, as ρ increased and ℓ decreased: then t could be constant, could decrease, or could increase, which was observed for WF and RIST. For instance, when the density increased by a factor of two, from 54 to 110 kg/m³, ℓ decreased by a factor of 0.7, and t increased by a factor of 1.5.
- *Case 3*, as ρ increased and ℓ remained constant or increased: then t increased at a higher rate than in Case 2, as observed for RIMA. For instance, when the density increased by a factor of two, from 47 to 90 kg/m³, ℓ increased by a factor of 3.7, and t increased by a factor of 8.

$$\rho \propto \frac{t}{\ell} \quad (8)$$

According to Figure 7, J_{Ic} seems to be much more sensitive to cell dimensions than K_{Ic} . For foams that follow Case 2, when the cell size was reduced at a particular density, so did J_{Ic} : as was observed for WF and RIST where RIST had lower J_{Ic} values than WF. Furthermore, the J_{Ic} differences within foam grades increased as the density increased resulting in low exponential values for RIST compared with WF. For foams that follow Case 3, J_{Ic} in general was less sensitive to density variation, as was observed for RIMA.

From the above, it is evident that the relationship between cell dimensions and relative density was different for the studied foams, and this strongly affected the fracture toughness of the foams. Therefore a more empirical law equation, similar to Equation (6), might better represent the relationship between fracture toughness and relative density, rather than Equation (7). In the proposed power law model the constants c and n depend on the raw material and on the manufacturing process, which determines the foam grade and the relationship between cell characteristics and relative density. The empirical constants for the studied ROHACELL[®] foams are presented in Table 4. Further tests on a wider range of foam densities should be undertaken to confirm these findings.

Fracture toughness ROHACELL [®] foam grade	K_{Ic} (MPa.m ^{0.5})		J_{Ic} (N/mm)	
	c	n	c	n
WF	5.91	1.30	7.25	1.35
RIST	5.08	1.28	2.91	1.11
RIMA	1.36	0.80	0.22	0.20

Table 4: Empirical constants for fracture toughness power law equation

6 CONCLUSIONS

The Mode I fracture characteristics of polymethacrylimid ROHACELL[®] RIMA, WF and RIST foams were obtained by testing single edge-notched bending specimens loaded in three-point bending. The fracture toughness, K_{Ic} , of the foams was obtained using a semi-analytical solution and Linear Elastic Fracture Mechanics Finite Element Analysis (LEFM-FEA). The fracture toughness values obtained by the two methods agreed very well.

For the studied foams, it was established that the relationship between cell dimensions and relative density was different, and that this relationship strongly affected the fracture toughness. Based on this behaviour, an empirical power law model was proposed, and its parameters determined for each foam grade.

It was also found that the Mode I toughness of the foams was very sensitive to the pre-crack tip, which was related to the blade cutting edge quality that was used for the pre-crack generation. Hence, careful initial specimen preparation is critical to obtaining accurate results. A procedure for ensuring accurate experimental results through careful preparation of the specimen pre-crack was proposed.

REFERENCES

- [1] H. Seibert, "PMI foam cores find further applications", *Reinf. Plast.*, 44 (1), 36-38 (2000).
- [2] M. Kleineberg, L. Herbeck, C. Shoppinger, "Advanced liquid resin infusion-A new perspective for space structures", 23rd SAMPE Europe International Conference, Paris (2002).
- [3] EL Fasanella, KE Jackson, CE Sparks, AK Sareen "Water Impact Test and Simulation of a Composite Energy Absorbing Fuselage Section", *J. Am. Helicopter Soc.*, 50 (2), 150-164 (2005).
- [4] M. Burman, "Fatigue crack initiation and propagation in sandwich structure", PhD thesis, Report N. 98-29, Department of Aeronautics, Royal Institute of Technology, Stockholm, Sweden, (1998).
- [5] D. Zenkert and J. Backlund, "PVC sandwich core materials: Mode I fracture toughness", *Composites Compos. Sci. Technol.*, 34, 225-242 (1999).

- [6] S. K. Maiti, M. F. Ashby and L. J. Gibson, “Fracture toughness of brittle cellular solids”, *Scripta Metall.*, 18, 213-217 (1984).
- [7] A. McIntyre and G.E. Anderston, “Fracture properties of a rigid polyurethane foam over a range of densities”, *Polymer*, 20 (2), 247253 (1979).
- [8] DIN 53421. Testing of rigid cellular plastics. Compression test.
- [9] ISO 527-2. Plastics-Determination of tensile properties-Part 2: Test conditions for moulding and extrusion plastics
- [10] DIN 53294. Testing of sandwiches. Shear test.
- [11] ASTM E1820-01. Standard test method for measurements of fracture toughness.
- [12] ASTM D790. Standard test methods for flexural properties of unreinforced and reinforced plastics and electrical insulating materials.

THE FRACTURE PROPERTIES OF LIGHTWEIGHT SANDWICH STRUCTURES BASED ON LATTICE ARCHITECTURES

Y. Shen^{*}, S. McKown[†], S. Tsopanos[†], C.J. Sutcliffe[†], R. Mines[†] and W.J. Cantwell[†]

^{*} Department of Engineering, University of Liverpool, Liverpool L69 3BX, UK

email: ^{*} syoeva@liverpool.ac.uk, [†] smackown@liverpool.ac.uk, [†] sozos@liverpool.ac.uk,
[†] cjs1@liverpool.ac.uk, [†] em14@liverpool.ac.uk, [†] cantwell@liverpool.ac.uk

Key words: Sandwich structures, Lattice structure, Experimental mechanics

Summary. *Continuous metallic lattice structures have been manufactured using a selective laser melting (SLM) rapid prototyping technique. The lattices are assemblies of repeating unit-cells and, unlike metal foams, exhibit a high level of homogeneity in terms of their mechanical properties. A brief summary of the lattice structures manufactured, the mechanical properties of the lattices, and the performance of a sandwich beam with a lattice core are reported here.*

1. INTRODUCTION

There is considerable interest in the potential offered by metallic foams, such as those based on aluminium and steel for use in a range of energy-absorbing structures. Extensive research has shown that metal foams offer many advantages including electromagnetic wave shielding, low thermal conductivity and excellent toughness. One of the principal limitations of these systems is the irregularity of the cell structure within the metal foam, an effect that can result in overly-conservative design criteria.

Recently, a number of workers have shown that it is possible to design core architectures that offer greater strength and stiffness to weight ratios than those offered by traditional foamed materials [1-6]. The complex topology of the unit-cells in these cores can now be realized using the selective laser melting (SLM) manufacturing process. A range of metals, including aluminium, steel, titanium, and nickel-based super-alloys, can be processed using a high quality fibre laser to selectively melt a bed of metal powder particles into solid material [7]. Hence, a hierarchical structure of extreme complexity can be built up layer by layer. Initial studies have shown that sandwich structures based on lattice architectures offer an excellent resistance to blast loading such as that generated by a plastic explosive [8]. Further work is required, however, to fully characterise and understand the response of those structures under both static and dynamic loads.

2. LATTICE TOPOLOGY

Lattice cuboids of equal edge lengths, 20 mm, see Figure 1 (a), were manufactured from 316L stainless steel powder for static and dynamic testing. The topologies of the unit-cells are shown in Figure 1 (b), and are referred to as pillar-octahedral [$0^\circ, \pm 45^\circ$], or octahedral [$\pm 45^\circ$]. Each of them has a cubic unit-cell size of 2.5 mm, giving respective unit-cell relative densities of approximately 3% and 4%.

The lattice structures in this study have strand densities that were determined to be ninety-nine point nine percent dense and show evidence of the layered laser manufacturing technique along their lengths, see Figure 1 (c). The cross-sections of the strands in the lattice structures were circular in shape as shown in the scanning electron micrograph presented in Figure 1 (d).

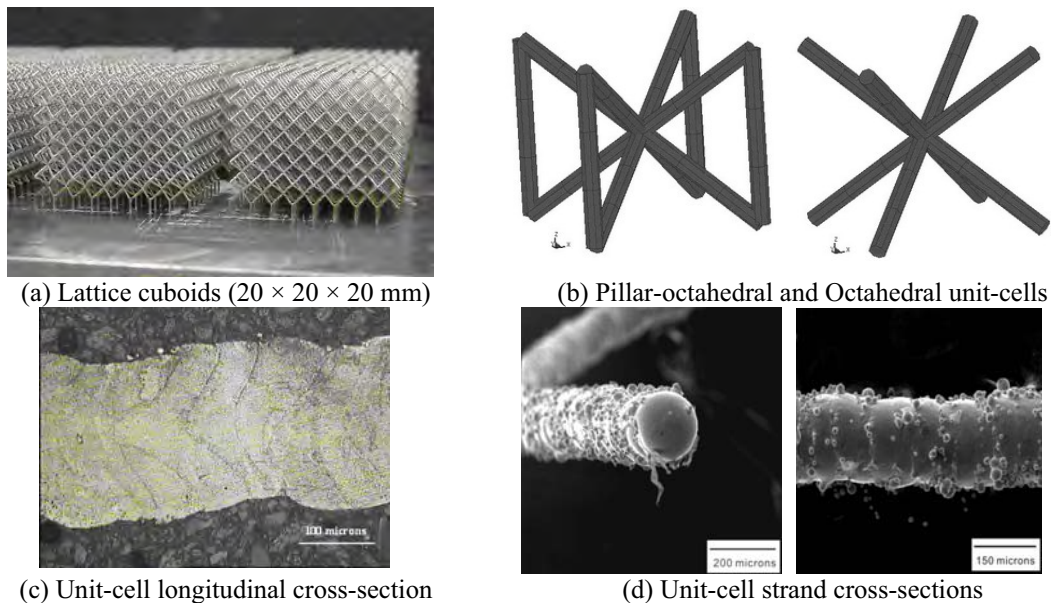


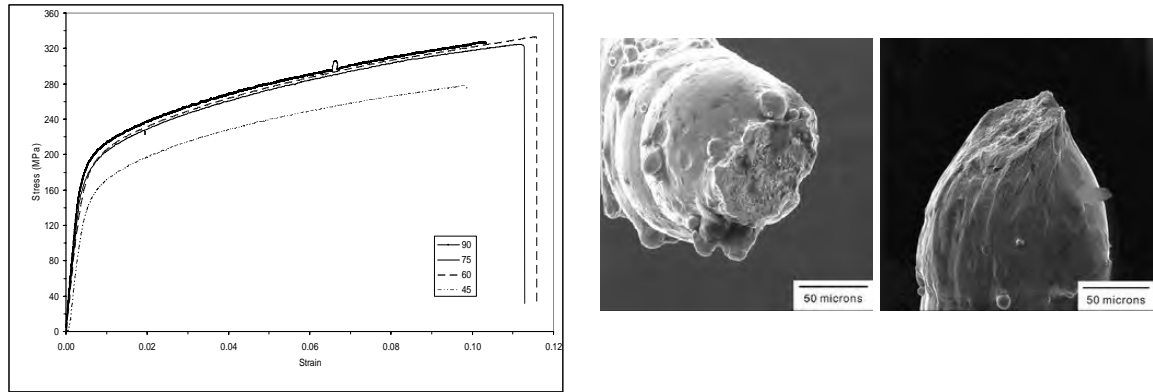
Figure 1: Geometric details of the lattices.

2.1 Tensile Tests on 316L strands

Tensile tests were conducted on 316L strands which were built at angles of 45, 60, 70 and 90 degrees using a 1000 microseconds laser power of 5000 watts. This strands were produced in order to investigate the effect of built angle on mechanical behaviour. The strands were subjected to tensile loading at a crosshead displacement rate 0.5 mm/min.

Figure 2 (a) shows typical stress-strain traces for the 316L strands. The average elastic modulus results obtained from the tensile tests on the 316L strands suggest a value of 50 GPa, this being only 26% of the elastic modulus of the plain 316L steel. It is evident from Figure 2 (a) that the stress of the 316L strands built at 60, 75 and 90 degrees are similar with the exception of the strands at 45 degrees. It is clear that the maximum stress reduced by approximately 18% by changing the strand angle from 0 degrees to 45 degrees. Two SEM photographs of 316L strands showing the broken ends following tension testing are shown in

Figure 2 (b). It is clear that the strands were stretched until broken, and full density is observed.



(a) The stress-strain responses of the 316L strands (b) Broken ends of a strand following a tension test

Figure 2: Tensile test results and micrographs

2.2 Quasi-static Compression on the Lattice Structures

Initial compression tests were conducted on lattice structures A to C and on sandwich structure D. The $[\pm 45^\circ]$ lattice geometry was incorporated into sandwich structure D, based on plain weave carbon-fibre epoxy composite skins, using a hot-stamping manufacturing technique [9]. The resulting sandwich blocks exhibited excellent bonding at the core-skin interface [10]. The lattices were subjected to compression loading at displacement rates ranging from quasi-static to approximately 3 m/s (average global strain-rates of 10^{-4} s^{-1} to $1.5 \times 10^2 \text{ s}^{-1}$). After testing, a number of the lattice structures were examined in a Hitachi S-2460N scanning electron microscope.

Typical engineering stress-strain curves following compression tests on the lattice structures following tests at a quasi-static strain-rate are shown in Figure 3. The trends are typical of those displayed by cellular materials. Following the initial elastic region, the stress reaches a plateau due to the initiation of plastic bending or buckling failure. The plateau region, a result of progressive crushing of the cell layers, extends up to densification of the cells. A relatively high degree of linearity in the elastic region suggests localized yielding of the strands is not as significant as that observed in metal foams [11]. This is likely to be a result of the presence of regular hierarchical structures in the repeating unit-cells of the lattices.

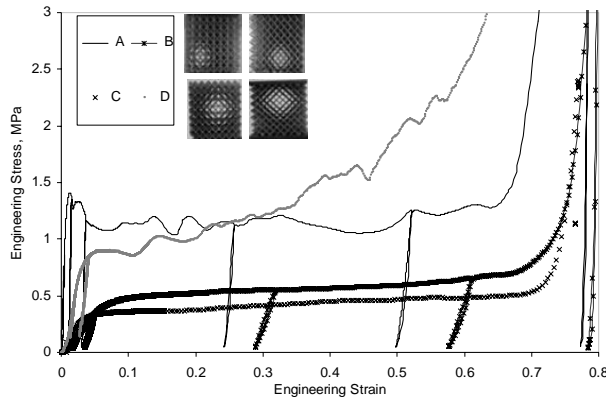


Figure 3: Typical Engineering stress-strain curves for Lattices A to D.

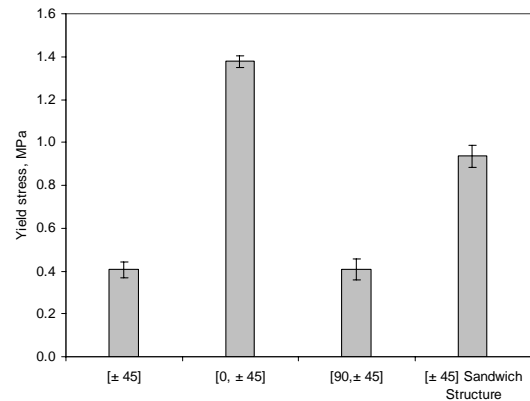


Figure 4: Summary of the collapse-stresses for different lattice structures.

The transition from the elastic to the plastic region in the stress-strain curves involves fundamentally different deformation mechanisms for the $[\pm 45^\circ]$ and $[0^\circ, \pm 45^\circ]$ lattices. The $[\pm 45^\circ]$ system exhibits a smooth stress-strain trace, with no discernable yield point and a continuously increasing stress with increasing applied strain. In contrast, Lattice B has a well-defined yield point associated with plastic bending of the vertical strands, followed by global shear failure, triggered by localised buckling instabilities in the 0° strands. The stress-strain curve of the Lattice C presents a smooth plateau region and no recognizable yield point. The struts were oriented along the horizontal edges of cubic unit-cell and there were no vertical strands. Sandwich structure D displayed a similar stress-strain behaviour to Lattices A and C in the beginning of the elastic and plastic regions, and then started to exhibit an uneven plateau followed by a steep rise.

A summary of the compressive properties of structures A to D is shown in Figure 4. Here, it is clear that the $[0^\circ, \pm 45^\circ]$ lattice offers a significantly higher yield stress than the other structures, this being due to the presence of 0° vertical pillars in the $[0^\circ, \pm 45^\circ]$ structures.

The photographs in Figure 5 highlight the smooth stress-strain response of the $[\pm 45^\circ]$ lattice structure with no localised failure. The photo of the $[0^\circ, \pm 45^\circ]$ lattice clearly shows that localized buckling leads to shear banding. Localised deformations are observed in Figure 5 (c), following global deformation, which exhibits similar progression to the $[\pm 45^\circ]$ lattice. The sandwich block exhibits two diagonal shear bands at a cross-head displacement of 2.5 mm; following an increased stain, sandwich structure D exhibits a barrel shape due to the top and bottom cells being bonded to the carbon-fibre composite skins. SEM photographs were taken of the compressed lattice blocks and the deformation of individual unit-cells was examined. In the photos taken from the top of the $[90^\circ, \pm 45^\circ]$ lattice, Figure 6, diamond-shaped cells are observed, caused by the 90° strands restricting the cells extending in the vertical direction, rather than in the direction of the other diagonal.

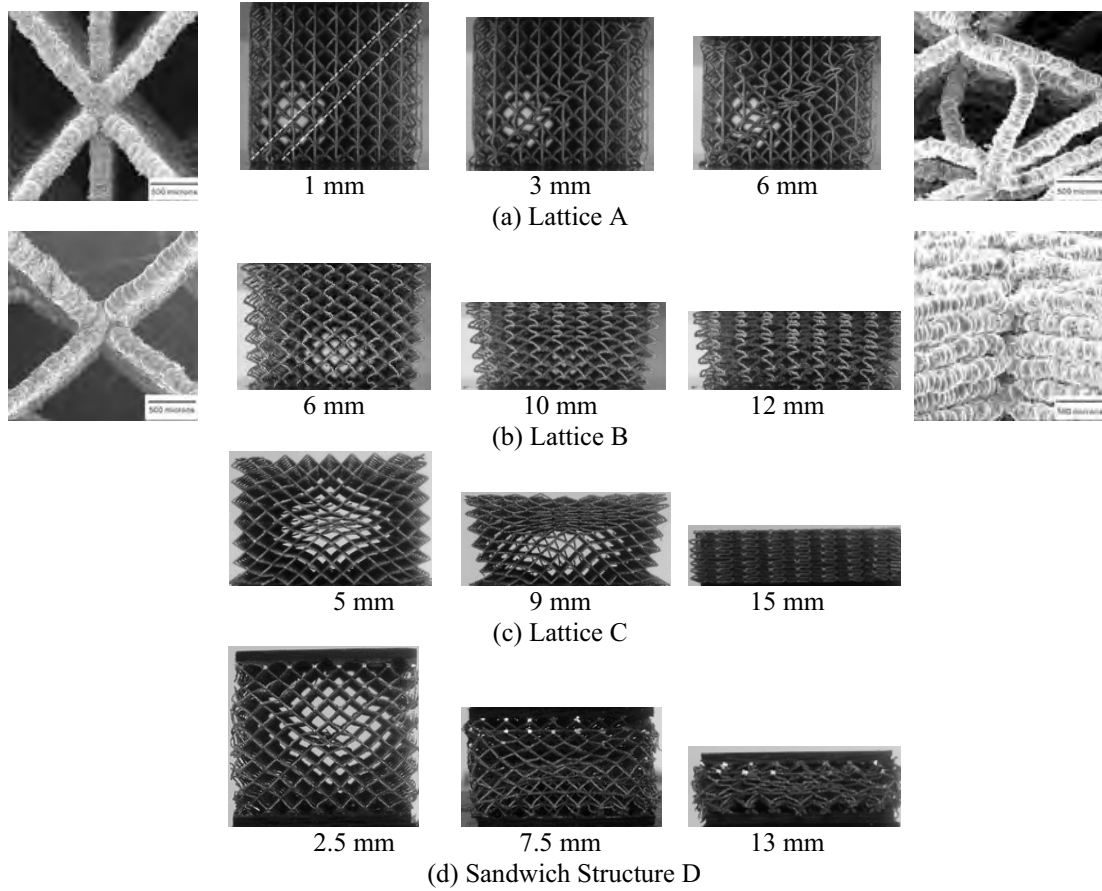


Figure 5: The deformation mechanisms for Lattices A to D, the dimensions correspond to the crosshead displacement.

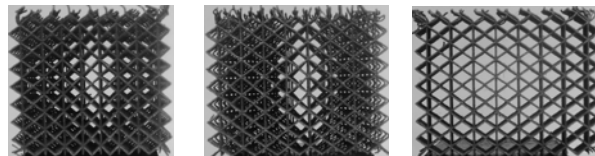


Figure 6: Photos taken from the top of the $[90^\circ, \pm 45^\circ]$ lattice structure.

Following the compression tests, the data were characterised in terms of the relative density (ρ/ρ_s) using the equation

$$\frac{N}{N_s} = m \times \left(\frac{\rho}{\rho_s} \right)^n \quad (1)$$

where N and N_s are the modulus or yield strength of the lattice and parent material respectively. The constants m and n were evaluated, by fitting curves to plots of relative modulus (and yield) versus relative density. The constant m was approximately 1 for both the relative modulus and the yield strength of the $[0^\circ, \pm 45^\circ]$ and $[\pm 45^\circ]$ lattices. The relative modulus yielded values for n of 2.2 and 2.8 for the $[0^\circ, \pm 45^\circ]$ and $[\pm 45^\circ]$ lattices respectively.

The relative yield values for n were 1.5 and 1.9 for the $[0^\circ, \pm 45^\circ]$ and $[\pm 45^\circ]$ lattices respectively. The results for the $[0^\circ, \pm 45^\circ]$ lattice are comparable to an open-cell foam [11], which is a bending-dominated structure in which the modulus increases as the square of the relative density and yield stress increases with relative density to the power 1.5.

The compression tests were conducted at displacement rates up to 3 m/s. Figure 7 shows that the compression strength increased steadily by approximately twenty-five percent over the range of rates considered. It can be seen from Figure 8 that there is no significant difference in the samples following compression test at 1mm/min and 3m/s.

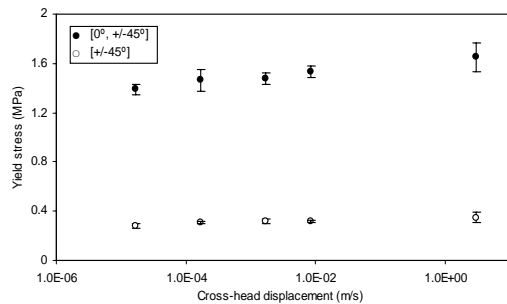


Figure 7: The variation of yield stress with crosshead displacement rate

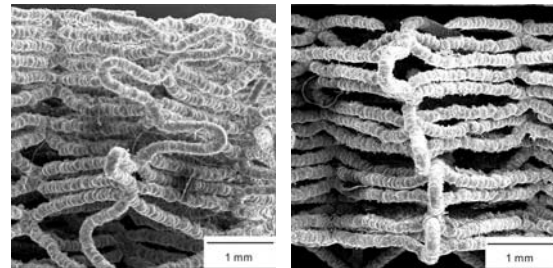


Figure 8: SEM photographs of the $[0^\circ, \pm 45^\circ]$ samples following compression test at 1mm/min. and 3m/s

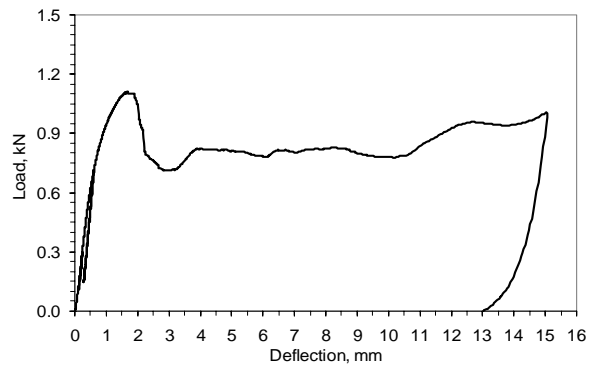
2.3 Three Point Bend Tests on the Sandwich Beams

The flexural response of the sandwich beams with the $[\pm 45^\circ]$ lattice cores were investigated under three-point bending. Loading rates from 0.25mm/min to 4m/s were employed to investigate the flexural response of these sandwich structures.

Sandwich beams of mass 20 g, length 100 mm, width and depth 20 mm were manufactured with $[\pm 45^\circ]$ lattice cores and skins based on 4 plies of carbon-fibre reinforced plastic using a hot compaction process. No adhesive was used at the skin-core bond interface, since the controlled pressure applied during manufacture allowed the pre-preg resin to flow over the strands at the lattice surfaces. No evidence of delamination was observed, when the beams were subjected to quasi-static and impact loads under three-point bending, see Figure 9 (a). Typical quasi-static lattice sandwich beam load-displacement curves are shown in Figure 9 (b) with a peak load of around 1.1 kN and an initial stiffness 1.77 kN/mm.



(a) Sandwich beam subjected to three-point bend loading



(b) Loading rate 0.25mm/min.

Figure 9: Three-point bend test on a lattice sandwich beam.

Previous work on sandwich beams based on a metal core has shown that such structures fail in a number of modes: face yielding, face wrinkling, core yielding and indentation [11]. Similar failure modes were observed during this study, as shown in Figure 10. Failure of the skin initiates at the initial peak load, followed by progressive crushing of the core. During indentation, localised crushing of the core occurs by plastic bending of the strands, similar to that seen in the compression tests. The indentation pressure on the foam core is only slightly higher than the uniaxial compressive strength [11]. It can be seen in Figure 10 (c) that the loading crushes the lattice, bending the face sheet to accommodate the lattice core deformation. Ashby et al [11] identified two competing collapse mechanisms in sandwich beams in three point bending: Mode A and Mode B. In this study, the lattice sandwich beam sheared in the collapse Mode B. Here, a cylinder indenter was used here and no mid-span plastic hinge was observed, only the existence of shearing at the outer supports, see Figure 10 (d). This was caused by a transverse shear force in core, and plastic collapse by core shear can result.



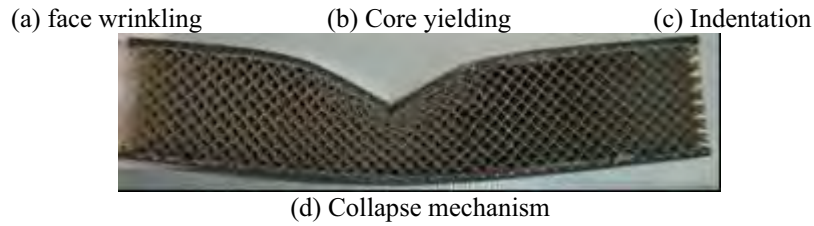


Figure 10: Failure modes of sandwich beams

Drop-weight tests produced a linear response between the residual deflection and impact energy, as shown in Figure 11. SEM photographs also showed that the energy absorbed by the lattice core increases with deflection by cell collapsing, whilst the upper skin showed more damage. Localised deformation of the lattice core below the indenter was investigated using a SEM. Two regions were observed, as circled in Figure 12: cells underneath the indenter and cells beside the indenter. In region I, the cells underneath the skin buckled. This region is clearly compression dominated. In contrast the cells in region II, the strands were stretched. This evidence suggests that the impact energy of the projectile was mainly absorbed by lattice cell collapsing and stretching.

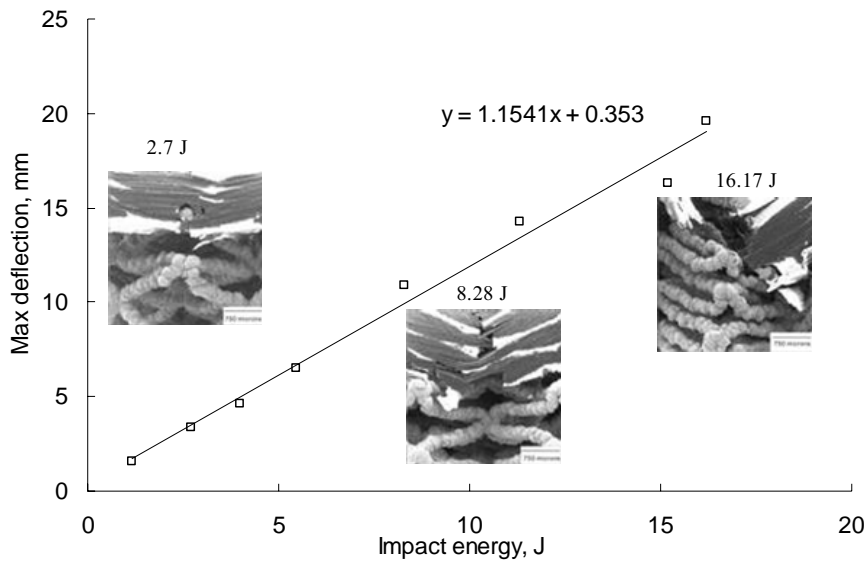
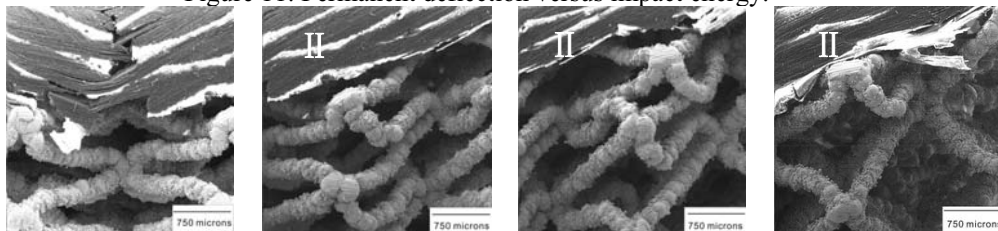


Figure 11: Permanent deflection versus impact energy.



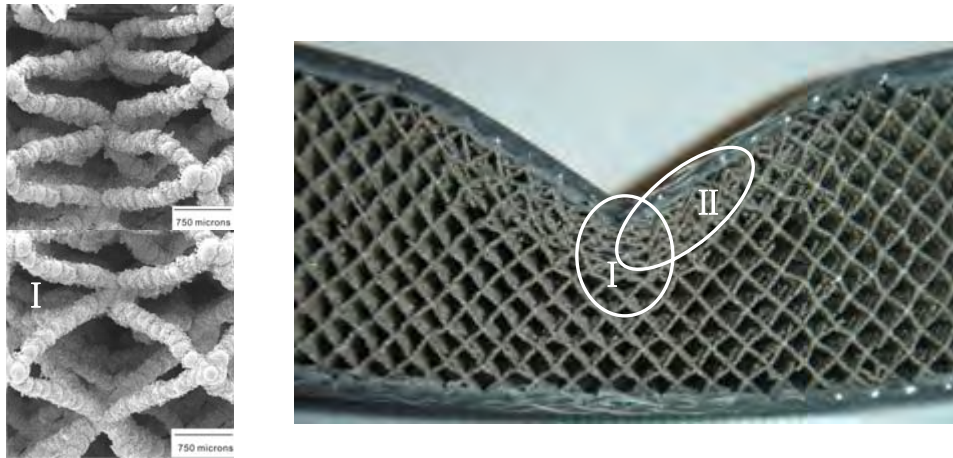


Figure 12: Localised failure of the lattice core

FE simulations also indicate that stretching of the strands occurred in the core-skin interface regions either side of the indenter. This may explain why delamination does not occur as the strain energy is transferred into the deformed strands.

2.4 Modified Three Point Bend Test

The modified three point bend specimen (MTPB) developed by Cantwell et al [12] was used to characterise the interfacial fracture toughness of the sandwich structures. The Mode I interlaminar fracture toughness G_{IC} may be determined using the experimental compliance method (Berry's method) approach, based on the plot of the log compliance vs log crack length. This can then be used to give G_{IC} as follows [13]

$$C = Ka^n \quad (2)$$

where n is the slope of this plot, so:

$$G_{IC} = \frac{nP\delta}{2ba} \quad (3)$$

where P is the load, δ is the indenter displacement, b is the specimen width and a is the crack length.

Lattice sandwich beams of 25mm width, 150 mm length were prepared and the lower skin and core was removed at one end, leaving a section of the upper face-sheet material protruding from the remaining sandwich specimen. Since the MTPB specimen is used for testing structures with very thick facings, 12 plies of carbon-fibre reinforced plastic were used in upper skin with a thickness of 3 mm, Figure 13. Loading rates of 0.5mm/min and 3m/s were employed.

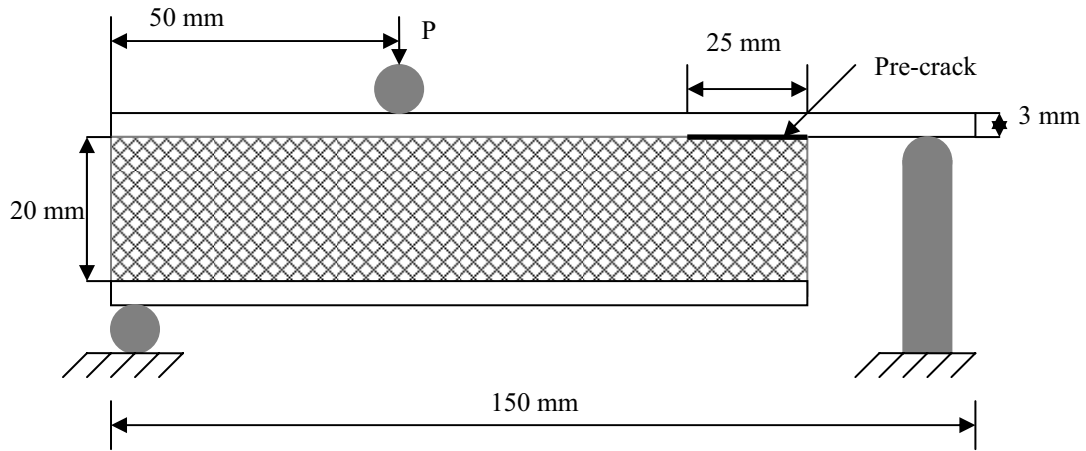
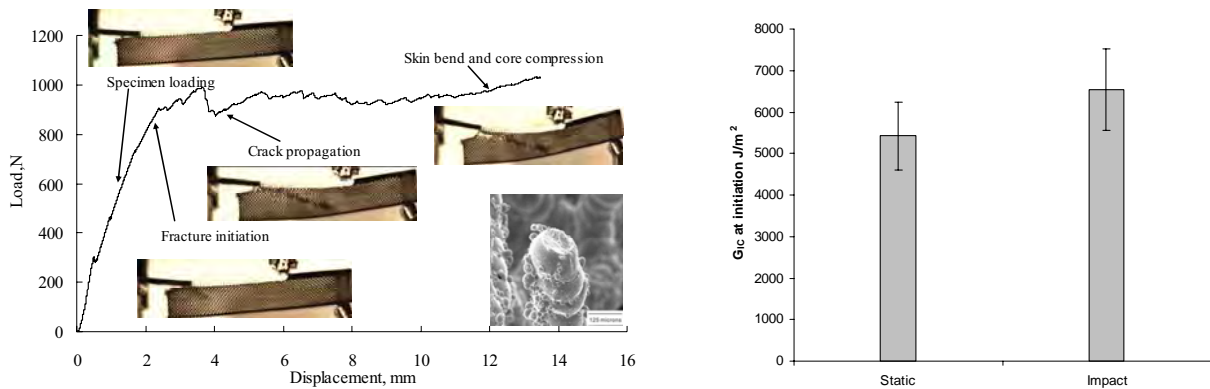


Figure 13: Schematic of the modified three point bend (MTPB) sandwich specimen.



(a) Typical load-displacement curve following on MTPB test

(b) Initiation G_{IC} at quasi-static (0.5mm/min) and impact (3m/s) loading rates

Figure 14: MTPB test results

A typical load versus crosshead-displacement record obtained from a quasi-static MTPB test is showed in Figure 14 (a). Crack propagation was monitored optically and was unstable as highlighted in the figure. An increasing load was applied to the MTPB sample, strands attached to the upper skin started to stretch, a shear band occurred at fracture initiation, crack propagation extended from the pre-crack resulting in a slight drop in load, afterwards, load steady increased causing by skin bending and localised core crushing. A SEM photograph showed strand failures similar to those observed in the tensile tests. The initial fracture toughness G_{IC} was used to characterise the delamination resistance of the lattice sandwich structure since crack propagation in the MTPB test involved tearing of the core but no strand extraction out of skin. Relatively high G_{IC} values were obtained, which were approximately $5500 J/m^2$ at quasi-static rates and $6500 J/m^2$ under low velocity impact loading. Figure 14 (b) suggests that the G_{IC} increased by approximately fifteen percent from 0.5mm/min to 3m/s.

3. CONCLUSIONS

A series of quasi-static and low velocity impact tests have shown that the mechanical properties depend on the unit-cell geometry. This offers the possibility of using SLM metal lattice structures in load-bearing applications, for which metal foams are not favoured due to their in-homogeneity. The experimental data have shown that the 316L lattice structures exhibit a moderate rate sensitivity. Sandwich structures have been manufactured using a simple process without the need for a core-skin adhesive. These samples showed excellent bonding at the interface with no delamination being observed when loaded statically and dynamically in three-point bending. An analysis of the composite sandwich beams showed that metal lattices can be used as cores with excellent delamination resistance. Optimisation of the unit-cell could improve the specific mechanical properties leading to an increase in the competitiveness of SLM metal lattices relative to open and closed cell metal foams.

REFERENCES

1. F.W. Zok, H.J. Rathbun, Z. Wei, and A.G. Evans, *Design of metallic textile core sandwich panels*, Int. J. of Solids and Structures, Vol. 40, No. 21, pp. 5707-5722 (2003).
2. S. Chiras, D.R. Mumm, A.G. Evans, N. Wicks, J.W. Hutchinson, K. Dharmasena, H.N.G. Wadley, and S. Fichter, *The structural performance of near-optimized truss core panels*, Int. J. of Solids and Structures, Vol. 39, No. 15, pp. 4093-4115 (2002).
3. J. Wang, A.G. Evans, K. Dharmasena, and H.N.G. Wadley, *On the performance of truss panels with Kagomé cores*, Int. J. of Solids and Structures, Vol. 40, pp. 6981-6988 (2003).
4. V.S. Deshpande, N.A. Fleck, and M.F. Ashby, *Effective properties of the octet-truss lattice material*, J. Mechanics and Physics of Solids, Vol. 49, No. 8, pp. 1747-1769 (2001).
5. V.S. Deshpande, and N.A. Fleck, *Collapse of truss core sandwich beams in 3-point bending*, Int. J. of Solids and Structures, Vol. 38, No. 36-37, pp. 6275-6305 (2001).
6. V.S. Deshpande, M.F. Ashby, and N.A. Fleck, *Foam topology: bending versus stretching dominated architectures*, Acta Materialia, Vol. 49, No. 6, pp. 1035-1040 (2001).
7. W.K. Brooks, J. Todd, and C.J. Sutcliffe, *The production of open cellular lattice structures using selective laser melting*, Sixth National Conference on Rapid Prototyping, Design, and Manufacturing (2005).
8. S. McKown, Y. Shen, W.K. Brookes, C.J. Sutcliffe, W.J. Cantwell, G.S. Langdon, G.N. Nurick, and M.D. Theobald, *The quasi-static and blast loading response of lattice structures*, submitted to the Int. J. of Impact Engineering.
9. G. R Reyes and W. J. Cantwell, *The mechanical properties of fiber-metal laminates based on glass fiber reinforced polypropylene*, Comp. Sci. Tech., Vol. 60, pp. 1085-1094 (2000).
10. Y. Shen, S. McKown, S. Tsopanos, W.K. Brookes, C.J. Sutcliffe, R. Mines and W.J. Cantwell, *The impact response of sandwich structures based on high-performance lattice structures*, IMPLAST, Bochum, Germany, 2007.
11. M.F. Ashby, A. Evans, N.A. Fleck, L.J. Gibson, J.W. Hutchinson and H.N.G. Wadley, *Metal Foams: A design guide*, Butterworth-Heinemann, Oxford 2000.

12. Cantwell W.J., Scudamore R.J., Davies P. and Ferrer J-B., Proc. 11th International Composite Materials, Woodhead, 1997, pp905-914
13. ISO 15024, 2001 Fibre-reinforced plastic composites-Determination of mode I interlaminar fracture toughness, G_{IC} , for unidirectionally reinforced materials.

EFFECT OF SANDWICH CORE PROPERTIES ON ULTIMATE STRENGTH OF A WIND TURBINE BLADE

Kim Branner^{*}, Find M. Jensen^{*}, Peter Berring^{*}, Amit Puri[†], Andrew Morris[§] and John P. Dear[†]

^{*} Wind Energy Department, Risø National Laboratory
Technical University of Denmark
Frederiksborgvej 399, Building 118, DK-4000 Roskilde, Denmark
e-mail: kim.branner@risoe.dk, web page: <http://www.risoe.dk>

[†] Department of Mechanical Engineering
Imperial College London
South Kensington, London, SW7 2AZ, UK
e-mail: j.dear@imperial.ac.uk, amit.puri01@imperial.ac.uk

[§] Power Technology
E.ON UK
Ratcliffe-on-Soar, Nottingham, NG11 0EE, UK
e-mail: Andy.P.Morris@eon-uk.com

Key words: Sandwich webs, Wind turbine blade, Full-scale test, Parameter study.

Summary. *The aim of this study is to investigate how the sandwich properties in the webs in a wind turbine blade influence the ultimate strength of the whole blade. A parameter study is performed using a highly detailed finite element model. The numerical results are compared with a full-scale test of the box girder from a 34m wind turbine blade using one particular sandwich web design.*

1 INTRODUCTION

We currently see a substantial growth in the wind energy sector world wide and this growth is expected to be even faster in the coming years. By the end of 2006 almost 1% of the world's electricity generation was produced by wind turbines. According to BTM Consult [1] the forecast for 2011 is 2% of world's electricity generation and the estimation for 2016 is 4% of world's electricity generation. This means that a massive number of wind turbine blades will be produced in the coming years and therefore there is a very large potential for saving material in these structures. This work is a step in an ongoing effort to optimize the usage of the materials in wind turbine blades.

Modern wind turbine blades are often constructed with a load-carrying box girder (main spar) that supports the outer shell. The purpose of the box girder is to give the blade sufficient strength and stiffness, both globally and locally. Globally, the blade should be sufficiently

stiff in order not to collide with the tower under all types of loading. Locally, the webs, together with the stiffness of the outer shell, ensure that the shape of the aerodynamic profile is maintained. The materials used are highly advanced composites that have high strength- and stiffness-to-weight ratios. The webs usually extend from the root of the blade to a position close to the tip, and the load carrying flange of the box girder is generally a single skin construction. The webs are usually quite thin sandwich structures and the main purpose of these is to take the shear loads on the blade. However, non-linear effects at high loading result in higher loading of these webs and may result in lower ultimate strength of the whole blade than expected when the design is based on linear calculations.

Earlier full-scale tests of wind turbine blades have shown substantial damage in the webs after ultimate failure [2-4]. It is often difficult to make solid conclusions on the failure sequence. However, there are indications that the ultimate failure in some cases is initiated by collapse of the sandwich structure of the webs [3-5]. In another study, slices from the box girder of a wind turbine blade were tested to failure under a type of 3-point bending. It was found that the probable reason for ultimate failure was shear fracture of the core in the webs, leading to debonding of the skins and then ultimate failure [6]. The applied load was not a realistic blade loading but the study showed that it is important to take the non-linear behaviour of the core material into account to explain the failure sequence. The focus of the research presented in a partner paper [7], is the failures that can occur with sandwich structures, and possible means of detecting damage inside the components by use of Digital Image Correlation (DIC).

In this paper it is investigated how the sandwich properties of the webs influence the ultimate strength of the box girder and therefore the ultimate strength of the whole blade. A parameter study with different core densities is performed using a highly detailed finite element (FE) model. The numerical results are compared with a full-scale test of the box girder from a 34m wind turbine blade using one particular sandwich web design. This paper is building on experimental and numerical work already published in [4,5] and is part of an ongoing effort to understand the observed full-scale test results.

2 FULL-SCALE TEST

2.1 Box girder

The tested box girder is an essential part of a 34m blade designed for a 1,5MW wind turbine and manufactured by SSP Technology A/S. The box girder is made of prepreg glass fibre/epoxy and most of the fibres are orientated in the longitudinal direction to carry the flapwise loads and limit tip deflection. The box girder is the load carrying part of the wind turbine blade and is bonded between the aerodynamic shells during the manufacturing process. The box girder was shortened to 25.4m before the test as failure in the tip is not critical [8]. Test setup is shown in Figure 1.

A complete 34m wind turbine blade from SSP-Technology (box girder including the aerodynamic shells) has previously been through full-scale testing. These tests have shown that it was able to withstand the required loads for certification. After the box girder had

passed all these required static and dynamic tests, it was tested to failure flapwise. This last test showed that the shear webs were the most critical part of the blade and they have therefore been reinforced in these new tests. These reinforcements are shown in Figure 2a. Because of the reinforcements other failure mechanism can then be studied as described in [3]. Tophat reinforcement is also introduced in the root section to avoid unwanted buckling failure in this region, see Figure 2b. Failure in the root section is unrealistic since the aerodynamic shell on the real blade will prevent buckling here (see also [4]).



Figure 1: Full-scale test of load carrying box (box girder) from a 34m wind turbine blade

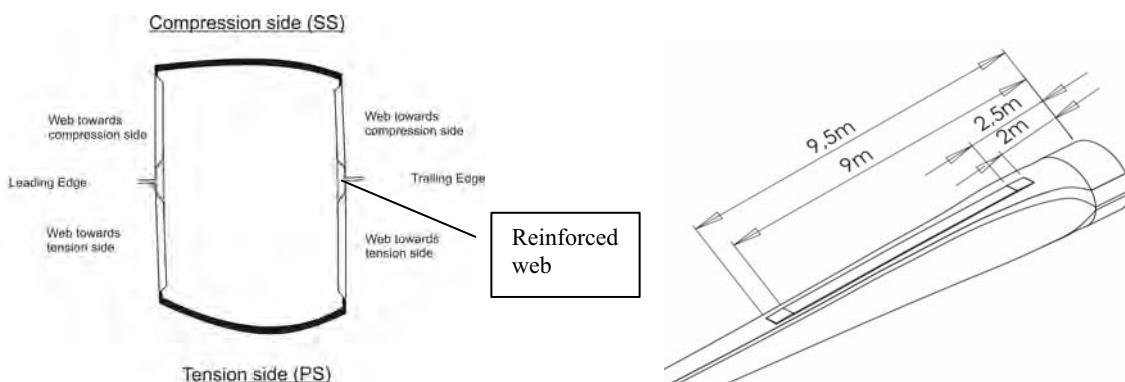


Figure 2: a) 2D sketch of the box girder with reinforcement. b) Tophat reinforcement on compression side.

2.2 Loads and supports

Since the tip was cut off, the moment transferred from the tip is compensated at distance of 25m. The loads were applied at 13.2m, 19m and 25m from the root as shown in Figure 3.

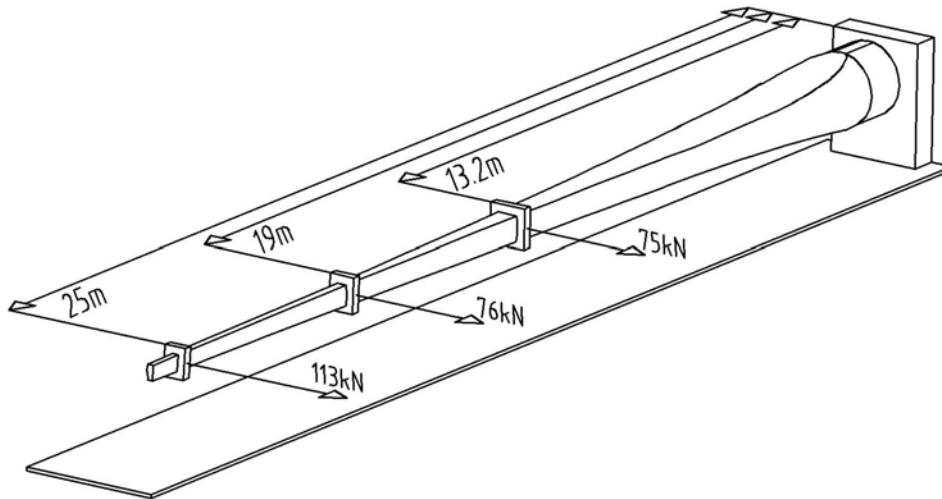


Figure 3: Sketch of box girder with applied forces.

The percentage of load used in this paper refers to the ultimate failure load of the complete original wind turbine blade.

Three simple supports mounted with roller-skates were used to eliminate twisting and distortion of the box girder during the flapwise tests, see Figure 4. They were placed at distance of 9m, 13.2m and 19m from the root.

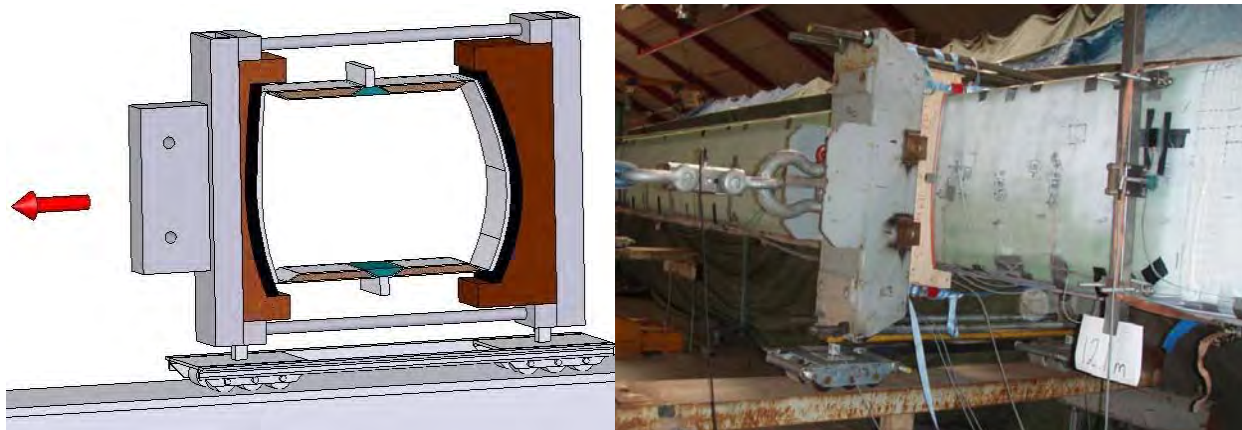


Figure 4: a) Sketch of roller-skate support. b) Roller-skate support at 13.2m

2.3 Ultimate failure

The box girder was tested until failure and it seems that the ultimate failure is initiated by

failure in the sandwich webs. Figure 5a shows a frozen frame picture from the test video immediately before ultimate failure. It seems to show initial face debonding of the outer skin on the shear web's sandwich section, leading to ultimate collapse of the box girder.

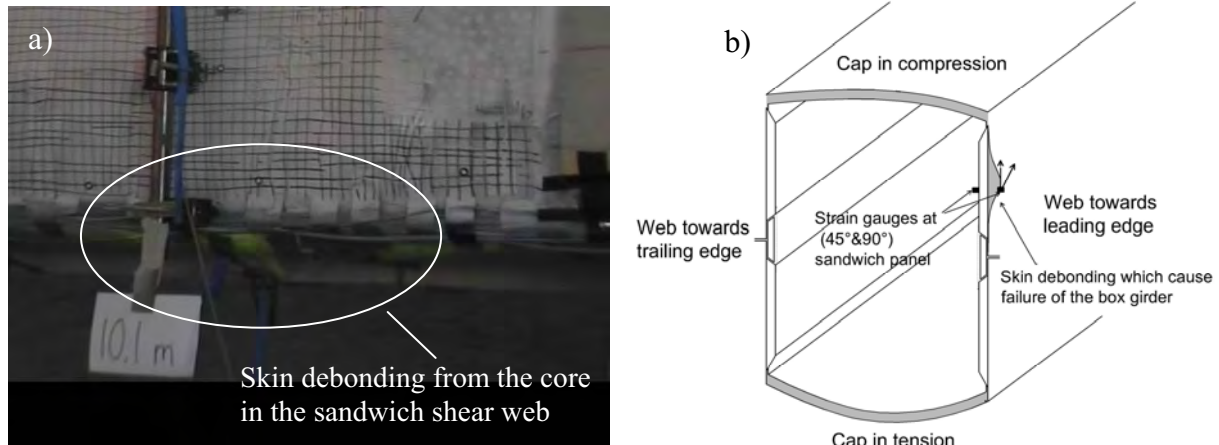


Figure 5: a) Frozen frame picture immediately before ultimate failure. b) Skin debonding of the sandwich web towards leading edge.

While other blades may have stronger (or weaker) webs, the FE-study and full-scale tests have shown that it is generally important to consider the Brazier loads (crushing pressure) in the design process. Brazier loads are non-linear in nature, so only geometrically non-linear, FE-analyses will take this phenomenon into account. It is also important to note that even when non-linear effects are included in the FE analysis, it can still be difficult to estimate the failure load. This is because strain based failure criteria often cannot predict phenomena like the skin debonding and elastic instabilities.

The debonding of the skins may arise from shear fracture in the core, which then spread to the skin-core interface and grow in delamination causing skin debonding. This was the concluded sequence of failure found in [6], when slices from the box girder of a different wind turbine blade were tested. This hypothesis is initially studied in this paper by performing a parameter study with different core densities in the webs.

3 COMPARISON WITH NUMERICAL MODEL

3.1 Finite element model

A large finite element model of the load carrying box girder, which carries up to 90% of the flapwise loads in the wind turbine blade structure, was analyzed during this work using MSC-Patran and MSC-Marc.

The cross section of the box girder can be divided into two main groups:

- Caps (flanges)
- Shear webs

The **caps/flanges** are thick laminates, with most of the fibres in the longitudinal direction to limit tip deflection. These caps are modelled with 8-noded layered shell elements (Quad8), using a thick shell formulation (takes shear deformation into account). The elements are located at the mid-thickness of the caps and shell offsets are therefore not needed.

The **shear webs** are sandwich structures, which main purpose is to transfer the flapwise shear forces. The webs are modelled with a combination of shell and solid elements. The thin skins on each side of the webs consisted mainly of biax lamina and are modelled with 8-noded layered shell elements placed in the mid-thickness of the material. The core material in the shear webs are modelled with one 20-noded orthotropic solid brick elements (Hex20) through the thickness. Furthermore, the reinforcement of the webs (see Figure 2a) consists of adhesive and is modelled with 20-noded solid brick elements (Hex20).

The corner stiffness of the FE-model is adjusted by a shell element so the deformation measured during the experimental testing fits the numerical results. For a more detailed description of this adjustment see [3].

A relative coarse mesh density is furthermore applied at the first 6 meter and the last 5 meter of the box girder to minimize the degrees of freedom. From 6 to 21 meter the FE-model consists of a mesh with 128 elements circumferentially and an element aspect ratio no bigger than 2. The entire model has 480000 nodes. The analyses are done through a computer cluster with up to 240 nodes (one processor machines). In this particular case, 26 nodes are used. A part of the model is shown in Figure 6.

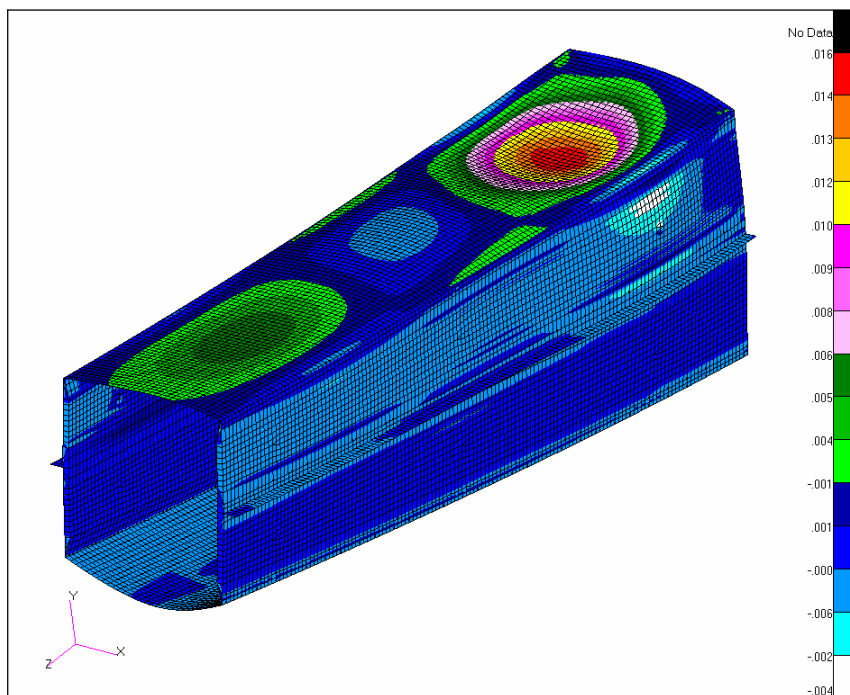


Figure 6: Section of finite element model from 9.5m to 12.3m from root.
Strain in global x-axis (transverse) is shown.

3.2 Comparison

During the full-scale test of the box girder, strain has been measured at different locations. Figure 7 shows strain gauge locations at 10m from the root. Also in Figure 7, the experimental transverse (vertical or 90°) strains for both faces of the sandwich web are compared with both linear and non-linear FEA. The strains presented in Figure 7 are measured on the upper part of the web towards the leading edge, where the failure was observed (see Figure 5).

The longitudinal strains caused by bending of the box girder, leads to associated strains in the transverse direction due to the Poisson's ratio effect. The transverse strains are positive (tension) in the shear webs of the upper half part of the box girder where the bending cause compression and the transverse strains are negative (compression) in the lower half part.

Initially Poisson's ratio results in linearly increasing transverse strain with load as observed in Figure 7. However, as the load increases, the strains become non-linear with respect to applied load and it is noted that the graphs deflect towards compressive strains.

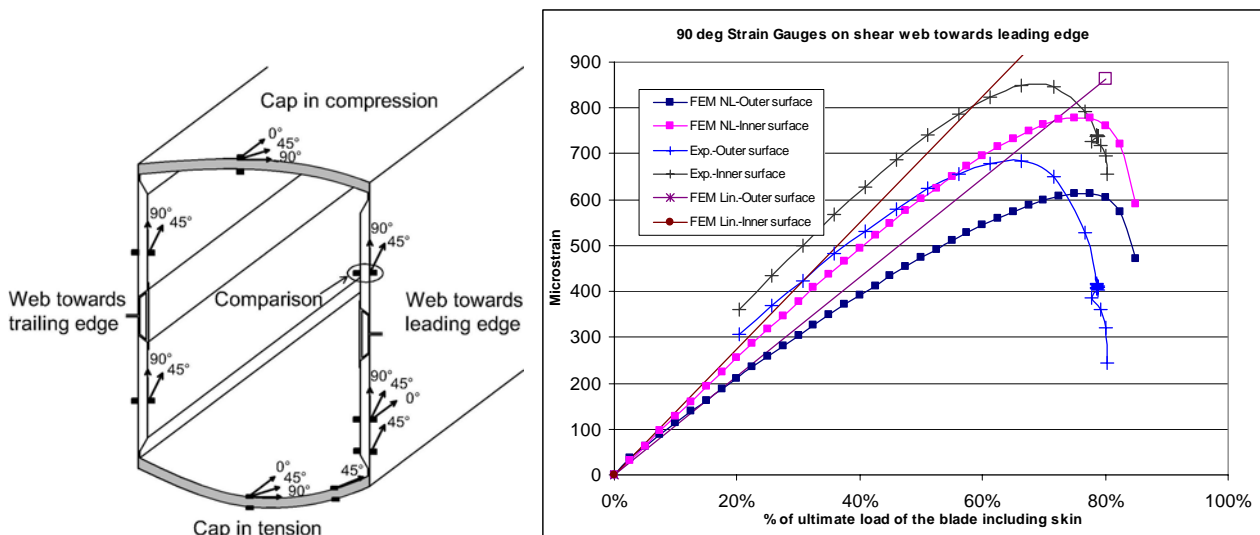


Figure 7: a) Strain gauge locations at 10m from root. b) Back to back strain gauges on upper web part. The load scales refer to a previous full-scale test where the aerodynamic shell was included

The difference between the linear and the non-linear results is, at least in part, caused by the Brazier effect. The crushing pressure is flattening the cross-section and introduces compressive strains into the shear webs. However, this crushing pressure varies with the square of the applied load, resulting in the noted deviation from linear responses. The flattening of the cross-section will probably initiate buckling, that then accelerate the failure as observed. Other non-linear phenomena, such as changes in geometry and loading configuration (which follows the geometry in the non-linear analysis), will also contribute to the observed non-linearities. For further discussion of this see [5].

The non-linear FE-analysis is in good agreement with the measured results, except that the

strains reach their maximum at 75% of the ultimate failure load of the complete original wind turbine blade, rather than at the measured 65%.

4 PARAMETER STUDY

A parameter study is performed, where the core properties in the webs are varied by choosing different core densities between 45 kg/m^3 and 250 kg/m^3 from Divinycell H Grade [9].

The tested box girder is quite flexible in the corners as the connection between the thick flanges and the webs are thin laminates compared with the other structural parts of the cross section (see Figure 2a). This means that when the flanges are flattened by the crushing pressure from the Brazier effect, the resulting bending moments are not transferred into the webs, but almost solely taken by the corners (see Figure 8a). Therefore, the webs are taking little part in the overall deformation of the cross section. A first series of analyses in the parameter study also show that the core properties have minor influence on the overall non-linear behaviour of the box girder and little influence on the strains in the webs (see Figure 9). It is found that the core density have almost no influence on when the vertical strains drop. It is found that the box girder section loses its stiffness at approximately 86% loading for all core densities.

The shear strain in the core is found to be small and there is no indication that debonding of the skins may arise from shear fracture in the core. It is rather caused by local instability of the skin.

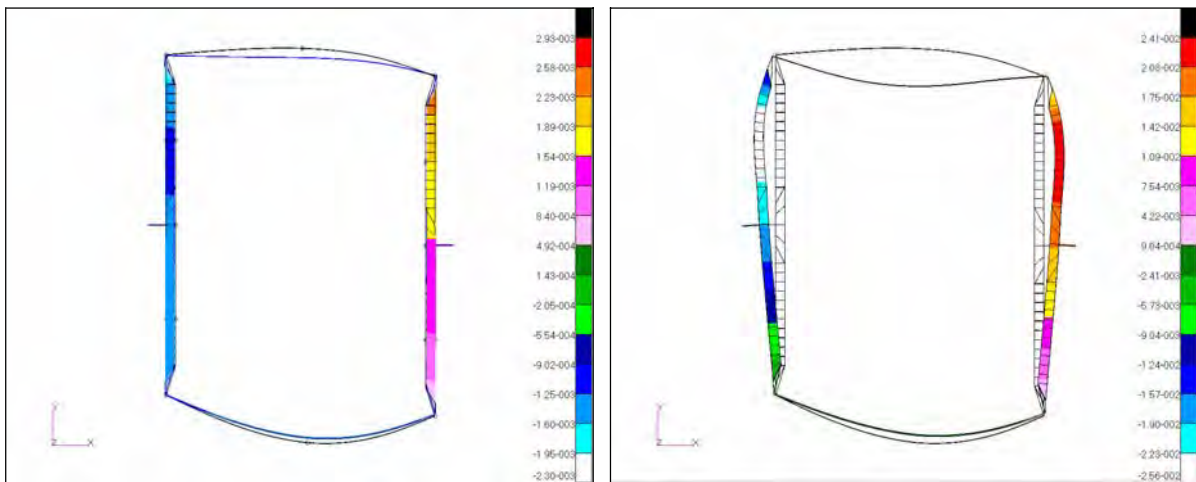


Figure 8: Cross section at 10m from root, H80 core. The deformed section is scaled with 2 and the fringe is transverse deformation (x-axis). a) Soft corners at 85% loading. b) Stiff corners at 95% loading.

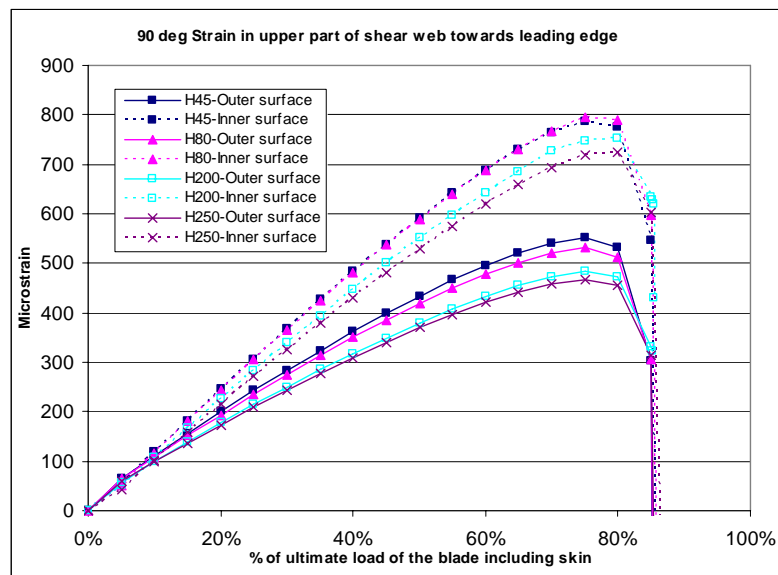


Figure 9: Vertical strain at upper web part 10m from root for soft corners and different core densities. The load scales refer to a previous full-scale test where the aerodynamic shell was included.

Other wind turbine designs have much stiffer corners and in a second series of analyses the bending stiffness of the corners were increased approximately 25 times. In this case the flattening of the flanges by the crushing pressure will result in bending that is transferred into the webs as shown in Figure 8b. At lower load the transverse deflection (x-axis) of the webs is more or less symmetric about the midplane between the flanges. As the load increases the maximum transverse deflection move towards the upper flange (the one in compression) and the highest rotation is seen at the upper corners.

The webs are now taking much more part in the overall deformation of the cross section and large bending strains are seen in the upper part of the webs (see Figure 10). Again it is found that the core properties have small influence on the overall non-linear behaviour of the box girder and little influence on the strains in the webs (see Figure 10). However, it is seen in Figure 10 that the core density have somewhat influence on when the inner vertical strain drop. It is found that the box girder section loses it stiffness at approximately 92% loading for H45 and approximately 97% loading for H250.

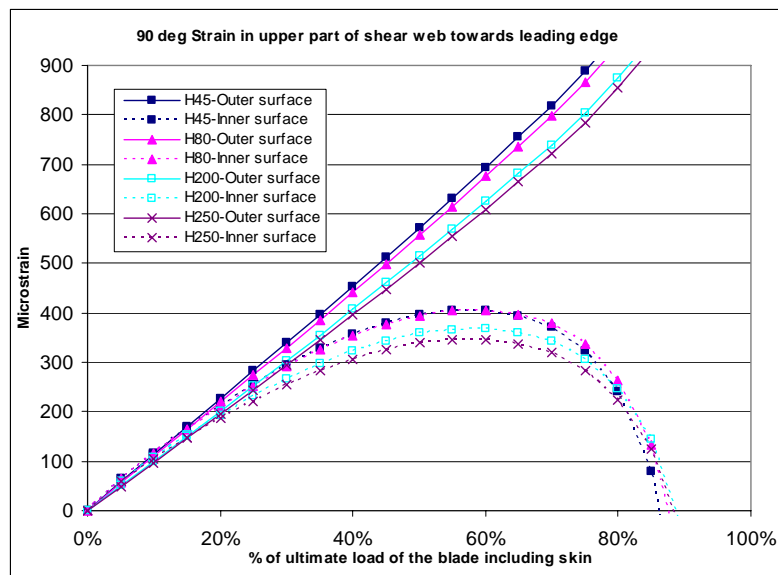


Figure 10: Vertical strain at upper web part 10m from root for stiff corners and different core densities. The load scales refer to a previous full-scale test where the aerodynamic shell was included.

5 CONCLUSIONS

The aim of the study presented in this paper is to investigate how the sandwich properties in the webs of the box girder from a wind turbine blade influence the ultimate strength of the whole blade. A parameter study is performed, where the core properties in the webs are varied by varying the core densities between 45 kg/m^3 and 250 kg/m^3 . The influence of the corner stiffness is also studied as both soft and stiff corners have been analysed.

A soft corner FE-model is compared with full-scale test of a box girder from a 34m blade designed for a 1,5MW wind turbine. It is found that the non-linear FE-analysis is in good agreement with the measured results. The box girder was tested until failure and it seems that the ultimate failure is initiated by failure in the sandwich webs causing skin debonding. The FE-analysis showed that the shear strain in the core is small and there is no indication that debonding of the skins may arise from shear fracture in the core. It is rather caused by local instability of the skin.

From the soft corner models it is found that the core density has almost no influence on the ultimate strength. It is found that the box girder section loses its stiffness at approximately 86% loading for all core densities.

It is found that the corner stiffness greatly influence the overall non-linear behaviour of the box girder as the webs are taking much more part in the overall deformation of the cross section when the corners are stiff. From the stiff corner models it is seen that the core density has somewhat influence on the ultimate strength. It is found that the box girder section loses its stiffness at approximately 92% loading for the 45 kg/m^3 core and approximately 97% loading for the 250 kg/m^3 core.

ACKNOWLEDGEMENTS

The work is partly supported by the Danish Energy Authority through the 2005 Energy Research Programme (EFP 2005). The supported EFP-project is titled "Improved design of large wind turbine blades of fibre composites – phase 3" and has journal no. 33031-0078. The support is gratefully acknowledged.

REFERENCES

- [1] BTM Consult ApS, *International Wind Energy Development - World Market Update 2006*, Ringkøbing, Denmark, (2007).
- [2] E. Jørgensen, K.K. Borum, M. McGugan, C.L. Thomsen, F.M. Jensen, C.P. Debel and B.F. Sørensen, "Full scale testing of wind turbine blade to failure - flapwise loading", Risø-R-1392(EN), Risø National Laboratory, Denmark (2004).
- [3] F.M. Jensen, B.G. Falzon, J. Ankersen and H. Stang, "Structural testing and numerical simulation of a 34m composite wind turbine blade", *Composite Structures*, 76, 52-61 (2006).
- [4] F.M. Jensen and A. Morris, "Full-scale testing and Finite Element simulation of a 34 metre long wind turbine blade", *11th NAFEMS World Conferences*, Vancouver, Canada (2007).
- [5] F.M. Jensen, P.M. Weaver, L.S. Cecchini, H. Stang and R.F. Nielsen, "The Brazier Effect in Wind-Turbine Blades and its Influence on Design", Submitted for publication.
- [6] K. Branner, "Modelling Failure in Cross-Section of Wind Turbine Blade", *2nd NAFEMS Nordic Seminar*, 31 May - 1 June 2006, Copenhagen/Roskilde, Denmark, (2006).
- [7] J.P. Dear, A. Puri, A.D. Fergusson, A. Morris, I. Dear, K. Branner and F.M. Jensen, "Digital Image Correlation Based Failure Examination of Sandwich Structures for Wind Turbine Blades", *8th International Conference on Sandwich Structures*, (2008).
- [8] F.M. Jensen, K. Branner, P.H. Nielsen, P. Berring, T.S. Antvorskov; B. Lund, C. Jensen, J.H. Reffs, R.F. Nielsen; P.H. Jensen, M. McGugan, K. Borum, R.S. Hansen, C. Skamris, F. Sørensen, R.S. Nielsen, J.H. Laursen, M. Klein, A. Morris, A. Gwayne, H. Stang, J. Wedel-Heinen, J.P. Dear, A. Puri and A. Fergusson, "Full-scale Test of a SSP34m box girder 1 – Data Report", Risø-R-1588(EN), Risø National Laboratory, Denmark (2008).
- [9] DIAB, "Divinycell H", Technical Manual, DIAB International AB, www.diabgroup.com, (2007).

BEHAVIOR OF REINFORCED CONCRETE SANDWICH PANEL WITH STEEL CONNECTORS UNDER OUT-OF-PLANE FLEXURE

Mohammad Adil* and Marcus M. K. Lee*

* School of Civil Engineering and the Environment
University of Southampton
University Road, Southampton SO17 1BJ, United Kingdom
e-mail: adil@soton.ac.uk , m.m.k.lee@soton.ac.uk web page: <http://www.civil.soton.ac.uk>

Key words: Sandwich panel, Reinforced concrete leaves, Steel connectors, Composite action, Finite element model.

Summary. *A combination of experimental data and modeling is being used to investigate the effects of changing the connector diameter on the composite behaviour of Concrete Sandwiched Panels (CSP). The composite behaviour with different diameters of connectors has been studied numerically, including the overall lateral load capacity of the CSP, the relative flexural contribution of the reinforced concrete (RC) leaves, the connector as a shear transferring mechanism and the failure modes. Existing experimental data from literature[1] were used to develop and validate a finite element model for these panels, with shell elements simulating the RC leaves and beam elements the connectors; the flexural behaviour of the model is described.*

1 INTRODUCTION

A schematic of a typical CSP is given in Figure 1. The sandwiched panel is made up of EPS (Expanded Polystyrene) foam surrounded by a steel mesh and spray-coated with a concrete skin on both sides. The bending action due to eccentric load or lateral load is resisted as tensile and compressive stresses developed in the RC leaves while the out-of-plane shear forces are resisted by the shear connectors.

The performance studies[1] has revealed that these panels are light weight and quickly constructable with inexpensive material in variety of ways. They are able to resist heavy gravity loads beside earthquake, fire and cyclone (heavy winds).

More economical and effective design of such sandwich panels may be possible, if the composite behavior and the failure mechanism are better understood.

In previous work[2], a two-dimensional finite element mesh using four-node quadrilateral elements for RC leaves and two-node truss elements pinned to the center of each layer was used to model the sandwich panel and compared to analytical results for mid span deflection. Also two-dimensional vierndeel truss model[3] was used for the analysis and design of partially composite sandwiched panels. This paper reports the failure mechanism and composite behavior under lateral flexural loads of the sandwiched panel, including a comparison of numerical and experimental results.

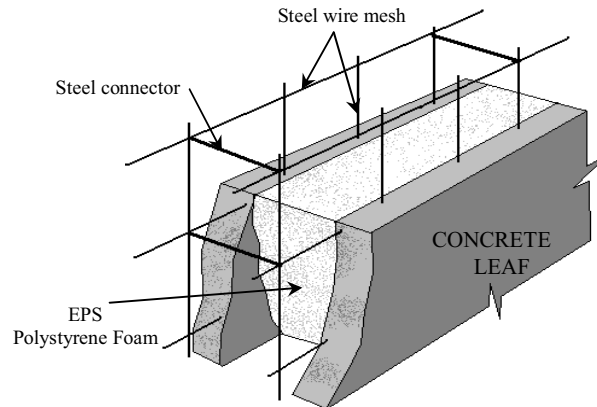


Figure 1 : A typical concrete sandwiched panel (CSP).

2 METHOD

A numerical study investigating the role of connectors in developing the composite action between the two RC leaves, including the effects on flexural capacity of the panel is reported herein. The experimental results available for validation are based on four-point bending[1], hence the model was also based on the similar loading arrangement. Shell elements were used to model the leaves, with fifteen integration points defined through the thickness of RC leaf.

2.1 Experimental

A schematic for the flexure test used by M2 Emmedue[1] is given in Figure 2. Three identical panels were tested, each with a core thickness of 60mm. Tests are also conducted on panels with 80mm core.

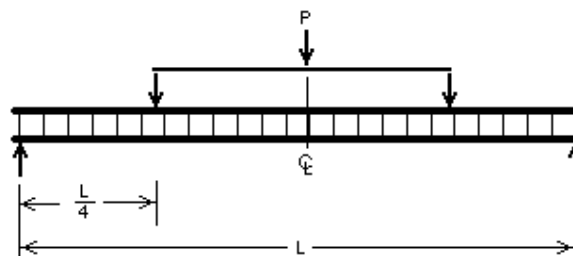


Figure 2 : Schematic of four point flexure test.

The load P was applied by means of a hydraulic jack with load capacity of 60000 pounds. The total load P transmitted to two loading points were placed at $L/4$ from the centerline at each side of the panel. Two deflection gauges, one on each face, were placed at the centre of the panel. Finally, the average mid-span deflection was plotted against the total load, as shown in Figure 3.

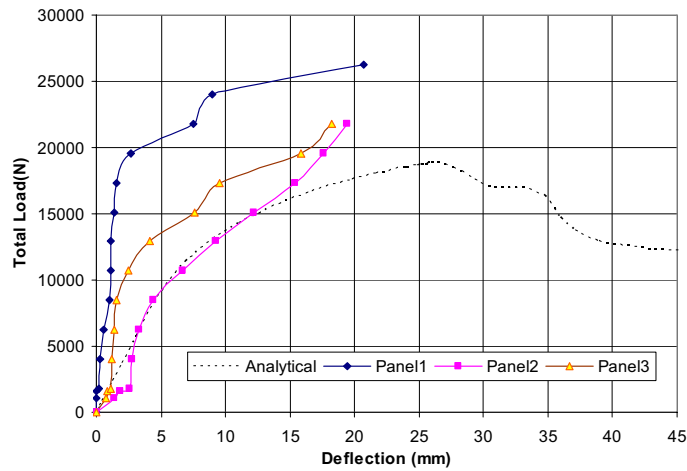


Figure 3: Load deflection curves for four point flexure test with $\phi 3$ mm connector with 60mm core thickness.

The panel reinforcement consist of two electro-welded steel meshes of 2.5mm diameter steel wires with horizontal spacing of 62mm and vertical spacing of 67mm.

The light weight concrete had an average cube strength of 51.0MPa after 28 days. The steel mesh used had average tensile yield strength of 700MPa.

The effect of change in diameter of the connector was not investigated experimentally, hence a numerical model of the panel simulating the experimental setup was developed. The diameter of the connectors in the panel was varied to investigate its influence on the structural behavior of the panels.

2.2 Modeling

The bending behavior of the sandwich panel involves stiffness contribution of steel connectors (~ 100 connectors/ m^2) along with the two concrete leaves being connected. The analysis of such complex system requires a finite element approach. In this paper, development of a model for composite behavior using the commercial finite element software ABAQUS[7] is described. The joint between the connectors and leaves was considered to be fixed and the length of connector is considered to be between inner faces of leaves (Figure 4). To eliminate local failure at the support and the point of application of load, the sharp edge load was modeled as uniform pressure on a thin strip and the edge support was taken as roller while the mid-span was considered as a horizontally immovable symmetric boundary. The solution convergence of the finite element analysis, to match the experimental results, was controlled by working out different tension stiffness properties or RC leaves.

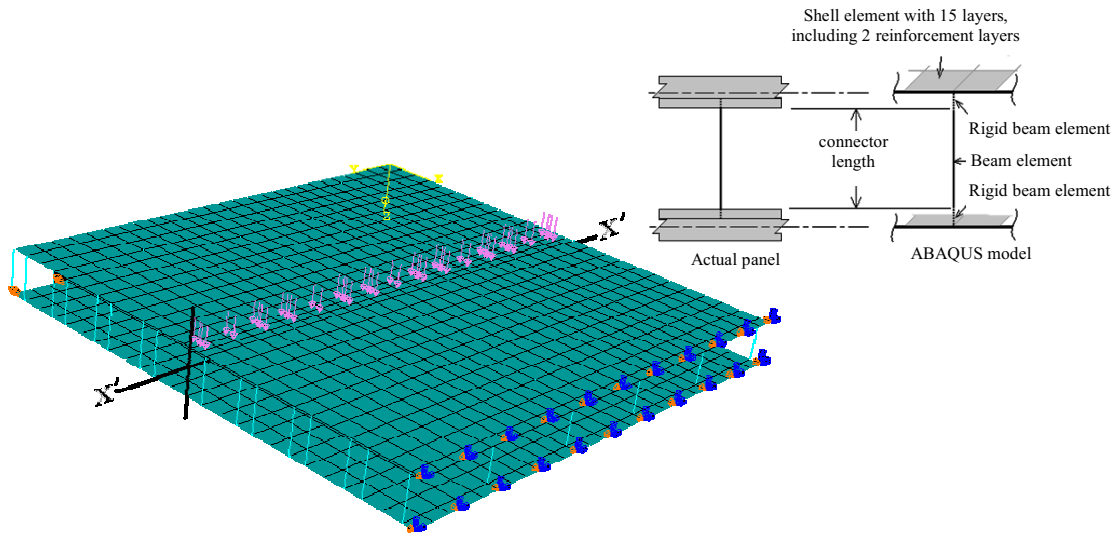


Figure 4 : ABAQUS FEM model of sandwich panel, showing the boundary condition, load and meshing, element detail is shown in top right.

The half model of the $1100 \times 1100 \text{ mm}^2$ sandwich plate is shown in Figure 4. Two layers of shell elements were defined with 15 layers including two reinforcement layers (transverse and longitudinal), the layer has been meshed as 27×27 , where top layer has a denser mesh at the point of application of load (loaded area = $40 \times 1100 \text{ mm}$). Research[6] shows that in ABAQUS, unlike the general layered shell element, the shell element designed for reinforced concrete can better predict the behavior for RC slabs, especially for lightly reinforced.

The modulus of elasticity and poisson ratio are the two basic quantities required to define elastic material for static analysis. The material properties used are the test values used in experiment, shown in Table 1. The FAILURE RATIO option in ABAQUS was used to define the concrete failure behavior and tension stiffening was considered for simulating reinforcement-concrete interaction. The assumed tension stiffening and compression hardening are shown in Figure 5. The parameters of concrete damage plasticity model used are given in Table 2.

Material property	Value used in ABAQUS
Modulus of Elasticity, $E_c = 4000\sqrt{f'_c}$	28500 MPa
Poisson ratio	0.2
Density	$2.3 \times 10^{-6} \text{ kg/mm}^3$

Table 1. Elastic properties of concrete defined for the model.

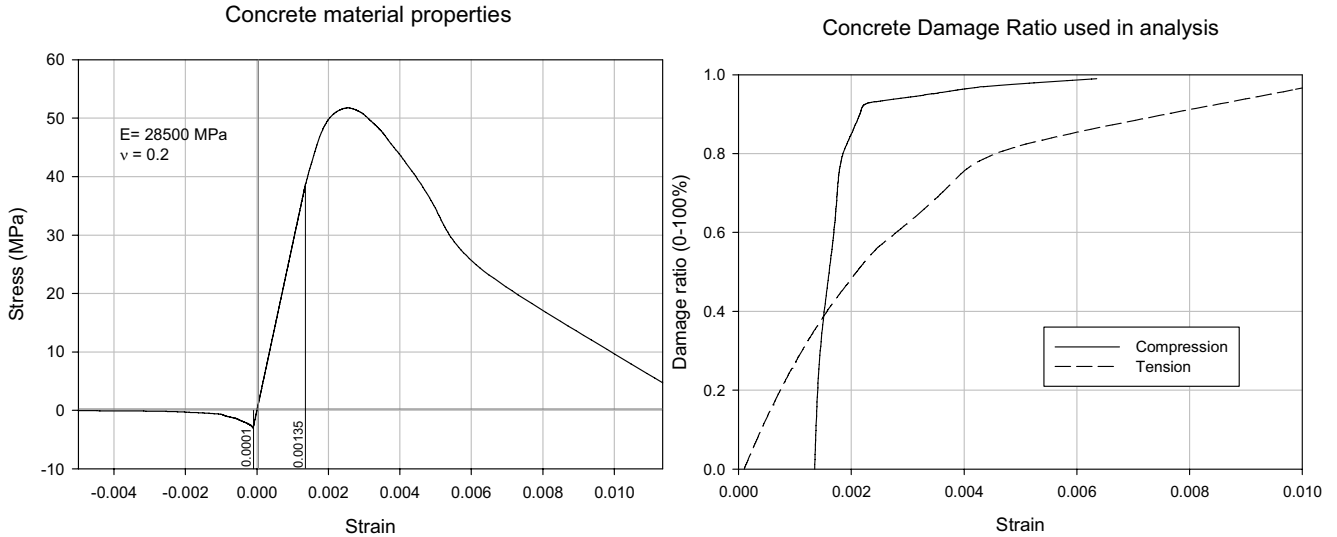


Figure 5. Nonlinear properties of concrete defined for the FEM model.

Material property	Value used in Abaqus
Dilation angle, ψ	56°
Flow potential eccentricity, ϵ	0.1
σ initial equibiaxial compressive yield stress	1.16
σ initial uniaxial compressive yield stress	0.667
* K_c ratio	0
Viscosity parameter, μ	0

* is the ratio of the second stress invariant on the tensile meridian, $q(TM)$, to that on the compressive meridian, $q(CM)$. This defines the behaviour of concrete in 3D loading.

Table 2. Parameters of CONCRETE DAMAGE PLASTICITY model used in ABAQUS.

The reinforcement was defined as the shell element REBAR property within a 35 mm thick 25MPa concrete Rebar Longitudinal and Transverse of 2.5mm ϕ ($4.9 \times 10^{-6} m^2$) 0.07m c/c. The connectors were defined by wire elements of 3mm ϕ ($7.068 \times 10^{-6} m^2$) Truss Element (i.e. no bending stiffness).

The Arc length or modified Riks procedure in ABAQUS was used for the analysis. The distributed load defined in the Riks step of analysis was ramped from the initial (zero) value to the specified.

Geometric nonlinearity is considered using the Nlgeom property of the analysis step. Fifteen simpson integration points through both of the concrete leaf's thickness was used instead of the default five points of Simpson's rule to obtain smooth stress and strain profiles through the depth, as shown in Figure 7. A linear search algorithm has been employed that

uses a line search scale factor to scale the correction to the solution to prevent possible divergence in the iteration steps. Research[4] showed that these techniques better capture both the concrete crushing and concrete cracking with strain softening as well as increase the speed of convergence.

In Bi-Steel panels[5] the connectors were assumed to be rigidly connected with steel plates and the plate was considered to resist torsion. This rigid connection was modeled with spring system that can resist moment as well as torsion. In our case the concrete leaves provide rigid support to the connectors. The embedded ends of the connectors were modeled as rigid beam elements as shown in Figure 4, which is provided by increasing the diameter to 20mm. As the concrete leaves were rigid enough for torsion, no torsion springs are provided.

To compare with the experimental results, load and displacement data from the analysis were extracted for several increments of load. A node in the middle of the mid section of bottom face were selected at a distance of $L/4$ from the support. In the analysis procedure selected, the displacement were recorded at this node with gradual statically increasing load. Von Meises stress, stress tensor and plastic strains (logarithmic strains) and rebar forces were also selected as output parameters. The stress-strain variations at selected increments are shown in Figure 7.

3 RESULTS

3.1 Experimental

Figure 3 illustrates the variation of mid span deflection of the bottom leaf in three similar panels namely PANEL1, 2 and 3 tested experimentally, plotted against gradually increasing load “P” shown in Figure 2. The test results have variations due to some unidentified reasons, but they depict the overall behavior like point of failure, peak load and deflection. The average ultimate failure tensile load was recorded as 32000 N (7000 Pounds), but the figure only shows the results till maximum deflection of 22mm has reached and the panel did not remain stable afterwards. All panels showed drop in stiffness after deformation of 2.5mm then regain of stiffness after the deformation of 7.5mm and the drop in stiffness after the deformation of 9mm following gradual increase till failure. As observed, this initial drop is due to the cracks at points of bearings (support and loading) and the regain is due to redistribution of load in concrete leaves and reinforcement. Major failure is the development of typical flexural cracks at $L/4$ from the support.

3.2 Modeling

To match the flexural behavior of the FE model with the experimental one, a sensitivity study was conducted to determine the best solution parameters. This involved trying different boundary conditions, properties of concrete and mesh size to test their influence on the behavior of the model. Finally the properties of the most suitable model (detailed above) were adopted for the rest of the analysis with variation of the stiffness of the connectors only. Figure 3 compares the load-deflection interaction of the selected model with the experimental ones. The failure pattern agrees well with that observed in the experiment. Similarity in the

load-deflection pattern of the model is found with the least stiff of the three panels (Panel 2).

Figure 6 shows the load-deflection curves from the analyses for different diameter connectors. After the initial drop in stiffness, the bottom leaf base is cracked and the upper leaf only serves as a structural (load carrying) member.

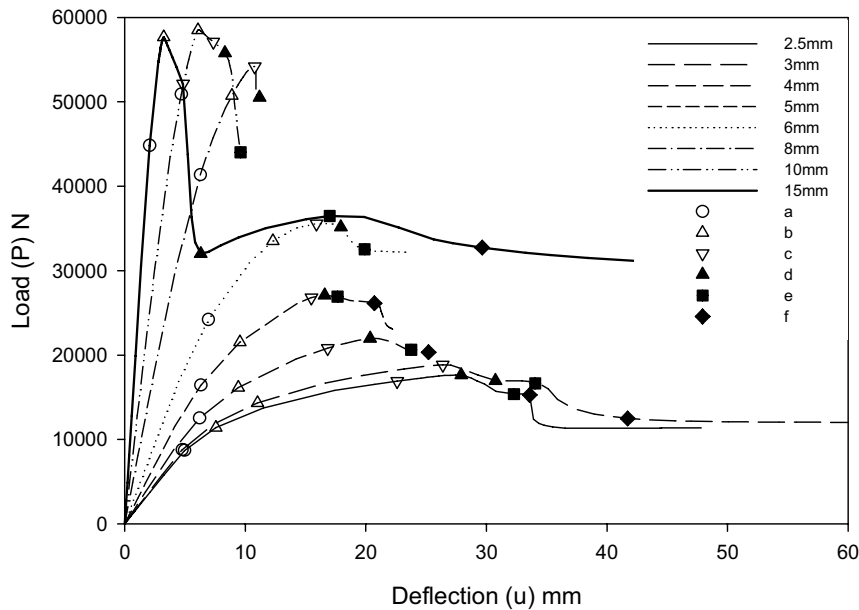


Figure 6. Load-deflection curve from analysis result of sandwich panel.

3.3 Overall stiffness behavior for different connector diameter

The variations of stress during the loading history (points a-f) in Figure 6 are shown in Figure 7. It shows that initially, there is no composite interaction between the two leaves, as both leaves have separate tension and compression zones, showing the bending behavior of concrete leaves with variation of the connector stiffness (diameter), each graph displays depth-wise stress and strain distribution at notable load increments. It is obvious from Figure 6 that with all diameters of connector the panel has behaved linear load-displacement pattern up to the displacement of 5mm, after which its stiffness drops. For the less stiffer connectors the failure mode is ductile while for much stiffer connectors as for 15 and 10 mm connectors as the panel shows brittle failure.

The effect of increasing the diameter of the connector on the initial stiffness “K” of the whole panel is shown in Figure 8. This graph is based on a constant core thickness “s” (length of connector).

Here it is clear that the overall stiffness of the panel does not change much for the smaller diameters and marginal increase in overall stiffness is observed for the larger diameter. This is due to the development of the composite action with stiffer connectors, where composite behavior is seen in strain distribution for panels with connector diameter larger than 6mm.



Figure 7. Stress and strain distribution diagrams for the selected load increments (a-f) marked in Figure 6.

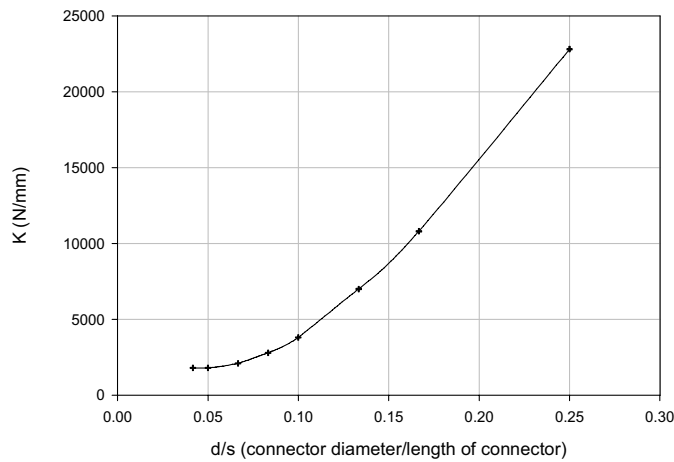


Figure 8. Effect of increase in diameter of connector on the linear stiffness of panel (load/mid-span deflection). [s=60mm]

3.4 Flexure stiffness variation of concrete leaves with changing connector diameter

Figure 9 plots the contribution of the top and the bottom leaves (for section at L/4) in resisting the bending moment with the variation of load for different diameter of connectors. The moment ratios shown here is the ratio of the bending moment resisted by the leaf to the total bending moment at that section. For all diameters of connector, initially the moment is distributed almost equally between the two leaves. Afterwards, cracking at the bottom face of the bottom leaf causes exponential decrease in the bending stiffness of the bottom leaf. The reason for this is that the bottom leaf reinforcement is initially in compression, hence, and top leaf has to resist much of the bending moment. As the neutral axis in the bottom leaf shifts to the level of reinforcement, the stresses in the bottom leaf reinforcement reverses and it start contributing to take load until the reinforcement in top leaf start yielding.

3.5 Development of composite action

In Figure 9, the connectors with 6mm or higher diameter, the composite behavior is visible in the form of negative moment contribution ratio. As the bottom leaf reinforcement comes in tension, the whole bottom leaf section takes tensile stresses and the top leaf comes in compression, demonstrating both leaves act together compositely.

3.6 Contribution of bending stiffness of connector to composite action

Figure 10 shows the change in bending moment “BM” to moment capacity “ M_p ” ratio for connectors of different diameter with change in load. Here, the maximum bending moment is monitored at its fixed/embedded end. The monitored connector is at the section where shear force and overall bending moment are the maximum. The maximum bending moment is at the ends where the connector is embedded in concrete leaves.

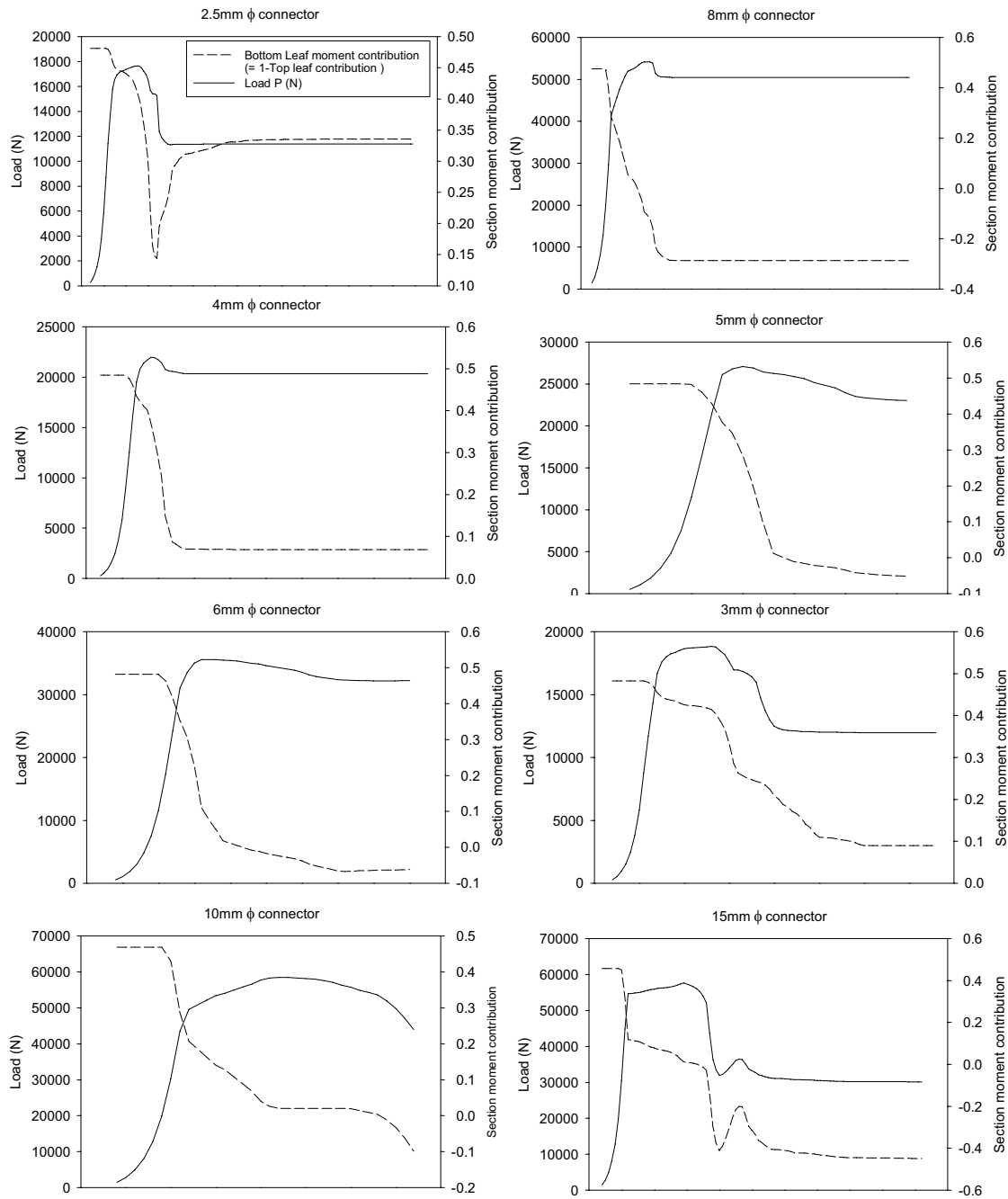


Figure 9. Bending moment contribution of bottom leaf (top leaf contribution=1-Bottom Leaf contribution) for different diameters of connector at section L/4.

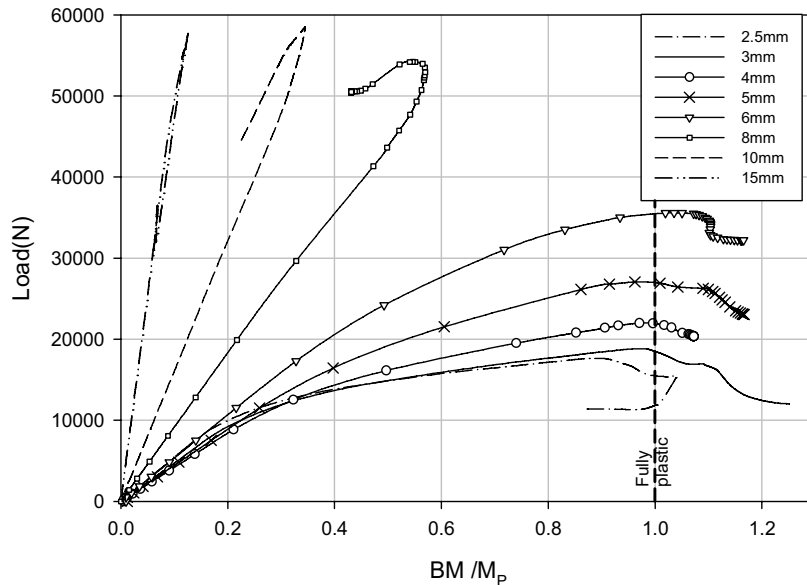


Figure 10. Plot “P” against the ratio of maximum Bending moment in the connector to the plastic moment capacity of connector. (M_p = Plastic moment of connector).

3.7 Failure Mechanism

Figure 11 shows the final deflected shape of the panel with the 3mm connector. This deflected shape shows that the connectors between the loading point and the supports failed in shear between the two leaves. For the cases of connector with diameter larger than 6mm the, concrete leaves at the critical section fails by cracking at their bottom faces prior to full plastification of connector.

Also from Figure 10, the connectors with diameter below 8mm fully plastify at the point of application of load, this fact is reflected in the figure where the graph extends beyond the line marked by BM/M_p equal to 1. From the analysis with stepwise load increment, it was observed that first the connectors point of application of load plastify and then with increase in load this behavior propagates to the connectors towards the support. Finally the mechanism observed is shown in Figure 11.

4 CONCLUSION

This paper emphasizes on the use of CSP as a flexure member or practically as a roof/floor member with lateral loads, as the analysis work is based on flexural loads.

The contribution of connector in developing composite action can be understood much better if the effect of change in length of connector (“s” length between the leaves) is also studied.

Two modes of failure were obtained : cracking of the concrete leaves and yielding of the connectors. It is observed that these failure modes largely depends upon the diameter of connector.

Future work will include finite element analysis of a shear load model to investigate what behavior and mode of failure would these panels follow under in-plane shear load. Other investigations that are possible using finite element software include the behavior of axial loads and dynamic behavior as vertical wall/floor panel in different configurations of building.

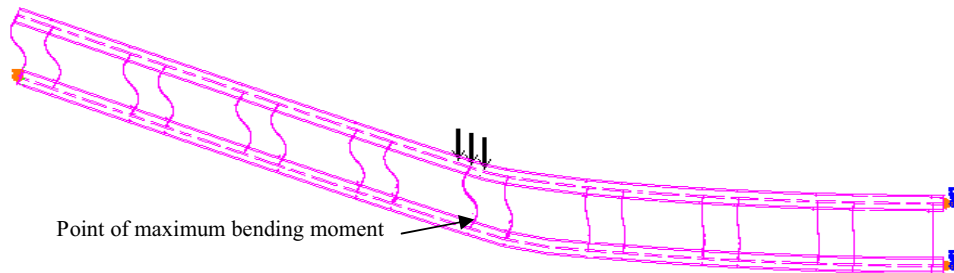


Figure 11. Deflected shape of ABAQUS model at collapse load with 3mm connectors.

REFERENCES

- [1] M2 Emmedue, Italy.
- [2] Papanicolaou. C.G., Triantafillou. T.C., “Analysis and minimum cost design of concrete sandwich panels under out-of-plane loading”, *Structural Concrete*, Vol.5, No. 1, pp 10-27. (2005)
- [3] Kim E. Seeber, Rex C. Donahey., “Method of designing partially composite concrete sandwich panels and such panels”, *United States Patent*, Pub. No.: US 2004/0181379 A1, Sep. 16, 2004.
- [4] Karl E. Barth, HaiyongWu “Efficient nonlinear finite element modeling of slab on steel stringer bridges”, *Finite Elements in Analysis and Design* 42, pp 1304 – 1313, (2006)
- [5] Corus UK Ltd *Bi-Steel Design and Construction Guide*, Second edition, (2003)
- [6] Kitjapat phuvoravan and Elisa D. Sotelino “Nonlinear Finite Element for Reinforced Concrete Slabs”, *J. Struct. Engng.*, Volume 131, Issue 4, pp. 643-649 (April 2005)
- [7] ABAQUS/Standard version 6.6-1

INVESTIGATION OF APPLICABILITY OF CORK AGGLOMERATES IN APPLICATIONS UNDER SHEAR STRENGTH

N. Pinto, A. Silva and L. Reis [†]

[†]Instituto Superior Técnico (IST)
Universidade Técnica de Lisboa
Avenida Rovisco Pais, 1049-001 Lisboa, Portugal
e-mail: pcasilva@mail.ist.utl.pt
e-mail: lreis@ist.utl.pt
web page: <http://www.ist.utl.pt>

Key words: Cork Agglomerates, Cork Core, Shear Strength, Shear modulus, Experimental mechanics.

Summary. *The cork is a raw material of great value for the Portuguese economy. However, its application is restricted to some traditional sectors, not having reached all of its potential use, moreover by means of agglomerate. Cork agglomerates are known by its excellent thermal and acoustic insulation properties allowing its use in structural appliances in aeronautic and aerospace industry. The core of a sandwich beam at first instance fail due to shear forces, in this perspective, the scope of this work is to study and characterize the behavior of agglomerates NL10 and NL 30 when subjected to shear force. To address this, experiments were developed for agglomerates with specimens of different sizes as well as testing of the materials rohacell and honeycomb, according to ASTM C 273-00, whose purpose is to compare its mechanical properties. The achieved results were satisfactory, however there is still need for further investigation so that those agglomerates can be used for the established purposes. The dimension of the grains of the agglomerates must be optimized, since the agglomerate NL 30, because it has two types of grains, has showed a better performance in comparison to NL 10. The great advantage of this material in comparison to its direct competitors, namely rohacell and honeycomb, is the fact that it is a natural material.*

1 INTRODUCTION

Nowadays since the development and technological innovation have environmental concerns, it is now a crucial question and a condition in the majority of the technological procedures. Having in mind this paradigm we must state that innovation must occur in a ponderable way and preponderance in materials that allow development and at the same time respecting the Nature. The cork is a natural material of great value for the Portuguese economy; yet, its appliance is restricted to some traditional sectors, not having reached all of its potential use, moreover by means of agglomerate. As a consequence, the scope of this

investigation is to study the mechanical behavior of different types of cork agglomerates in shear experimental tests and compare the results of the same test applied to materials like, rohacell and honeycomb, i.e. materials normally used for core sandwich structures. On the other hand, the use of these agglomerates in this work are justified by their thermal and acoustic properties, without losing structural performance in relation to materials normally identified and traditionally used in the aeronautic and aerospace industry, previously identified (rohacell and honeycomb). It is achieved a greater integration of those structures with the environment (raw material) and less waste of energy and environmental impact in the end of the structures lifetime which contain cork. Since the sandwich core acts primarily in shear, the current work presents an experimental study of a particular core of natural cork agglomerates NL10 and NL30, tested in shear according to ASTM C 273-00. Composite sandwich structures are finding increased use in engineering applications due to a large number of advantages over traditional materials, including higher strength and flexural rigidity to weight ratios, controlled thermal and electrical properties, enhanced corrosion resistance and customized manufacture. Typically, two strong and stiff skins that carry most of the in-plane and bending loads are adhesively bonded to a low-density core that will mainly bear the transverse shear and normal loads. The sandwich core provides the structure with high flexural stiffness and strength without an overly large weight penalty, [1].

2 MATERIAL DATA AND SPECIMEN SHAPE

Tests were performed using three types of different cores, respectively: Cork agglomerates, Rohacell and ECA honeycomb. The last two did not produce valid results, since the adhesives used were not suitable. To overcome this situation it was necessary to consult the catalogues of the manufacturer. The specimen of cork agglomerates and the adhesives were provided by the manufacturer Corticeira Amorim – Indústrias SA. Fig. 1 presents the specimens used in the experimental work. Table 1 shows the properties of the agglomerates NL 10 and NL 30 and Table 2 shows the references to the adhesives used during the tests. Should be referred that only with PM1 adhesive it was obtained valid results. From now on, the dimensions 144x55x12mm and 600x50x50mm are named Type 1 and Type 2.

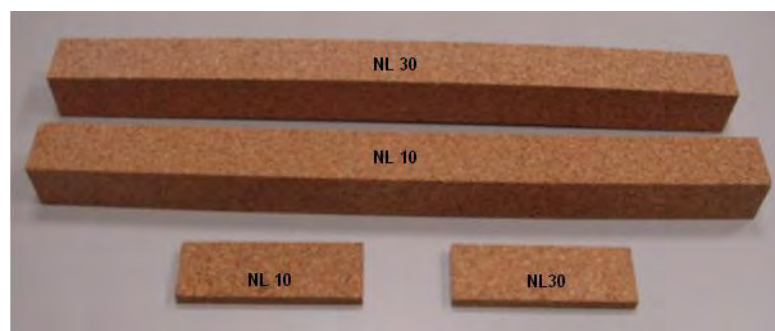


Figure 1: Specimen NL10 e NL30 for different sizes

Material	Ref.	Dimensions [mm]	Granule Average Size [mm]	Density [kg.m ⁻³]
Cork Agglomerates	NL 10	144 x 55 x 12	2/3	125
	NL 30	144 x 55 x 12	2/3 + 3/4	216
	NL 10	600 x 50 x 50	2/3	125
	NL 30	600 x 50 x 50	2/3 + 3/4	216

Table 1 : References of the cork agglomerates properties

Adhesives	Reference
Corticeira Amorim	PM1
Corticeira Amorim	G03

Table 2 : References of the adhesives used

3 TEST PROCEDURES

The test method used the guidelines of ASTM C 273-00, which allows the determination of shear properties of sandwich constructions or cores, associated with shear distortion of planes parallel to the facings. Test configuration does not produce a pure shear stress state in the specimen, but the specimen geometry is prescribed so as to minimize secondary stresses, [2]. The load is applied at the ends of the rigid plates so as to distribute the load uniformly across the width of the specimen. Adam states in its article [3], the existence of local variations of stress, due to lateral forces and/or bending moments occur at the edge of the loaded plates and also due to the fact that the test ends in the edge zone free from the specimen. It is also referred that, if the length of the specimen is sufficiently long relating to thickness, it can achieve greater standardization of shear stress, therefore reducing its influence in local concentrations of stress in the middle of the specimen where the resistance to the shear is determined. According to the test protocol, the specimen should have a thickness equal to the thickness of the sandwich and a width not less than 50 mm. The requirement on the length in order to minimize secondary stresses is to be at least 12 times the thickness and having the line of action of the direct tensile force passing through. Fig. 2 shows the test fixture used in the experimental tests. Since the first publication of the standard in 1951, it has always been specified that the line of action force should pass through the diagonal corners of the specimen as it is shown in Fig. 2, and it is stated that the line of action force when passing through the diagonal provokes impact/bending in the free edge of the specimen, [3]. Intuition says that it should be applied a parallel force to the faces, but a parallel force to the faces provokes equally a lateral undesirable force. Both forces come to a distribution and concentration of stresses on the free edge of the specimen. Due to this factor of concentration of stresses the specimen may have a premature failure, [4]. Tests were carried out using Instron 8502 testing machine – it is a servo-hydraulic testing machine with a load cell of 30kN.

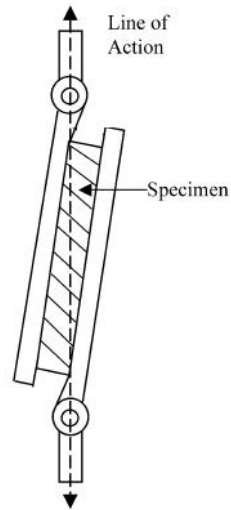


Figure 2: Test fixture used in the experimental test.

In the experimental tests the load was applied at a constant rate of movement of the testing machine cross-head at a rate of 1 mm/minute, so that the maximum load occurred between 3 and 6 minutes. The shear stress, τ , and effective shear modulus, G , were calculated from following formulas as recommended by ASTM C 273, [5]:

$$\tau = \frac{P}{L.b} \quad (1)$$

$$G = \frac{S.t}{L.b} \quad (2)$$

$$S = \frac{\Delta P}{\Delta \delta} \quad (3)$$

Where L , b , t are the specimen length, width and thickness, respectively, S is the slope of the elastic portion of the load–deflection curve, P is the applied load and δ is the relative displacement of the steel plates. The average shear strain, γ , was obtained from:

$$\gamma = \frac{\delta}{t} \quad (4)$$

4 RESULTS AND DISCUSSION

For all agglomerated, even those of different sizes, the same behavior was observed during the three phases. In the initial phase, from Fig. 3 to Fig. 10, represented by (a), the regime is predominantly elastic. It was observed that in the beginning of the curve of strength-displacement there was an inflection at the entrance of the elastic regime, most likely influenced by the visco-elastic property of cork or due to the auto alignment of the load line. The first phase ends when the first failure occurs, on the free edge of the specimen, from Fig. 3 to Fig. 10, represented by (b). With observation and some calculation it was concluded that those first failures occurred when it was reached the shear yield strength at 2% of distortion. During the second phase, after being reached the shear yield strength, from Fig. 3 to Fig. 10 represented by (c), begins a visco-plastic deformation, giving place to a greater progression of failures contributing to a maximum tension, as the failure of greater size is placed in central area of specimen, and along the force line other failures arise that constitute together with that line angles of 45°. During the third phase, after break, the load goes to zero which leads to the test conclusion, from Fig. 3 to Fig. 10 represented by (d). For a better understanding, figures taken from experimental tests are also presented, Fig.(s) 4, 6, 8 and 10.

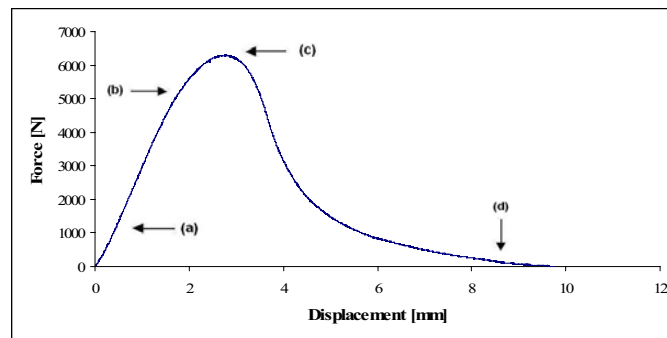


Figure 3: Evolution of the behavior of agglomerate NL10 type 1

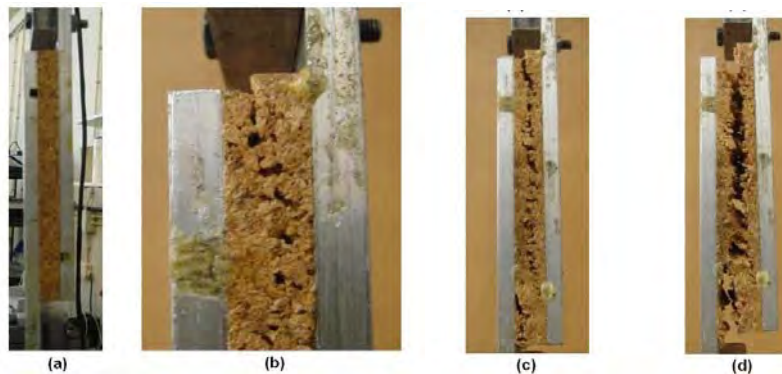


Figure 4: Evolution of the behavior of agglomerate NL10 type 1: (a) beginning of the test, (b) visco-plastic deformation, (c) rupture and (d) end of the test

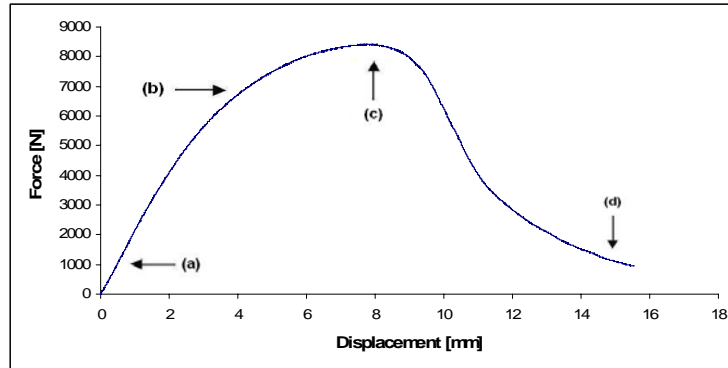


Figure 5: Evolution of the behavior of agglomerate NL10 type 2

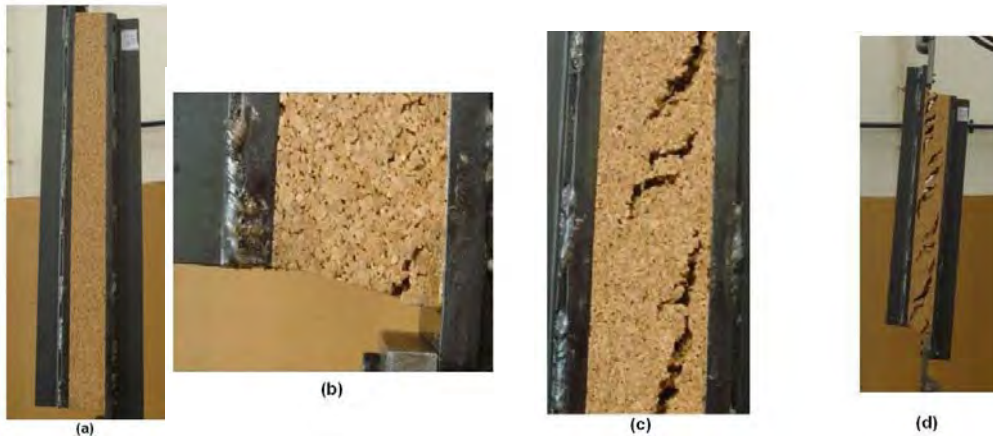


Figure 6: Evolution of the behavior of agglomerate NL10 type 2: (a) beginning of the test, (b) beginning of visco-plastic deformation, (c) rupture and (d) end of the test

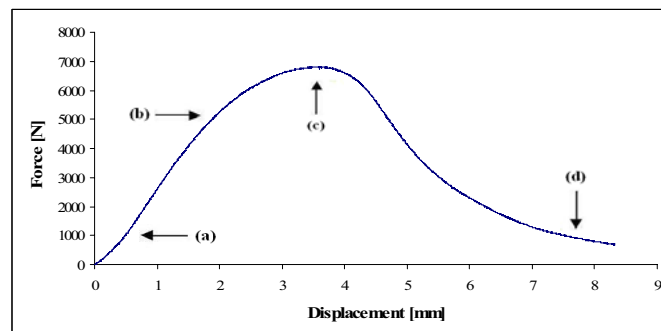


Figure 7: Evolution of the behavior of agglomerate NL30 type 1

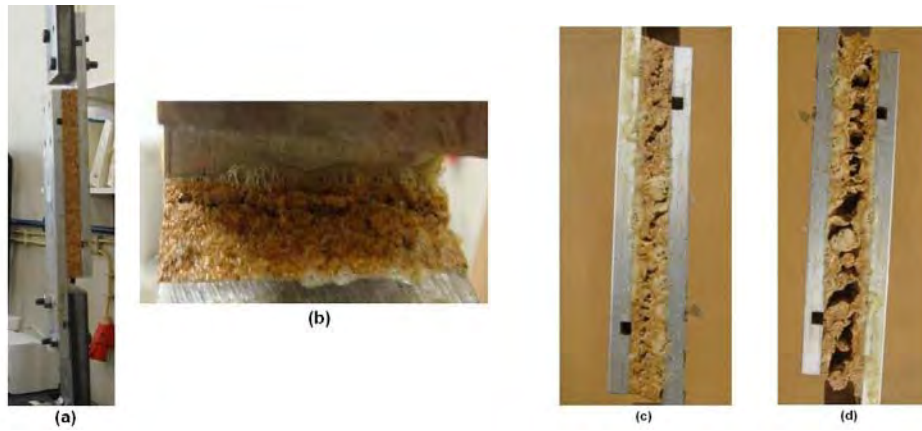


Figure 8: Evolution of the behavior of agglomerate NL30 type 1: (a) beginning of visco-plastic deformation, (c) rupture and (d) end of the test

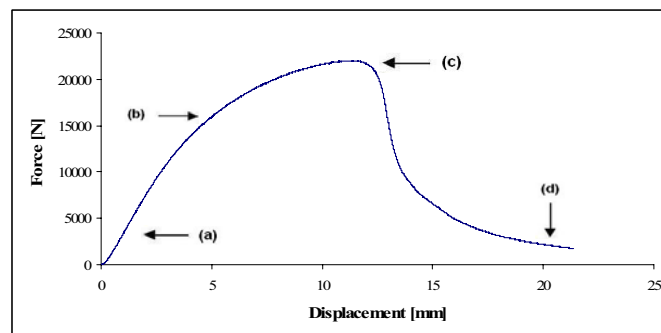


Figure 9: Evolution of the behavior of agglomerate NL30 type 2

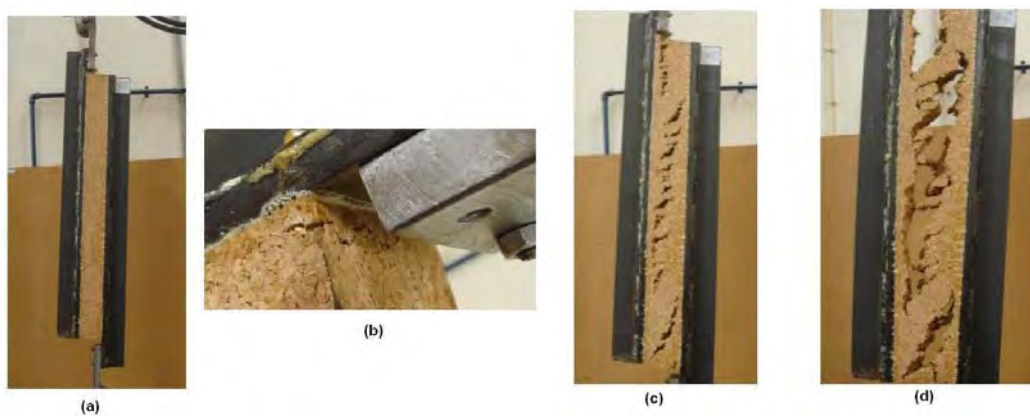


Figure 10: Evolution of the behavior of agglomerate NL30 type 2: (a) beginning of the test, (b) beginning of visco-plastic deformation, (c) rupture and (d) end of the test

Concerning the mechanical behavior of the agglomerate and for a better illustration of their behavior's evolution the results are grouped, in a graphic form, by dimension of the specimens. Three tests were conducted using agglomerates NL10 (type 1). The curves strength-displacement, Fig. 11, and shear stress- shear strain, Fig. 12, present an identical shape in the three tests, except on the 2nd test where the strength value was very high in relation to the other two. This situation may be due to the heterogeneity of the agglomerate, or it may be due to non-uniformity in the distribution of the adhesive in the agglomerated grains. Three tests were also performed using agglomerated NL30 (type 1). The curves force-displacement present an identical shapes in the three tests, despite the maximum force being different, the initial declivity is very similar between the three tests.

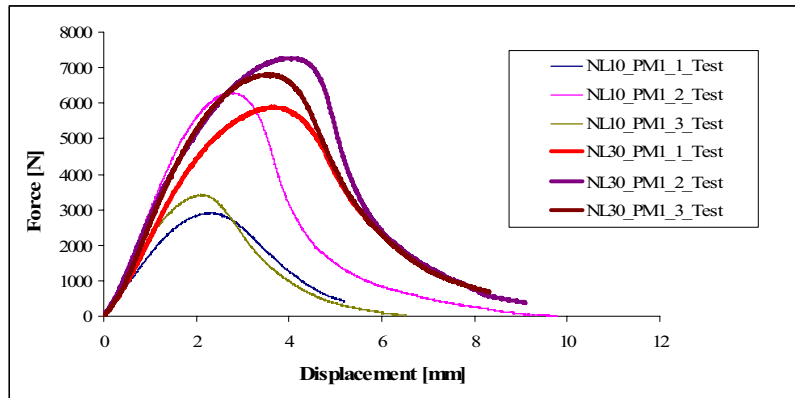


Figure 11: Evolution of behavior of agglomerate NL10 e NL30 type 1

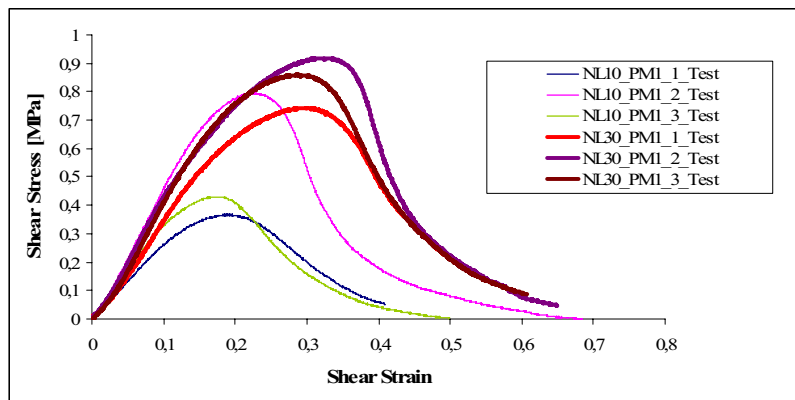


Figure 12: Shear Stress-Shear Strain evolution for agglomerates NL10 and NL30 type 1

The same number of tests were carried out using agglomerates NL10 (type 2). The curves force-displacement, Fig. 13, and shear stress-shear strain, Fig. 14, present an identical shape, both in the three tests, despite that in the first test a major visco-plastic deformation have occurred. In the tests executed with these agglomerated there were minor variations in the results. Five tests were conducted using agglomerate NL30 (type 2). The reason behind higher number of tests is due to the fact that greater discrepancy in the results has been observed between the first and the two following tests. Such situation was clarified with two more tests whose results approach the values of the first. The curves force-displacement presents an identical shape in the five tests, but only with a variation of the maximum force, second and third test. Despite this difference, the maximum force occurred almost of the same displacement, except in test 1.

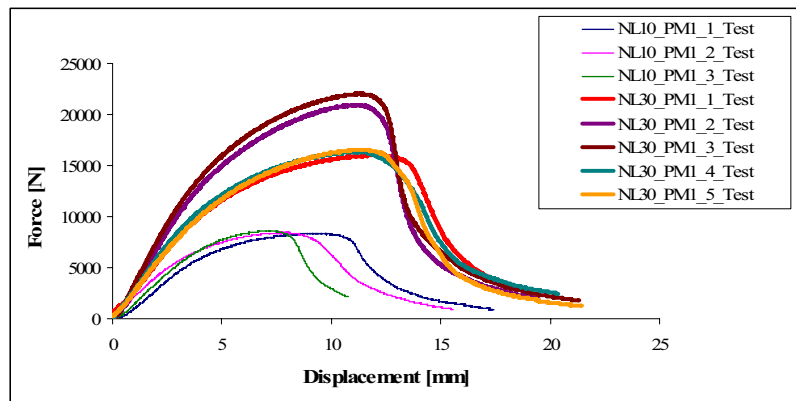


Figure 13: Evolution of behavior of agglomerate NL10 e NL30 type 2

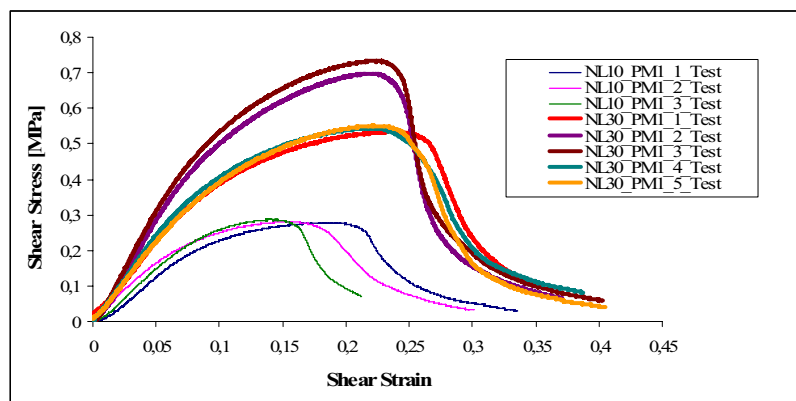


Figure 14: Shear Stress-Shear Strain curve for agglomerates NL10 and NL30 type 2

Concerning to the scale factor it is visible that is more accentuated in agglomerate NL30 compared to agglomerate NL10. This is possibly due to the non uniformity of the grains proportion that constitutes the agglomerate during the manufacturing process, since the agglomerate has more than one type of grain. This irregularly may be explained by the initial different behaviors in the elastic zone, Fig. 15, by contrast with agglomerate NL10 in which that irregularly is not so visible, Fig. 16. In Table 3 is showed that the shear modulus for agglomerate NL10 type 1 (minor dimension) is 3.70 MPa and the type 2 (greater dimension) is 3,32 MPa, for agglomerate NL30 of type 1, the shear modulus is 4.40 MPa and for type 2 is 5,42 MPa. Table 4 shows the values for Rohacell and Honeycomb obtained from the manufactures.

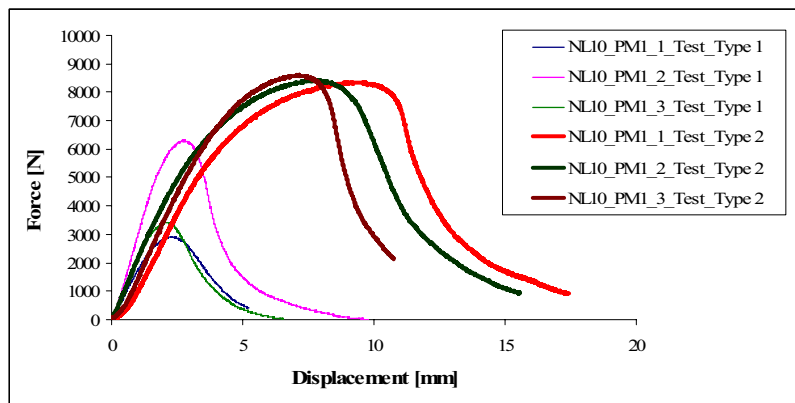


Figure 15: Evolution of behavior of agglomerate NL10 type 1 and type 2

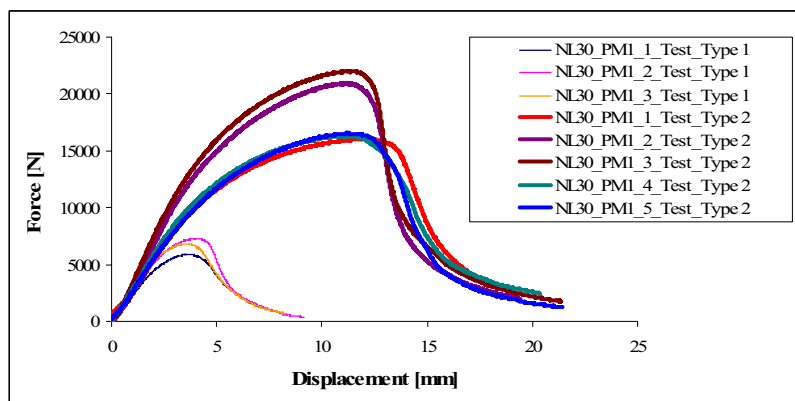


Figure 16: Evolution of behavior of agglomerate NL30 type 1 and type 2

	Ultimate Strength [MPa]	Shear Modulus [MPa]	Shear Yield Strength 2% [MPa]
Agglomerate NL10 - Type 1	0,532	3,70	0,482
Agglomerate NL30 - Type 1	0,841	4,40	0,600
Agglomerate NL10 - Type 2	0,282	3,32	0,232
Agglomerate NL30 - Type 2	0,612	5,42	0,457

Table 3 : Results obtained from experimental tests

	Density [kg.m⁻³]	Shear Modulus [MPa]	Shear Yield Strength 2% [MPa]
Rohacell PMI Foam	75	42	1,3
ECA Honeycomb	48	38 (L), 24 (W)	1,16 (L), 0,62 (W)

Table 4 : Manufacturer values

5 CONCLUSIONS

It can be assumed that the grain's dimension that constitutes an agglomerate influence the obtained results. The agglomerate NL30 consists of two different sizes of grains while agglomerate NL10 only one size of grain. The results show that agglomerate NL30 has better shear mechanical properties for both types of tested specimen.

In agglomerate NL10 for the two types of size of the specimen it was observed that the specimen of smaller size presents better mechanical properties in comparison to the bigger size, for agglomerate NL30 it was the opposite. This may be due to variation in the proportion of the agglutination system, direction of compression, The scale effect is more evident in agglomerate NL30, possible due to the non-uniformity of the proportions of grains that constitute the agglomerate upon the manufacturing process.

After the separation of load plates, all surfaces of the specimen presented shape type with direction at 45° caused by the shear efforts. The agglomerates NL30 for different tests have obtained elastic and visco-plastic behaviors more extensive than agglomerate NL10.

For every type of agglomerates the shear yield strength occurs for a distortion of 2%.

Comparing these results with the results obtained by Silva et. al. [6] for different types of agglomerates, the agglomerate NL30 has a shear modulus superior to agglomerate 8123, which had obtained the better mechanical properties.

In relation to density and despite that agglomerate 8123 presents a minor granule average size (0,25mm – a grain), it is higher than that of agglomerate NL30 (0,67 and 0,75 mm – two

grains).

In comparison to other materials, namely rohacell and honeycomb, considering only manufacturer catalogues for these materials, it was verified that these have minor density and greater mechanical capacity in relation to tested agglomerates.

ACKNOWLEDGMENTS

The authors acknowledge the support from Corticeira Amorim Indústria, SA, for providing the raw materials for testing, as well as all the technical details necessary to test and evaluate the natural cork composites. Also, the support of OGMA, SA is greatly appreciated.

REFERENCES

- [1] B. Bekisli; L. J. Grenestedt, “Experimental evaluation of a balsa sandwich core with improved shear properties”. *Composites Science and Technology*, 64, 667-674 (2004).
- [2] D. J. O’Connor, “A Comparison of Test Methods for Shear Properties of the Cores of Sandwich Construction”. *J. Test. Eval.*, 17(4), 241-246. (1989).
- [3] D. F. Adams, “Shearing Testing of Sandwich Panel Core Materials”. [HTTP://WWW.COMPOSITESWORLD.COM/HPC/ISSUES/2007/JANUARY/1557](http://www.compositesworld.com/hpc/issues/2007/january/1557) (2007).
- [4] E. E. Gdoutos, I. M. Daniell and K. A. Wang, “Failure of Cellular Foams Under Mutiaxial Loading”. *Composites Part A – Applied Science and Manufacturing*, 33(2), 163-176 (2002).
- [5] ASTM C 273; Standard Test Method for Shear Properties of Sandwich Constructions. *American Society for Testing and Materials Annual Book of ASTM Standards* (2000).
- [6] A. Silva.; J. Lopes, P. Almeida, L. Reis amd M. Leite, “Experimental Testing of a Natural Cork-Based Composite”, *Conference - Composites Testing and Model Identification, Porto* (2006).

STRENGTH VARIABILITY OF INSERTS IN SANDWICH PANELS

Nikhil Raghu^{*}, Mark Battley^{*} and Temoana Southward[†]

^{*} Centre for Advanced Composite Materials (CACM)
University of Auckland
Private Bag 92019 Auckland, New Zealand
e-mail: m.battley@auckland.ac.nz,
web page: <http://www.mech.auckland.ac.nz/Composites/CACM.html>

[†] Air New Zealand Design Engineering
Auckland, New Zealand
e-mail: Temoana.Southward@airnz.co.nz

Key words: Sandwich, Insert, Potting, Modeling, Core, Variability, Aircraft.

Summary. *Bonded inserts are commonly used to introduce localized loads into sandwich panels. The high variability in the strength of such inserts seen in experimental studies is not recognized in current design methods. This paper investigates sources of variability in the pull-out strength of metallic inserts in aramid honeycomb sandwich panels. A finite element model is used to investigate the sensitivity of core stresses to potting depth in partially potted inserts, which is found to be significant. Experimental specimens showed large variations in potting radii and cell wall dimensions, both critical parameters since the failure mode is predominantly core shear adjacent to the potting. Foam core specimens with rotationally symmetric and consistent potting volumes were also tested. The foam core specimens show significantly lower variability in pull-out strength than honeycomb specimens.*

1 INTRODUCTION

Sandwich panels are widely used in commercial aircraft, particularly in secondary structures and cabin interiors to achieve lightweight components with high strength and stiffness to weight ratios. However, the low strength of the core materials can cause difficulties with localized loads, such as fasteners. Inserts of higher density materials can be used to transfer loads into the sandwich. In commercial aircraft interiors, the typical approach is to machine a hole in the sandwich, place a metal insert into the hole and surround it with a suitable potting compound, such as an epoxy resin. Typical sectioned components with inserts can be seen in Figure 1.



Figure 1. Through, fully potted and partially potted blind inserts in sandwich panels

When subjected to an out-of-plane tensile load, these types of inserts typically fail in the core material adjacent to the potting or in the potting surrounding the insert. Industry design procedures (such as [1]) have been developed based on analytical solutions [2] and empirical data. However these design methods do not usually recognize the high level of variability observed in test data. Currently, aviation authorities and aircraft manufacturers require large numbers of specimens to be tested for every specific configuration of panel, potting compound and insert type – an expensive and time-consuming procedure. A description of the specific insert/sandwich configuration investigated in this paper is outlined in Table 1.

Initial experimental results for failure load of through and blind inserts show significantly higher variability in the batch of samples that contained specimens only partially filled with potting compound [3]. Box and whisker plots in Figure 2 show the differences in statistical parameters. Partial depth filling of the potting compound (where the compound is not bonded to the bottom face) can occur due to a number of material and manufacturing parameters, especially the flow characteristics of the potting, panel thickness, and the depth that the honeycomb is machined to. It was hypothesized that partial potting of inserts would result in variations in core shear stress due to there being a less rigid connection between the insert and the face sheet.

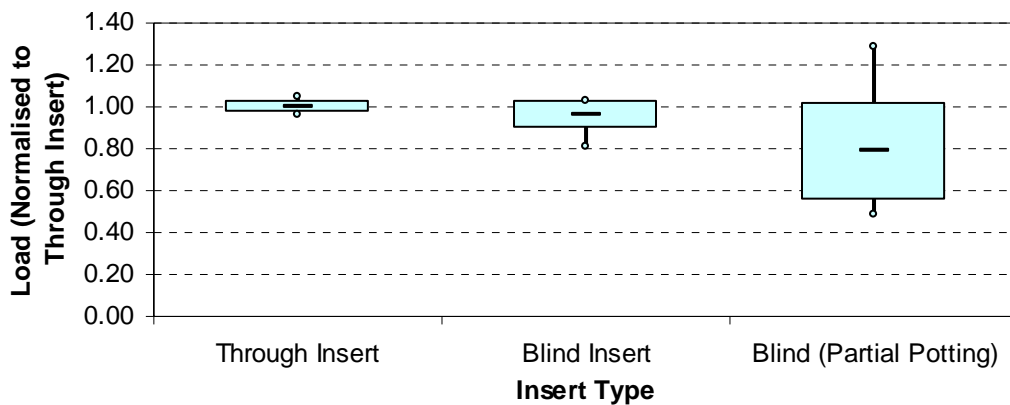


Figure 2 Failure load of inserts in 1” honeycomb panels. The upper and lower points of the bold vertical lines show the maximum and minimum loads, with the mean represented as the bold middle line. The edges of the box represent the coefficient of variance.

	Material	Radius	Height
Insert	Blind, Aluminium	7.125	9.52
Potting	3M EC-2216™ B/A Epoxy	10	
		Thickness	
Face Sheets	2 plies 7781 style E-glass/Phenolic	0.508	
Core	Hexcel® HRH-10-1/8"-3.0	25.4	

Table 1 Parameters of insert/sandwich configuration investigated in this paper, dimensions in millimetres.

The shear resultant in a centrally loaded circular plate decays hyperbolically as the distance from the load increases. The pull-out strength of an insert failing by core shear would therefore be sensitive to any variations in potting radius. Moreover, in the case of honeycomb cores, the discrete cellular nature results in varying potting filling shapes and therefore potting radii, as shown in Figure 3.

For low density honeycomb materials, failure typically initiates in the core by the shear buckling of a single-thickness cell wall connected to the potting. While current design methods utilize global (continuum) properties for the core, the initiation of failure in inserts is of a much more localized nature and is affected predominantly by the buckling strength, and therefore the relevant properties of the cell wall.

This paper investigates the effect of varying potting depths on the stress distributions within the core material, and the inherent variability in potting radii and cell wall dimensions. Foam core panels are also tested in order to compare the effect of much more consistent potting shapes, radii and material properties.

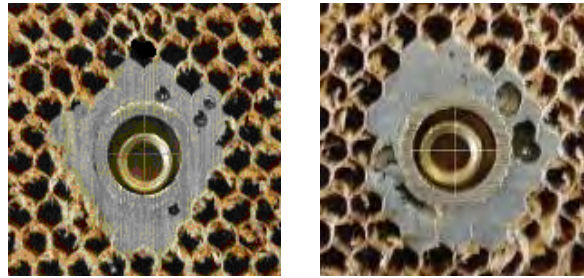


Figure 3 Images of fully potted insert specimens with top face sheet removed.

2 NUMERICAL MODELS

An important requirement in constructing FE models for this research was the ability to quickly and easily change parameters of interest. These potentially included all dimensional parameters, material properties, loads and constraint conditions. The linear-elastic models were developed using the ANSYS V10 Classic Finite Element environment. Commands for generating, solving and post-processing are scripted as input files using the ANSYS Parametric Data Language (APDL).

Rotational symmetry enables the problem to be reduced to an axi-symmetric FE model, using PLANE183 8-node plane elements, resulting in the displacement at any point consisting of only radial and axial components. Figure 4 shows an image of the meshed model.

Pressure was applied to the top surface of the insert to generate an 850N load, which corresponds to the end of the linear region of the experimental loading curve. In-plane and out-of-plane displacements were restrained at the symmetry axis and panel support area respectively. The key results of interest are the in-plane stresses in the face sheets and at their interfaces with the core, and the distribution of transverse shear and normal stresses in the core and potting.

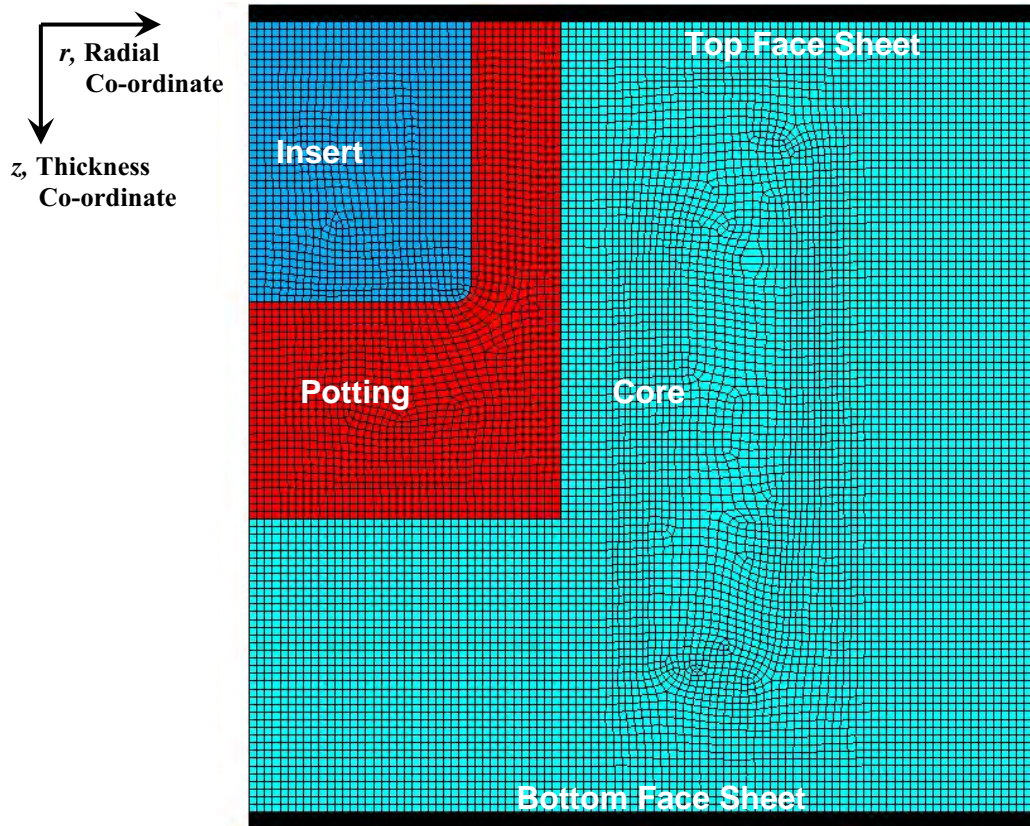


Figure 4 Meshed model of partially potted insert, with co-ordinate system definitions.

Successfully converged solutions using these elements to model inserts have been obtained by Bozhevolnaya et al [4] using element sizes in the order of 0.1-0.3mm near the material interface. The configurations of interest typically show decay lengths that are the same as the panel radius. Therefore, a mapped mesh of a constant nominal element size was used.

A global element size of 0.25mm and 15 elements across the faces resulted in converged solutions for radial stresses in the outer surfaces of the face sheets, and for transverse stress through the depth of the core. This size still resulted in quick computation times and the mapped mesh results in a much cleaner consistent element shape. An important measure for convergence is the percentage error in strain energy norm, which, for this element size is approximately 2.5% in the core material. As expected, the stresses near the tri-material junctions result in a singularity, so maximum stresses reported at the core/face sheet interfaces are not relevant. However, the stresses of interest in this research are mainly those in the core, and the outer surfaces of the face sheets. The results for transverse core shear stress and panel deflection correlated well with those predicted by classical anti-plane sandwich theory as shown in Figures 5 and 6. While classical sandwich theory can predict the average stresses well in this case, it cannot capture the non-uniformity in stress distribution through the thickness of the core caused by partial potting of inserts.

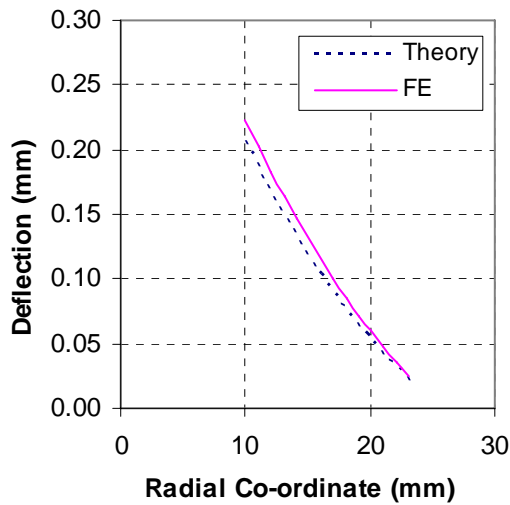


Figure 5 FE results and theoretical values of panel deflection (mid-thickness)

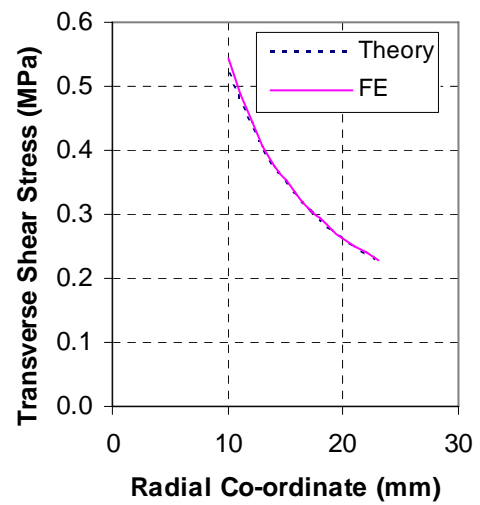


Figure 6 FE and theoretical values of shear stress in the core.

3 PARTIALLY POTTED INSERTS

Partially potted inserts are more typical in thicker sandwich panels (1.00”) and above, where the insert height is smaller than the height of the core. The depth to which the potting fills the panel is primarily dictated by the relative bore-hole depth and the viscosity of the potting compound [1]. For typical potting compounds used, the cavity under the insert does not fill completely if the volume around the sides of the insert is smaller than the volume under it. This difference in volume can result in the potting filling the sides quicker and blocking the vent hole at the top of the insert before the cavity is completely filled. In non-perforated honeycomb cores (such as Nomex[®]), remaining air cannot be displaced, causing partial filling.

Two different guidelines exist in industry for a minimum required depth of filling under the insert. In aircraft panels, typical manufacturer and in-house procedures recommend that the potting fill to a minimum depth of 0.04” (1.02mm) below the insert [5]. While standards set by the European Space Agency for spacecraft specify a minimum depth of 7mm below the insert [1]. Minimum requirements for bore-hole depth are also specified, as the small cell wall sizes can obstruct the flow of potting and effective venting of air.

Theoretical models exist to predict the stress state around through-thickness and full-potted inserts [1, 2]. However there is a lack of work done investigating the effect of partial filling on the distribution of stresses in the sandwich constituents. This section discusses the influence of potting height on the stress states in a panel with a partially potted insert.

Blind inserts in a typical sandwich panel with varying potting heights were investigated using the linear elastic axi-symmetric finite element model. Five potting heights were investigated, varying from 10.5mm (the minimum aircraft standard) to 22mm.

Contour plots of transverse shear stresses in the panel (Figure 7) show the change in stress distributions in the potting and core. Transverse distributions of out-of-plane shear stresses in

the core were recorded at a radius of 10.5mm. These distributions, graphed in Figure 8, show significant increases in maximum stress with smaller potting heights. Inserts with a potting height meeting the minimum standard (10.5mm) show a 26% larger transverse core shear stress than fully-potted inserts. The shape of the stress distributions shows that the stresses are concentrated adjacent to the potting boundary. Therefore, a smaller potting height, which results in a smaller potting/core interface area demonstrates an increase in the shear stress in this vicinity. The shear stress then decreases rapidly in depths where there is no potting. This suggests that the relatively flexible honeycomb core material directly underneath the potting does not apply the same levels of shear stress to the adjacent core as the potting. Figure 8 also shows the average stress through the core which is almost identical for all potting heights. Partial potting has the effect of changing the position and magnitude (Figure 9) of the maximum shear stress.

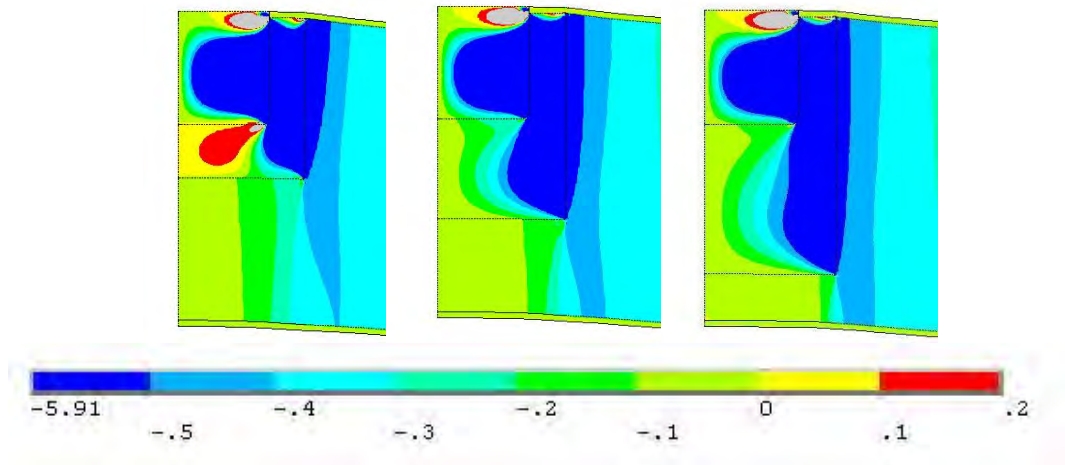


Figure 7 Contour plots of transverse shear stress for three different potting heights.

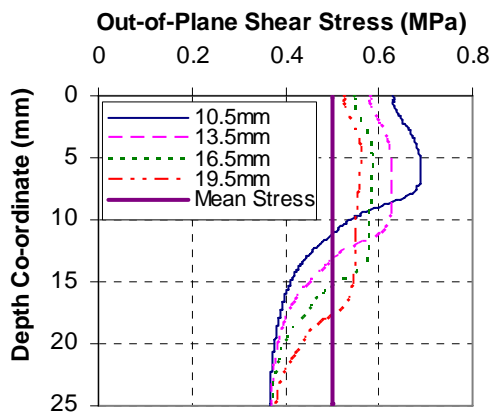


Figure 8 Distribution of shear stress through the thickness of the core material.

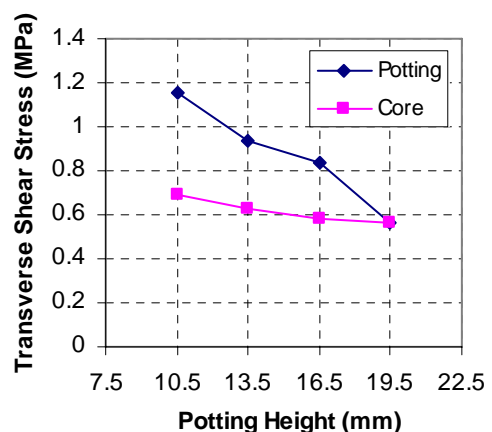


Figure 9 Maximum shear stresses in the potting and core 0.5mm from the material junction.

Tensile out-of-plane loading of an insert generates a transverse normal stress in the core underneath the potting. Figure 10 shows the radial distributions of transverse normal stress in the core at a depth of 0.5mm below the potting/core intersection. The peak stresses are generated in the vicinity of the corner of the potting compound. It is interesting to note that these normal stresses decay rapidly towards zero at a radius of about 15mm, just 5mm larger than the potting radius.

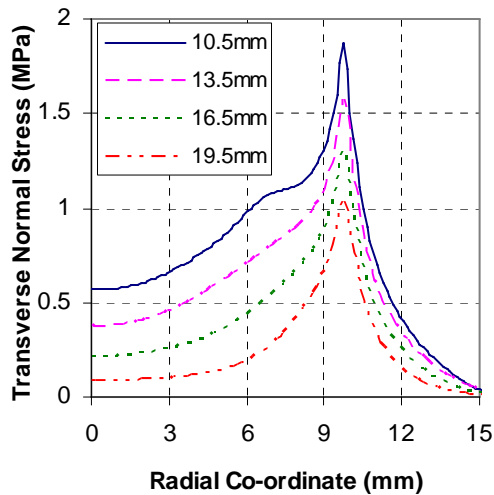


Figure 10 Radial distribution of normal stress in the core below the potting

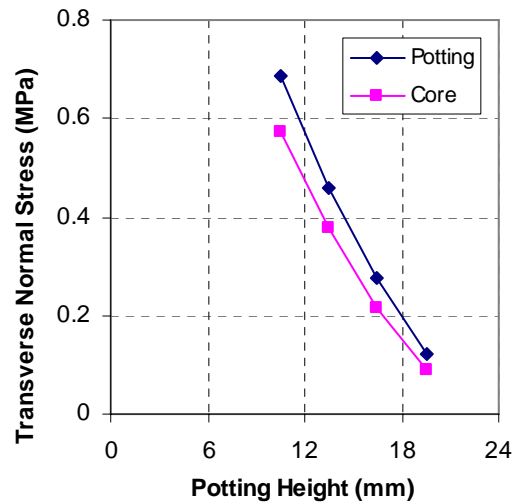


Figure 11 Core normal stress directly below the centre of the potting.

Maximum transverse normal stresses are presented in Figure 11 to show the trend in significant changes in the potting and core for various potting heights. The trends show a small amount of non-linearity in the relationship to potting height. The normal stress in the potting is slightly more sensitive than the core.

The increase in normal stresses in the core and potting underneath the insert for smaller potting heights fits in well with the trends seen with core shear stress. The normal stresses increase due to the flexibility of the core material underneath the potting. The lower shear modulus of the honeycomb core results in an inability for the load to be transferred into the adjacent cells as shear. A higher proportion of the load is therefore carried as a tensile stress in the core underneath the potting.

The transverse stresses in the core surrounding a partially potted insert are significantly affected by the potting depth. The manufacturing process for these inserts is such that the filling depth cannot be controlled, resulting in variability in potting depth. This variability will in turn affect the variability of pull-out strength seen in experiments.

4 VARIABILITY IN POTTING RADIUS

Potting radius has been identified as a significant factor influencing the failure load of an insert [1]. The discrete cellular nature of honeycomb cores can result in different numbers and locations of opened cells during drilling. This depends on the location of the bore-hole relative to the repeating pattern of cells. For example, Figure 12 illustrates how two different drilling co-ordinates can result in significantly different potting shapes. The research discussed in this section investigates the inherent variability in potting radius due to this phenomenon.

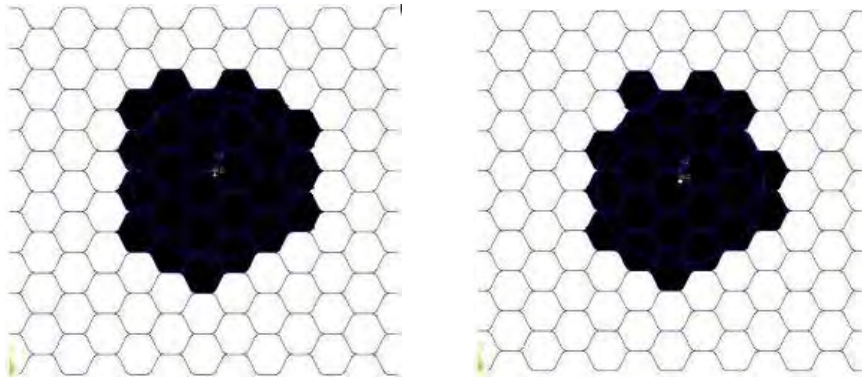


Figure 12 Computer generated images for determining random distribution of potting radii.

In order to obtain a truly random distribution of potting radius, a theoretical approach was used. This involved generating random sets of drilling co-ordinates to create bore-hole locations within a unit cell. The bore-hole diameter was then plotted on a honeycomb core pattern representing the nominal cell size and shape for Nomex HRH-10-1/8-3.0. All cell walls within the boundary of the bore-hole diameter of 9/16" were considered to be removed, and the corresponding opened cell was assumed to fill with potting. The resulting potting shapes were then processed using UTHSCSA ImageTool[®] software to measure the effective potting radii. A sample size of ten randomly generated co-ordinates was selected to give statistically significant values of mean and more importantly, standard deviation.

Effective Potting Radii from Random Bore Hole Locations (mm)	
Mean (μ)	9.86
Standard Deviation (σ)	0.264
Minimum	9.28
Maximum	10.22
Coefficient of Variance (σ/μ)	2.7%

Table 2 Statistics of effective potting radii for randomly generated bore-hole locations

Table 2 shows the statistical parameters of effective potting radii. The mean effective potting radius for Nomex HRH-10-1/8-3.0 is 9.86mm. This is slightly below mean experimental values of 10.33mm measured from sectioned specimens. This discrepancy could be attributed to the idealisation of cell dimensions with the computer generated images or also possible tearing of adjacent cell walls that may occur in practice. The coefficient of variance is 2.7%, which agrees well to 2.5% observed in experimental values [3]. According to existing predictive models based on shear failure of the core, this would result in the same variance in insert failure load assuming all other influential parameters are constant. This theoretical variability fits well with the relatively small standard deviations seen in experimental results for through-thickness inserts.

5 VARIABILITY IN HONEYCOMB CELL WALL GEOMETRY

The global properties of honeycomb cores are influenced primarily by the cell wall material and geometry. Moreover, in the case of loaded inserts, the shear resultant distribution is such that preliminary failure occurs in the cell wall immediately adjacent to the potting interface. Figure 13 shows buckled cell walls adjacent to the potting compound within a typical failed specimen. With typically used Nomex honeycombs such as HRH-10-1/8-3.0, this preliminary failure is documented by Zhang and Ashby [6] to occur due to cell buckling of the cell wall. The critical buckling load for a thin plate is related to the length, width and curvature of the plate, and is extremely sensitive to the thickness of the plate.

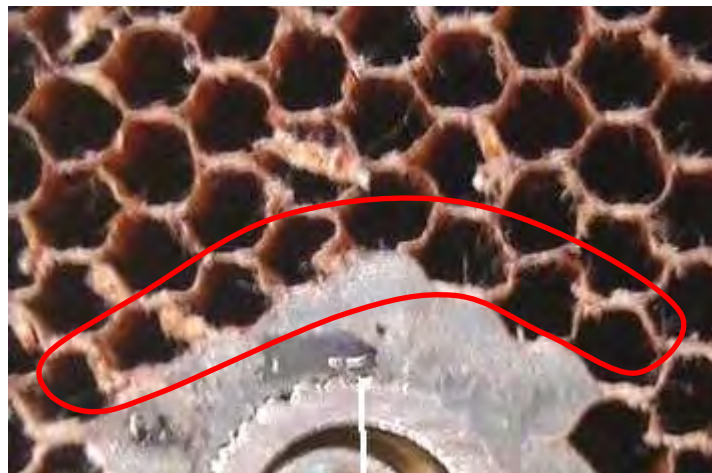


Figure 13 Image of insert specimen tested to failure with top face sheet removed. Buckled cells (encircled) surround the potting.

The sensitivity of local properties to cell wall geometry requires investigation of the statistical distribution of these parameters to determine the variance that can be expected in critical buckling load. Random sections of core were set in epoxy resin to create microscope specimens. The specimen surfaces were ground flat and polished to allow the determination of cell wall length and thicknesses. Measurements were taken in ImageTool© software after capturing photos of the specimens at 33x magnification on an optical microscope equipped

with a digital SLR camera. The measurements were calibrated by taking an initial image of a 0.01mm division stage micrometer, with the same image resolution as that of the specimens. A total of fifteen individual cell wall images were taken from two separate sections of core cut from a larger panel, and from five different core ribbon layers to get statistically representative values. Figure 14 shows the definitions of measured cell wall lengths and wall thicknesses. The wall length was measured between the corner glue fillets, and the wall thicknesses were measured at 5 equidistant locations along the wall. The statistical values from this experiment are presented in Table 3 below.

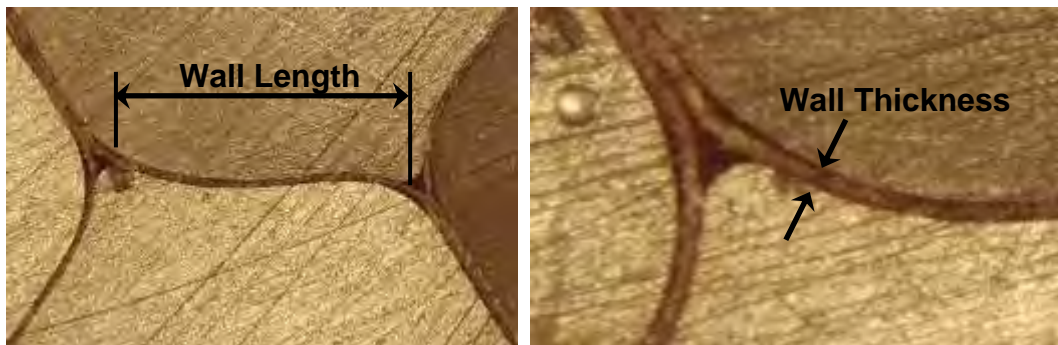


Figure 14 Microscope images of honeycomb specimens showing definition of dimensions.

Cell Wall Lengths and Thicknesses		
Parameter	Wall Length (mm)	Wall Thickness (μm)
Mean (μ)	1.64	46.1
Standard Deviation (σ)	0.05	5.4
Minimum	1.59	38.8
Maximum	1.76	57.6
Coefficient of Variance (σ/μ)	2.8%	11.8%

Table 3 Statistics of cell wall lengths and thicknesses from image measurements

The measured values for wall length show a reasonably small coefficient of variance (2.8%), which compares reasonably well with that seen in experimental failure loads for through inserts (4.7%). This would result in a similar variance in critical buckling shear stress as it is linearly proportional to this dimension. The most interesting result is the variance seen in wall thickness (11.8%). The critical buckling shear stress of a plate is related to the cube of the thickness, so this value would actually result in very high amounts of variability in critical stress (40%).

The reasons for this variability not showing in insert tests may be that this is not representative of the ultimate load carrying capability of an insert. Buckling of the first cell wall represents the onset of failure, but the maximum load is not likely to occur until several cell walls, or another sandwich constituent fails. Moreover, there will be a “smoothing” of the variability due to the large number of cell walls.

6 FOAM CORE PANELS

In order to explore whether this variability was confined to the nature of cell filling in discrete honeycomb cores, foam core samples were manufactured and tested. It was postulated that the foam core, more representative of a homogenous material with respect to machining than honeycombs, would yield much more consistent geometries, and therefore produce more consistent results. A total of two samples with two different inserts, each consisting of five specimens were manufactured using an undercutting tool to ensure a constant potting radius of 10mm.

A blind and a through insert were selected for the experiments. The panels consisted of 1.00" thick Rohacell R51A closed-cell foam core (polymethacrylimide), with a nominal density of 51.3kg/m³ and nominal shear strength of 0.786MPa. The face sheets consisted of two layers of 100gsm plain-weave E-glass and ADR243 epoxy resin supplied by Adhesive Resin Technologies Ltd. The panels were fabricated using a hand-lay-up technique, with the amount of resin calculated for a theoretical 50% volume fraction. The panel was placed under vacuum to ensure good wetting and consolidation of the materials and then subjected to a post-cure as per manufacturer recommendations. The potting compound used was again 3M[®] EC2216B/A epoxy adhesive.

Out-of-plane tensile tests were conducted on all specimens, with the experimental results presented below normalized to experimental values for honeycomb specimens. The through thickness inserts displayed very good consistency in failure mode, strength and load-extension curve shape. The coefficient of variance was remarkably low at less than 1% for the through insert.

	Honeycomb (Through)	Honeycomb (Blind)	Foam (Through)	Foam (Blind)
Sample Mean	1.000	1.008	0.911	0.902
Coefficient of Variance	0.047	0.070	0.009	0.016
Maximum	1.070	1.078	0.921	0.917
Minimum	0.920	0.847	0.900	0.886

Table 4 Statistical values of failure load of honeycomb and foam core insert samples, normalized to through insert honeycomb sample.

7 CONCLUSIONS

Potential causes of variability in the pull-out strength of potted inserts in sandwich panels have been investigated. Experimental results showed higher amounts of variability in samples containing partially potted inserts. An axi-symmetric finite element model was developed and used to investigate the effect of potting depth on stresses in the core material in the vicinity of the potting. The shear stresses in the core show significant sensitivity to this parameter. Variations in potting depth will therefore result in much more variation in strength of partially

potted inserts than with fully potted or through insert configurations.

Significant variability is also seen in fully potted and through insert configurations, possibly due to variability in potting shapes and radii, and also cell wall dimensions. Randomly generated bore-holes on images of honeycomb core allowed the determination of inherent variability in potting radius. This theoretical coefficient of variance (2.5%) fits well with that found in experimental results for through-thickness inserts.

Cell wall dimensions, particularly length and thickness are critical parameters in determining the buckling strength of the cell wall. Microscope images of honeycomb specimens were used to determine the variability in these parameters. While the length showed small levels of variability (2.8%), the thickness showed extremely high variation (11%) which would be expected to result in a coefficient of variance of about 40% in critical buckling load. This level of variability is not generally observed in failure loads, presumably because the maximum load of an insert is related to progressive failure of multiple cell walls.

To further investigate whether the variability seen in honeycomb panels was confined to the nature of cell filling, foam core samples were manufactured and tested. The foam specimens allowed for a more consistent, axi-symmetric potting shape, radii and material properties. The foam panels showed significantly lower coefficients of variance than honeycomb panels for both through thickness and blind inserts. This suggests that variability in pull-out strength seen in honeycomb panels is due to the discrete nature of the core resulting in varying potting shape, radii and local cell wall properties.

The discrete nature of honeycomb core materials means that variability in the strength carrying capability of inserts can be expected to be higher than for foam cores. The significant sensitivity of core stresses to potting height suggests that suitable process controls should be implemented to ensure that blind inserts are always fully potted. This will not only improve the strength of the insert, but will also reduce variability.

8 ACKNOWLEDGEMENTS

The work presented has been possible due to the support of the Foundation for Research Science and Technology (FRST) and Air New Zealand Ltd.

REFERENCES

- [1] European Space Agency, *Insert Design Handbook*, ECSS-E-30-06, 2004.
- [2] Thomsen, O.T. and W. Rits, *Analysis and design of sandwich plates with inserts - a high order sandwich plate theory approach*. Composites Part B: Eng., 1998. **29B**: p. 795-807.
- [3] Raghu, N., *Failure of Inserts in Sandwich Panels*, ME Thesis, Department of Mechanical Engineering. University of Auckland, 2008.
- [4] Bozhevolnaya, E., et al., *Local Effects in the Vicinity of Inserts in Sandwich Panels*. Composites Part B: Engineering, 2003(35): p. 619-627.
- [5] Shur-Lok Corporation, *Sandwich Panel Fasteners Design Manual*. 1996: Shur-Lok Corporation.
- [6] Zhang, J. and M.F. Ashby, *The out-of-plane properties of honeycombs*. International Journal of Mechanical Sciences, 1992. **34**(6): p. 475-489.

MECHANICAL CHARACTERIZATION AND STRUCTURAL BEHAVIOUR OF COMPOSITE SANDWICH STRUCTURES FOR TRAIN APPLICATIONS

Alberto Zinno^{*}, Charles E. Bakis[†] and Andrea Prota^{*}

^{*} Department of Structural Engineering, University of Naples “Federico II”
Via Claudio 21, 80125 Naples, Italy
email: alberto.zinno@unina.it, aprota@unina.it

[†] Department of Engineering Science and Mechanics, Pennsylvania State University
212 Earth and Engineering Science Building, University Park PA 16802, United States
email: cbakis@psu.edu

Keywords: Sandwich structures, Failure mode maps, Experimental testing, Phenolic/Glass skins.

Summary. *The mechanical characterization and the analytical procedures described in the paper are aimed at the structural design for the roof of a train vehicle. Sandwich structure was considered, made of glass fabric in phenolic resin with polymeric foam or Nomex honeycomb core. Static tests were run on the face sheet material and on the sandwich panels. Failure mode maps are created for the sandwich specimens to compare the analytical failure prediction and experimental behavior. The analytical and experimental results are also compared with a numerical analysis.*

1 INTRODUCTION

Sandwich composite structures consist of two thin, stiff and strong fiber reinforced composite face sheets (skins) separated by a thick layer of low density material (core) which may be much less stiff and strong. The role of the face sheets, due to the higher elastic properties, is to withstand bending and in-plane actions, while the transverse shear loads are sustained by the core. The bending stiffness of this type of structural arrangement is much larger than that of a single solid plate of same total weight made of the same materials as the faces. For this reason, composite sandwich structures are widely used in high-performance applications where weight must be kept to a minimum, for example aerospace structures, high-speed marine craft and trains, and racing cars.

Common materials for the sandwich skins are composite or wood laminates and thin aluminium sheets. Polymeric expanded foams are frequently used for the core which, for more demanding applications, can alternatively be made of aluminium or aramid composite honeycomb. It is quite difficult or impossible to generally define the best combination of sandwich constituents because the choice of materials depends not only on strength and stiffness requirements but also on process and cost considerations. Moreover, other interesting

properties of the constituents can influence the design choices, such as fire and environmental resistance, thermal and acoustic insulation, vibration damping and damage tolerance.

The peculiar morphology of a sandwich panel—the layered and multimaterial structure—requires special attention during the design phase. Reliable stiffness and strength predictions can be made only by using suitable, accurate methodologies accounting for the intrinsic structural complexity and the several failure modes that a panel can experience. The theoretical analysis of sandwich panels is summarized by Allen [1] and more recently by Zenkert [2] and Vinson [3], including a systematic design strategy for stiffness and strength. It has been recognised that sandwich beams could fail by a number of competing mechanisms. Numerous investigators [4-6] have used the “failure mode map” concept for sandwich beams in bending to show the dependence of failure mode upon the geometry and the relative strength of both skins and core. While the skins can behave in a relatively simple manner, the mechanical modelling of the core material, particularly for foams or honeycombs, is less straightforward. The response of the core to shear loading mainly depends on the material used in the core and on the ratio of the core density to that of the solid material constituting the core. Gibson and Ashby [7] give a thorough overview of the literature on cellular materials, while Zhang and Ashby [8] model the elastic and collapse behaviour for honeycomb materials.

In the present work, sandwich structures are considered for the structural design of the roof of a train vehicle (Fig. 1). In particular, the face sheets are made of E-glass fabric reinforced phenolic prepreg, while the core is made of either polymeric foam or aramid fiber reinforced phenolic honeycomb (Nomex). In the following sections, the experimental mechanical characterisation of sandwich beams and constituent materials is discussed. Afterwards, the experimental results are compared with analytical and numerical analyses.



Figure 1: The train investigated into the study [9]

2 EXPERIMENTAL CHARACTERIZATION

2.1 Laminate tests

The selected face sheet laminates consist of glass fabric in a phenolic resin, chosen for its

capacity to resist high temperatures. The experiments involved both tensile and three-point bending tests to evaluate the in-plane tensile and shear properties and the short-beam strength.

Static tensile tests (Fig. 2a) were run on 1x15x250 mm coupons, tested in one series with the warp fibers parallel to the load and in a second series with warp fibers perpendicular to the load. These tests were performed in accordance with the ASTM D3039M standard [10]. Static shear tests (Fig. 2b) were run on 2x25x250 mm tensile coupons with a $[+45/-45]_{2s}$ stacking sequence in accordance with the ASTM D3518M standard [11]. Three strain gauges were applied to each coupon. Short-beam tests in accordance with the ASTM D2344M standard [12] were run on 6x12x36 mm specimens, made by parallel laminating of prepreg.

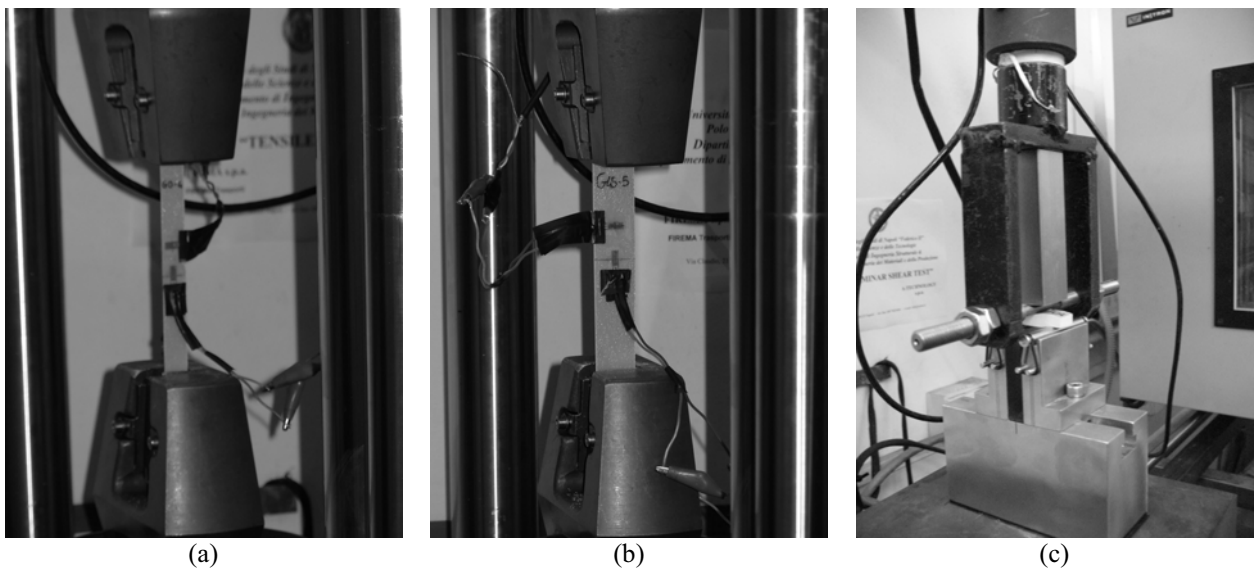


Figure 2: The testing fixtures used for laminate tests (a) tensile tests, (b) shear tests and (c) short beam tests.

All tests were run on a 10 kN universal test frame controlled by an electronic control unit which allows monitoring the applied load and the stroke of the top cross head. Strain signals were acquired by a digital data acquisition system. Tests were conducted at a constant cross head velocity of 1 mm/min.

Table 1 reports elastic properties and strength values obtained in static tests of face sheet material. Due to the nearly balanced nature of the fabrics, laminates with the warp fibers perpendicular to the load are characterized by values close to those with warp fibers perpendicular to the load.

Test	E (GPa)	σ_u (MPa)	ν (-)	G (GPa)	τ_u (MPa)	σ_{sb} (MPa)
Tensile warp direction	25.5	288	0.15	-	-	-
Tensile \perp warp direction	23.0	326	0.13	-	-	-
Shear	-	-	-	3410	43.3	-
Short-beam	-	-	-	-	-	21.3

Table 1: Results for face sheet laminate tests.

2.2 Sandwich beam tests

The selected beams are sandwich panels with equal laminated E-glass/phenolic composite face sheets consisting of four 0/90 woven plies stacked in the $[0/90]_s$ arrangement. The core is either a 130 kg/m^3 high-performance expanded polymer foam or a 48 kg/m^3 aramid fiber reinforced phenolic honeycomb (Nomex) with a nominal cell size of 3.18 mm.

Three point bending tests (Fig. 3) were run on $13 \times 100 \times 500$ sandwich beams in accordance with the ASTM C393M and D7250M standards [13-14]. Three electrical resistance strain gauges were applied on specimens while the displacement of the midspan was monitored using a LVDT. Each type of sandwich structure was tested with two different support spans: $L_1=325 \text{ mm}$ and $L_2=265 \text{ mm}$. All tests were run on a 10 kN universal test frame as described in the previous section. Beam tests were conducted in stroke control with a cross head speed of 6 mm/min. The load was applied by a 25 mm wide flat steel block.

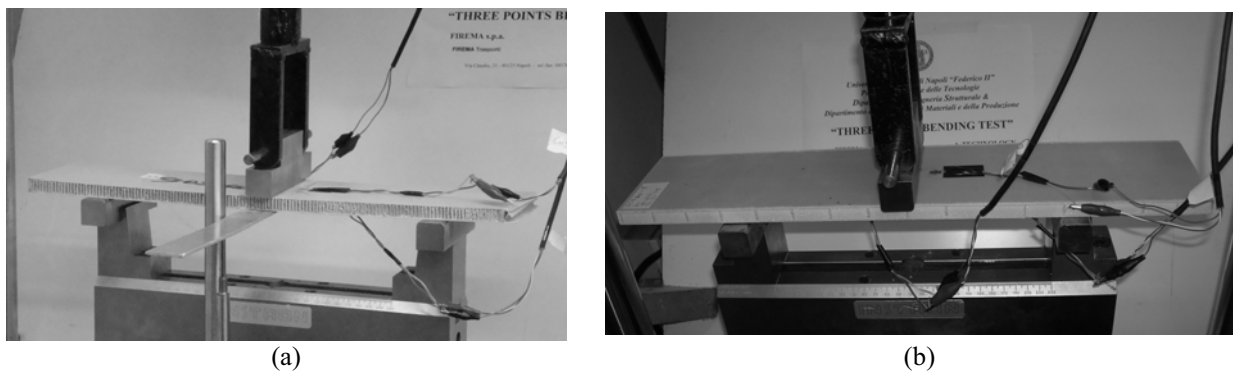


Figure 3: Flexural testing fixtures (a) glass/Nomex sandwich, (b) glass/foam sandwich.

3 REVIEW OF BEAM THEORY FOR SANDWICH PANELS

This section deals with the elastic analysis of sandwich beams in three-point bending in order to evaluate the stresses in the core or skin and hence the applied loads corresponding to various failure mechanisms. Consider a simply supported sandwich beam (Fig. 4) of span L , width b and central load W . Each skin has thickness t and the two skins are separated by a relatively thick core of thickness c . It is assumed that all three layers are perfectly bonded together and the face material is much stiffer than the core.

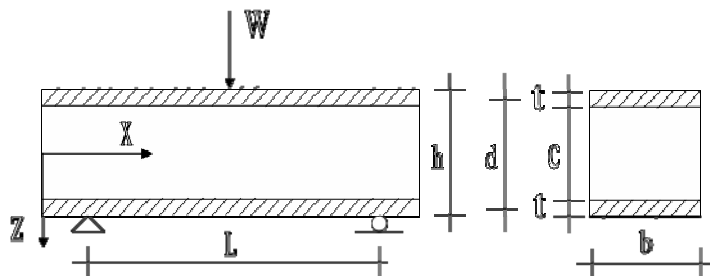


Figure 4: Simply supported sandwich beam and its cross section.

The stresses and deflections in a beam of this type may be found, to a first approximation, by the use of ordinary bending theory. This theory is based on these assumptions: the beam bends in a cylindrical manner with no curvature in yz -plane; cross-sections which are plane and perpendicular to the longitudinal axis of the beam remain so when the bending takes place.

The sandwich structure is assumed to act compositely. Therefore, its flexural rigidity, D , is the sum of the flexural rigidity of both skins and the core, measured about the centroidal axis of the entire cross section:

$$D = E_f \frac{bt^3}{6} + E_f \frac{btd^2}{2} + E_c \frac{bc^3}{12} \quad (1)$$

where E_f and E_c are the moduli of elasticity of face and core, respectively, and d is the distance between the center lines of the upper and lower faces.

In real sandwich beams, the second term is invariably dominant. In fact, the first and the third terms amount to less than 1% of the second term when

$$\frac{d}{t} > 5.77 \quad (2)$$

$$6 \frac{E_f}{E_c} \frac{t}{c} \left(\frac{d}{c} \right)^2 \geq 100.$$

So, equation (1) becomes:

$$D \approx E_f \frac{btd^2}{2} \quad (3)$$

In a simply-supported beam with a central load, the maximum bending moment M is at midspan and the corresponding maximum stress σ_f in the skins is given by:

$$\sigma_f = \pm \frac{M}{D} E_f \frac{d}{2} = \frac{WL}{4dt}. \quad (4)$$

If the core is too weak to provide a significant contribution to the flexural rigidity of the sandwich, the shear stress may be assumed constant over the depth of the core. The constant shear stress in the core is then given by:

$$\tau_c \approx \frac{Q}{bd}. \quad (5)$$

The total deflection δ_{max} at midspan of a sandwich beam loaded in three-point bending is the sum of the deflection due to the bending of the face sheets and the shear of the core:

$$\delta_{max} = \frac{WL^3}{48D} + \frac{WL}{4AG} \quad (6)$$

3.1 Face sheet failure

The expression for the maximum stress (Eq. 4) in the face sheets can be used to predict the beam failure due to the skin failure modes—i.e., face ultimate strength, face wrinkling and intra-cellular buckling. In a symmetric beam, the stress is the same in the compression and tension faces.

For composite faces, the critical face is generally the compressive. The failure occurs when the axial stress in either of the skins, σ_f , reaches the in-plane ultimate strength, σ_f .

$$\sigma_f = \sigma_{fi}. \quad (7)$$

In the case of wrinkling of the compression face, the wavelength of the buckled face is of the same order as the thickness of the core. This problem may be analyzed as the buckling of a beam (the face sheet) supported transversely by an elastic foundation (the core). With three-point bending, wrinkling of the top skin occurs in the vicinity of the central load. Allen [1] gives the critical compressive stress σ_{fw} that results in wrinkling:

$$\sigma_{fw} = B_1 E_f^{\frac{1}{3}} E_c^{\frac{2}{3}}, \quad (8a)$$

where

$$B_1 = 3 \left[12(3 - \nu_{cz})^2 (1 + \nu_{cz})^2 \right]^{\frac{1}{3}} \quad (8b)$$

and ν_{cz} and E_c are respectively the out-of-plane Poisson's ratio and Young's modulus of the core.

A sandwich with a honeycomb core may fail by buckling of the face in a small region where it is unsupported by the walls of the honeycomb. The following expression has been proposed [15] for the in-plane stress σ_{fi} in the skin at which intra-cellular buckling occurs:

$$\sigma_{fi} = \frac{2E_f}{(1 - \nu_f^2)} \left(\frac{t}{R} \right)^2, \quad (9)$$

where R is the cell size of the honeycomb core.

3.2 Core failure

Sandwich structures loaded in bending can fail due to core failure. Pertinent modes are shear failure or indentation by local crushing in the vicinity of the loads application.

Shear failure occurs when the applied shear stress, τ_c , equals the shear strength, τ_{cu} , of the core:

$$\tau_c = \tau_{cu}. \quad (10)$$

The honeycomb core showed two different values of the ultimate shear strength in the two in-plane directions, depending on the direction of the honeycomb ribbon.

Indentation failure is predicted when the out-of-plane compressive stress, σ_z , equals the out-of-plane compressive strength, σ_{cc} , of the core. Knowing the length of contact, δ , between the central loading bar and the top face sheet, it is assumed that the load is transferred uniformly to the core over this contact length. The out-of-plane compressive stress in the core is assumed to be given by:

$$\sigma_z = \frac{W}{b\delta}. \quad (11)$$

To evaluate the core failure mechanism, stiffness and strength properties for the Nomex honeycomb and foam core are required. The out-of-plane Poisson's ratio, required for the failure analysis, can be taken, to a first approximation, as that of the solid materials ν_s . The out-of-plane Young's modulus of the Nomex honeycomb is given by the rule of mixture expression:

$$\frac{E_c}{E_s} = \frac{\rho_c}{\rho_s}, \quad (12)$$

where ρ_c and E_s are the density and Young's modulus of the solid honeycomb material, respectively. For a honeycomb with regular hexagonal cells, Wierzbicki [16] gives the following expression for the ultimate out-of-plane compressive strength:

$$\sigma_{cc} = 3.25\sigma_{sc} \left(\frac{\rho_c}{\rho_s} \right)^{5/3}, \quad (13)$$

where σ_{sc} is the compressive strength of the solid from which the core is made. Petras and Sutcliffe [17] derive the following expressions for the out-of-plane shear strengths of regular hexagonal honeycomb core:

$$\frac{\tau_{c31}}{E_s} = 1.7 \left(\frac{\rho_c}{\rho_s} \right)^3, \quad (14a)$$

$$\frac{\tau_{c32}}{E_s} = 2.6 \left(\frac{\rho_c}{\rho_s} \right)^3. \quad (14b)$$

Based on a analysis of the manufacturer's modulus and strength data, For the foam core the following expressions are derived for the foam core:

$$\frac{E_c}{E_s} = 1.16 \left(\frac{\rho_c}{\rho_s} \right)^{1.28}, \quad (13)$$

$$\frac{\sigma_{cc}}{\sigma_{sc}} = 1.10 \left(\frac{\rho_c}{\rho_s} \right)^{1.63}, \quad (14)$$

$$\frac{\tau_c}{\sigma_{sc}} = 0.78 \left(\frac{\rho_c}{\rho_s} \right)^{1.28}. \quad (15)$$

4 CONSTRUCTION OF A FAILURE MODE MAP

Based on the summary given in the previous section, the failure loads depend on: properties of the skin and solid core material (Table 2); relative density of the core; thickness of both skins and core; beam span and loading details. Therefore $W=f(t/l, t/\delta, \rho_c/\rho_s)$. The actual behavior is then governed by the mode with the minimum failure load.

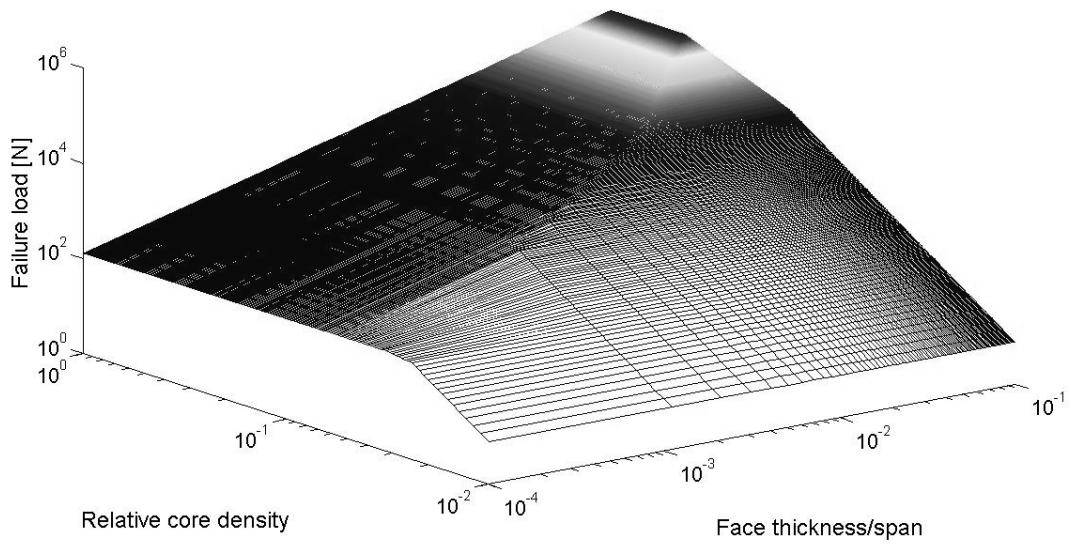
Failure maps have been drawn, using the Matlab [18] programming language, for the two types of tested sandwich structures. The failure modes and loads are plotted as a function of core relative density and skin thickness to span ratio, at fixed core thickness to span ratio.

	ρ_s (kg/m ³)	ν_s (-)	ρ_c (kg/m ³)	E_c (MPa)	τ_{c31} (MPa)	τ_{c32} (MPa)	σ_c (MPa)
Nomex	724	0.40	48.0	138	0.69	1.21	2.24
Foam	1200	0.40	131	86.0	1.95	1.95	2.50

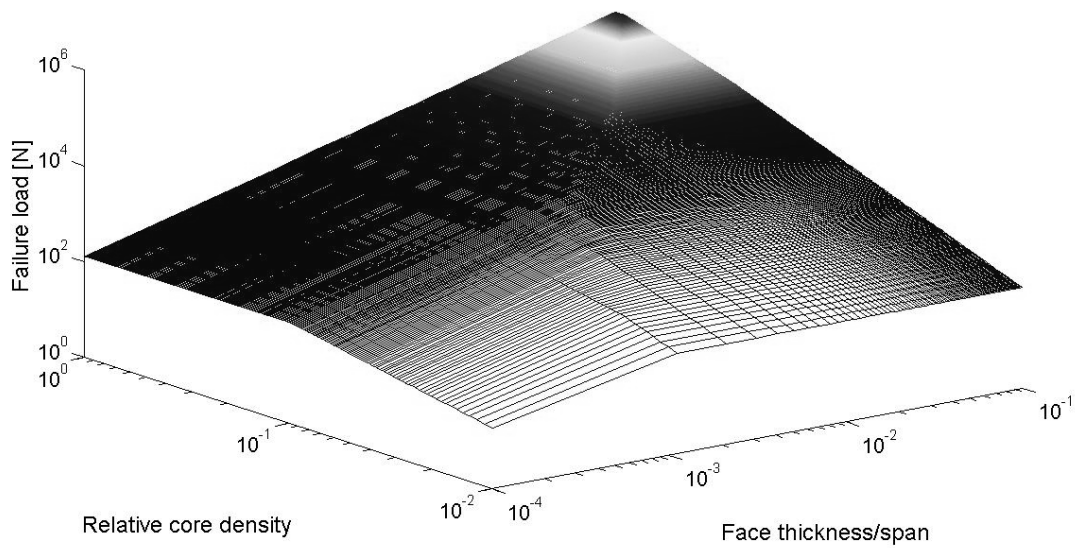
Table 2: Nomex and foam core properties.

Figures 5(a) and 5(b) show the failure load surfaces for glass/Nomex honeycomb and

glass/foam sandwich beams, respectively.



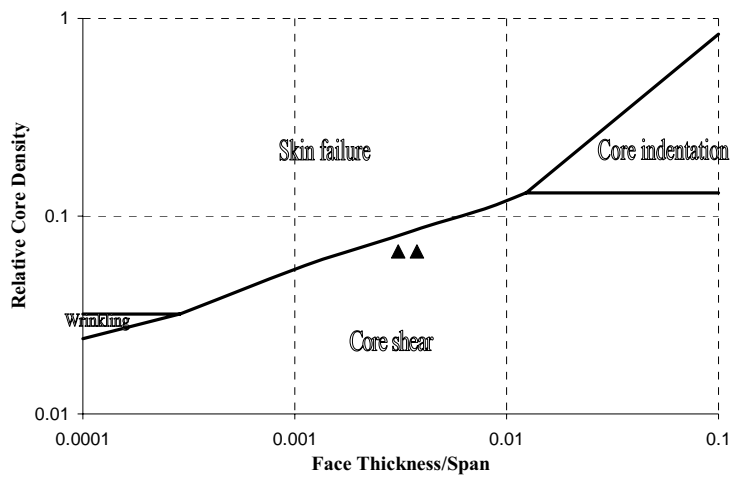
(a)



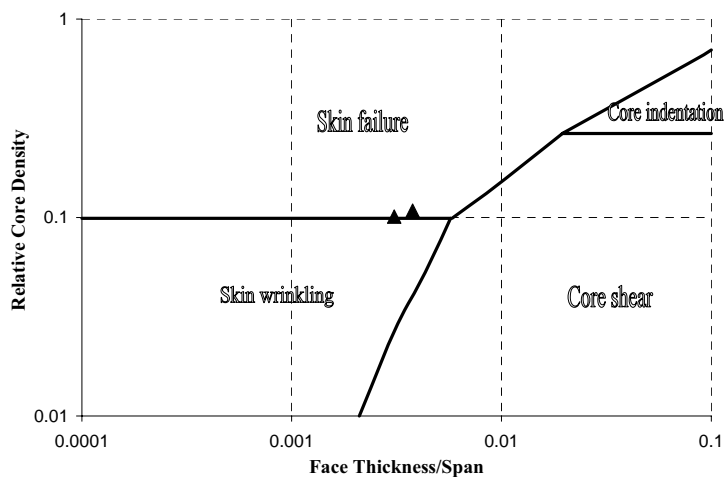
(b)

Figure 5: Failure load surfaces: (a) glass/Nomex sandwich; (b) glass/foam sandwich.

Figures 6(a) and 6(b) show the failure mode maps for glass/Nomex honeycomb and glass/foam sandwich, respectively. When plotting two experimental measurements for each type of core, it is observed that the experimental failure modes, as shown in Fig. 7, are consistent with the analytical predictions in each case. It is interesting to observe that, for a honeycomb core, the intra-cellular buckling mode represents less severe condition than the wrinkling failure due to the small hexagonal cell size. However, the wrinkling surface represents a small area of the failure mode map since the honeycomb sandwich has a high modulus in the out-of plane direction, thus limiting the wrinkling phenomenon.



(a)



(b)

Figure 6: Failure mode maps: (a) glass/Nomex sandwich; (b) glass/foam sandwich. The ▲ symbols identify experimental measurements.

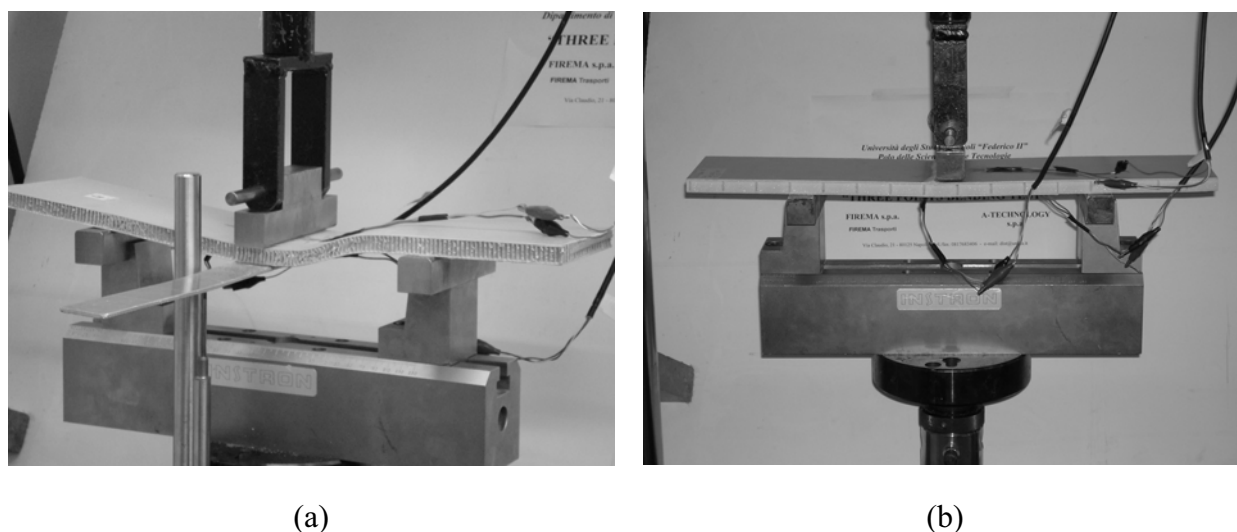


Figure 7: Experimental failure modes: (a) glass/Nomex sandwich (core shear); (b) glass/foam sandwich (face wrinkling).

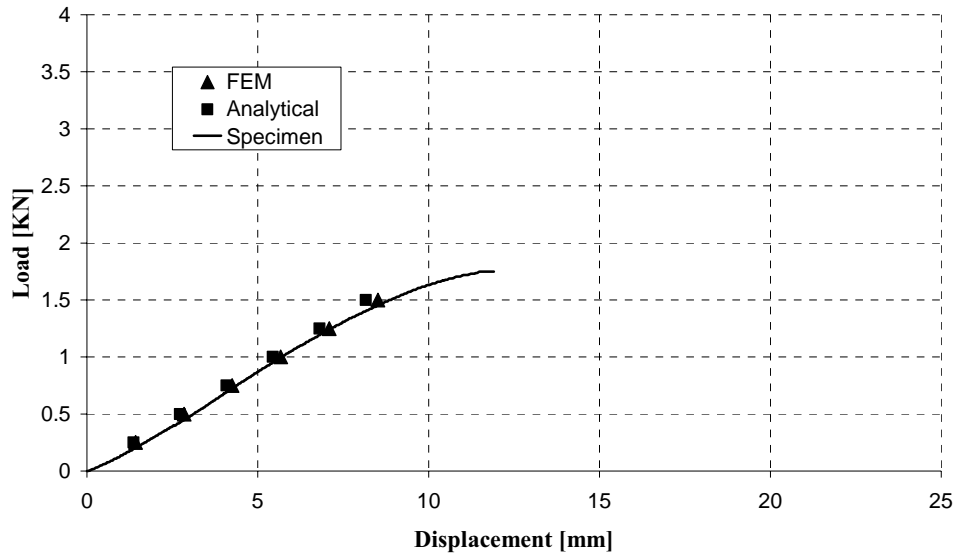
5 FINITE ELEMENT ANALYSIS

The aim of finite element modeling is to perform reliable simulations of the static behavior of composite sandwich panels to be compared with the experimental data for just one sandwich configuration. The analysis were performed using the finite element code ABAQUS®. The face sheet was meshed using 4-node shell elements, while the core was meshed using 8-node solid elements. A 2D-orthotropic material was used to define the glass fabric prepreg, and the composite function was used to create the stacking sequence of the face sheets. Isotropic and 3D-orthotropic materials were used for foam and honeycomb core, respectively. Skins and core material properties were defined only in the linear elastic range. Due to the symmetry of the structure, a quarter of beam was modeled and symmetry constraints were applied to the nodes on the plane of symmetry. Figures 8(a) and 8(b) show the comparison between the experimental, numerical and analytical stiffness of the glass/Nomex and glass/foam sandwich beams, respectively. The numerical stiffness are perfectly matched with the experiments, while the analytical behavior is influenced by the various assumptions and approximations.

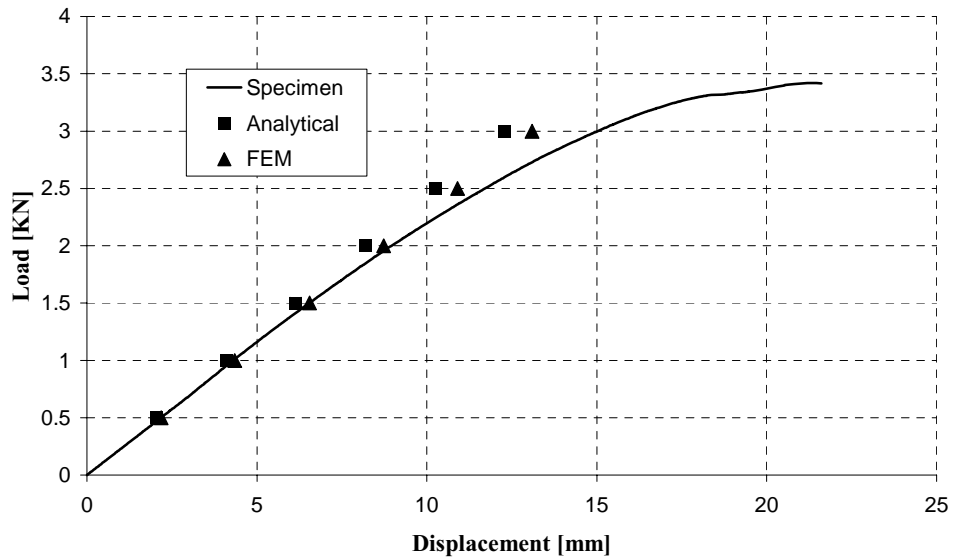
6 CONCLUSION

A mechanical characterization activity documented in this paper was carried out for both the face sheet materials, to asses the mechanical properties of the skin for which there is a lack of reliable data on glass/phenolic, and to validate and calibrate analytical and numerical models for the sandwich construction. The failure mode map is shown to be a good tool to predict the failure loads and modes as functions of the geometry and materials of the sandwich structure. Moreover, the study underlines the capacity of the numerical model to simulate the elastic flexural stiffness of a sandwich beam. Ongoing work will apply this

modeling capability to design problems involving phenolic sandwich composites for train applications.



(a)



(b)

Figure 8: Comparison of experimental load-displacement curves with analytical and numerical results: (a) glass/Nomex sandwich; (b) glass/foam sandwich.

6 ACKNOWLEDGEMENTS

The authors wish to thank the Firema Trasporti for financial support.

REFERENCES

- [1] H.G. Allen, *Analysis and design of structural sandwich panels*, Pergamon Press, 1969.
- [2] D. Zenkert, *An introduction to sandwich construction*, Engineering Materials Advisory Services, 1997.
- [3] J.R. Vinson, *The behavior of sandwich structures of isotropic and composite materials*, Technomic Publishing, 1999.
- [4] E.W. Kuenzi, *Sandwich design criteria*, Forest products laboratory, 1959.
- [5] T.C. Triantafillou, L.J. Gibson, "Failure mode maps for foam core sandwich beams", *Material Science and Engineering*, 95, 37-53 (1987).
- [6] Y. Shenhar, Y. Frosting, E. Altus, "Stresses and failure patterns in the bending of sandwich beams with transversely flexible cores and laminates composite skins", *Composite Structures*, 35, 143-152 (1996).
- [7] L.J. Gibson, M.F. Ashby, *Cellular solids: structure and properties*, Pergamon Press, 1988.
- [8] J. Zhang, M.F. Ashby, "The out-of-plane properties of honeycombs", *International Journal of Mechanical Science*, 34(5), 475-489, 1992.
- [9] Anonymous, *Imperiale in composito per una carrozza ferroviaria modulare di tipo regionale*, Firema Trasporti, 2006.
- [10] Anonymous, *Tensile properties of polymer matrix composite materials*, ASTM, D3039M, 2002.
- [11] Anonymous, *In-plane shear response of polymer matrix composite materials by tensile test of a $\pm 45^\circ$ laminate*, ASTM, D3518M, 2001.
- [12] Anonymous, *Short-beam strength of polymer matrix composite materials and their laminates*, ASTM, D2344M, 2000.
- [13] Anonymous, *Core shear properties of sandwich constructions by beam flexure*, ASTM, C393M, 2006.
- [14] Anonymous, *Determining sandwich beam flexural and shear stiffness*, ASTM, D7250M, 2006.
- [15] Anonymous, *Composite construction for flight vehicles*, U.S. Military Handbook, 1959.
- [16] T. Wierzbicki, "Crushing analysis of metal honeycombs", *International Journal of Impact Engineering*, 12, 157 (1983).
- [17] A. Petras, M.P.F. Sutcliffe, "Failure mode maps for honeycomb sandwich panels", *Composite Structure*, 44, 237-252 (1999).
- [18] D. Hanselman, B. Littlefield, *Mastering Matlab 5*, Matlab Curriculum Series, 1998.

ANALYSIS OF FULL-SCALE AEROSPACE SANDWICH PANELS UNDER PRESSURE LOADING

Duncan A. Crump^{*}, Janice M. Dulieu-Barton^{*} and John Savage[†]

^{*} School of Engineering Sciences (SES)
University of Southampton
University Road, SO17 1BJ, UK
e-mail: dac400@soton.ac.uk, J.M.Barton@soton.ac.uk

[†] GE Aviation
Kings Avenue, Hamble-Le-Rice
SO31 4NF, Hampshire, UK
e-mail: John.Savage3@ge.com

Key words: structural analysis, aerospace sandwich structure, full scale tests, manufacturing

Summary: *This study provides a detailed consideration of five manufacturing options that are used to produce aerospace sandwich panels used in secondary structure. The structural performance of each of the manufacturing options is considered along with a cost analysis. A means of using optical strain analysis techniques on full scale panels is devised through the design of a test rig that is capable of applying uniform static and cyclic pressure to the panels.*

1 INTRODUCTION

Increasing environmental pressure on the aviation industry to reduce the ‘carbon footprint’ of aircraft has led to considerable research into the improvement of fuel efficiency. An important factor in improving fuel efficiency is reducing the weight of the structure of the airframe. To this end, composites are increasingly utilised in airframe manufacture. For example, the Airbus A380 has upwards of 22% by weight made from composites [1], and the new Boeing 787 is expected to be made from 50% composite structure [1]. The excellent strength and stiffness to weight ratios of composites in comparison to traditional metallic materials are well known, but these property improvements come at a cost premium. The aerospace composite structure manufacturing industry is becoming more competitive. Even small reductions in cost can be important in winning a contract for component manufacture, as this reduces the final cost of the aircraft and makes it more attractive to airlines.

There has been extensive research regarding the optimisation of production methods for the use of composites in primary aircraft structure, however little work has concentrated on secondary structure. The overall aim of this project is to investigate methods for reducing the cost of manufacturing carbon fibre sandwich panels for use in aircraft secondary structure, concentrating primarily on ‘gap fillers’ on the wing leading and trailing edges. Such panels

are currently manufactured as sandwich panels that use layers of pre-impregnated (pre-preg) carbon fibres and Nomex Honeycomb that are laid-up on to a tool by hand before being consolidated and cured in an autoclave.

The inherent disadvantages of the hand lay-up/autoclave process have been discussed in the literature, e.g. [2] and [3]. The process is heavily dependent upon labour, and the autoclave introduces large capital and running costs [4]. The present paper describes how the cost of manufacture can be reduced by removing the autoclave cure from the process and replacing it with oven cure and vacuum bag consolidation. Studies of the entire manufacturing process from receipt of material to full assembly of components have identified that the autoclave curing process introduces a significant 'bottleneck' in production as shown in Figure 1. The bottleneck is caused primarily by the need to resort to batch processing of components in the autoclave. This is because the number of autoclaves that a company can purchase and install is restricted by high capital and running costs. To avoid backlogs of components and increase efficiency batches are created that require the same curing cycle. Therefore components often wait in the production line until there are sufficient to fully occupy an autoclave. Another consideration is that the loading and unloading of the autoclave can only be carried out at one end, which also slows the process. Furthermore the tooling is such that it must withstand high pressures and is therefore heavy and difficult to manoeuvre. Introducing an oven cure, would mean that components could be loaded at one side and removed from the other creating better production flow, the cost of tooling would be reduced and batch sizes could be smaller or larger, as appropriate because ovens are much less costly to purchase and run than autoclaves. In replacing the autoclave with an oven cure the production bottleneck would be changed as shown by the dotted lines in Figure 1 with lay-up being the main cause of a new but less severe bottleneck.

The aim of this study is to demonstrate that it is possible to change the manufacturing process and hence material, so that an autoclave cure is not required. In doing this it is essential that the mechanical performance of the end product is practically identical to the autoclave cured product. In the work described in this paper, panels are manufactured from five combinations of processing technique and face sheet materials, which are defined as the manufacturing options. Each manufacturing option (MO) represents an incremental step in taking the component from a fully autoclave cured product to a fully resin infused out-of-autoclave cured product. The panels are analysed for both cost and structural integrity. A programme of tests on full-scale representative panels is planned, because of the heterogeneous nature of composite material and its variability. The results will be used to validate a Finite Element (FE) analysis of the panels. It is proposed that in future the mechanical testing can be omitted, but at present this is an essential component in the development of an analysis procedure for assessing the performance of components made from the different MOs.

The proposed experimental analysis of the panels will employ two full-field optical techniques, namely digital image correlation (DIC) [5] and thermoelastic stress analysis (TSA) [6]. To apply these techniques it is necessary that the surface of the panels can be viewed directly whilst under load with either two digital cameras for the DIC or with an infrared detector for the TSA. To do this a test rig has been designed that can apply a pressure load

to the panels that is representative of the service load and allows optical viewing of the loaded specimen without the distraction of loading shackles in the field of view.

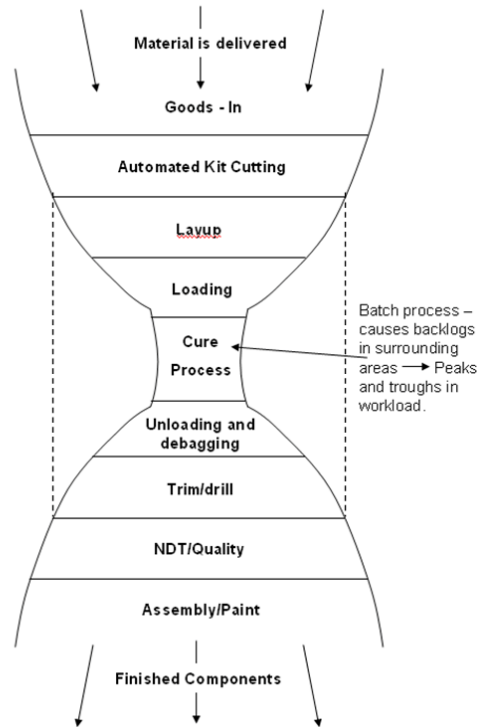


Figure 1: Bottleneck caused by autoclave

The present paper describes the design of the five test panels, concentrating on a step-by-step description of the manufacturing process for each panel, so that the time savings in each manufacturing option can be identified. The paper also describes mechanical characterisation tests performed on tensile specimens manufactured from the five combinations of face sheet material and process, so that an initial comparison can be made between the quality of the material produced by each of the MOs. FE models of the full-scale test panels are developed, using the material properties derived from the mechanical characterisation tests. A detailed description of the design and commissioning of the custom designed test rig used for the optical analysis is also provided in the paper.

2 TEST PANEL DEFINITION

This study investigates typical trailing edge access panels, which are classified as wing secondary structure on a commercial passenger aircraft. These panels are bolted to the main wing beam and 'A-frames' along three sides, allowing one of the longer edges to be free to deflect under service load. The panels are subjected to aerodynamic out-of-plane loads across their surface. For the purposes of this work, the loading configuration is represented by a uniform pressure load applied across the surface of the panel, which is constrained by bolts on

three edges. In order to compare the performance of the components made from different manufacturing processes, a full-scale generic component representative of current industry secondary structure wing trailing edge panels was designed.

A review of previous designs of CFRP face sheet/honeycomb core sandwich secondary structure identified a number of ‘common’ features as follows:

- Face sheets are of quasi-isotropic lay-up with 12 plies at 0.125 mm per ply,
- Panels are long and narrow – between 700 and 1500 mm long by 300 wide,
- Cut-outs and notches are used to account for neighbouring structure,
- Inserts and solid pucks are used for attachments,
- Simplistic block-like core geometry.

Consideration of the above features allowed the development of the geometry of a generic panel (Figure 2). Features such as inserts, attachments, cut-outs and notches have been set-aside in the current study, as these would lead to stress concentrations that are dependent on the ply lay-up and orientation and would detract from a straightforward evaluation of the manufacturing processes. Taking into account the above considerations a generic panel was defined as shown in Figure 2. The generic panel is flat and has a plan area of 0.9 m x 0.3 m. The Nomex honeycomb core is 0.6 m x 0.2 m and 12.5 mm thick. A non-core stiffened flange is included as this is a key feature in such panels and is essential for attachment purposes. The flange has a total cured thickness of approximately 3 mm, half formed by the tool-side face sheet, and half by the bag-side face sheet.

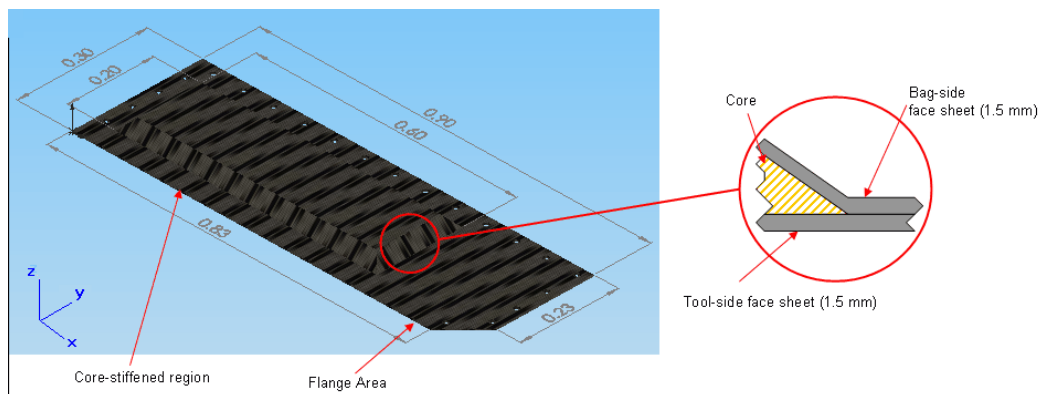


Figure 2: Generic Panel Design

3 MANUFACTURING OPTIONS

Five material and processing combinations (known as Manufacturing Options (MOs)) were selected for the mechanical performance comparison. The five MOs are listed below:

1. Unidirectional prepreg tape cured in an autoclave.
2. Woven prepreg cured in an autoclave.
3. Non-crimped fabric with separate resin film cured in an autoclave.
4. Woven side-preg and oven cured.
5. Non-crimped fabric with separate resin film using RFI process.

3.1 Prepreg tape autoclave cured (MO1)

MO1 is based on the traditional approach for manufacturing aerospace components, which makes use of unidirectional prepreg tape. The process involves hand lay-up of individual plies that are spliced together from the tape, which provides a cured ply thickness of 0.125 mm. Therefore to make the generic component shown in Figure 2, 12 plies are required to make the 1.5 mm face sheets. A lay-up was defined that would produce quasi-isotropic face sheets. This choice was based on current design guidance outlined in [7]. Therefore a $[0^\circ, 45^\circ, -45^\circ, 90^\circ, 0^\circ, 45^\circ, -45^\circ, 90^\circ, 0^\circ, 45^\circ, -45^\circ, 90^\circ]$ lay-up was used for each face sheet. These were constructed in a symmetrical configuration about a Nomex honeycomb core.

Prior to the laying-up process the Nomex core must undergo a stabilisation process so that it does not deform or crush when the curing/vacuum pressure is applied. The stabilisation process was identical to that used in production and used a foam adhesive to strengthen the chamfered edges of the core and a film adhesive is applied to the flat faces to provide some rigidity. The stabilisation requires that the core undergoes a separate cure before it can be introduced into the sandwich panel lay-up.

Hexcel's 914C-TS-5-34% prepreg tape was used to produce the face sheets. The individual plies were laid-up by hand on a flat mould tool comprising a sheet of steel. As the stack was constructed it was vacuum 'debulked' after each ply was introduced in an identical fashion to the process used in production. The debulk process is essential in production as it removes trapped air from the stack that could cause porosity during the curing process. To perform the debulk, a vacuum bag was constructed on the mould tool that enclosed the stack and a vacuum applied for approximately 20 minutes. When the tool side face sheet had been laid-up the Nomex honeycomb core was positioned on the face sheet. The bag side face sheet plies were then laid-up over the core material. A debulk was carried out as each of the 12 plies were added to the stack. The unidirectional tape was difficult to form over the shaped core, and therefore the 12 bag side face sheet plies took longer to lay-up than the 12 tool side plies. Once the component was fully laid up on to the tool, a final vacuum bag was then formed around the component that was used during the curing process. The bagged tool and stack was then placed into an autoclave for curing.

When the component was placed into the autoclave, a full vacuum was applied. Then the autoclave curing pressure was applied. When the autoclave pressure reached approximately 1 bar the vacuum was reduced to a value of 0.2 bar to prevent void formation within the component due to disparity in the vapour pressure. When the curing pressure of 3 bar gauge was achieved, the temperature was increased. The component was heated to 120°C at a rate of 2°C/minute. The ramp rate controls the viscosity of the resin, so that the resin can flow and 'wet out' occurs throughout the component before the resin starts to cure. Initially the temperature in autoclave was held at 120°C for 60 minutes. The temperature was then ramped at 2°C/minute to the final curing temperature of 175°C. The cure temperature was held for 120 minutes. Once the cure cycle had been completed the autoclave was allowed to cool at 3°C per minute, with the pressure held at 3 bar until the temperature was 60°C or below ensuring the component was held in position as it cooled to below the gel temperature.

During the lay-up procedure the time spent on each step in the process was noted to allow

an estimation of the number of labour hours spent to produce such a panel. It was estimated that this component took approximately 14.6 hours to lay-up, with a further 5 hours to perform the core stabilisation. These times do not include the length of the two cures. The autoclave cure, including time for pressurisation, and depressurisation, took approximately 5.7 hours and the core stabilisation cure 3.5 hours. Therefore an estimate of the total time to lay-up and cure a component using MO1 is 28.8 hours. This process is time consuming due to the large number of individual plies and therefore the large number (23) of debulks that must be manually set-up. The nature of the material also means it is not easily draped over shaped objects, such as the core, and this also adds to the time it takes an operator to lay-up an individual ply. The number of plies required to achieve the thickness leads to a large labour input in the manufacturing process with the cost of the component reflecting this input. On the positive side the large number of plies required to build the panel face sheets leads to significant flexibility in defining the ply orientations. This has allowed designers to tailor the material properties for the final laminate, but the time taken for lay-up and debulk is excessive indicating that a material with fewer plies is more desirable.

3.2 Woven prepreg autoclave cured (MO2)

MO2 uses a woven prepreg that incorporates a predefined amount of fibres in both the longitudinal and transverse directions in the same ply. Each ply is equivalent to two plies of the UD tape, laid in a cross-ply (0° , 90°) configuration and has a cured ply thickness of 0.25 mm. This method reduces the number of plies required in MO1 and hence lay-up and debulk time, with the 1.5 mm thick face sheets of the generic panel requiring 6 plies of this material. The cross-ply nature of the woven prepreg leads to an alteration in the lay-up of the panels. A $[0^\circ, 45^\circ, 0^\circ, 45^\circ, 0^\circ, 45^\circ]$ lay-up was used for each face sheet, orientated symmetrically about the core material and was assumed to be comparable to the lay-up in MO1.

Hexcel's 8552S/37%/AGP280C five harness satin weave prepreg was used to produce the face sheets. The process for lay-up and cure described in section 3.1 was again used for panel manufacture. As in MO1, the Nomex honeycomb core had to undergo the core stabilisation process prior to its inclusion in the generic panel. The time spent on each step in the process was, again, recorded to allow estimation of the labour hours to produce the panel using MO2. It was estimated that components manufactured in this way took 8.9 hours, and not including the 5 hours for the core stabilisation. These figures do not include the time for cure, but are identical to MO1. Therefore an estimate of the total time for lay-up and cure of a component manufactured using MO2 is 23.1 hours. The lay-up time represents a 19.8% reduction in the number of labour hours, largely attributed to the reduction in plies and debulks. However the woven prepreg was also easier to drape over the shape of the core, so the time to form the bag side face sheet was reduced.

3.3 Non-crimp dry fabric with resin film autoclave cured (MO3)

MO3 combines dry non-crimp fabric and resin film materials proposed for the resin infusion with a traditional autoclave cure. Hexcel's NC2 dry fabric was used, which consists

of 4 individual layers of UD material that are loosely stitched together to hold its form. Each ply of the NC2 has a lay-up of $[0^\circ, 45^\circ, -45^\circ, 90^\circ]$, with a total fibre weight of 560 gsm. The resin is introduced as a layer of resin film between each ply. The resin is Hexcel's DLS1726 (320 gsm). Because each ply of the NC2 consists of 4 layers of UD material, each 1.5 mm thick face sheet only requires 3 plies of the NC2 fabric. These were laid up as follows $[0^\circ, 0^\circ, 0^\circ]$, i.e. equivalent to MO1.

The layer of resin film was adhered to the under side of the NC2 fabric, before they were both laid up, resin side down, on to a flat mould tool. After each layer was laid-up, a vacuum debulk was required. When the 3 plies that formed the tool side face sheet had been laid-up the Nomex honeycomb core was positioned. The bag side plies could then be laid-up over the core material, with a debulk after each layer. Once the component was fully laid-up on the tool, a final vacuum bag was then formed around the component that was used during the cure process. The bagged tool and component were placed into the autoclave. A similar cure process as MO1 was used except the initial dwell temperature was increased from 120°C to 130°C , and the final post-cure temperature was increased from 175°C to 180°C as defined by the resin manufacturers.

It was estimated that this process took approximately 6.7 hours to lay-up, with a further 5 hours for the core stabilisation. The time for cure was identical to MO1. Therefore an estimation of the total time to lay-up and cure a component using MO3 is 20.9 hours. This represents a further 9.5% reduction in manufacturing time from MO2. The reduction in labour time is attributed to the reduction in the number of plies and debulks, as well as the material being easy to drape over the shaped core, and because each ply was laid in the same direction, there were no need for multi-directional alignment.

3.4 Woven side-preg oven cured (MO4)

MO4 removes the costly autoclave cure, by combining a woven side-preg with an oven cure. Hexcel's DLS1726/40%/285T2/AS4C-6K, a side-preg 2 x 2 twill woven fabric, uses a similar fibre mat to that described in MO2, and the same resin system as that in MO3. This resin system has been specifically formulated for use in vacuum only cure. The lay-up for this component is identical to that in MO2, so 6 plies are required for each face sheet. The lay-up procedure was identical to the method described in section 3.2, for MO2. When the final vacuum bag had been made, the bagged tool and component were placed in an oven. In the oven a full vacuum was applied to the component then the component was heated to 130°C at a rate of $2^\circ\text{C}/\text{minute}$. The oven was held at 130°C for 60 minutes, before a second ramp at $2^\circ\text{C}/\text{minute}$ up to 180°C was initiated. The oven was held at 180°C for 120 minutes, before the component was allowed to cool at 3°C per minute.

Estimations of the time to lay-up showed it took approximately the same amount of time as MO2, i.e. 8.9 hours to lay-up and 5 hours to core stabilise. The component cure time has, however, been reduced from 5.7 hours to 5 hours, by replacing the autoclave with an oven cure, and removing the pressurisation and depressurisation stages. An estimation of the total time to lay-up and cure a component through MO4 is 22.4 hours, which represents a 3% reduction in manufacturing time from MO2.

3.5 Non-crimp dry fabric with resin film oven cured (MO5)

MO5 uses Hexcel's NC2 dry fabric with DLS1726 resin film, i.e. as used in MO3. These are laid-up in an identical approach to that described for MO3. Once the component had been placed in the final vacuum bag, the bagged tool and component were put in the oven for cure. The oven cure was identical to that for MO4,

Estimations of time for this component are, 6.7 hours for lay-up, 5 hours for core stabilisation, 5 hours for component cure and 3.5 hours for core stabilisation cure. A total manufacture time for this component of 20.2 hours, which represents a 12.6% reduction in manufacturing time from MO2. MO5 benefits from significantly reduced lay-up and cure times over the other manufacturing options. However, the performance of the material needs to be assessed prior to making any claims that this approach is better than MO1 or MO2.

4 MECHANICAL PROPERTIES OF FACE SHEET MATERIALS

An initial comparison of the performance of the face sheet materials produced by the five MOs was obtained from tensile tests. The test data also provided input into the FE models of each panel. To ensure the tensile test specimens had experienced an identical cure cycle to the generic panels, separate panels of the face sheet material were laid-up in an identical manner to the generic panel and cured with the generic panels. The test specimens were manufactured from the panels and tested as specified in ASTM D3039 using an Instron 5569 servo-mechanical test machine. Five specimens of each orientation and MO were tested. The specimens were orientated so that the longitudinal direction (L) was in the x-direction shown in Figure 2 and the transverse (T) was in the y-direction. The mechanical properties of the quasi-isotropic face sheets specimens can be seen in Table 1, enabling a direct comparison of the MOs.

Table 1 : Mechanical properties of Quasi-Isotropic Laminates

MO		E_L (GPa)	E_T	ν_{LT}	ν_{TL}	σ_{FXL} (MPa)	σ_{FT} (MPa)
1	<i>QI</i>	48.7	50.4	0.086	0.149	565	597
2	<i>QI</i>	47.1	49.3	0.262	0.25	534	568
3	<i>QI</i>	44.5	44.3	0.317	0.274	595.	579
4	<i>QI</i>	42.2	41	0.241	0.248	532	549
5	<i>QI</i>	45.2	46.7	0.32	0.258	640	667

For the longitudinal modulus there is practically no difference between the two autoclaved, prepreg products. Comparing the out-of-autoclave materials with MO1 shows a 7% reduction in longitudinal modulus for MO5, an 8% reduction for MO3 and 13% reduction for MO4. A similar pattern is observed for the transverse modulus. Although in a there is no difference in materials between the autoclave cured NCF material in MO3 and the oven cured NCF material in MO5, there appears to be a slight improvement in modulus. The resin system used for MO3 and MO5 has been formulated for oven cure and will therefore wet-out the fibres better during an oven cure; this can explain the improvement. The reduction in modulus for

MO4, compared to MO2 can be attributed possibly to the poor wet out of the side-preg resin through the woven material. It is interesting to note, the Poisson's ratio values vary enormously with MO1 being significantly different to MO3 and MO5 which are all made from non crimp materials; at present there is no explanation for this. The material manufactured using MO1 has a longitudinal failure stress of 565 MPa and transverse failure stress of 597 MPa, while the material manufactured through MO5 shows an improved longitudinal failure stress of 640 MPa and a transverse failure stress of 667 MPa. This represents an increase in strength of approximately 12% through the use of the out-of-autoclave MO. This is an unexpected result as it is generally accepted that the autoclave will produce a higher quality product. The increase in strength must be attributed to the resin used and possible improved wet-out. This will be confirmed by microscopic investigation in future work. From these results it can be concluded that the out of autoclave product shows no significant changes in mechanical properties, although the differences in Poisson's ratios will have an effect on the behaviour of the generic panels when loaded in bending.

5 FEA OF PANELS

At this stage it was decided that a simple model was required to ascertain if the changes in the face sheet materials could be incorporated into a model and also to inform the design of the test rig. The model was constructed in ANSYS 11.0 using two basic shapes. The first was the size and shape of the total plan area of the generic panel. The second, the size and shape of the Nomex core, was extruded to form the volume of the core by a z-axis offset with taper in x and y to produce the chamfer. The first area and those areas that bound the core volume were the face sheets. The Nomex core was assumed to be a singular isotropic, solid volume with the relevant associated properties [8]. The flange area contains all twenty four plies, while the areas bounding the volume have sections of twelve plies thereby summing to twenty four. The model comprised Solid185, an eight-noded brick element for the core and Shell181, a four-noded element suitable for laminates, for the face sheets. The service constraints were represented by holding the model on the three fixed sides, such no out-of-plane deflection was allowed. The in-plane constraints were achieved by selecting two points on the perimeter of the panel at which deformation was prevented in any direction. The fixing bolts have not been modelled as the current research is concerned with the panel performance rather than the localised stresses around the bolt holes.

The correct fibre orientation was maintained on the chamfered edges of the core by locally changing the element coordinate systems so that z was always normal to the surface of core. It was considered that as the generic panel is only constrained on three edges the application of the pressure load would result in a relatively large out-of-plane deflection. Therefore a geometrically non-linear solver was used. The service load that the panel must withstand is a pressure load of 0.0275 MPa, which was applied as a force of 9.03 N in the z-direction (see Figure 2) on each of the 759 nodes of the mould side face sheet. The maximum out-of-plane deflection (that occurred near the centre of the free edge) and the maximum principal stress (located near the edge of the core on the outside of the bag side face sheet) were used as an initial comparison; the results are provided in Table 2.

The model shows that there is very little variation in the maximum deflection and the maximum principal stress between the manufacturing options. Although it does appear that MO5 produces a practically identical product to MO2, the model does not consider manufacturing variations, resin infiltration and interlaminar shear strength; these can only be investigated through experiment. In general, at this stage, the model shows that a maximum deflection of the order of 40 mm can be expected, which was accommodated in the design of the test rig described in the next section.

Table 2: Maximum out-of-plane deflections from FE model

MO		Max Deflection (mm)	Max Principal Stress (MPa)
1	QI	38.6	247
2	QI	37.2	211
3	QI	41.3	208
4	QI	42.1	200
5	QI	37.0	214

6 DESIGN OF TEST RIG

To make an experimental comparison of the mechanical performance of the panels made for the five manufacturing options a test rig has been custom designed that can replicate the in-service pressure loading conditions. In service the panels are subjected to a pressure load across the mould side face sheet, which is constrained by bolts on three sides. To experimentally model the pressure load a water filled cushion is used to impart the load into the panel in a uniform fashion. This approach has been used successfully in the past, e.g. [9]. The design differs to those used previously, as to use TSA and DIC it is necessary to have optical access to the surface of the bag side face sheet. The test rig was designed to be used with a standard Instron 8802 servo-hydraulic test machine. The final design is shown in Figure 3. The rig is formed from two main parts. The first part is a ‘table’ structure that supports the pressurised water cushion. The water cushion is from Flexitec, and can withstand 0.345 MPa, i.e. much greater than the pressure required to model the service load. The cushion is deformable, so is completely constrained by the rig. The second section is the connection from the actuator of the test machine to the test panel. This is a box type structure that fits over the water cushion table to which the panel is bolted. As the actuator moves downwards the test panel is forced against the water cushion. The applied pressure is developed by the force of the test panel against the incompressible water cushion, and monitored by a pressure gauge.

At present the test rig is being commissioned. It is envisaged that future publications will include results from the DIC and the TSA. Such techniques would offer a strain map of the panel under load that could be directly compared to the FE models for validation. Significant challenges in the application of these techniques to full scale structures need to be addresses. Previous work by the authors [10] has shown that the techniques can be applied to sandwich

structure. To apply DIC and to obtain a full field map of the structure it will be necessary to apply a correlation device across the structure, current work is focusing on using the peel-ply imprint in the surface of the face sheets for this [11]. A further complication for both TSA and DIC is the repositioning of the equipment and the joining of images to obtain a full-field map. Repositioning is more complex with DIC because of the need to collect data in the deformed and undeformed states. The test rig is able to apply the cyclic load required for TSA, however incremental readings will be required as the depth of focus of TSA lens systems could not accommodate the 40 mm deflections predicted by the FE.

7 CONCLUSIONS AND FUTURE WORK

This paper has presented a study of the possibility of reducing the manufacturing costs of carbon fibre/ Nomex honeycomb sandwich aircraft secondary structure. An analysis of the time taken to produce panels from five manufacturing options has shown that by removing the autoclave cure and using RFI the number of labour hours required for lay-up can be reduced by 55%. This is because the time in the oven cure is less, but more importantly the fibre mats used in the RFI negate the number of lay-up and debulking operations required. The fibre mats are much thicker than the prepreg and sufficient resin infiltration from film through the thick mats was in question. Initial mechanical tests have shown that the in-plane properties of material are equivalent to that produced in an autoclave. However, the resin infiltration will affect the through thickness properties and more work is required to establish if the material performance changes when loaded in transverse shear.

Initial FEA has shown that the deflection of the panels is similar regardless of the manufacturing options. Clearly under in-service load this will not be the case as the FEA does not model the variability of composite sandwich panels. The paper has described the design of a test rig so that the mechanical performance of panels produced by the five manufacturing options can be compared through a programme of full-scale tests. The rig permits the application of optical strain measurement techniques such as TSA and DIC. These techniques will provide full field data that will be used to validate the FE model and also to study the behaviour of the panels under repeated load and evaluate the damage tolerance of the different manufacturing options.

REFERENCES

- [1] National Composites Network, www.ncn-uk.co.uk
- [2] Chestney, J.A. and Sarhadi, M. *A Prototype Manufacturing Cell for Automated Assembly of Fibre Reinforced Composite Preforms*. in *4th International Conference on Automated Composites*. 1995. Nottingham UK Institute of Materials.
- [3] Abraham, D. and McIlhagger, R, *Investigations into Various Methods of Liquid Injection to Achieve Mouldings with Minimum Void Contents and Full Wet Out*. *Composites Part A: Applied science and manufacturing*, 1998. 29: p. 533-539.
- [4] Dexter, H.B. *Development of Textile Reinforced Composites for Aircraft Structures*. in *4th International Symposium for Textile Composites* 1998. Kyoto, Japan.

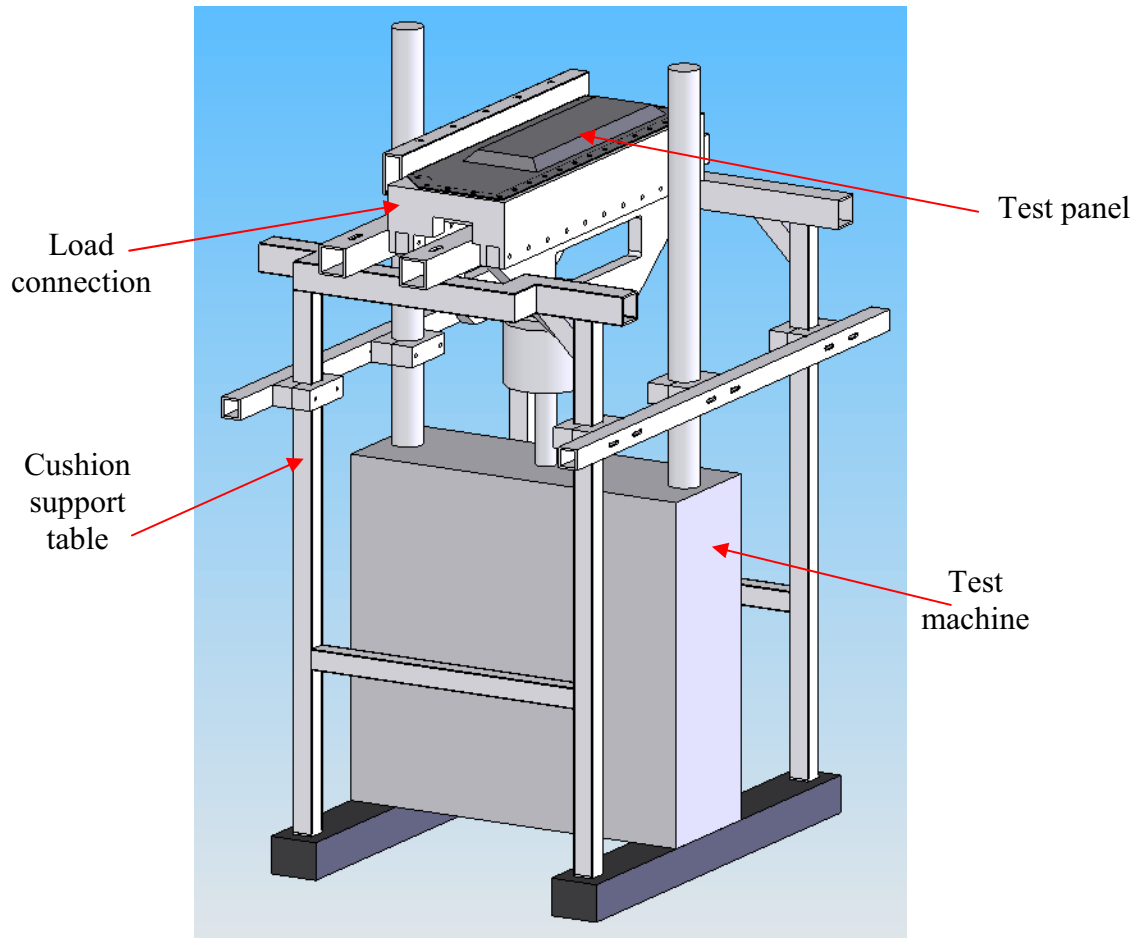


Figure 3: Final Pressure Rig Design

- [5] Corr, D. and Accardi, M. *Digital Image Correlation Analysis of Interfacial Debonding Properties and Fracture Behaviour in Concrete*, Eng Fract Mechs, 2007, Vol 74, p109-121.
- [6] Dulieu-Barton, J. M. and Stanley, P. *Development and applications of thermoelastic stress analysis*. Journal of Strain Analysis, 1998, Vol 33, No 2, p 93-104.
- [7] Niu, M. *Composite Airframe Structures*, 1992, Adaso Adastra Engineering Center.
- [8] Petras, A., Sutcliffe, M. P. F. *Indentation resistance of sandwich beams*, Composite Structures, 1999, Vol 46, 1, p 413-424.
- [9] Jolma, P., Segercrantz, S. and Berggreen, C. *Ultimate failure of debond damaged sandwich panels loaded with lateral pressure – An experimental and fracture mechanics study*, Journal of Sandwich Structures and Materials, 2007, Vol 9, No 2, p 167-196
- [10] Crump, D., Dulieu-Barton, J. M. and Savage, J. *Manufacturing Options for Secondary Aircraft CFRP Sandwich Components*, ICCM 16, Kyoto, Japan, 2007
- [11] Crump, D., Dulieu-Barton, J. M. and Savage, J. *Full field Strain Analysis of Aircraft Sandwich Structures*, SEM 11, Orlando, USA, 2008

THERMOFORMING OF CLOSED CELL POLYMER FOAM AND ITS RESIDUAL COMPRESSIVE MECHANICAL PROPERTIES

M. Åkermo *

* Aeronautical and Vehicle Engineering
Kungliga Tekniska högskolan (KTH)
Teknikringen 8, 100 44 Stockholm, Sweden
e-mail: akermo@kth.se, web page: <http://www.ave.kth.se>

Key words: Sandwich structures, Manufacturing, Modelling, Experimental.

Summary. *This paper aims to investigate the deformation behaviour of a closed cell polymer foam during forming at temperatures above the glass transition temperature of the foam. Further, the residual compressive properties are measured and the results are correlated with measurements on photographs showing the resulting core cell geometry. It is shown that different mechanisms are active for thermoforming in the tensile and compressive directions, but that the resulting mechanical properties seems to be predictable using established models and geometrical expressions.*

1 INTRODUCTION

Traditionally, manufacturing of structural sandwich components are limited to simple geometrical shapes or to labour consuming and therefore costly manufacturing processes. For very large structures, this may be difficult to change. However, considering the variety of medium sized applications where structural sandwich components may find its place, from automotive to aeronautical, a demand for more cost efficient production rises. Thermoforming is one potential option.

Thermoforming has been shown to enable efficient manufacturing of complex shaped sandwich structures [1] using polymer foam core. The process utilises that most polymer foams are formable at temperatures above its glass transition temperature, enabling adoption to double curved shapes with high draw ratio. The drawback with this method is however that during forming, the initially isotropic core material changes through alignment with the strain field. The result is a product with different core properties than the virgin core. Before offering this technique to more advanced applications, it is consequently highly desirable to be able to predict this change in core cell structure and the resulting mechanical properties of the foam.

This study aims to investigate the residual compressive mechanical properties of a thermoformed closed cell polymer foam core. Although most forming processes involve both tensile and compressive deformation, these are herein studied separately in order to simplify the evaluation. The change in core cell geometry following thermoforming during tensile and compressive loading, respectively, is studied using microscopy. Finally, the residual

compressive properties are measured and the results are compared to models on the mechanical properties of anisotropic cores.

2 THEORETICAL BACKGROUND

The mechanical properties of polymer foams are largely determined by geometrical features of the material and by the properties of the solid material [2]. Polymer foams are geometrically distinguished as being either open or closed with isotropic or anisotropic mechanical properties. However, considering single cells, their shape are generally not truly spherical, but isotropic core properties are often a result of a randomised distribution of anisotropic core cells. Anisotropy is thus both a matter of cell geometry and its distribution in space inside the core.

In this work, the mechanical compressive properties following thermoforming will be compared to model predictions based on the cubic array assumption, where the cells are considered as cubic arrays of square transverse sections. Adjoining cells are staggered so that their members meet at their midpoints, see eg [2]. The cell wall material is isotropic, so that the anisotropy arises solely from the cell shape. Considering closed cell foams, these models enables capturing deformation mechanisms as extension or compression and bending of the cell walls, where the latter is more pronounced for low density materials [2]. Further, as the cell membranes stretch, the contribution from the axial cell-wall stiffness to the elastic moduli increases.

Based on these assumptions, it has been shown that for isotropic closed cell foam material the following relation between foam compressive modulus, E , and the modulus of the solid material, E_s , can be derived from (neglecting the gas pressure contribution) [2]:

$$\frac{E}{E_s} = \phi^2 \left(\frac{\rho}{\rho_s} \right)^2 + (1 - \phi) \left(\frac{\rho}{\rho_s} \right) \quad (1)$$

, where ρ and ρ_s are the density of the foam and of the solid material, respectively. ϕ is the fraction of material in the cell wall membrane. In the same way an expression for the compressive strength, here defined as peak stress during compressive failure, σ^* can be determined from the strength of the solid material, σ_s^* [2]:

$$\frac{\sigma^*}{\sigma_s^*} = 0.3 \left(\phi \frac{\rho}{\rho_s} \right)^{1.5} + 0.4(1 - \phi) \left(\frac{\rho}{\rho_s} \right) \quad (2)$$

A comprehensive model describing the compressive behavior of anisotropic foam is presented by Huber and Gibson [3] based on the previously described cubic array assumption. The model shows that, given that the rise direction of the cell has dimension h and the square transverse-section, l , the cell has anisotropy $R=h/l$ and the compressive modulus ratio can be written

$$\frac{E_3}{E_1} = \phi \frac{2R^2}{(1 + (1/R)^3)} + (1 - \phi) \frac{2R}{1 + (1/R)} \quad (3)$$

,where E_3 is the modulus in the core cell rise direction and E_l in the transverse direction. The compressive modulus ratio thus strongly depends on the anisotropy. Since loading in the cell rise direction deflects the shorter cell edges, the stiffness in the cell rise direction is greater than in the plane normal to it.

During thermoforming, the core cells align with the direction of tensile deformation or the direction perpendicular to the compressive deformation for tensile and compressive thermoforming, respectively, see *Figure 1*. However, note that in this work the components will be tested in the core cell rise direction or transverse direction, respectively, independently of method of deformation.

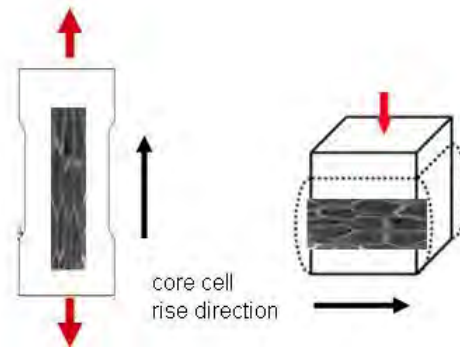


Figure 1. Schematic figure showing how the cells deform during tensile and compressive loading, respectively.

Considering thermoforming in the tensile direction, a model describing the foam deformation and load response of the cubic array core have been developed by Akkerman and Pronk [4]. Experiments have show that this model is applicable on the material and process considered in this study if a second relaxation term is added [5]. During thermoforming the load response is clearly viscoelastic showing rate dependence.

The herein presented mechanical models are based on simplified and idealised geometrical models. Today, techniques for generation of more realistic geometries into finite element code exists, which in the future enables more extended modelling, as e.g. [6].

It needs to be remarked that the herein presented models rely on the cell being “perfect”, i.e, free of wrinkles and with even membrane thickness. A number of studies have indicated that imperfections have a large influence on the mechanical properties, however that cell wall wrinkling has the largest impact, e.g. [7], while the influence of thickness variations seems to be significantly smaller. However, during thermoforming in the tensile direction the cell walls and membranes are thinning and eventually yielding. Finding a maximum degree of deformation before weakening the core is one of the aims of this study.

The geometry of cellular foams is commonly determined using Scanning Electron Microscopy (SEM). The anisotropy of cellular foams has previously been determined measuring the distance between core walls along several lines and at different angles [3]. The measurements are then fitted to an elliptical form using least square method. The core anisotropy is consequently equal to some average anisotropy. Since the test samples produced

herein do not provide photographs on more than on average 10 core cells, a large statistical base do not exist. In this study each core cell is instead measured and fitted to an ellipsoide. The average core anisotropy is calculated as the average anisotropy in the core cell rise direction and transverse direction, respectively. The modulus ratio is thereafter predicted using Equation 3. In order to distinguish these results from compression test results, the resulting modulus ratio will herein be named SEM.

Assuming that the volume is conserved and that all cells are initially spherical ($R=1$), a theoretical anisotropy R_{theory} can be calculated from the known degree of deformation during thermoforming, Δ , according to

$$R_{theory} = \sqrt{(1 + \Delta)^3} \quad (4)$$

This value will be used for comparison for specimens showing no significant change in density following thermoforming. Using this value for predicting the modulus ratio (Equation 4) a purely theoretical estimation is obtained, herein referred to as “theory”.

3 EXPERIMENTS

3.1 Materials

The material used in the study is a closed cell polymethacrylimide (PMI) foam core Rohacell® WF71 from Röhm Degussa GmbH with a specific density of 78 kg/m^3 . In model predictions, the density of the solid material is set to 1200 kg/m^3 .

3.2 Preparation of thermoformed samples

Specimens prepared for thermoforming in the tensile direction had a dog bone like geometry with outer dimensions $150 \times 250 \text{ mm}$, thickness 20 mm , see [8] for further details. This geometry was set as a compromise ensuring uniform heat and stress distribution, while producing enough material for further tests.

In order to avoid global buckling, specimens prepared for thermoforming in the compressive direction were cubic with height 30 mm and a transverse sectional area of $20 \times 20 \text{ mm}$.

According to recommendations from the manufacturer [9], the samples should be dried for at least 3 h in 130°C prior to thermoforming. Although these recommendations are mainly to avoid humidity in sandwich components in e.g. aeronautical applications, the procedure was followed in order to resemble the real process.

Thermoforming was performed in an Instron 4505 from Instron GmbH, equipped with a hot air heating chamber. The temperature was controlled using an in-built thermocouple inside the oven and one either inside the sample (for tensile direction) or inside a dummy placed close to the thermoformed sample (for the much smaller samples in compressive direction).

When the thermocouple inside the specimen (or dummy) showed stable temperature (the set temperature) thermoforming was performed to a predetermined degree of (tensile or compression) deformation. Thereafter the oven was opened and the sample rapidly cooled off at maintained deformation, thereby freezing the deformed structure. When the specimen was

cold and thus thermally stable, the Instron was opened and the deformed sample could be removed. Thermoforming was performed at different temperatures (200 and 220°C), to different degrees of elongation/compression (0-55%) and at different deformation speeds (10-300 mm/min). This paper, however, mainly focuses on the results from the base-line deformation at 200°C and deformations speed 10 mm/min. It should be noted that thermoforming in the compressive direction resulted in an even core compaction in the compressive direction and corresponding swelling in the transverse direction without any signs of local crushing of cell layers, as expected for cold compression. To ensure that the thermal properties of the core were not changed by the heating and deformation, the most severely heated samples was tested using Differential Scanning Calamity, DSC [8]. No change or degradation of the polymer material could be detected following thermoforming.

3.3 Compression tests

From the thermoformed samples, specimens for compression test were cut in two directions: the direction of tensile/compression thermoforming and the transverse direction, respectively.

Due to limitations in geometry of thermoformed specimens, the samples from tensile thermoforming were milled to cubes with side length 15 mm and samples from compressive thermoforming to cubes with side length 10 mm. Since the nominal core cell size is small (radius <0.5 mm), also this smaller test geometry was considered to include enough number of cells to consider edge effects negligible.

Compression test were performed in the Instron testing machine according to ASTM standard D1621-00 at compressive strain rate $1.67 \cdot 10^{-3} \text{ s}^{-1}$, according to standard. Each specific sample was measured prior to testing in order to enable calculating the true stress and strain. Further, each sample was weighed and its density reported.

3.4 SEM

In order to provide specimens for SEM, transverse-sections (about $5 \cdot 5 \text{ mm}^2$), were cut from the middle of the thermoformed specimens. In order to provide a smooth surface with clean-cut cells, the thermoformed specimens were cooled with liquid nitrogen, and broken along the direction of thermoforming or the transverse direction, respectively. The broken surfaces were sputtered (coated) with Au/Pd to obtain the required conductivity using a Denton Vacuum Desk II from Denton Vacuum, USA.

The SEM photographs were analysed using the image software ImageJ [10] from National Institute of Health, USA. In order to determine the shape anisotropy of each cell, the following procedure was undertaken: The cell diameter was measured at different angles with approximately 15° interval, see *Figure 2*. The results were read into an in-house written numerical code finding the ellipse that best fit the measurements (least square method). The results are reported in terms of anisotropy (major/minor axis) and the in-plane rotation of the ellipse. The average anisotropy was calculated according to the description in Chapter 2.

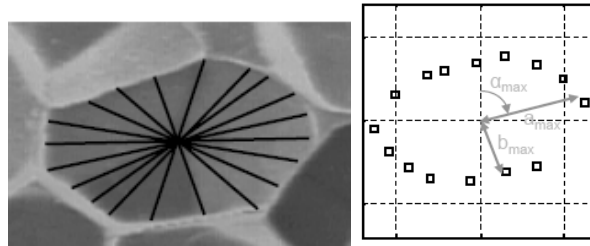


Figure 2. The core cell measurements are fitted to an ellipsoid of anisotropy $R=a_{max}/b_{max}$ in the direction α_{max}

4 RESULTS AND DISCUSSIONS

4.1 Specimens thermoformed in the tensile direction

Figure 3 shows how the foam compressive modulus and strength, respectively, depends on the degree of tensile deformation during thermoforming. Both are normalised based on the properties of the virgin core material in order to visualise the deviation. Following theory, both stiffness and strength increases in the cell rise direction and decreases in the transverse direction. Considering the modulus this change is more pronounced, with an increase/reduction of up to 50%. The difference in strength is smaller, $\pm 30\%$. The results show clear trends, but the scatter is large. This is partly explained by the high sensitivity to fluctuations in forming temperatures around the used thermoforming temperature 200 °C. At his temperature, the mechanical properties of the solid material reduce significantly for each degree of increased thermoforming temperature [5].

For specimens thermoformed in the tensile direction, the density seem to remain constant at the level of the virgin core material [8]. Figure 4 shows a comparison between measured anisotropy and predicted values using Equation 4. As can be seen, theoretical prediction and experimental measurements follow a very similar trend up to a deformation level of approximately 40%. As expected, the core cells maintain their isotropic properties transverse to the cell rise direction. Measurements from photographs taken in the transverse direction showed an average anisotropy of $R=1.05 \pm 0.05$.

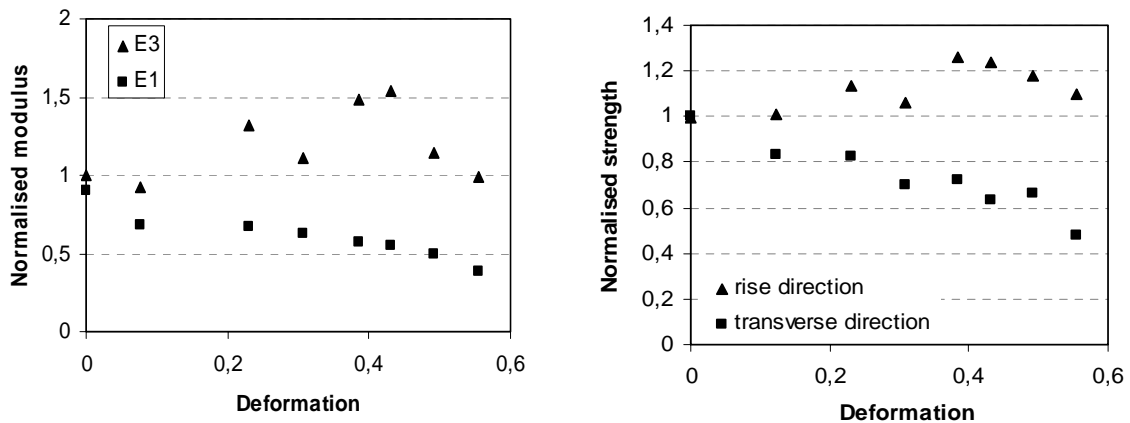


Figure 3. Normalised compressive modulus and strength, respectively, as function of tensile deformation

during thermoforming

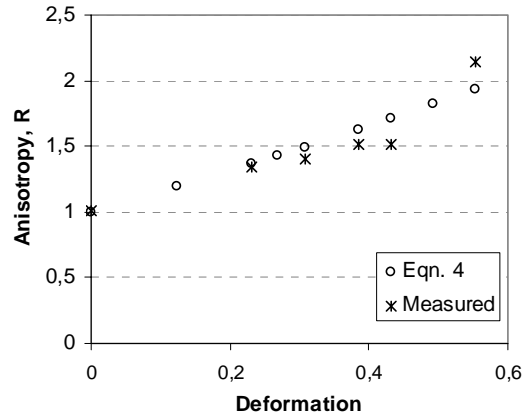


Figure 4. Comparison between measured core cell anisotropy and theoretical predictions

Figure 5a shows a SEM photograph of the virgin core material, while Figures 5b-5d show samples thermoformed in the tensile direction, to 23%, 38% and 55% deformation, respectively (please note that figure 4d is 90 degrees tilted).

Figure 6 shows the ratio between compressive modulus in the cell rise direction and transverse direction. The experimental results are compared with estimations from measurements on the cell foam geometry (SEM) as well as theoretical predictions based on the conserved volume principle (theory), Equations 3 and 4. As can be seen, all results follow the same trends. The deviation between the experimentally based values and the theoretical estimation increases at higher degrees of thermoforming deformation.

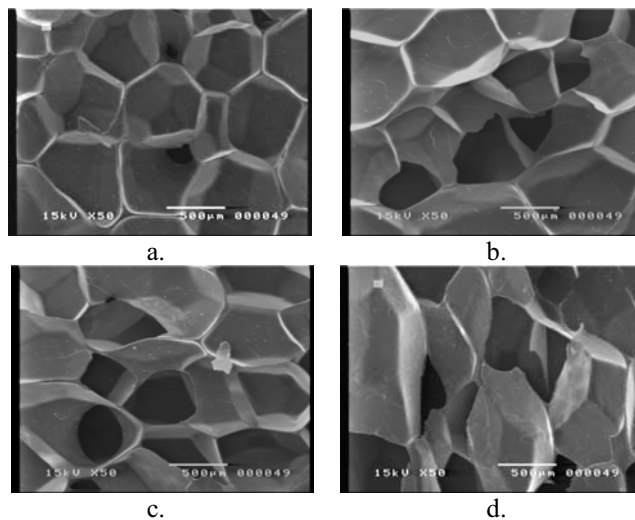


Figure 5. Samples thermoformed to a. 0% elongation (virgin core), b. 23% elongation, c. 38% deformation, d. 55% deformation (tilted)

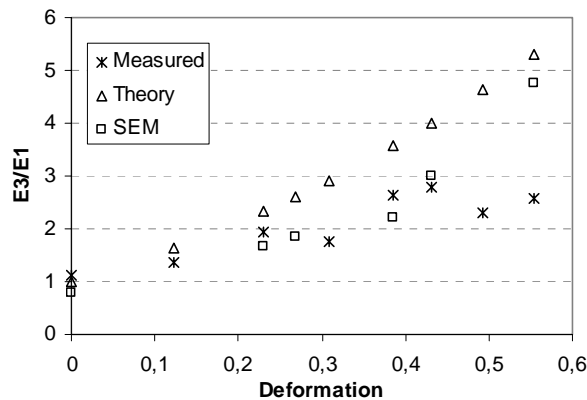


Figure 6. Comparison between measured modulus ratio, estimations from SEM photographs and theory for sample thermoformed in tensile direction.

4.2 Specimens thermoformed in the compressive direction

Figure 7 shows how the foam compressive modulus and strength, respectively, depend on the degree of compressive deformation during thermoforming (normalised based on the properties of the virgin core material). As expected, the modulus and strength increases in the core cell rise direction following thermoforming. Further, it is interesting to note that the reduction in modulus in the transverse direction is significant, 80%, but that the compressive strength is only slightly reduced. This is explained by the core densification occurring during forming, see Figure 8. The densification is significant and indicates that the core swelling is negligible compared to the core compaction: a reduction in height with 50% increases the density with 100%. Since the core material is liquid like during thermoforming, it can be argued that the structure maintains its strength in the transverse direction, but that the stiffness is significantly reduced. In Figure 7, theoretical values for the normalised modulus and compressive strength are given based on the measured density of thermoformed samples (Equations 1 and 2). As can be seen, for these experiments the predicted values follow the experimental data in the cell rise direction, 3. However, since the theoretical model considers the material as isotropic (same properties in all directions), the thermoformed core materials must be considered somewhat destroyed compared to a virgin core of higher density.

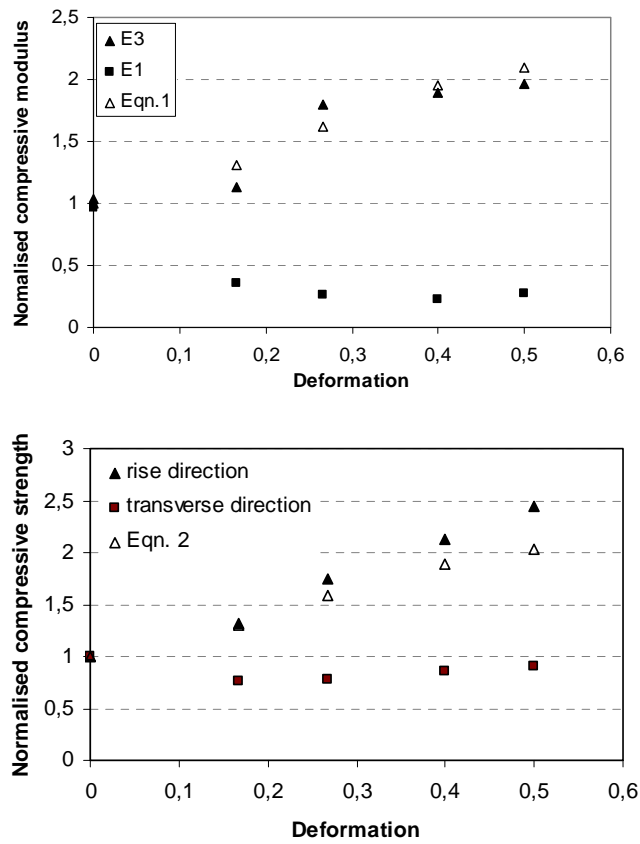


Figure 7. Normalised compressive modulus and strength, respectively, as function of compressive deformation during thermoforming

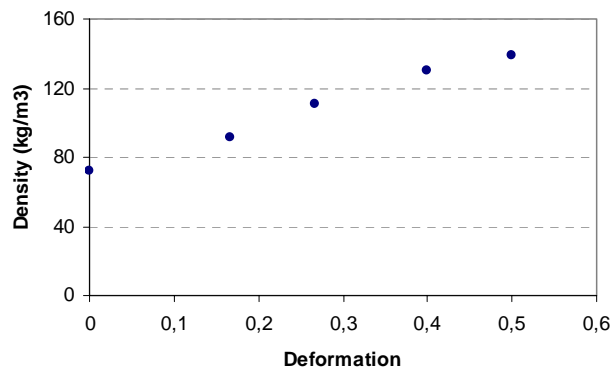


Figure 8. Core densification as function of compressive deformation during thermoforming

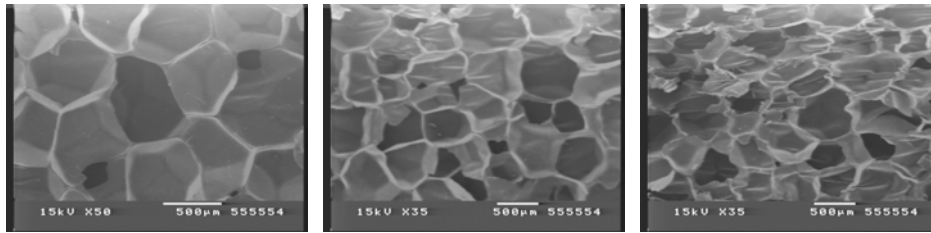


Figure 9 Samples thermoformed in the compressive direction to a 17% deformation, b. 27% deformation, c. 50% deformation.

Figure 9 shows SEM photographs of samples thermoformed in the compressive direction. The average cell anisotropy is measured to: compressive deformation 17% $R=1.2$, deformation 27% $R=1.3$, deformation 40% $R=1.9$, deformation 50% $R=1.9$. In the photographs, cell wall buckling can be detected already at 27% compression.

Figure 10 shows the ratio between compressive modulus in the cell rise and transverse direction for samples thermoformed in the compressive direction. The experimental results are compared with estimations from measurements on the cell foam geometry, as described in Section 2. Since the density is changed following thermoforming, the theoretical approximation, Equation 4, does not hold and is therefore not included in the comparison. The results show poor agreement between measurements and predictions based on the core cell geometry. This is probably due to the excessive reduction in modulus following densification.

The temperature during thermoforming significantly influences the results. It has been shown that when forming at 220°C [11], the core densification after 25% compressive deformation is almost halved compared to at 200°C (i.e. 95 kg/m³ compared to 111 kg/m³). Consequently, further experiments are needed investigating the mechanical properties following thermoforming at higher temperatures.

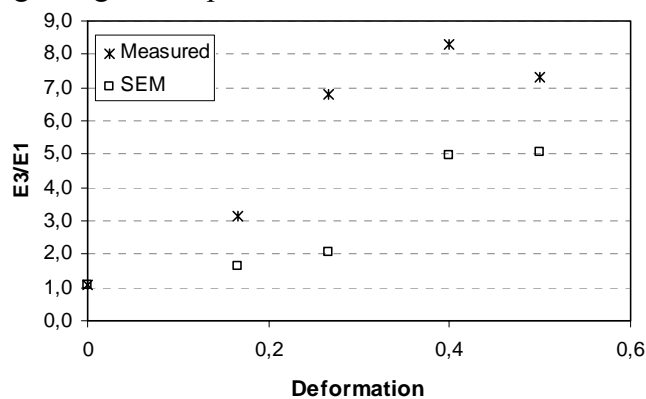


Figure 10. Comparison between measured modulus ratio and estimations from SEM photographs for sample thermoformed in compressive direction

4 CONCLUSIONS

Thermoforming is a promising method for efficient production of polymer foam core

sandwich structures with complex geometry. However, the presented work shows that the compressive mechanical properties changes following thermoforming. Considering the compressive modulus, the properties in the core cell rise direction (tensile direction) increases with 50% for samples thermoformed to 40% elongation. In the transverse direction the trend is opposite, with a reduction of 40%. Corresponding values for the compressive strength is 30% increase/reduction. For the considered thermoforming temperature, excessive elongation (>40%) causes a reduction in the mechanical properties.

Thermoforming in the tensile direction occurs without significant change in density. The study shows that up to the optimal level of maximum tensile deformation, the change in core cell geometry and corresponding mechanical properties can be predicted. The results have been verified by performing measurements from photographs showing the core cell geometry of specimens thermoformed to different degrees of elongation.

For samples thermoformed in the compressive direction densification occurs. At almost 100% increase in density, the compressive modulus increases with 100% in the core cell rise direction and reduces with 80% transversely. However, considering the compressive strength, only a small reduction in the core cell transverse direction can be measured (compared to the virgin core material) and an increase in strength in the core cell rise direction with up to 250%. It has been shown that the trends for the rise direction can be predicted from established models taking the core cell densification into account.

REFERENCES

- [1] O. Rozant, P.-E. Bourban, and J.-A. E. Månson, “Manufacturing of Three Dimensional Sandwich Parts by Direct Thermoforming”, *Composites: Part A*, 32, 1593-1601 (2001).
- [2] L.J. Gibson and M.E. Ashby, *Cellular solid*, 2nd edition, Cambridge (1997).
- [3] A.T. Huber, L.J. Gibson, “Anisotropy of foams”, *Journal of Materials Science*, 23, 3031-3040 (1988).
- [4] R. Akkerman and R. Pronk, “Vacuum forming of thermoplastic foam”, *Polymer engineering and science*, 10, 2064-2074 (1999).
- [5] S. Stutz, *A Model for Foam Deformation at High Temperature*, Department of Aeronautical and Vehicle Engineering, KTH Stockholm, Semester project work (2006).
- [6] S. Ribeiro-Ayeh, *Finite Element Modelling of the Mechanics of Solid Foam Materials*, Dissertation, Aeronautical and Vehicle Engineering, KTH, Stockholm, Sweden (2005).
- [7] J. Grenestedt, “On interactions between imperfections in cellular solids”, *Journal of Material Science*, 40, 5853-5857 (2005).
- [8] A. Kopacs, *Thermoforming of closed cell polymer foam core*, Department of Aeronautical and Vehicle Engineering, KTH Stockholm, Diploma work (2006)
- [9] Personal communication with Alexander Roth, Röhm-Degussa, Germany (2006).
- [10] www.rsbweb.nih.gov (2008)
- [11] J. Fragner, *On the residual compressive properties following thermoforming of closed cell polymer foam core: compressive deformations*, Department of Aeronautical and Vehicle Engineering, KTH Stockholm, Diploma work (2007).

ADVANCED MANUFACTURING OF LARGE, COMPLEX FOAM CORE SANDWICH PANELS

Pierre C. Zahlen^{*}, Martin Rinker[†] and Clemens Heim^{*}

^{*} Composite Technology Center GmbH
Airbus-Strasse 1, 21684 Stade, Germany
e-mail: pierre.zahlen@airbus.com, web page: <http://www.ctc-gmbh.com>

[†] Fraunhofer-Institut für Werkstoffmechanik (IWM)
Walter-Hülse-Straße 1, 06120 Halle, Germany
e-mail: martin.rinker@iwmh.fraunhofer.de, web page: <http://www.iwmh.fraunhofer.de>

Key words: sandwich infusion, load introduction, mould-integrated resin distribution system, automated preforming, liquid composite moulding.

Summary. *Infusion strategies for large, complex CFRP foam core sandwich panels with closed cell foam cores were investigated for open mould liquid composite moulding (LCM) technologies. For closed cell foam core no through the thickness resin flow is possible. If no through the thickness channels in the foam core are being introduced (e.g. open holes, core joints, pins, etc.) the infusion of the sandwich requires resin distribution media on both skins. In a first approach standard distribution medium was used. In a second step a tool integrated resin distribution system was developed for the infusion of the tool-sided skin. To demonstrate that aerospace quality is achievable manufacturing trials with monolithic specimen and complex sandwich panels including damage containment, load introduction and tool integrated resin distribution technology were carried out in a laboratory environment. The investigations show that aerospace quality can be achieved for large CFRP sandwich panels in LCM technology. However the achievable quality depends heavily on the panel/component materials, design details, geometry and the chosen technology approach and strategy for the infusion. Besides the quality factors today's composite aeronautical components have to meet the demand of the market for low cost structures and high production rates. Therefore an industrial concept approach for LCM of CFRP foam core sandwich panels was developed. Conceptual approaches for the key factors of the automation - the automated handling and preforming of the sandwich component – are shown in this paper as well as the results of practical automation trials. Full automation of the manual sandwich lay up process for the considered component complexity is possible. This automation technology has large potentials to increase the profitability and the quality of the parts manufacturing.*

1 INTRODUCTION

Advanced sandwich structures offer a wide range of potentials for the production of commercial aviation's structural applications. Reduced complexity of component surfaces (e.g. no stringers), reduction of parts count and the possibility for tailored reinforcements and

load introduction areas combined with liquid resin infusion technology (LRI) are only some examples for cost and lead-time reduction potentials of sandwich structures [1,8]. However sandwich structures are not yet state of the art for primary commercial aviation structures. One development prerequisite that needs to be fulfilled in order to tap those potentials and deliver a business case is the robust and economic manufacturing of sandwich panels with representative complexity and size in an industrial, commercial aviation environment at high production rates. Therefore this paper discusses different technology elements with respect to feasibility and achievable quality for the advanced manufacturing of large, complex foam core sandwich panels. These technology elements are then being integrated in one industrial concept and results of practical trials for the automated sandwich preform lay-up are presented.

In this context “advanced manufacturing” means that for primary structures of commercial aviation airframe components a high level of quality, automation and process stability has to be achieved for quantities well exceeding 400 airframes per year. “Large” means a typical panel size in the order of magnitude of 6 by 2 meters (and larger) and overall panel thickness in the range of 2 to 40mm (e.g. skin panels of box structures that can be found in vertical and horizontal tail planes and wings). “Complex” means panels with monolithic areas, sandwich areas and transition areas between both as well as local and/or global surface curvature. Moreover complex can mean reinforcements and inserts integrated into the sandwich system. The foam cores considered in this paper are closed cell Polymethacrylimide (PMI) foams.

Remark: The investigations and results presented in this paper are complementary to the work presented during the ICSS 8 by Rinker et al. in the paper “Damage and failure progression of CFRP foam-core sandwich structures“ [13].

2 LIQUID COMPOSITE MOULDING AND SANDWICH INFUSION

Today a large variety of open mould liquid composite moulding (LCM) technologies can be found. Examples for today’s LCM technologies are the Seemann Composites Resin Infusion Molding Process (SCRIMP™; [2,3]), different variants of the Vacuum Assisted Resin Transfer Molding Process (VARTM; e.g. [4, 10]), the Double Bag Vacuum Infusion Process [5], Vacuum Assisted Process (VAP) using semi-permeable membranes [6]. Summerscales and Searle give a detailed review of developments in resin infusion processes [7]. Van Tooren et al. showed the feasibility of sandwich infusion with E-glass fibre and closed cell PVC cores on a general aviation component for low production rates [12].

For a typical LCM build-up the textile, non impregnated, semi-finished products are placed in the mould thus defining the surface shape of the component to-be by the mould surface. The open surface (non mould side) of the semi-finished product stack is then prepared with layers of different auxiliary materials for the infusion process (typically release film with pin holes, peel ply, resin distribution media, resin and vacuum gating, membranes) and sealed by the so called vacuum bagging against the environment. For the impregnation the air within the build-up is being evacuated and the resin infusion is being performed. After full impregnation and curing of the resin, the part can be de-moulded. LCM technologies offer the possibility of

out of autoclave infusion and curing, achieving high fibre volume contents ($\sim 50\%$ - $\sim 60\%$) without high differential pressures ($\Delta p < 10^5$ Pa). Depending on the processing and curing temperatures required by the resin system a chamber oven with atmospheric pressure or the workshop floor at room temperature is used for the infusion in an out of autoclave scenario. If the resin system can be processed at room temperature, the target material properties of the component might also require a post cure after the room temperature curing to reach the needed properties (e.g. T_g).

In order to apply LCM technology for the manufacturing of closed cell foam core sandwich panels one has to provide special means of resin distribution on and/or resin transportation to the mould sided skin. Otherwise a proper impregnation of both skins on large sandwich panels is not possible as the mould sided skin is isolated from the resin distribution on the non mould side of the sandwich panel by the resin tight foam core. Figure 1 shows different means for resin distribution and resin transportation in the sandwich panel. In order to simplify the sketches no auxiliary materials, e.g. resin distribution medium or vacuum bagging, is shown on the sandwich stack. In principle one can introduce holes or channels through the thickness of the foam core as shown in I). Concept II) shows surface grooves or channels in the foam core on the mould side. In III) channels in the tool surface are shown (the so called “tool integrated resin distribution system”) and IV) depicts a layer of resin distribution medium between the tool and the sandwich skin. There are already solution approaches to this problem existing (e.g. [2, 14]).

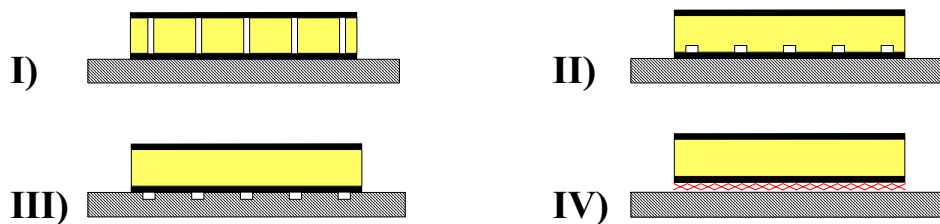


Figure 1: Examples of different concepts for resin distribution and transportation for the mould sided skin of the sandwich panel

For the sandwich studies presented in this paper only concept III) and IV) have been investigated. The vacuum build-up and infusion concept for concept IV) is shown in Figure 2. The vacuum build-up for concept III) is basically identical to concept IV) if one replaces the resin distribution medium by the tool integrated resin distribution system.

The non cured sandwich lay-up with the different auxiliary materials and gating on the tool is being sealed with a vacuum foil against the environment. The resin gating is being connected to the resin reservoir. The vacuum gating is being connected to the vacuum pump via a resin trap. Resin trap and resin reservoir as well as the resin reservoir and the vacuum build up are being connected via closed valves and the build up is being evacuated. Next follows the heating up of the overall build up and of the resin in the resin reservoir to infusion temperature. Because of the pressure difference between the resin reservoir (ambient pressure) and the vacuum in the resin trap and the part the resin will flow via the resin gating into the resin distribution medium. The skins of the sandwich lay-up are then being

impregnated by the resin flow in the thickness direction out of the resin distribution medium. When the part is fully impregnated the resin reservoir will be sealed against the environment and the valve between resin reservoir and resin trap will be used for pressure compensation. Then the component is being cured at curing temperature. Besides temperature and differential pressure the shape and progression of the flow front in the component are important processing parameters influencing the part quality [8].

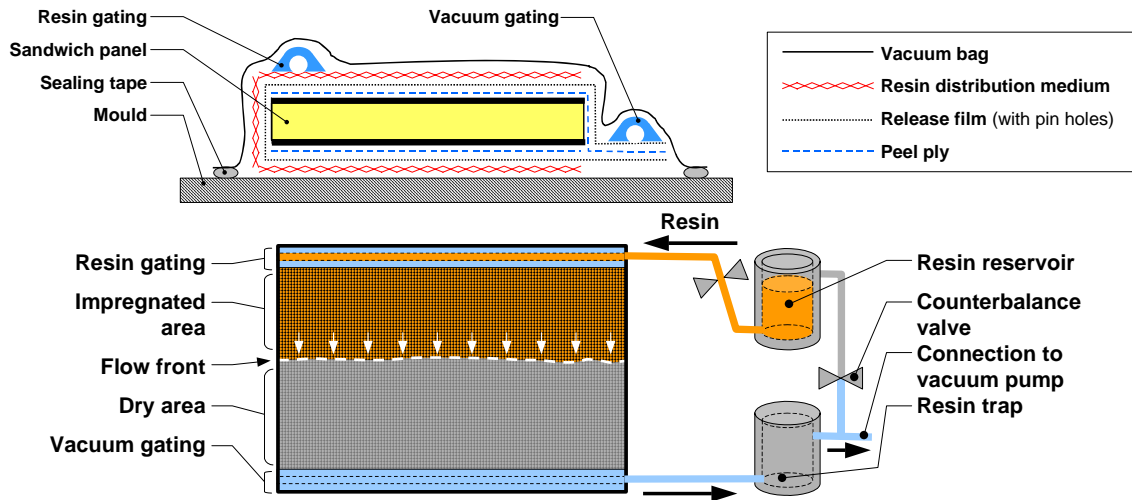


Figure 2: Vacuum build up and infusion concept

3 INFUSION INVESTIGATIONS

The previous chapter describes different means for resin distribution during the infusion of LCM sandwich components. Only the concepts III) and IV) with resin distribution medium on both sides of the sandwich lay-up are being discussed with respect to infusion strategies for large and complex sandwich panels. For monolithic components one sided as well as two sided resin distribution medium was investigated.

Figure 3 shows a large and complex sandwich panel schematically. Typical complexities that have to be considered in order to assess manufacturing feasibility and quality are thick monolithic laminates (A-A) in load introduction areas, sandwich areas (B-B), areas of transition between monolithic laminates and sandwich (A-A) and reinforcing elements to be integrated into the sandwich core for co-curing and/or co-bonding(C-C).

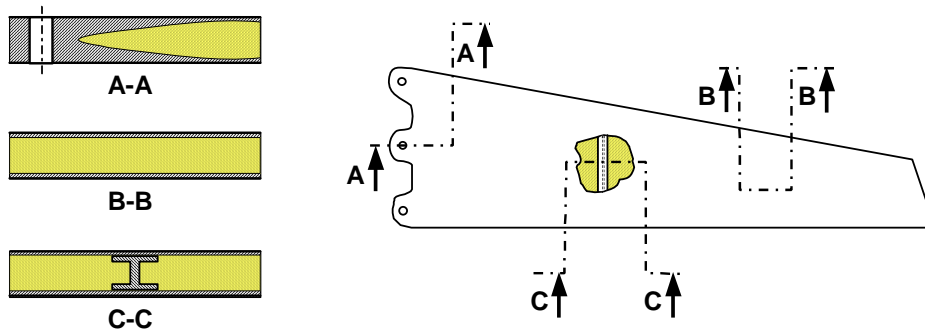


Figure 3: Sketch of large and complex sandwich panel with typical complexities

In the following chapters each one of these complexities will be discussed in isolated investigations looking at infusion behaviour and quality. These findings are then used to develop an infusion strategy for a panel combining the different complexities (in principle as shown in Figure 3) followed by the results of a large scale infusion demonstration test using the proposed infusion strategy.

3.1 Thick monolithic laminates

In order to investigate infusion behaviour, fibre volume content (FVC), porosity and thickness tolerances for thick laminates in LCM technology a **stepped monolithic CFRP wedge** was manufactured (the non impregnated fibre lay-up is shown in Figure 4). The amount of layers increases in four steps (13-, 26-, 52-, 105-layers) and the overall dimensions are ~600mm by ~1140mm. The specimen was built up quasi isotropic out of triaxial non-crimped fabric (NCF) with an area weight of ~415g/m² and HTS fibres. The infusion strategy was straight forward with gating along the complete width on both ends of the lay-up and the infusion direction from the thick to the thin end. The gating system as well as the resin distribution medium was only on the top side of the lay-up. The infusion was performed with Hexcel RTM 6 resin in a chamber oven.

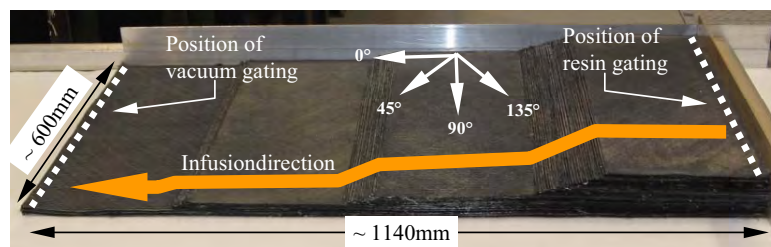


Figure 4: Dry NCF preform in position and ready for vacuum bagging

During the infusion a constant and straight flow front of the resin was observed. As expected the propagation speed of the resin front slowed down at end of the infusion. Visual inspection after demoulding didn't reveal any significant flaws. Thickness measurement was performed for 133 points in each area of constant thickness.

Amount of single layers [-]	105	52	26	13
Average thickness [mm]	39,63	19,66	9,84	4,90
Standard deviation [mm]	0,24	0,15	0,08	0,09

Table 1: Results of thickness measurements of monolithic CFRP wedge

Even for 105 layers a small standard deviation of 0,24mm can be observed.

Destructive testing and optical analysis revealed a porosity below 0,1%. In one area of the panel the ultra sonic NDT showed increased damping. However even in this area the destructive testing revealed a porosity below 0,6%. The fibre volume fraction in the overall component was found to be between 58% and 59%.

With respect to the aerospace application for load introduction the measured thickness tolerances can be handled when considered early in the development phase by design and sizing (cheapest solution with respect to manufacturing). The tolerances could be further reduced by the use of caul plates or a different mould concept for the infusion or by adjusting them at the cured part (e.g. milling or shimming).

3.2 Sandwich areas

One major driver for the qualification of new manufacturing technologies in the aerospace environment is the reproducibility of a constant manufacturing quality. This is fundamental for the investigated infusion concept, because of the manufacturing of large complex sandwich components in one step (one step value creation). A foam core sandwich panel was manufactured according to the principle shown in Figure 2 (~1,2m by ~0,5m overall panel size, 21,5mm overall thickness with a core thickness of 20mm and a $[45^\circ/0^\circ/-45^\circ]_s$ laminate stacking; infusion in the short direction). The investigated sandwich specimens were cut out of this panel and had a final dimension of 550mm x 50mm. During the infusion the visible flow front was very even and a visual inspection of the un-moulded component showed no relevant flaws. To further check manufacturing quality several methods are possible, which can be divided in two main groups: destructive and non destructive testing. Whereas in serial production non destructive testing methods dominate because of lower costs, destructive testing is necessary in research and development projects and finally for qualification. Therefore mechanical tests are necessary to investigate the material and structural behavior and also to validate the calculation method for dimensioning of the component.

For sandwich structures the **4-Point-Bending test** is frequently used, because of the complex load case which can be effectuated for the sandwich [8]. However this test is not only useful for investigation of the material behavior of new sandwich components [13], but also to check the manufacturing quality. A small standard deviation is an indication for good quality during manufacturing. The standard derivation of 6 infusion sandwich specimens was measured for the static breaking load and the associated bending stiffness. It must be declared, that the bending stiffness stated in Table 2 is not the mechanical bending stiffness, but the bending force relating to bending deflection. The test parameters were oriented at the international norm ASTM C 393.

Specimen Number	Breaking Load	Bending Stiffness*
1	1333 N	153,20 N/mm
2	1494 N	161,33 N/mm
3	1324 N	157,43 N/mm
4	1351 N	156,03 N/mm
5	1329 N	146,17 N/mm
6	1320 N	156,03 N/mm
Average	1358 N	155,03 N/mm
Standard Deviation	4,97%	3,28%

*relation of bending force to bending deflection

Table 2: Results of 4-Point-Bending Tests for representative sandwich area

Taking into account that only 6 specimens were tested and the wide range of possible sources of error which can occur in the overall manufacturing process, the measured standard deviation of both breaking load and bending stiffness are very satisfactory and correlate well with the theoretical values.

3.3 Transition from monolithic to Sandwich

Several infusion trials were performed looking at transition areas from monolithic to sandwich. These areas will have to fulfil geometrical requirements as well as load introduction requirements. The general design principle is shown in Figure 5. It can be said that the quality of the components was good if the flow front progression during infusion was uniform. In the monolithic areas of the test specimen resin poorness occurred where irregularities during infusion had been observed. Based on the visual monitoring of the infusion through the window of the chamber oven the reason for these irregularities was race tracking and irregular flow patterns at the specimen boundaries. The boundaries are typical areas, where the geometry and lay up usually didn't fully represent the final component. This can be a source for bagging errors (e.g. wrinkles) supporting race tracking during infusion.

Based on the gathered experience a large test specimen (~2,2m by ~1,2m) for shear-compression tests was manufactured. The geometry and lay up is very close to a final application and hence the boundary conditions for the long sides of the panel were very realistic. Figure 5 shows the manufacturing of this component. During the vacuum bagging one has to be very careful when draping and sealing the open ends of the specimen in order to prevent channels between the specimen and the vacuum bag (typical problem area as described above as there is no smooth transition but rather a step between specimen and tool). Areas like this could be avoided by introducing a smooth transition and trimming of the specimen after curing to the 90° angle required for the test. The flow front during the infusion was very constant. However the flow front on the tool side of the panel was a little faster than the flow front on the visible side, due to the not complete synchronised two flow medium systems. It is planned to investigate inner quality by destructive testing after the shear compression test.

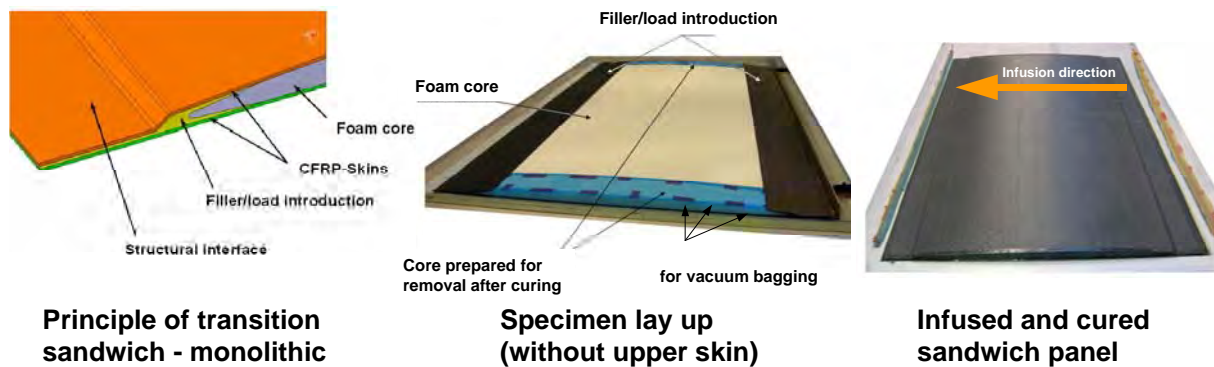


Figure 5: Design principle transition sandwich monolithic and test panel manufacturing

3.4 Sandwich Areas with Integrated Reinforcing Elements

The type of CFRP sandwich structures considered so far (without reinforcements in thickness direction), are optimised for in-plane loads (compression, tension or shear loads), but are not optimised for loads in thickness direction. This behaviour is due to the low foam stiffness and strength compared to the CFRP skins. Reinforcing elements that are integrated into the sandwich (see sketch in Figure 3 showing an integrated double T-beam in section C–C) can increase the transverse stiffness and strength significantly [13]. Besides the potential for load introduction improvement for the sandwich system they have the potential to act as crack stoppers. The range of possibilities to reinforce a sandwich structure is wide, but for the application in commercial aircraft a high ratio of stiffness and strength to weight as well as economic and reproducible manufacturing are key drivers. CFRP reinforcement elements qualify for use because of the demand of low weight. The integration of these elements into the sandwich structure in a one shot infusion process has high cost saving potentials compared to integration after the sandwich fabrication, because no additional manufacturing step on the cured structure is needed. However reinforcing elements can have negative influence on the infusion process. Therefore trials were performed to investigate possible impacts of different integrated reinforcing elements on the infusion process and first results can be presented here. It must be said that the first trials were aimed at a quick understanding of possible effects of reinforcing elements on the sandwich infusion and that the components for these trials were manufactured with very simple hand made methods. Hence large potential for improvement in an industrial process for reinforcement elements manufacturing does exist. This needs to be considered when looking at the presented numbers.

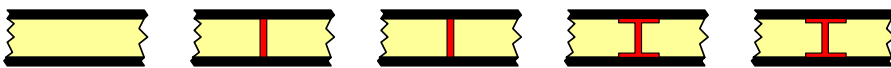
There are generally two basic principles for the integration of CFRP reinforcing elements like pins, I-beams, double T-beams or box sections in the infusion process: If the reinforcing elements are already cured before the assembly and infusion process of the sandwich, they will be bonded (with the epoxy infusion resin as adhesive) to the surrounding core and the textile during the infusion process. This principle is called **co-bonding**. The pre-cured reinforcing CFRP elements are rigid and have their final dimensions before the infusion and curing process for the sandwich panel. This can be a possible error source for minor

manufacturing quality coming for example out of tolerance problems.

The second principle for integration is the co called **co-curing** process. Here the reinforcing elements are preforms of dry carbon fibres. These preforms are assembled together with the sandwich core and skins for a one shot infusion and curing. During this process all CFRP members still have a certain “flexibility”, so less tolerance problems are expected. However there is the danger of undulations and impregnation problems in the reinforcing elements.

The test panels were infused using the same build up and concept as described in Figure 2 (~2,3m by ~0,6m overall panel size, 22,5mm overall thickness with a Rohacell 71 RIST core, a core thickness of 20mm and a [45°/0°/135°/90°/135°/0°/45°] skin laminate stacking; infusion in the short direction, the infusion direction was parallel to the linear reinforcing elements). The reinforcing elements were co-cured as well as co-bonded. During the infusion race tracking along the reinforcing elements was observed. The investigated sandwich specimens were cut out of the panels and had a final dimension of 50mm x 50mm.

In Table 3 the experimental measured strengths of out of plane compression test with reinforced and non-reinforced sandwiches are stated (test according to the German standard DIN53 291). Firstly it must be declared, that the standard deviation of the not reinforced sandwich is very small, which indicates both a high manufacturing quality and a good conducted mechanical test. The manufacturing complexity increases from sandwich without reinforcement to I-beam reinforcement significantly and so the possible sources of errors too. Finally the manufacturing of the double T-beam reinforced sandwich is most complex.



Specimen Number	Without reinforcement	I-Beam Co-bonding	I-Beam Co-curing	Double T-Beam Co-bonding	Double T-Beam Co-curing
C1	4,32 MPa	30,02 MPa	42,79 MPa	39,14 MPa	49,93 MPa
C2	4,30 MPa	28,77 MPa	42,92 MPa	41,67 MPa	45,97 MPa
C3	4,23 MPa	29,66 MPa	46,52 MPa	48,18 MPa	49,35 MPa
C4	4,42 MPa	27,24 MPa	44,65 MPa	41,19 MPa	48,95 MPa
C5	4,29 MPa	27,85 MPa	45,23 MPa	42,42 MPa	49,04 MPa
C6	4,33 MPa	27,99 MPa	45,89 MPa	43,79 MPa	42,68 MPa
Average	4,31 MPa	28,59 MPa	44,67 MPa	42,73 MPa	47,65 MPa
Standard Deviation	1,46%	3,81%	3,45%	7,18%	5,88%

Table 3: Results of out of plane compression test for several reinforcement concepts

The experimental results support these assumptions: The standard deviations increase with the increase of manufacturing complexity. Moreover the results support another assumption: The difference between co-curing and co-bonding technology seems to influence the resulting quality. The co-bonded reinforcements yield increased standard deviations. It is assumed that the co-cured specimens have a higher level of structural integration in the final sandwich than the co-bonded ones as textile reinforcements are permeable for the resin and therefore impose less obstacles for a proper impregnation and bonding to surrounding textile and foam structures. Whereas the pre-cured reinforcing elements are rigid, can block resin flow and

hinder proper bonding of the inner flange and shear web surfaces to the surrounding core structure. Non wetted areas and gaps between the pre-cured reinforcing elements and the core were found in sections of the specimen. In addition the bonding of the cured double T-flange to the textile skin is more critical for the pre-cured reinforcing elements. Basic investigations of pin-reinforcements, followed by a down-selection of the required reinforcing elements as well as further, detailed investigations will have to follow to finally proof these assumptions and optimize the infusion on the overall component.

3.5 Infusion strategy for large sandwich component with combined complexities

The infusion strategy for components discussed in this paper (see Figure 3 and Introduction) is driven by several requirements. Assuming a solid foam core without holes, no through the thickness impregnation in the foam core areas is possible and hence a resin gating/distribution on both sides of the panel is required. Thick monolithic areas require provisions for increased resin feeding during the infusion in order to allow full impregnation. Avoidance of too long impregnation ways and the location/configuration of reinforcements in the part and their influence on the impregnation process will also impose requirements on the layout of the infusion pipework. It is obvious that many influence factors have to be considered in order to achieve an optimised infusion strategy. Figure 6 shows a basic concept for the infusion strategy for the type of components discussed in this paper that is developed with experience coming out of several infusion trials on components (monolithic and sandwich) in the range of approximately 0,5m² to 2m² as described in previous chapters.

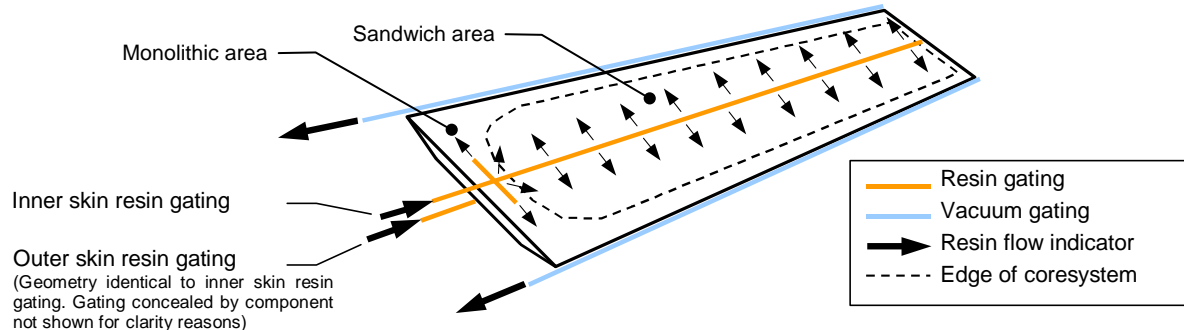


Figure 6: Infusion strategy (mould not shown)

3.6 Large scale CFRP sandwich infusion demonstration

In order to get a first understanding of large scale CFRP sandwich infusion for complex components a manufacturing trial was performed. The test component included thick monolithic areas (~40mm thick), sandwich areas (skin thickness ~1,5mm to 3mm, core thickness ~10mm to ~30mm), as well as transition areas between both. The core was divided into several pieces. The skins were build up out of several triaxial NCF layers (~415g/m² each) according to skin thickness requirements and the transition between monolithic and sandwich areas was built up with woven fabric layers (~360g/m² each). The overall size of the

component was ~6m by ~2m and the infusion strategy described above (see chapter 3.5) was applied. A room temperature, two component resin system with a viscosity in the range of RTM6 was used. With this arrangement it is possible to observe the flow front on the visible (inner) surface of the component during the infusion. The flow front developed as expected and was quite even during the infusion which took about 1,5 hours. Future manufacturing trials will have to show the feasibility of this infusion strategy with the final materials, inserts and reinforcements configuration.



Figure 7: Large scale sandwich infusion demonstration (manual lay-up and infusion)

4 TOOL INTEGRATED RESIN DISTRIBUTION SYSTEM

As already discussed it is necessary to provide a resin distribution system on both sides of sandwich panels with closed cell foam core. The concepts I) and II) illustrated in Figure 1 (holes through the foam or grooves in the foam surface) will require machining of each foam core before processing. Moreover there will be areas of pure resin in the finished components which will lead to extra weight and probably crack initiation problems. The tool integrated resin distribution system doesn't have these disadvantages. However it needs to be investigated if this technology is applicable to the LRI process in an industrial environment. Therefore investigations with an integrated resin distribution system were performed. The principle is based on resin distribution via small channels in the tool surface. During the lay up peel ply is put onto the tool followed by the CFRP skins with the core material. Next follows the usual vacuum bagging and gating system installation.

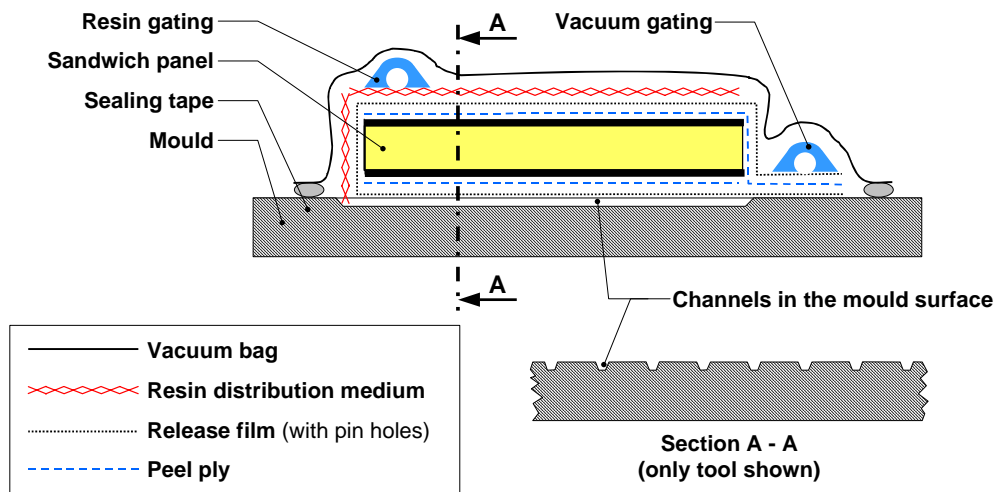


Figure 8: Infusion concept with tool integrated resin distribution system

The distribution of the channels over the tool is important, because depending on the shape and arrangement (e.g., straight channels, diamonds, etc.) the flow front of the resin is affected. For example, resin can specifically be directed at certain areas of the part. Also, the geometry of the channels and the effective cross-section influences the distribution of the resin. Channel size and geometry must be chosen in a way, that on one hand the channels are large enough to distribute the resin as needed, but on the other hand they have to be small enough to avoid imprints and fibre undulation in the part. It was found out, that the surface quality of components manufactured in LRI with a tool integrated resin distribution system is comparable to a component manufactured on a common steel tool without channels. The only difference is the surface roughness because of the peel ply that is needed in order to remove the resin channels from the component surface after curing and de-moulding.



Figure 9: Tool integrated resin distribution system and component surface

The are large potentials in this technology, especially if one looks at the large structures under discussion in this paper. In order to be able to exploit this technology in an industrial environment further research is required in the area of resin flow behaviour and the interaction between component design, thickness distribution and corresponding channel distribution and channel geometry.

5 INDUSTRIAL CONCEPT

So far the investigation discussed the different manufacturing complexities for advanced manufacturing of large, complex foam core sandwich panels in infusion technology. Integration of the basic technologies (without core-integrated elements) was shown in a large sandwich infusion demonstration. A concept for embedding these technologies in an industrial concept is described in the following chapters. The proposed concept focuses on automated processing of the build up and preparation for infusion.

5.5 Process chain overview

The basic process chain of the industrial concept is shown in Figure 10. The preparation of the tool is followed by the lay-up of the semi-finished products and auxiliary materials inside the tool. Next the sealing of the vacuum bagging and preparation for the infusion is done, followed by the infusion and curing process in the oven.

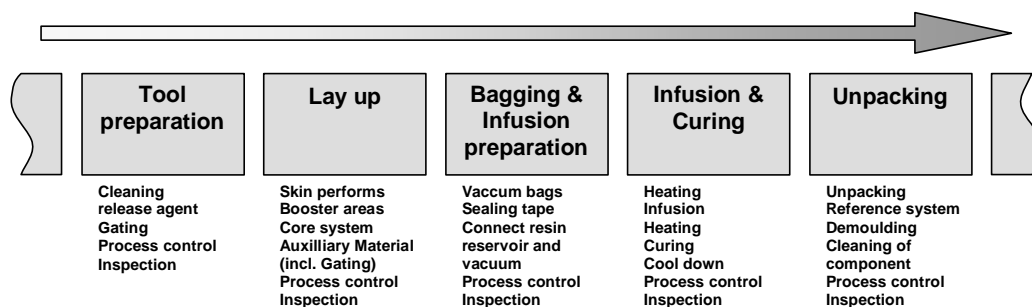


Figure 10: Basic process chain of the industrial concept

During the **tool preparation** resin residua have to be removed from the tool surface. An automated approach could be surface blasting with carbon dioxide ice which disappears without residua on it's own [11] combined with rotating brushes. This cleaning process can be highly automated. An optical control either by a worker or a digital camera-computer system with optical recognition analysis ensures a properly cleaned tool. A good overview of candidates for optical recognition technologies is given in Weimer et al. [9]. These optical recognition technologies could be transferred to the requirements of a tool surface quality control with respect to resin residua. After the cleaning the surface preparation of the tool follows. The state of the art approach are release agents that are being applied to the surface in liquid state manually or automated followed by a further optical control. Next follows the preparation of the tool sided resin infusion gating and connection tubes. In the **lay-up** process the different auxiliary materials, textiles and core elements are being positioned into the

prepared tool. The last step is the lay-up and installation of the resin infusion and vacuum gating. These lay-up activities can be done by hand or in an automated manner with customised vacuum bagging and gating. However the fully automated lay-up of a textile sandwich preform in the dimensions and complexity discussed here is not state of the art therefore it will be discussed in more detail later on. During the **bagging and infusion preparation** the sandwich lay-up will be sealed on the tool against the environment with vacuum tight foils and sealing tape. The different gating systems are being connected to the resin reservoir and the vacuum pump respectively. Alternatively they could be connected to a quick coupling adapter on the tool that can be automatically or manually coupled to the resin and vacuum supply in the oven. This quick coupling adapter could also be used as the interface for process control sensors on the tool or in the sandwich lay-up (e.g. temperature sensors). After a successful vacuum test follows the transfer of the prepared vacuum build up on the tool into the oven for **infusion and curing**. Then the oven is heating up to infusion temperature, the sandwich lay-up is being infused, cured and cooled down. After disconnecting the supply and sensor connections the cured component in the tool will be transferred to the **unpacking** station. Here the vacuum bagging and gating on top of the component will be removed. Before de-moulding of the component the reference system has to be transferred from the mould to the tool. Once de-moulded the component will be cleaned and is now ready for follow on process steps.

If it is sensible, with respect to the business case, all the described processes have high potential for automation and can be considered to be medium risk technologies with respect to automation. However the lay-up of the textile sandwich preform is considered to be of high risk with respect to full automation. Nevertheless it is very lucrative to look at the automation of the sandwich lay-up from the value creation point of view. Design and Manufacturing trials showed that for the type of components under investigation the amount of single textile layers can easily go beyond 600 to 700 pieces, most of which are quite long and slender. In a manual labour process this will result in a time consuming lay-up work including a high risk of quality issues (e.g. lay-up accuracy and reproducibility, alignment and fibre orientation errors, damaging and distortion of fibre layers). In a process optimised for an industrial environment the amount of single layers needs to be reduced by bundling of single layers with adequate performing concepts. Moreover one could think of skin layer preforms already including auxiliary materials like peel ply, membranes or distribution media (e.g. connected to skin layer by stitching or binder). However for the automation trials described in this paper the worst case scenario was assumed: the lay-up of a large amount of single layers enclosing the sandwich core without prior preforming.

5.6 Lay-up automation trials for CFRP sandwich preforms

Automation trials for fully automated sandwich preforming were performed with a KUKA robot at the Composite Technology Center GmbH in Stade (CTC GmbH). With the given equipment a full scale trial was not possible. For capability assessment it was decided to choose the transition area between thick monolithic CFRP and the sandwich area as depicted in Figure 3 cut A-A. This area contains a sandwich core with complex surfaces that is

completely embedded in CFRP layers. The component size for these trials was ~1m by ~1,8m with monolithic CFRP areas of up to ~37mm thickness and sandwich areas with ~30mm core thickness and ~2,6mm skin thickness. An experimental vacuum gripping system was designed and build for the robot head with a vacuum valve system that can be controlled by the robot's control unit. Only the reinforcement layers embedding the core and the core itself were automatically laid up, the outer skins were laid up manually as the experimental gripping system wasn't large enough due to weight restrictions imposed by the robot.

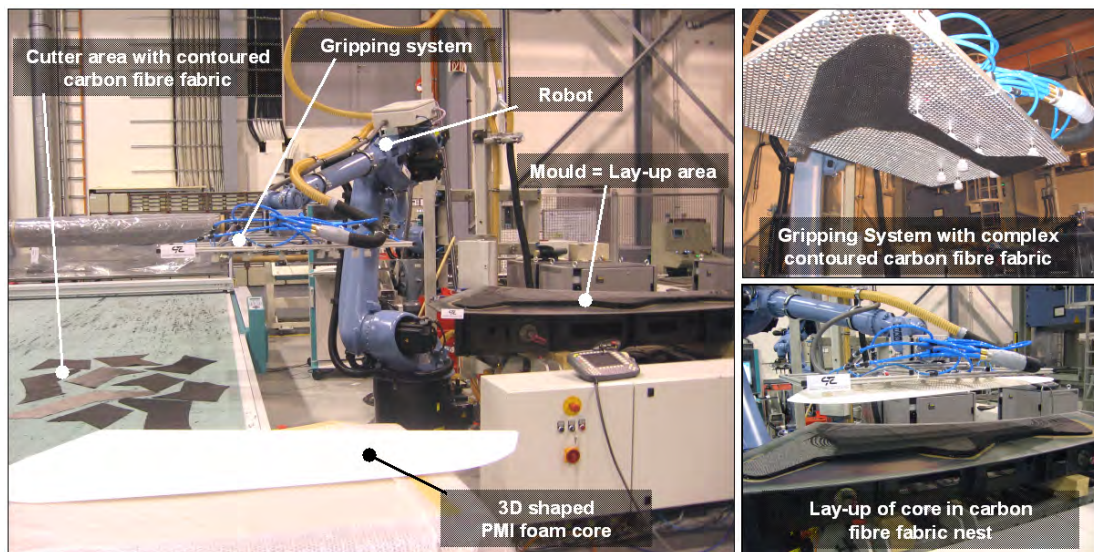


Figure 11: Lay-up automation trials with robot at the CTC-GmbH in Stade

Figure 11 shows the robot with the experimental gripping system next to the CFRP cutter, the experimental mould and the core system in the forefront of the main picture. The trials showed that the planned automation is possible with commercial of the shelf components and a simple custom made frame for the vacuum gripper field. Although only 8 control channels for the 16 vacuum suction cups were available it was possible to handle all the complex single layers of the component area under investigation. Travelling speeds of the gripping system on the robot was up to approx. 1m/sec with higher speeds technically possible if more suction cups and more vacuum capacity can be provided in order to avoid losing of single layers during the transition from the cutter to the lay-up area. The robot manual states a repeat accuracy of +/- 0,15mm. This accuracy doesn't include possible influences of the experimental griping system (e.g. flexibility of the suction cups). Repeat accuracy trials should be performed to quantify possible influences. However from the gathered experience so far it is assumed that a repeat accuracy in the range of the robot can be achieved. If improvement of overall lay up accuracy is necessary or if further sources of tolerances have to be considered (e.g. positioning accuracy of the lay-up mould relative to the robot-cutter system) a wide range of commercially available technologies could be utilised in order to improve positioning accuracy (e.g. highly precise mechanical positioning aids, optical systems for positioning adjustment).

The lay-up test component was preformed after 50% of the lay-up work (i.e. half of the panel including the foam core). A single bag vacuum build up was sealed over the component in the mould and vacuum and heat was applied in a chamber oven. After the preforming the foam core was removed for visual inspection of the preform. The obtained preform looked very good and uniform with smooth and accurate thickness transitions. Further preforming and infusion trials will have to be performed in order to quantify the achievable quality for components manufactured in this automated way.

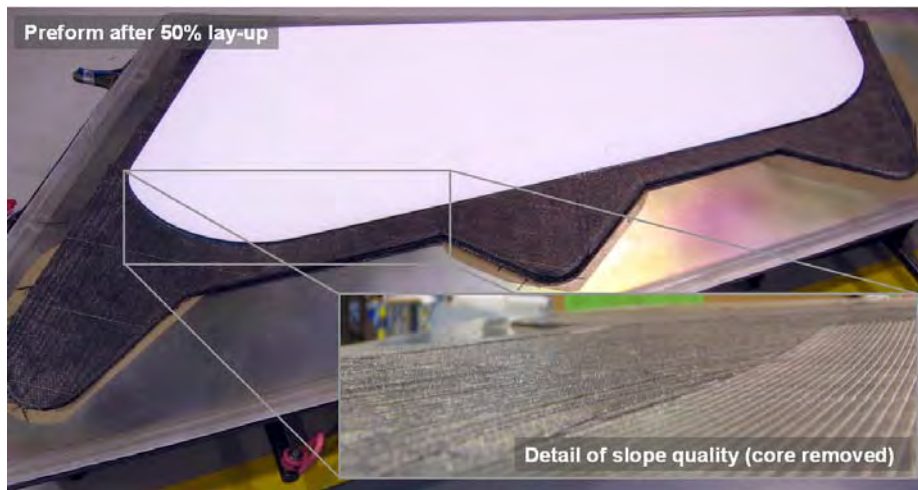


Figure 12: Automatic lay-up after preforming in a chamber oven

For a full scale application a larger cutter area and robot with greater range and larger gripping system would be required to handle a bigger amount of larger, different single layers. It was already mentioned that the situation investigated here is a worst case scenario. In a mature concept the amount of layers can be reduced through proper preforming and the area required for supplying the textile components to the robot can be reduced by a storage and logistic centre.

9 CONCLUSIONS

Manufacturing trials and quality investigations for large, complex foam core sandwich panels showed that high quality parts with a complexity going beyond flat and rectangular sandwich panel is possible. The achievable quality depends heavily on the panel/component materials, design details, geometry and the chosen technology approach and strategy for the infusion. Although complex specimen were manufactured all of the presented investigations are still simplified manufacturing trials. The geometrical boundary conditions and local design resulting from these simplifications can have negative influence on the infusion process. Unfortunately the optimisation of these boundary conditions with respect to the manufacturing trial can increase the specimen complexity significantly. If the component design requires the integration of core reinforcing elements there can be a major impact on achievable part quality and economic manufacturing. In further investigations the detailed

need for the design of reinforcing elements and their arrangement in the large component needs to be further detailed to focus the investigations. Further test infusions of large and complex components including final reinforcement element strategy and resin system need to be conducted.

Tool integrated resin distribution system is an alternative to resin distribution media and will increase part surface quality as well as the manufacturing economics. The lay-out and feasibility is heavily depending on the final textile build up and geometry of the target component as these inputs are required for the distribution grid optimisation. Further investigations will have to follow.

The proposed concept for fully automated preforming of sandwich components showed very promising results. Full automation of the manual sandwich lay up process for the considered component complexity is possible. This technology has large potentials to increase the profitability for the manufacturing. For infusion processes small differences in the component lay up can have large negative impacts on the process. The proposed automation will deliver a higher degree of accuracy and reproducibility compared to the manual lay up and hence increase the quality of the parts.

10 ACKNOWLEDGEMENT

The work presented in this paper was partially funded by the *Bundesministerium für Wirtschaft und Technologie* of Germany (Federal Ministry of Economics and Technology). The authors wish to acknowledge this support.

REFERENCES

- [1] A. S. Herrmann, P. C. Zahlen, I. Zuardy, "Sandwich Structures Technology in Commercial Aviation", 7th International Conference on Sandwich Structures, Aalborg, Denmark, (2005).
- [2] W. H. Seeman, "Plastic Transfer Molding Techniques for the Production of Fiber Reinforced Plastic", US Patent US 4.902.215, (1990).
- [3] W. H. Seeman, "Plastic Transfer Molding Apparatus for the Production of Fiber Reinforced Plastic", US Patent US 5.052.906, (1991).
- [4] E.J. Rigas, T. J. Mulkern, "Process and Apparatus for Improved Composite Fiber Volume Fraction and Dimensional Stability by Removal of Accumulated Excess Resin Using the Vacuum Assisted Resin Transfer Molding (VARTM) Process", US Patent US 7.147.818 B1, (2006).
- [5] J. C. Waldrop et al., "Double Bag Vacuum Infusion Process for Manufacturing a Composite and Composite Obtained Thereby", European Patent EP 1 235 672 B1, (2005).
- [6] J. Filsinger et al., "Verfahren und Vorrichtung zur Herstellung von faserverstärkten Bauteilen mittels eines Injektionsverfahrens", German Patent DE 100 13 409 C1, (2000).
- [7] J. Summerscales, T. J. Searle, "Low-pressure (vacuum infusion) techniques for moulding large composite structures", Proceedings of the Institution of Mechanical Engineers, Part L: Journal of Materials: Design and Applications, ISSN 1464-4207, Volume 219,

- Number 1/2005, Professional Engineering Publishing, (2005).
- [8] M. Rinker, P. C. Zahlen, R. Schäuble, “Herstellung von CFK-Sandwichplatten: Untersuchung des Verformungs- und Versagensverhaltens”, *Konstruktion Zeitschrift für Produktentwicklung und Ingenieur-Werkstoffe*, ISSN 0720-5953, Ausgabe 7/8 2007, pages IW6-IW9, Springer-VDI-Verlag, (2007).
 - [9] C. Weimer, A. Miene et al., “Prozessbegleitende Schadensanalyse (PROSA) - Ein wesentlicher Baustein für die kosteneffiziente Fertigung und Analyse von CFK-Strukturen”, *Deutscher Luft und Raumfahrt Kongress 2006*, Braunschweig, Germany, DGLR, (2006).
 - [10] T. Shono et al., “A-VARTM Technology Application for Japan’s New Regional Jet Aircraft“, *16th International Conference on Composite Materials*, Kyoto, Japan, (2007).
 - [11] G. Spur, E. Uhlmann, F. Elbing, “Dry-ice blasting for cleaning: process, optimization and application“, *Wear*, Volumes 233-235, December 1999, Pages 402-411, Elsevier, (1999)
 - [12] M. J. L. van Tooren, M. P. Dirven, A. Beukers, “Vacuum Injection in Aviation Manufacturing Processes“, *Journal of Composite Materials*, Vol. 35, No. 17, Sage Publications, (2001).
 - [13] M. Rinker, P. C. Zahlen, R. Schäuble, “Damage and failure progression of CFRP foam-core sandwich structures“, *8th International Conference on Sandwich Structures*, Porto, Portugal, (2008).
 - [14] E. N. McClure, S. A. Jackson, P. J. Sweesy “Grooved Core Pattern for Optimum Resin Distribution”, *US Patent US 6.656.411*, (2003).

